UC Berkeley
UC Berkeley Electronic Theses and Dissertations

Title

From the Molecular to the Bulk: A Size-Resolved Perspective on the Structural and Thermodynamic Properties of Hydrated Ions

Permalink
https://escholarship.org/uc/item/8s68p6d9

Author

Cooper, Richard J.

Publication Date

2016

Peer reviewed|Thesis/dissertation

eScholarship.org Powered by the California Digital Library
University of California

From the Molecular to the Bulk: A Size-Resolved Perspective on the Structural and Thermodynamic Properties of Hydrated Ions

by

Richard John Cooper

A dissertation submitted in partial satisfaction
of the requirements for the degree of

Doctor of Philosophy

in

Chemistry

in the

Graduate Division

of the

University of California, Berkeley

Committee in Charge:
Professor Evan R. Williams, chair
Professor Kristie A. Boering
Professor Robert M. Glaeser

Fall 2016

From the Molecular to the Bulk: A Size-Resolved Perspective on the Structural and Thermodynamic Properties of Hydrated Ions

©2016

by

Richard John Cooper

Abstract

From the Molecular to the Bulk: A Size-Resolved Perspective on the Structural and Thermodynamic Properties of Hydrated Ions

by

Richard John Cooper

Doctor of Philosophy in Chemistry

University of California, Berkeley

Professor Evan R. Williams, Chair

In this dissertation, phenomena related to ion hydration are investigated in gas-phase clusters of ions and water molecules. Hydrated ions are generated using electrospray ionization and trapped using a Fourier transform ion cyclotron resonance mass spectrometer. A variety of ion activation techniques are used to probe the structures and reactivities of these ions, including infrared photodissociation (IRPD), ultraviolet photodissociation, blackbody infrared dissociation, and electron capture dissociation. IRPD spectra of alkali metal ions, ion pairs, and the protein denaturant guanidinium reveal how the delicate balance of noncovalent interactions between ions and water molecules establishes inner shell hydration motifs that can affect the hydrogen bond network of surrounding water molecules. In the case of guanidinium, molecular hydration structures determined by IRPD spectroscopy and *ab initio* calculations reveal that the ion is amphiphilic, and this is related to its bulk property as a protein denaturant in solution. The effects of ions on the hydrogen bond network of water are investigated by studying extensively hydrated ions in nanometer-sized droplets, or "nanodrops". IRPD spectra of nanodrops containing a single La^{3+} ion and up to 550 water molecules indicate that the trivalent ion can frustrate the onset of crystallinity in these cold water clusters by altering the hydrogen bond network of water located remotely from the ion. Spectroscopy of nanodrop surfaces provides further evidence that multiply charged ions can affect the structural and electrostatic properties of nanodrops. These experimental data are supported by molecular dynamics simulations analyzed with custom-built software, and provide compelling evidence that ions can affect the structure of water well outside the first solvation shell – a point of contentious debate in the current literature. Using an extrapolation method, properties derived from cluster measurements such as surface "free" O–H stretching frequencies are related to their corresponding values at neutral interfaces, providing a link between cluster and bulk measurements. In addition to the aforementioned structural studies, thermodynamic information about the reductions of hydrated transition metal ions is obtained using the ion nanocalorimetry technique. A major improvement to this technique is introduced where ion-electron recombination energies are derived from laser calibration experiments. A value for the absolute reduction potential of the standard hydrogen electrode is deduced from the absolute reduction potential measured for the Cu^{2+}/Cu^{+} redox pair, which should be more accurate than previously reported values. Ion nanocalorimetry is also used to measure, for the first time, the one-electron reduction potentials of several transition metal ions that are difficult to probe in solution due to the phenomenon of potential inversion.

This work is dedicated to my parents

Table of Contents

.

Acknowledgements

This dissertation would not have been possible without the guidance and support of many people. First and foremost, I would like to thank Prof. Evan Williams for instilling in me the qualities needed to conduct high-quality scientific research. Of equal importance, he taught me how to communicate my results effectively both in writing and orally. The numerous group meetings and manuscript drafts were crucial to my development as a young scientist, and Evan devoted considerable time and effort to these activities.

My parents, Dr. Michael Robert Cooper and Mrs. Linda Worch Cooper, have always emphasized the importance of education and have encouraged me in all of my endeavors. While my interests have changed throughout time, their support has remained steadfast. Moving across the country to purse my scientific passions was a big change for my family, and I thank them for their understanding.

Throughout my graduate career I have drawn inspiration from the incredibly talented mentors that I have had the opportunity to learn from. I would like to thank my first mentor, Dr. Terrence Chang, for his warm introduction to research in the Williams group and for his patience while teaching me the ropes on our experimental setup. Our friendship outside of the lab and his sense of humor made adjusting to life in graduate school much easier. Dr. Sven Heiles was also responsible for a large part of my scientific maturation. Sven's passion for science and piercing intellect made a large impression on me, and his attitude towards research is infectious. This greatly helped me to "jump start" my own scientific career. Our collaborations remain the highlight of my academic life at Berkeley.

The greatest asset of the Williams group is its people, and I have always enjoyed working and conversing with other group members. I hope that the friendly and supportive group ethos continues to thrive well into the future. I want to acknowledge Matthew DiTucci for his instrumental role in my research. We have worked together to solve the toughest problems I have ever encountered, and without his help my progress would have advanced much more slowly. Our shared interests outside of lab – music, beer, and splatoon – made me look forward to coming into work every day even during difficult times.

I would like to thank my roommates of five years and good friends, Andrew Neel and Anna Parker, for making life outside of lab a blast. Exploring the great state of California with all of my Berkeley friends will be something that I can always cherish.

My girlfriend Nicole deserves much credit for patiently understanding the late nights and long hours this job sometimes requires. Her presence in my life is a great source of joy for me, and brings perspective to my scientific career. Our many adventures outside of lab, including shredding gnar in Tahoe and backpacking, have greatly enriched these past 5 years.

Finally, I would like to thank my dissertation committee members, Prof. Kristie Boering and Prof. Robert Glaeser.

Chapter 1

Introduction

1.1 The Cluster Approach

Noncovalent interactions between ions, biomolecules, and water are essential for many physical processes and govern much of the rich chemistry of life. These noncovalent interactions include hydrogen bonding, Coulomb forces between permanent charges, and van der Walls interactions. Although the strengths of these interactions are typically much weaker than covalent and ionic bonds, multiple noncovalent interactions can act in concert to produce highly specific and stable associations between portions of macromolecules and even complexes of macromolecules. Perhaps the most well known example of this is the helical structure of DNA that is imparted by specific, directional hydrogen bonds between nucleobases. On the molecular level, these interactions can be fleeting and yet are responsible for the proper function of physiological processes. One example of this is potassium ion channel proteins that are found in the majority of living organisms and that regulate muscular and neurological signaling. Ion channel proteins are embedded in cellular membranes and regulate cellular potentials by the selective transmission of potassium ions either into or out of the cell. The basis of this selectivity arises from interactions between the potassium ion and backbone carbonyl groups in the pore of the membrane protein.[1-3] As the potassium ions pass through the pore, they must shed their inner hydration shells, and the pore architecture stabilizes this transition by mimicking the electrostatic environment of the inner hydration shell. Ions that have larger or smaller hydration shells are not transmitted through the membrane. Numerous other examples of ion-water interactions abound, some of which have implications for geophysical processes. In the earth's atmosphere, ion-induced nucleation is a significant pathway to aerosol formation.[4-6] Electrostatic interactions between ions such as HSO_4^- and water vapor can stabilize embryonic particles and lower the barrier to nucleation. Understanding these noncovalent interactions in detail is therefore a prerequisite for understanding complex physicochemical processes.

It is well known that interactions between ions and water molecules can also lead to changes in the macroscopic properties of the solvent. Dissolved ions affect the physical properties of water including its viscosity, density, surface tension, and conductivity. Ions can even affect the phase of water by depressing its freezing point. While bulk properties of ionic solutions can readily be measured, obtaining a molecular-level understanding of the origins of these properties is less straightforward. A variety of spectroscopic techniques including vibrational,[7-12] THz,[13-15] NMR,[16,17] and x-ray absorption[18,19] spectroscopies have been used to investigate how ions affect the dynamics of water in ionic solutions and to assess how ions change the hydrogen-bonded structure of the solvent. Scattering techniques such as neutron diffraction can provide structural information about the inner hydration shells of ions.[20-22] However, deducing detailed information about specific noncovalent interactions in experiments probing the condensed phase is challenging for several reasons. Because bulk solutions must be electrically neutral, counter-ions are always present which makes it difficult to characterize interactions between a single ion and water. There is evidence that the effect of ions and counter-ions on the dynamics of water can be interdependent and nonadditive,[9] obfuscating the interpretation of experimental results. Furthermore, the high concentrations of ions that are necessary for many of these techniques (~1–6 M) limits the available hydration water for each ion and can lead to ion pairing. Other factors such as the presence of impurities in samples as well as the interfering signal from bulk water can also complicate analysis of these measurements.

An alternative approach is to investigate ion hydration in gaseous clusters of ions and water molecules. These experiments often take advantage of the mass-to-charge (m/z) selectivity of mass spectrometers to isolate specific systems of interest. Hydrated ions can be generated directly from aqueous electrolyte solutions using electrospray ionization and transferred into ion traps where information about their structure, reactivity, and energetics can be obtained using a variety of techniques. The precise control over system composition is the chief advantage of this approach, and hydrated cations,[23-28] anions,[29-33] and even ion pairs[34-37] have been studied in isolation. One major question that arises in the context of cluster studies is how do the results and conclusions from gas-phase experiments relate to those made in solution? A promising way of addressing this issue is by measuring cluster properties as the extent of hydration is increased. By investigating the step-wise solvation of ions it is possible to link the properties of ions in the gaseous and condensed phases, and to characterize the transition between them. An illustrative example comes from gas-phase studies of hydrated SO_4^{2-} clusters. In solution, the ion is stable, but as a bare anion SO_4^{2-} is inherently unstable due to the electrostatic repulsion between its electrons and will spontaneously eject an electron.[38,39] Photoelectron spectroscopy and mass spectrometry experiments on mass-selected $SO_4^{2-}(H_2O)_n$ clusters indicate that at least three water molecules are needed to stabilize the dianion against electron ejection.[40,41] Measurements of the ionization energies of $SO_4^{2-}(H_2O)_n$ clusters indicate that as the extent of hydration is increased from $n = 4$ to to $n = 40$, the ionization energies smoothly approach their bulk value.[42] Other cluster properties have also been observed to converge to bulk properties, as will be discussed in detail below. Gas-phase measurements on size-selected hydrated ions overcome many of the challenges inherent in condensed-phase measurements and can offer complementary information.

1.2 Probing Hydrated Ion Structure with Infrared Photodissociation Spectroscopy

In infrared absorption spectroscopy, the property that chemical bonds have characteristic stretching frequencies is exploited to infer structural information about molecules. Performing direct infrared absorption experiments on ions is typically not feasible under laboratory conditions due to the low sensitivity of the technique. Relatively high number densities of gas phase molecules are needed for absorption experiments (~10^{10} molecules/cm^3)[43] whereas space-charge effects limit the number densities of ions trapped in mass spectrometers to ~10^8 molecules/cm^3.[44] Infrared spectra of gaseous ions are typically acquired using "action" spectroscopies such as infrared photodissociation (IRPD) spectroscopy.[45-48] The absorption of one or more infrared photons can induce the fragmentation of an ion, and this mass change can easily be detected in a highly sensitive mass spectrometer. The extent of fragmentation will be greater when the incident photon energy is resonant with a vibrational mode of the ion. An infrared photodissociation rate constant can be calculated from the extent of fragmentation measured after a set irradiation time, and IRPD spectra are constructed by plotting these rate constants as a function of photon energy. Over the past two decades, tunable infrared laser sources have become widely available, which has rapidly accelerated the adoption of this technique.[46] Table-top laser systems that include 1064 pump lasers and optical parametric amplifiers and oscillators (OPO/OPA) produce tunable light in the mid-infrared range (~1000–4000 cm^{-1}) and are relatively inexpensive (< $100K). The particular system in use at Berkeley can generate modest power (~10–50 mW) from ~2600–4000 cm^{-1} where O–H, N–H, and C–H stretches occur.[49] This commercial laser system is coupled to a home-built 7.0 T Fourier transform ion cyclotron resonance (FT-ICR) mass spectrometer. The advantages of using a FT-ICR mass spectrometer for these photodissociation experiments are that ions can be easily stored, temperature controlled and manipulated in the ion trap and that it is straightforward to achieve overlap between the infrared beam and trapped ions.

Two questions that frequently arise when discussing the IRPD technique are how closely do IRPD spectra resemble infrared absorption spectra and how, in detail, do any differences emerge? For ions with high internal energies and low barriers to dissociation, the absorption of a single photon can be sufficient to induce photodissociation on a time scale faster than the energy can be radiatively re-emitted, and in these cases the IRPD spectra will resemble linear absorption spectra.[45] Ions with higher barriers to dissociation or lower internal energies may require the absorption of several infrared photons to produce measurable photodissociation on the time scale of the experiment. This process involves gradual ion heating where the energy of each absorbed photon is statistically redistributed throughout the vibrational modes of the ion by a process known as intramolecular vibrational relaxation (IVR).[50,51] For ions where multiple photons are required for dissociation, infrared frequencies and intensities can deviate from linear absorption spectra. To circumvent this obstacle, ion "tagging" techniques have been developed where molecular messengers such as H_2, Ar, He, and Ne are introduced into the ion trap where they can form weak associations with ions at low temperatures (~4–40 K).[52-57] Under these conditions, the absorption of a single photon by the ion is sufficient to detach these weakly bound molecules such that linear, high-resolution spectra can be obtained. A disadvantage of this approach is that the molecular tags can perturb the structure of the ion itself leading to large frequency shifts. For example, photodissociation experiments on H_2-tagged protonated glycine indicate that tagging can shift the frequency of the carboxylic acid O–H stretch by 55 cm^{-1}.[58] In the experiments described herein, a tag-free approach is taken. Hydrated ions are equilibrated to 130 K in the trap such that they often have sufficient internal energies to dissociate from the absorption of ambient blackbody photons. Dissociation occurs by the sequential loss of water molecules from the cluster ion. The absorption of a single infrared photon will increase the rate of dissociation, and in such cases IRPD spectra resembling linear absorption spectra can be obtained.[59]

1.3 Isolating Ion-Water and Water-Water Interactions

1.3.1 Specific Ion Effects.

Many physical properties of ionic solutions exhibit nonideal behavior and depend strongly on the identity of the ions, and these "specific ion effects" play important roles in chemistry and biology. IRPD spectroscopy is ideally suited to study specific ion effects because it can be used to investigate the structures of individual ions in isolation. It has long been established that the solubilities of proteins in water can be significantly altered by the addition of salts.[60] The ordering of cations and anions on their ability to precipitate or solubilize proteins in solution is known eponymously as the Hofmeister series (Figure 1.1). Anions generally exhibit a wider range of Hofmeister behavior than cations,[61] with strongly hydrated anions like sulfate and fluoride promoting folded protein structure and more weakly hydrated ions like thiocyanate tending to denature proteins. Cations have a weaker effect on protein structure than anions, but there are notable exceptions like the common protein denaturant guanidinium. Remarkably, the Hofmeister series correlates with a broad range of physical properties including nonionic surfactant solubility,[62] enzyme activity,[63] surface tension,[64] ion hydrodynamic radii,[65] and the surface activity of ions.[66] Despite the well-established ordering of these specific ion effects, the molecular underpinnings of the Hofmeister series remain hotly debated.[61,67-72] There are two principal schools of thought on how ions can affect protein solubilities. One mechanism, proposed by Franz Hofmeister himself, is that ions can affect the bulk hydrogen bond network of water and thereby either strengthen or weaken the hydrophobic effect. The other mechanism is that direct noncovalent interactions between ions and the protein backbone or side-chains can affect protein structure. The extent to which each of these mechanisms plays a role in observed Hofmeister phenomena is unclear.

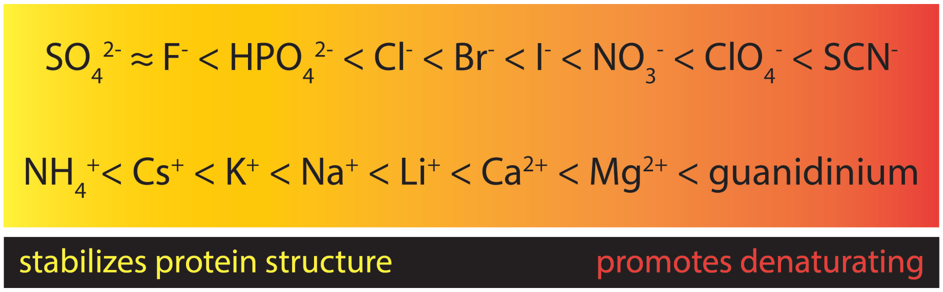

Figure 1.1 Typical Hofmeister Series

The traditional explanation for Hofmeister phenomena is that strongly hydrated ions (kosmotropes) can induce structural changes in the hydrogen bond network of water that strengthen hydrogen bonding between water molecules, whereas more weakly hydrated ions (chaotropes) tend to weaken hydrogen bonding between water molecules. This is important because in order for a protein to unfold it must create a cavity in the solvent to accommodate the larger, disordered structure. The free energy barrier associated with creating this cavity will be higher in solutions where interactions between ions and water molecules are stronger.[73] Historically, evidence for this theory came from neutron diffraction experiments as well as size exclusion chromatography on hydrated ions that suggest some ions can affect water molecules outside of their first hydration shell.[72,74] More recently, the ability of ions to affect the hydrogen bond network of water outside of their first hydration shell has received considerable experimental scrutiny.[7-11,13-15,18,19] Femtosecond anisotropy decay experiments conducted by Bakker and coworkers indicate that singly and doubly charged ions do not affect the reorientation dynamics of water molecules outside the first solvation shell, leading the authors to conclude that the effect of ions of the hydrogen bond structure of water is "negligible".[10,11] Yet the high ionic strengths used in these studies (~2–12 M) raises questions about the interpretation of these results. For example, in a 6 M solution of a binary salt MX, there would only be ~5 water molecules available to hydrate each ion which is certainly not sufficient to probe second-shell effects. In contrast, results from IRPD studies of hydrated, multiply charged anions[75-77] and X-ray scattering measurements of solvent ordering around colloidal nanoparticles[78] indicate that ion-solvent patterning can extend beyond the second hydration shell. In chapters 5 and 6 we explore the influence of multiply charged cations on the hydrogen bond structure of aqueous nanodrops and find evidence for ion-solvent interactions that extend into at least the third hydration shell.

Direct ion-protein interactions can also play a role in Hofmeister phenomena. It is postulated that ion pairing between ions in solution and charged residues on the protein surface can drive conformational change, and there is some experimental evidence for such interactions. Surfactant monolayers on aqueous salt solutions have been used to model the water-protein interface, and spectroscopic experiments on these systems indicate that the extent of ion pairing between anions and positively charged surfactants correlates with the Hofmeister series.[79] X-ray absorption experiments on aqueous salt solutions likewise indicate that ion pairing between cations and carboxylate groups can occur.[80] Direct interactions are also thought to be responsible for the efficacy of protein denaturants such as urea and guanidinium (Gdm^+).[81-89] These species are particularly interesting because their position in the Hofmeister series appears to be in stark contrast to the underlying trend of charge density. This suggests that the molecular structures of denaturants like Gdm^+ contribute to their effectiveness. The high concentrations of chemical denaturants required to induce protein unfolding (~ 5 M) ensure that ion-protein interactions will occur in solution. It is believed that denaturants drive protein unfolding by stabilizing more expanded conformations of proteins. Single molecule fluorescence resonance energy transfer (FRET) experiments on solutions of proteins and chemical denaturants indicate that the denatured state of a protein continues to expand as the concentration of denaturant is increased.[90-93] This strongly suggests that denaturants thermodynamically stabilize random coils in solution by facilitating solvation of their nonpolar surfaces, including the protein backbone and nonpolar side-chains. In chapter 2, hydration structures of the common denaturant guanidinium are elucidated by IRPD spectroscopy in conjunction with *ab initio* calculations. From these data, we show that the amphiphilic nature of Gdm^+ plays an important role in lowering the barrier to protein unfolding.

1.3.2 Ions and Water at Interfaces. The structure of water at interfaces is important for many physicochemical processes including protein folding, cell membrane formation, and chemical reactions that occur on the surfaces on sea spray droplets.[94] Although the importance of water interfaces has long been recognized, they remain difficult to characterize experimentally. Significant progress in this regard has been made with the advent of surface-sensitive spectroscopies such as sum-frequency generation (SFG).[95-97] SFG spectroscopy is a second-order optical technique that can be used to probe the structure of the first few layers of water molecules near interfaces. This technique has been used to elucidate the structure of water at the air-water interface where a band near 3700 cm^{-1} is observed that arises from dangling "free" O–H stretches that are directed away from the bulk solvent.[95-99] In addition to aqueous samples, SFG spectroscopy has also been applied to the study of aqueous electrolyte solutions.[66,100-109] One of the most remarkable findings is that certain ions are present in enhanced concentrations at air-water interfaces. For example, SFG spectra of halide-containing solutions indicate that the larger, "softer" anions Br^- and I^- have enhanced concentrations at the surface.[66] This observation runs counter to intuition because ions at the air-water interface must be partially desolvated. MD simulations indicate that as these highly polarizable anions approach the interface, a dipole moment is induced in the anions by interfacial water molecules.[109,110] The attractive interaction between the induced dipole and surface water molecules thus offsets the energetic penalty of partial desolvation. In contrast, ions with higher charge densities such as F^- and SO_4^{2-} have been observed to be repelled from the interface.[66,105,109,110] While SFG spectroscopy has offered insights into the structure of interfaces, the interpretation of spectra is complicated by a variety of factors. The SFG band frequency and line shape depends on the polarization and orientation of the incident laser beams, and resonances from surface water molecules can be very broad (~50 cm^{-1}). These factors introduce ambiguity in interpreting SFG spectra.

IRPD spectroscopy is also a surface-sensitive technique owing to the comparatively high surface-to-volume ratio of nanometer-sized droplets. Spectra of aqueous nanodrops containing a single ion and anywhere between tens to hundreds of water molecules can be sub-divided into two spectral regions. Relatively sharp, high-energy bands between 3600–3800 cm^{-1} arise from water molecules at the surface of the nanodrop that have dangling O–H bonds, akin to free O–H bands in SFG spectra. Lower-energy resonances between 3000–3600 cm^{-1} are due to hydrogen bonded O–H stretches in the interior of the nanodrop. It follows that IRPD spectra contain information about the hydrogen bond network of water in both the interior and surface of the nanodrop, and these spectra can be measured under conditions where they provide information similar to linear absorption spectroscopy. The sensitivity of IRPD to nanodrop structure has been used to study the location of ammonium and protonated aliphatic amines within nanodrops containing 20 water molecules.[111] This was achieved by comparing the IRPD spectra of these species to reference spectra of Rb^+ and *tert*-butylammonium at the same cluster size, which are known to reside in the interior and surface of a nanodrop, respectively. It was found that ammonium resides in the interior of the nanodrop whereas the protonated aliphatic amines are located at the surface, in accordance with the greater hydrophobicity of these ions. These systems are sufficiently small that they can serve as benchmarks for high-level *ab inito* calculations, which should provide further insights into the preferences that drive ions to interfaces. IRPD spectra of hydrated ions at fixed cluster size (n = 36 and 250) have also been used to evaluate how ions affect the hydrogen bond structure of water throughout the nanodrop.[112,113] At both of these sizes, ions solvated in the interior of the nanodrop can induce structural changes in the hydrogen bond network of water that propagates out to the surface. The effects of ion charge and polarity on nanodrop surface structure are explored as a function of cluster size in chapter 6 for nanodrops containing between ~20 – 550 water molecules. IRPD spectra in the free O–H region indicate that multiply charged cations can have a significant effect on the hydrogen bond structure and orientations of surface-bound water molecules. Using this size-resolved approach, we are able to infer properties of neutral aqueous interfaces from these cluster data.

1.3.3 Ion Pairing. In aqueous solutions, the propensity of ions and counterions to associate (i.e. to form ion pairs) is driven by a delicate balance of electrostatic interactions between ions and water molecules. Coulomb forces between oppositely charged ions promote the formation of contact ion pairs, and ion pairing generally increases with increasing ion charge. Counter to this force is the tendency for ions to interact with water molecules though ion-dipole interactions, which encourages complete dissolution in water. There are other factors at play too, including the temperature of the solution and the ionic radii of the ions involved. With regards to this last point, it has been found that ion pairing is more favorable between ions of similar charge density. This idea was first proposed by Collins and co-workers and is known as the “Law of Matching Water Affinities”.[114] Upon surveying free energies of solution for alkali metal salts, these researchers found that ion pair formation is energetically more favorable for ions with similar charge densities (e.g. CsI and LiF) and is less favorable for mismatched ion pairs such as LiI. The propensity for ion pairing is intimately related to the strength of ion-water interactions. A strongly hydrated ion with high charge density will only shed its hydration shell in the presence of a counterion that also has a high charge density, whereas two weakly hydrated ions associate due to their exclusion from stronger water-water interactions. This simple rule for ion pairing was devised for atomic ions and must be applied with caution to molecular ions where other factors must be considered such as hydrogen bonding between ions as well as the electronic structures of the ions.

Various experimental techniques have been used to characterize and quantify ion pairing in solution. Traditional spectroscopic techniques such as UV/vis, NMR and Raman spectroscopies have been extensively used to obtain ion association constants.[115-118] The basis of the spectroscopic approach is that ion pairing leads to a measurable spectroscopic signature that is distinct from the unassociated ions. For example, Raman spectroscopy has been used to deduce an ion association constant for the Mg^{2+}/SO_4^{2-} system.[117] Upon forming a contact ion pair (CIP) with Mg^{2+}, the asymmetric stretching mode of SO_4^{2-} is red-shifted by ~10 cm^{-1} compared to the uncomplexed ion. This leads to an asymmetric band shape in the Raman spectrum that can be decomposed into two separate components that correspond to the uncomplexed and complexed ions. An equilibrium constant for ion association can then be calculated from the ratio of the areas of these bands. Interestingly, the ion association constant derived from Raman spectroscopy is approximately 1 order of magnitude smaller than the value derived from electroanalytical methods like conductometry and potentiometry.[116] This discrepancy belies the notion that ion association in solution can be so neatly categorized. It has recently been appreciated that in addition to CIPs, solvent-separated ions pairs also exist that are separated by a single or double layer of water molecules (SIPs and 2SIPs, respectively).[115] In general, spectroscopic techniques are insensitive to the presence of these more loosely associated ion pairs. In contrast, while electroanalytical methods are sensitive to the overall extent of ion association in solution, they provide little information about the relative contributions from each type of ion pair. Dielectric relaxation spectroscopy (DRS) has emerged as a technique that is sensitive to both the extent and type of ion pairing in solution.[116,119-121] DRS involves measuring the response of a sample to perturbation by an electromagnetic field applied over a broad set of frequencies in the microwave region (0.01–1000 GHz). An important feature of DRS is that it is sensitive to the square of the dipole moment (μ) of any dipolar species. It follows that various types of ion pairs can be distinguished with DRS, and the technique has been used to measure ion association constants for each of the ions pairs present in the Mg^{2+}/SO_4^{2-} system.[119] Despite the success of this approach, DRS is not a widely used technique for several reasons.[115] The instrumentation required to generate the broad range of frequencies and make accurate measurements costs in excess of 1 millions dollars, and is not commercially available in full. Furthermore, the theory behind DRS is complicated and interpretation of the broad, featureless spectra requires extensive modeling with home-built software. The technique also offers very little structural information about how hydration shells are arranged around ion pairs.

Mass spectrometry-based methods can also be used to investigate aspects of ion pairing, especially with regard to how ion pairs are solvated by water. Neutral species cannot be detected in mass spectrometers, precluding the detection of charge-symmetric ion pairs. Nevertheless, mass spectrometry has been used to investigate charge-asymmetric ions pairs that are also present in solution.[122-124] The precise control over system composition afforded by mass spectrometry has enabled ions and counter ions to be studied in a single nanodrop. The fluorescence of Ce^{3+} in the presence of NO_3^- and OH^- was recently investigated in nanodrops containing ~20–40 water molecules.[125] It was found that Ce^{3+} fluoresced in nanodrops containing OH^- but that its fluorescence was quenched in nanodrops containing NO_3^-, attributed to the formation of a contact ion pair. Although relatively small nanodrops were used for this study, the technique could easily be extended to larger clusters that contain hundreds of water molecules. With this approach, it should be possible to measure how many water molecules are needed to separate an ion pair. An emerging application of IRPD spectroscopy is to study the nascent hydration of ion pairs. Hydration structures for metal hydroxides $MOH^+(H_2O)_n$ with up to $n = 5$ have recently been reported.[34-37] In chapter 4, the hydration of the ion pairs $[PbNO_3]^+(H_2O)_n$ and $[SrNO_3]^+(H_2O)_n$ with up to $n = 30$ is investigated using IRPD and theory, providing for the first time a comprehensive view of how the first two hydration shells are arranged around ion pairs. It is also found that charge transfer between an ion and counterion can have a significant effect on the hydration of an ion pair.

1.4 Characterizing the Transition from the Molecular to the Bulk

1.4.1 Islands of Stability: Magic Number Clusters. The transition from cluster to bulk properties is not always smooth and continuous; size-specific anomalies are frequently observed in cluster science. These “bumpy” transitions often occur at small enough cluster sizes that they are amenable to analysis by computational chemistry, which can provide valuable insights into the structure and reactivity of matter. Mass spectrometry coupled with laser ablation and pulsed discharge ionization techniques has been used to study the catalytic properties of cationic and anionic metal clusters.[126-130] Clusters of a specific composition are mass selected and reacted with a neutral gas, and the ensuing reaction is monitored with mass spectrometry. The influence of factors such as cluster size, charge state, and stoichiometry on cluster reactivity can thus be evaluated. For example, the catalytic oxidation of CO to CO_2 by $W_xO_{3x}^+$ clusters has been studied by guided ion beam mass spectrometry.[126] It was found that the species WO_3^+, $W_2O_6^+$, and $W_3O_9^+$ have the highest reactivity towards CO. These species have the same stoichiometry as bulk tungsten oxide, and calculations suggest that the enhanced oxidation reactivity of these clusters may be due to the presence of radical oxygen centers ($W{-}O^{\bullet}$) with elongated metal-oxygen bonds. In contrast, some metals like gold that are inert in bulk exhibit catalytic activity at small cluster size.[130] These nanocatalysis studies provide insights into the inherent reactivity of matter where reactions fundamental to heterogeneous catalysis can be studied in highly controlled environments. In addition to cluster reactivity, the stabilities of clusters can dramatically depend on size. Perhaps the most well known example of this is buckminsterfullerene (C_{60}), which was first discovered by laser ablation of a graphite rod and mass spectrometric detection of the resulting C_n clusters.[131] The special stability of the C_{60} cluster lead to its enhanced ion abundance in the mass spectra, prompting its discovery. It was later confirmed that this stability arises from its bonding geometry that consists of hexagonal and pentagonal carbon rings.

Especially stable clusters have also been reported for clusters of ions and water molecules. Early mass spectrometry studies of protonated water clusters, $H^+(H_2O)_n$, revealed a discontinuity in the distribution of ion intensities; the peak corresponding to $n = 21$ was especially abundant in the mass spectra.[132-134] It was postulated that this particularly abundant “magic number” cluster (MNC) arises from water molecules forming a stable, cage-like hydrogen bond network known as a clathrate hydration structure. Decades later, Johnson and co-workers probed the structures of $H^+(H_2O)_n$ clusters in the vicinity of $n = 21$ with IRPD spectroscopy and *ab initio* calculations.[135] The IRPD spectrum of $H^+(H_2O)_{21}$ has a spectral simplification compared to neighboring cluster sizes, which is consistent with the formation of a highly symmetric clathrate structure at this cluster size. An explicit structure for the $H^+(H_2O)_{21}$

cluster was finally assigned from high-resolution IRPD spectra of the cryogenically cooled ion.[136,137] The cluster consists of a clathrate cage that contains 20 water molecules, and the mobile proton is incorporated into the surface of this water framework. A single water molecule is entrained in the interior of the clathrate, similar to methane gas that is incorporated into ice clathrates. It has also been observed that the larger alkali metal ions Cs^+, Rb^+, and K^+ have MNCs near $n = 20$ in their mass spectra.[138-141] In chapter 2, the first spectroscopic evidence is presented that these alkali metals ions are suitable guests in water clathrates containing 20 water molecules, thereby explaining MNCs in their mass spectra. These results confirm the stabilities of these alkali metal ion clathrates previously predicted by theory,[142,143] and indicate that the charge density and size of the metal ion determines whether or not a stable clathrate will form.

Remarkably, MNCs have been reported for hydrated ions at even larger cluster sizes. MNCs at $n = 51, 53, 55, 57$ appear in the mass spectra of protonated water clusters[144] as well as clusters containing a hydrated electron.[145] Little is known about the structures of these MNCs although their stabilities are speculated to arise from particularly stable arrangements of water molecules that are minimally perturbed by these ions. Mass spectra of hydrated halide and iodate anions, $X^-(H_2O)_n$, reveal the presence of MNCs for X = I, Br, and Cl between $n = 49$ and 55 but not for F^- and IO_3^-.[146] This is consistent with the more strongly hydrated ions disrupting the inherent structure of water at these cluster sizes, thereby preventing the formation of an especially stable water hydrogen bond network. IRPD spectra of I^- and IO_3^- in the vicinity of $n = 50$ show that the spectra of IO_3^- are blue-shifted compared to I^-,[146] so it is plausible that structural differences between hydrated ions may persist even at these large cluster sizes. More detailed structural assignments for these larger MNCs will likely involve computational modeling of cluster geometries; IRPD spectra of extensively hydrated ions are rather broad and cannot be used alone to assign structural isomers. To do this will require sophisticated computational treatments of cluster potential energy surfaces and efficient algorithms for searching large amounts of conformational space. This presents a formidable yet interesting challenge to cluster science.

1.4.2 Connecting Cluster and Bulk Properties. While the advantages of studying ion hydration in gas-phase clusters are myriad, a principal question in interpreting gas-phase data is how do cluster measurements relate to the properties of ions in solution? In fact, there are several indicators that the properties of gaseous hydrated ions correlate with those in bulk solution. In both aqueous nanodrops and solution, metal ions can react with water to form hydrolysis products via the reaction $[M(H_2O)_n]^{z+} \rightarrow [MOH(H_2O)_{n-m-1}]^{(z-1)+} + (H_3O)_m^+$.[147,148] Metal ion hydrolysis in nanodrops was investigated for hydrates of trivalent lanthanides activated under low energy conditions by the absorption of ambient blackbody radiation. Depending on the cluster size, two dissociation channels were observed: the sequential loss of water molecules or the formation of hydrolysis products. For larger clusters dissociation occurs by sequential water loss, but at smaller cluster sizes the hydrolysis reaction dominates; the size where the two processes occur at equal rates is referred to as "turnover size". It was observed that the measured turnover sizes for 14 lanthanide ions correlates well with their bulk hydrolysis constants in solution.[147] This indicates that the relative reactivities of these metal ions towards water are similar in clusters and solution. Another property has been investigated in the gas-phase and solution is ion fluorescence. Laser photodissociation studies on fluorescent ions confined in nanodrops indicate a strong correlation between gaseous and bulk properties.[125] Upon 248-nm excitation, nanodrops with ~25 or more water molecules that contain either rhodamine 590^+, rhodamine 640$^+$, or Ce^{3+} emit fluorescent photons with energies and quantum efficiencies that closely match the corresponding ions in solution. At smaller cluster sizes, the fluorescent photon energies of these species deviate from their values in solution. This suggests that relatively few water molecules are needed to account for solvatochromic shifts ion in fluorescence.

The size at which cluster properties give way to bulk properties depends to some extent on the observable that is being measured. One cluster property that has been used to gauge the onset of bulk properties in cluster ions is water molecule binding energies. The binding energy of a water molecule to an ion-containing nanodrop reflects the strength of ion-water and water-water interactions within the cluster. As the size of the nanodrop is increased, interactions between the solvated ion and water molecules at the nanodrop surface will diminish. For larger clusters, the binding energies will therefore predominately reflect water-water interactions and the hydrogen bond structure of the cluster. These values should converge to that of the bulk solvent with increasing cluster size. Water molecule binding energies have been measured by a variety of gas-phase techniques including high-pressure ion source mass spectrometry (HPMS),[149-151] threshold collision-induced dissociation (TCID),[152-155] ultraviolet photodissociation (UVPD),[125,156] and blackbody infrared dissociation (BIRD).[157-159] Results from these experiments indicate that the binding energies of water molecules in the first hydration shell depend strongly on ion identity. For singly and doubly charged metal ions, inner shell binding energies can differ by up to ~20 kcal/mol and 40 kcal/mol, respectively.[160] These differences rapidly decrease with increasing cluster size, and for clusters with more than ~20 water molecules are on the order of 1 kcal/mol. UVPD measurements on hydrated divalent metals ions with between 19 and 124 water molecules attached indicate that for $n > 40$, water binding enthalpies remain fairly constant at ~10.4 kcal/mol. This value is very close to the bulk vaporization enthalpy of liquid water (10.6 kcal/mol), suggesting that these nanodrops are structurally similar to liquid water. Unpublished UVPD experiments conducted in our laboratory indicate that at significantly larger cluster sizes ($n > 300$), water binding enthalpies begin to trend towards the bulk sublimation enthalpy of ice (12.2 kcal/mol), coinciding with the onset of crystallinity in cold nanodrops. These results indicate that the structure of water in nanodrops converges to that in bulk with increasing droplet size.

One approach to explicitly relate cluster and bulk properties is by extrapolating cluster properties to infinite cluster size to infer bulk properties. This method is valid for cluster properties that vary smoothly with size, and has been used to relate ionization energies of $SO_4^{2-}(H_2O)_n$ clusters to the ionization energy of the ion in the condensed phase.[42] The cluster extrapolation method has also been used in ion nanocalorimetry experiments where the number of water molecules lost from the capture of an electron by a hydrated ion is used to measure the reduction enthalpy.[161] Ion nanocalorimetry is used in chapter 7 to measure cluster reduction enthalpies of $M^{2+}(H_2O)_n$ where M = Cu, Ni, Co, and Zn and $36 \leq n \leq 240$. By extrapolating these cluster data to infinite cluster size (i.e. infinite dilution), values for the absolute reduction enthalpies of these transition metal ions in solution are obtained. The absolute solution reduction enthalpy obtained from this extrapolation for the Cu^{2+}/Cu$^+$ couple is then used to establish an absolute half-cell potential that serves as an anchor for an absolute electrochemical scale. The cluster extrapolation method is also used in chapter 6 to infer the properties of air-water interfaces from IRPD spectra of hydrated ions with charge states ranging from -2 to +3. In particular, the frequency of the free O–H stretches in these clusters are measured as a function of cluster size in nanodrops containing between 20 and 550 water molecules. By extrapolating these measurements to infinite cluster size and interpolating between charge states, the free O–H stretching frequency of a surface-bound water molecule at the bulk air-water interface is determined to be centered on 3700 cm^{-1}, well within the relatively wide range of values obtained from SFG measurements.[97,99,162] This approach has a distinct advantage over previous estimates of the free O–H stretching frequency made at finite cluster size[112,113] in that surface curvature effects are accounted for in the extrapolation. The good agreement between cluster and bulk measurements underscores the power of the cluster extrapolation method.

1.4.3 The Emergence of Phase in Cluster Measurements. States of matter (liquid, solid, gas, plasma, etc) are well defined in bulk materials and are distinguished by the uniform physical properties of these materials. In contrast, the concept of phase in cluster measurements is more ambiguous and breaks down for collections of several atoms or molecules. An interesting question for cluster science, then, is how many atoms or molecules are needed for a distinct phase to develop in matter? The answer to this question can vary dramatically based on the composition of the cluster and the strength of intermolecular interactions within. Electron diffraction experiments indicate that the onset of bulk crystalline structure in CO_2 nanoparticles occurs with only a few tens of molecules,[163,164] whereas for Ar clusters at least ~10^5 atoms are needed.[165] Due to the high surfaces areas of clusters, surface effects play a large role in the crystallization process. If the bulk crystal structure leads to an energetically unfavorable arrangement of molecules at the cluster surface, then crystallization will be inhibited. Crystallization at small cluster size for CO_2 nanoparticles has in part been attributed to the favorable arrangement of molecules at the cluster surface.

The onset of crystallinity in $(H_2O)_n$ clusters is a subject of great interest owing to the ubiquity and complexity of the solvent. Even when neutral water clusters are cryogenically cooled well below the bulk freezing point of the solvent, crystallization may not occur because of surface constraints. Fourier transform infrared (FTIR) spectra of ice nanoparticles ranging in size from 100s to 1000s of water molecules along with MD simulations indicate that the nearly perfect tetrahedral structure of crystalline ice is not energetically favorable at the nanoparticle surface.[166-170] The dangling O–H bonds of surface water molecules reorient to optimize water-water hydrogen bonding, leading to structural disorder in the surface layer. Thus, nanodrops without sufficient interior volume to support crystalline ice will not crystallize. Recent infrared-modulated threshold ionization experiments on cold water clusters cooled to ~115 K indicate that the onset of crystallization occurs at approximately ~275 water molecules,[171] in agreement with earlier experiments.[172,173] This suggests that the structure of nanodrops containing fewer water molecules should have a phase that is structurally similar to liquid water or amorphous ice. Indeed, many IRPD spectra of hydrated ions with $n < 275$ measured at ~130 K in our laboratory closely resemble the bulk infrared spectrum of liquid water and amorphous ice.[112,113,174] This is especially true for singly charged ions that minimally perturb the hydrogen bond network of water within a nanodrop. For larger cluster sizes, however, it is expected that droplet crystallization can occur, although this process will be affected by the presence of an ion in the droplet. This idea is explored in chapter 5, where IRPD spectra of La^{3+}-doped nanodrops are measured at 133 K at cluster sizes ranging from 50 to 550 water molecules. The emergence of crystalline ice is observed at $n \sim 375$, an offset of 100 water molecules compared to neutral clusters. These experiments reveal that La^{3+} can affect the hydrogen bond network of water molecules located remotely from the ion, and provide a molecular interpretation for the macroscopic phenomenon of freezing point depression by salts.

1.5 Ion Nanocalorimetry

The thermodynamics of endothermic and exothermic reactions in solution can readily be measured using traditional calorimetry techniques where the heat consumed or evolved by a reaction can be calculated from the temperature change of the calorimeter and its heat capacity. Mass spectrometry is generally well suited to studying the thermodynamics of endothermic reactions where energy deposition in a cluster ion can be precisely controlled by the absorption of photons or by collisions with neutral gas molecules until dissociation occurs. On the other hand, evaluating the energetics of exothermic reactions in the gas phase is significantly more challenging; mass spectra of fragment ion abundances do not inherently provide information about the energetics of exothermic reactions. Recently, a technique known as "ion nanocalorimetry" has been introduced as a means of measuring the thermodynamics of exothermic reactions in the gas-phase.[156,160,161,175-188] When a hydrated ion undergoes a reaction such as the capture of an electron[161,185,186] or the absorption of a photon,[156,176] the energy of the reaction is dissipated into the vibrational modes of the cluster thereby increasing its internal energy and effective temperature. Water molecules are subsequently evaporated from the cluster until it returns to its initial temperature, and the extent of water loss is related to the amount of energy evolved by the reaction.

Extracting thermodynamic information from these experiments depends on accurately knowing the amount of the energy removed from the cluster ion by each departing water molecule. Evaporative water loss reduces the cluster internal energy through two mechanisms. First, a certain amount of energy is required for a water molecule to dissociate from the cluster; this is referred to as its binding energy. This includes the energy required to break hydrogen bonds and overcome the Coulombic attraction to the ion. Second, energy partitioning effects must be taken into account. Some of the cluster internal energy will partition into the translational, rotational, and vibrational modes of each departing water molecule and this energy must also be accounted for. The difficulty of the nanocalorimetry method lies in determining accurate values for both of these terms. In previous implementations of the technique, the reaction energy was obtained by modeling the cluster dissociation process.[175,178,185] As part of this modeling, water molecule binding energies were calculated from the Thompson liquid drop model (TLDM)[160] and energy partitioning was accounted for using the Klott's model for water evaporation.[189] The accuracy of these models determines the accuracy with which thermodynamic information can be obtained. Recent ultraviolet photodissociation experiments have cast doubt on the accuracy of the TLDM, and indicate that it systematically underestimates water molecule binding energies by ~ 1kcal/mol. While the magnitude of this error is small, it is compounded in nanocalorimetry experiments where typically ~8–16 water molecules dissociate from an ion.

Herein, a new approach is devised for accurately determining the energy involved in the recombination of an electron and a metal ion within an aqueous nanodrop. In electron capture experiments, the number of water molecules lost from the ion-electron recombination is easily measured in the mass spectrometer but the quantity of energy involved in the recombination is unknown. If a relationship could be established between the energy deposited into a cluster and the resulting water molecule loss, it could be used to deduce the energy resulting from electron capture. Nanodrops containing a suitable chromophore ion can absorb ultraviolet light.[156,176,190] After photoexcitation to an electronic excited state, the ion can relax back down to the ground electronic state by internal conversion and fluorescence. In cases where full internal conversion occurs, the energy of the absorbed photon is statistically redistributed into the vibrational modes of the cluster, resulting in cluster heating and evaporative water loss. Because the energy of a laser-generated UV photon is known with high accuracy and precision, laser photodissociation experiments can be used establish a relationship between energy deposition in a cluster and the resulting water loss by varying the incident photon energy. The extent of water loss due to photodissociation will depend on cluster size, ion identity and charge state, and accordingly calibration experiments must be performed as a function of cluster size, ion identity and charge state. This approach obviates the need for modeling water molecule binding energies and product energy partitioning; these factors are accounted for experimentally in the calibration.

Ion nanocalorimetry can be used to study aspects of electrochemistry that are difficult to probe in solution. In the gas-phase, single half-cell redox reactions can be probed in isolation without need for a reference electrode. Absolute one-electron reduction enthalpies have been measured for several metal ions, from which it is possible to calculate absolute reduction potentials for these species. If the corresponding *relative* one-electron reduction potentials of these species have been measured in solution, values for the absolute standard hydrogen electrode (SHE) can be obtained. This establishes an absolute electrochemical scale instead of the relative electrochemical scale that is currently used where the SHE is arbitrarily assigned a potential of exactly 0 V. Previous results from our laboratory indicate that the SHE has an absolute potential of 4.0–4.3 V.[161,181,185] In chapter 7, laser-calibrated nanocalorimetry experiments are used to deduce a more accurate value for the absolute SHE potential based on the Cu^{2+}/Cu^{+} redox couple.

Another application of ion nanocalorimetry is to investigate one-electron reductions of metal ions that are not observed in solution. Many divalent transition metal ions have measured two-electron reductions in aqueous solution, but the one-electron reduction is not observed. There are two possible reasons why this occurs. The 1+ species may not be stable in water. Or the 1+ species may be stable in water, but its reduction potential is more positive than the 2+ species (i.e. reduction of the 1+ species is energetically more favorable). This is known as "potential inversion".[191] For species that undergo potential inversion, spontaneous electron transfer will occur from the electrode to the 1+ species. In nanocalorimetry experiments, it is possible to circumvent this process because reduction is not controlled by the application of a potential to an electrode, but rather depends on the low-probability capture of a gaseous electron.[183] Thus, it is possible to reduce hydrated metal ions one electron at a time and investigate these "missing" one-electron reductions. This is discussed in chapter 7, where the one-electron reduction potentials of Ni^{2+}, Co^{2+}, and Zn^{2+} are measured for the first time.

1.6 References

(1) MacKinnon, R. *Angew. Chem. Int. Edit.* **2004**, *43*, 4265-4277.

(2) Zhou, Y. F.; Morais-Cabral, J. H.; Kaufman, A.; MacKinnon, R. *Nature* **2001**, *414*, 43-48.

(3) Doyle, D. A.; Cabral, J. M.; Pfuetzner, R. A.; Kuo, A. L.; Gulbis, J. M.; Cohen, S. L.; Chait, B. T.; MacKinnon, R. *Science* **1998**, *280*, 69-77.

(4) Lee, S. H.; Reeves, J. M.; Wilson, J. C.; Hunton, D. E.; Viggiano, A. A.; Miller, T. M.; Ballenthin, J. O.; Lait, L. R. *Science* **2003**, *301*, 1886-1889.

(5) Kulmala, M. *Science* **2003**, *302*, 1000-1001.

(6) Yu, F. Q.; Turco, R. P. *J. Geophys. Res-Atmos.* **2001**, *106*, 4797-4814.

(7) Fournier, J. A.; Carpenter, W.; De Marco, L.; Tokmakoff, A. *J. Am. Chem. Soc.* **2016**, *138*, 9634-9645.

(8) Tielrooij, K. J.; van der Post, S. T.; Hunger, J.; Bonn, M.; Bakker, H. J. *J. Phys. Chem. B* **2011**, *115*, 12638-12647.

(9) Tielrooij, K. J.; Garcia-Araez, N.; Bonn, M.; Bakker, H. J. *Science* **2010**, *328*, 1006-1009.

(10) Omta, A. W.; Kropman, M. F.; Woutersen, S.; Bakker, H. J. *J. Chem. Phys.* **2003**, *119*, 12457-12461.

(11) Omta, A. W.; Kropman, M. F.; Woutersen, S.; Bakker, H. J. *Science* **2003**, *301*, 347-349.

(12) Smith, J. D.; Saykally, R. J.; Geissler, P. L. *J. Am. Chem. Soc.* **2007**, *129*, 13847-13856.

(13) Sharma, V.; Bohm, F.; Seitz, M.; Schwaab, G.; Havenith, M. *Phys. Chem. Chem. Phys.* **2013**, *15*, 8383-8391.

(14) Funkner, S.; Niehues, G.; Schmidt, D. A.; Heyden, M.; Schwaab, G.; Callahan, K. M.; Tobias, D. J.; Havenith, M. *J. Am. Chem. Soc.* **2012**, *134*, 1030-1035.

(15) Schmidt, D. A.; Birer, O.; Funkner, S.; Born, B. P.; Gnanasekaran, R.; Schwaab, G. W.; Leitner, D. M.; Havenith, M. *J. Am. Chem. Soc.* **2009**, *131*, 18512-18517.

(16) Swift, T. J.; Sayre, W. G. *J. Chem. Phys.* **1966**, *44*, 3567-3568.

(17) Helm, L.; Merbach, A. E. *Coordin. Chem. Rev.* **1999**, *187*, 151-181.

(18) Schwartz, C. P.; Uejio, J. S.; Duffin, A. M.; Drisdell, W. S.; Smith, J. D.; Saykally, R. J. *Chem. Phys. Lett.* **2010**, *493*, 94-96.

(19) Cappa, C. D.; Smith, J. D.; Messer, B. M.; Cohen, R. C.; Saykally, R. J. *J. Phys. Chem. B* **2006**, *110*, 5301-5309.

(20) Mancinelli, R.; Botti, A.; Bruni, F.; Ricci, M. A.; Soper, A. K. *J. Phys. Chem. B* **2007**, *111*, 13570-13577.

(21) Mason, P. E.; Dempsey, C. E.; Neilson, G. W.; Brady, J. W. *J. Phys. Chem. B* **2005**, *109*, 24185-24196.

(22) Mason, P. E.; Neilson, G. W.; Dempsey, C. E.; Barnes, A. C.; Cruickshank, J. M. *Proc. Natl. Acad. Sci. U.S.A.* **2003**, *100*, 4557-4561.

(23) Ke, H.; van der Linde, C.; Lisy, J. M. *J. Phys. Chem. A* **2015**, *119*, 2037-2051.

(24) O'Brien, J. T.; Williams, E. R. *J. Phys. Chem. A* **2011**, *115*, 14612-14619.

(25) Cooper, T. E.; O'Brien, J. T.; Williams, E. R.; Armentrout, P. B. *J. Phys. Chem. A* **2010**, *114*, 12646-12655.

(26) Miller, D. J.; Lisy, J. M. *J. Am. Chem. Soc.* **2008**, *130*, 15393-15404.

(27) Bush, M. F.; Saykally, R. J.; Williams, E. R. *ChemPhysChem* **2007**, *8*, 2245-2253.

(28) Walters, R. S.; Pillai, E. D.; Duncan, M. A. *J. Am. Chem. Soc.* **2005**, *127*, 16599-16610.

(29) Heine, N.; Yacovitch, T. I.; Schubert, F.; Brieger, C.; Neumark, D. M.; Asmis, K. R. *J. Phys. Chem. A* **2014**, *118*, 7613-7622.

(30) Yacovitch, T. I.; Heine, N.; Brieger, C.; Wende, T.; Hock, C.; Neumark, D. M.; Asmis, K. R. *J. Phys. Chem. A* **2013**, *117*, 7081-7090.

(31) Garand, E.; Wende, T.; Goebbert, D. J.; Bergmann, R.; Meijer, G.; Neumark, D. M.; Asmis, K. R. *J. Am. Chem. Soc.* **2010**, *132*, 849-856.

(32) Goebbert, D. J.; Garand, E.; Wende, T.; Bergmann, R.; Meijer, G.; Asmis, K. R.; Neumark, D. M. *J. Phys. Chem. A* **2009**, *113*, 7584-7592.

(33) Roscioli, J. R.; Diken, E. G.; Johnson, M. A.; Horvath, S.; McCoy, A. B. *J. Phys. Chem. A* **2006**, *110*, 4943-4952.

(34) Marsh, B. M.; Zhou, J.; Garand, E. *Phys. Chem. Chem. Phys.* **2015**, *17*, 25786-25792.

(35) Marsh, B. M.; Voss, J. M.; Zhou, J.; Garand, E. *Phys. Chem. Chem. Phys.* **2015**, *17*, 23195-23206.

(36) Johnson, C. J.; Dzugan, L. C.; Wolk, A. B.; Leavitt, C. M.; Fournier, J. A.; McCoy, A. B.; Johnson, M. A. *J. Phys. Chem. A* **2014**, *118*, 7590-7597.

(37) Marsh, B. M.; Zhou, J.; Garand, E. *J. Phys. Chem. A* **2014**, *118*, 2063-2071.

(38) Boldyrev, A. I.; Simons, J. *J. Phys. Chem.* **1994**, *98*, 2298-2300.

(39) Simons, J. S.; Skurski, P.; Barrios, R. *J. Am. Chem. Soc.* **2000**, *122*, 11893-11899.

(40) Wang, X. B.; Nicholas, J. B.; Wang, L. S. *J. Chem. Phys.* **2000**, *113*, 10837-10840.

(41) Wong, R. L.; Williams, E. R. *J. Phys. Chem. A* **2003**, *107*, 10976-10983.

(42) Wang, X. B.; Yang, X.; Nicholas, J. B.; Wang, L. S. *Science* **2001**, *294*, 1322-1325.

(43) Casaes, R.; Provencal, R.; Paul, J.; Saykally, R. J. *J. Chem. Phys.* **2002**, *116*, 6640-6647.

(44) Gerlich, D. *Adv. Chem. Phys.* **1992**, *82*, 1-176.

(45) Polfer, N. C. *Chem. Soc. Rev.* **2011**, *40*, 2211-2221.

(46) Eyler, J. R. *Mass. Spectrom. Rev.* **2009**, *28*, 448-467.

(47) Oomens, J.; Sartakov, B. G.; Meijer, G.; Von Helden, G. *Int. J. Mass. Spectrom.* **2006**, *254*, 1-19.

(48) Bieske, E. J.; Dopfer, O. *Chem. Rev.* **2000**, *100*, 3963-3998.

(49) Bush, M. F.; O'Brien, J. T.; Prell, J. S.; Saykally, R. J.; Williams, E. R. *J. Am. Chem. Soc.* **2007**, *129*, 1612-1622.

(50) Grant, E. R.; Schulz, P. A.; Sudbo, A. S.; Shen, Y. R.; Lee, Y. T. *Phys. Rev. Lett.* **1978**, *40*, 115-118.

(51) Fung, Y. M. E.; Kjeldsen, F.; Silivra, O. A.; Chan, T. W. D.; Zubarev, R. A. *Angew. Chem. Int. Edit.* **2005**, *44*, 6399-6403.

(52) Dean, J. C.; Burke, N. L.; Hopkins, J. R.; Redwine, J. G.; Ramachandran, P. V.; McLuckey, S. A.; Zwier, T. S. *J. Phys. Chem. A* **2015**, *119*, 1917-32.

(53) Wolk, A. B.; Leavitt, C. M.; Garand, E.; Johnson, M. A. *Acc. Chem. Res.* **2014**, *47*, 202-210.

(54) Marsh, B. M.; Duffy, E. M.; Soukup, M. T.; Zhou, J.; Garand, E. *J. Phys. Chem. A* **2014**, *118*, 3906-3912.

(55) Leavitt, C. M.; DeBlase, A. F.; Johnson, C. J.; van Stipdonk, M.; McCoy, A. B.; Johnson, M. A. *J. Phys. Chem. Lett.* **2013**, *4*, 3450-3457.

(56) Rizzo, T. R.; Stearns, J. A.; Boyarkin, O. V. *Int. Rev. Phys. Chem.* **2009**, *28*, 481-515.

(57) Okumura, M.; Yeh, L. I.; Myers, J. D.; Lee, Y. T. *J. Chem. Phys.* **1986**, *85*, 2328-2329.

(58) Masson, A.; Williams, E. R.; Rizzo, T. R. *J. Chem. Phys.* **2015**, *143*, 104313.

(59) Prell, J. S.; O'Brien, J. T.; Williams, E. R. *J. Am. Soc. Mass. Spectr.* **2010**, *21*, 800-809.

(60) Kunz, W.; Henle, J.; Ninham, B. W. *Curr. Opin. Colloid. In.* **2004**, *9*, 19-37.
(61) Zhang, Y. J.; Cremer, P. S. *Curr. Opin. Chem. Biol.* **2006**, *10*, 658-663.
(62) Schott, H. *J. Colloid Interf. Sci.* **1973**, *43*, 150-155.
(63) Zhao, H. *J. Mol. Catal. B-Enzym.* **2005**, *37*, 16-25.
(64) Bostrom, M.; Kunz, W.; Ninham, B. W. *Langmuir* **2005**, *21*, 2619-2623.
(65) Collins, K. D.; Washabaugh, M. W. *Q. Rev. Biophys.* **1985**, *18*, 323-422.
(66) Petersen, P. B.; Saykally, R. J. *Annu. Rev. Phys. Chem.* **2006**, *57*, 333-364.
(67) Jungwirth, P.; Cremer, P. S. *Nat. Chem.* **2014**, *6*, 261-263.
(68) Lo Nostro, P.; Ninham, B. W. *Chem. Rev.* **2012**, *112*, 2286-2322.
(69) Marcus, Y. *Chem. Rev.* **2009**, *109*, 1346-1370.
(70) Nucci, N. V.; Vanderkooi, J. M. *J. Mol. Liq.* **2008**, *143*, 160-170.
(71) Gurau, M. C.; Lim, S. M.; Castellana, E. T.; Albertorio, F.; Kataoka, S.; Cremer, P. S. *J. Am. Chem. Soc.* **2004**, *126*, 10522-10523.
(72) Collins, K. D. *Methods* **2004**, *34*, 300-311.
(73) Graziano, G. *Phys. Chem. Chem. Phys.* **2011**, *13*, 12008-12014.
(74) Collins, K. D.; Neilson, G. W.; Enderby, J. E. *Biophys. Chem.* **2007**, *128*, 95-104.
(75) DiTucci, M. J.; Williams, E. R. *Chem. Sci.* **2016.** DOI: 10.1039/c6sc03722d
(76) DiTucci, M. J.; Heiles, S.; Williams, E. R. *J. Am. Chem. Soc.* **2015**, *137*, 1650-1657.
(77) O'Brien, J. T.; Prell, J. S.; Bush, M. F.; Williams, E. R. *J. Am. Chem. Soc.* **2010**, *132*, 8248-8249.
(78) Zobel, M.; Neder, R. B.; Kimber, S. A. *Science* **2015**, *347*, 292-294.
(79) Nihonyanagi, S.; Yamaguchi, S.; Tahara, T. *J. Am. Chem. Soc.* **2014**, *136*, 6155-6158.
(80) Uejio, J. S.; Schwartz, C. P.; Duffin, A. M.; Drisdell, W. S.; Cohen, R. C.; Saykally, R. J. *Proc. Natl. Acad. Sci. U.S.A* **2008**, *105*, 6809-6812.
(81) England, J. L.; Haran, G. *Annu. Rev. Phys. Chem.* **2011**, *62*, 257-277.
(82) Koishi, T.; Yasuoka, K.; Willow, S. Y.; Fujikawa, S.; Zeng, X. C. *J. Chem. Theory Comput.* **2013**, *9*, 2540-2551.
(83) Huerta-Viga, A.; Woutersen, S. *J. Phys. Chem. Lett.* **2013**, *4*, 3397-3401.
(84) Kubickova, A.; Krizek, T.; Coufal, P.; Wernersson, E.; Heyda, J.; Jungwirth, P. *J. Phys. Chem. Lett.* **2011**, *2*, 1387-1389.
(85) Heyda, J.; Kozisek, M.; Bednarova, L.; Thompson, G.; Konvalinka, J.; Vondrasek, J.; Jungwirth, P. *J. Phys. Chem. B* **2011**, *115*, 8910-8924.
(86) Mason, P. E.; Dempsey, C. E.; Neilson, G. W.; Kline, S. R.; Brady, J. W. *J. Am. Chem. Soc.* **2009**, *131*, 16689-16696.
(87) O'Brien, E. P.; Dima, R. I.; Brooks, B.; Thirumalai, D. *J. Am. Chem. Soc.* **2007**, *129*, 7346-7353.
(88) Mason, P. E.; Brady, J. W.; Neilson, G. W.; Dempsey, C. E. *Biophys. J.* **2007**, *93*, L4-L6.
(89) Moglich, A.; Krieger, F.; Kiefhaber, T. *J. Mol. Biol.* **2005**, *345*, 153-162.
(90) Merchant, K. A.; Best, R. B.; Louis, J. M.; Gopich, I. V.; Eaton, W. A. *Proc. Natl. Acad. Sci. U.S.A* **2007**, *104*, 1528-1533.
(91) Tezuka-Kawakami, T.; Gell, C.; Brockwell, D. J.; Radford, S. E.; Smith, D. A. *Biophys. J.* **2006**, *91*, L42-L44.
(92) Kuzmenkina, E. V.; Heyes, C. D.; Nienhaus, G. U. *J. Molec. Bio.* **2006**, *357*, 313-324.
(93) Schuler, B.; Lipman, E. A.; Eaton, W. A. *Nature* **2002**, *419*, 743-747.
(94) Knipping, E. M.; Lakin, M. J.; Foster, K. L.; Jungwirth, P.; Tobias, D. J.; Gerber, R. B.; Dabdub, D.; Finlayson-Pitts, B. J. *Science* **2000**, *288*, 301-306.

(95) Shultz, M. J.; Schnitzer, C.; Simonelli, D.; Baldelli, S. *Int. Rev. Phys. Chem.* **2000**, *19*, 123-153.
(96) Gragson, D. E.; McCarty, B. M.; Richmond, G. L. *J. Am. Chem. Soc.* **1997**, *119*, 6144-6152.
(97) Du, Q.; Superfine, R.; Freysz, E.; Shen, Y. R. *Phys. Rev. Lett.* **1993**, *70*, 2313-2316.
(98) Ji, N.; Ostroverkhov, V.; Tian, C. S.; Shen, Y. R. *Phys. Rev. Lett.* **2008**, *100*, 096102.
(99) Shen, Y. R.; Ostroverkhov, V. *Chem. Rev.* **2006**, *106*, 1140-1154.
(100) Hua, W.; Verreault, D.; Huang, Z.; Adams, E. M.; Allen, H. C. *J. Phys. Chem. B* **2014**, *118*, 8433-8440.
(101) Covert, P. A.; Jena, K. C.; Hore, D. K. *J. Phys. Chem. Lett.* **2014**, *5*, 143-148.
(102) Jubb, A. M.; Hua, W.; Allen, H. C. *Acc. Chem. Res.* **2012**, *45*, 110-119.
(103) Chen, X.; Yang, T.; Kataoka, S.; Cremer, P. S. *J. Am. Chem. Soc.* **2007**, *129*, 12272-12279.
(104) Gopalakrishnan, S.; Liu, D. F.; Allen, H. C.; Kuo, M.; Shultz, M. J. *Chem. Rev.* **2006**, *106*, 1155-1175.
(105) Gopalakrishnan, S.; Jungwirth, P.; Tobias, D. J.; Allen, H. C. *J. Phys. Chem. B* **2005**, *109*, 8861-8872.
(106) Raymond, E. A.; Richmond, G. L. *J. Phys. Chem. B* **2004**, *108*, 5051-5059.
(107) Liu, D. F.; Ma, G.; Levering, L. M.; Allen, H. C. *J. Phys. Chem. B* **2004**, *108*, 2252-2260.
(108) Jungwirth, P.; Winter, B. *Annu. Rev. Phys. Chem.* **2008**, *59*, 343-366.
(109) Jungwirth, P.; Tobias, D. J. *Chem. Rev.* **2006**, *106*, 1259-1281.
(110) Jungwirth, P.; Tobias, D. J. *J. Phys. Chem. B* **2002**, *106*, 6361-6373.
(111) Chang, T. M.; Cooper, R. J.; Williams, E. R. *J. Am. Chem. Soc.* **2013**, *135*, 14821-14830.
(112) O'Brien, J. T.; Williams, E. R. *J. Am. Chem. Soc.* **2012**, *134*, 10228-10236.
(113) Prell, J. S.; O'Brien, J. T.; Williams, E. R. *J. Am. Chem. Soc.* **2011**, *133*, 4810-4818.
(114) Collins, K. D. *Biophys. J.* **1997**, *72*, 65-76.
(115) Marcus, Y.; Hefter, G. *Chem. Rev.* **2006**, *106*, 4585-4621.
(116) Hefter, G. *Pure Appl. Chem.* **2006**, *78*, 1571-1586.
(117) Rudolph, W. W.; Irmer, G.; Hefter, G. T. *Phys. Chem. Chem. Phys.* **2003**, *5*, 5253-5261.
(118) Gorzsas, A.; Getty, K.; Andersson, I.; Pettersson, L. *Dalton Trans.* **2004**, 2873-2882.
(119) Buchner, R.; Chen, T.; Hefter, G. *J. Phys. Chem. B* **2004**, *108*, 2365-2375.
(120) Wachter, W.; Fernandez, S.; Buchner, R.; Hefter, G. *J. Phys. Chem. B* **2007**, *111*, 9010-9017.
(121) Akilan, C.; Rohman, N.; Hefter, G.; Buchner, R. *ChemPhysChem* **2006**, *7*, 2319-2330.
(122) Jagoda-Cwiklik, B.; Jungwirth, P.; Rulisek, L.; Milko, P.; Roithova, J.; Lemaire, J.; Maitre, P.; Ortega, J. M.; Schroder, D. *ChemPhysChem* **2007**, *8*, 1629-1639.
(123) McQuinn, K.; Hof, F.; McIndoe, J. S.; Chen, X. J.; Wu, G. H.; Stace, A. J. *Chem. Commun.* **2009**, *27*, 4088-4090.
(124) Jiang, L.; Wende, T.; Bergmann, R.; Meijer, G.; Asmis, K. R. *J. Am. Chem. Soc.* **2010**, *132*, 7398-7404.
(125) Donald, W. A.; Leib, R. D.; Demireva, M.; Williams, E. R. *J. Am. Chem. Soc.* **2011**, *133*, 18940-18949.
(126) Johnson, G. E.; Tyo, E. C.; Castleman, A. W. *Proc. Natl. Acad. Sci. U.S.A.* **2008**, *105*, 18108-18113.
(127) Kim, Y. D. *Int. J. Mass. Spectrom.* **2004**, *238*, 17-31.
(128) Zemski, K. A.; Justes, D. R.; Castleman, A. W. *J. Phys. Chem. B* **2002**, *106*, 6136-6148.

(129) Bohme, D. K.; Schwarz, H. *Angew. Chem. Int. Edit.* **2005**, *44*, 2336-2354.
(130) Haruta, A. *Chem. Rec.* **2003**, *3*, 75-87.
(131) Kroto, H. W.; Heath, J. R.; O'Brien, R. F.; Smalley, R. E. *Nature* **1985**, *318*, 162-163.
(132) Searcy, J. Q. *J. Chem. Phys.* **1975**, *63*, 4114-4119.
(133) Searcy, J. Q.; Fenn, J. B. *J. Chem. Phys.* **1974**, *61*, 5282-5288.
(134) Lin, S. S. *Rev. Sci. Instrum.* **1973**, *44*, 516-517.
(135) Shin, J. W.; Hammer, N. I.; Diken, E. G.; Johnson, M. A.; Walters, R. S.; Jaeger, T. D.; Duncan, M. A.; Christie, R. A.; Jordan, K. D. *Science* **2004**, *304*, 1137-1140.
(136) Fournier, J. A.; Wolke, C. T.; Johnson, C. J.; Johnson, M. A.; Heine, N.; Gewinner, S.; Schollkopf, W.; Esser, T. K.; Fagiani, M. R.; Knorke, H.; Asmis, K. R. *Proc. Natl. Acad. Sci. U.S.A.* **2014**, *111*, 18132-18137.
(137) Fournier, J. A.; Johnson, C. J.; Wolke, C. T.; Weddle, G. H.; Wolk, A. B.; Johnson, M. A. *Science* **2014**, *344*, 1009-1012.
(138) Zatula, A. S.; Ryding, M. J.; Andersson, P. U.; Uggerud, E. *Int. J. Mass. Spectrom.* **2012**, *330*, 191-199.
(139) Sobott, F.; Wattenberg, A.; Barth, H. D.; Brutschy, B. *Int. J. Mass. Spectrom.* **1999**, *185*, 271-279.
(140) Steel, E. A.; Merz, K. M.; Selinger, A.; Castleman, A. W. *J. Phys. Chem.* **1995**, *99*, 7829-7836.
(141) Selinger, A.; Castleman, A. W. *J. Phys. Chem.* **1991**, *95*, 8442-8444.
(142) Schulz, F.; Hartke, B. *Theor. Chem. Acc.* **2005**, *114*, 357-379.
(143) Schulz, F.; Hartke, B. *ChemPhysChem* **2002**, *3*, 98-106.
(144) Schindler, T.; Berg, C.; NiednerSchatteburg, G.; Bondybey, V. E. *Chem. Phys. Lett.* **1996**, *250*, 301-308.
(145) Knapp, M.; Echt, O.; Kreisle, D.; Recknagel, E. *J. Phys. Chem.* **1987**, *91*, 2601-2607.
(146) Chakrabarty, S.; Williams, E. R. *Phys. Chem. Chem. Phys.* **2016**, *18*, 25483-25490.
(147) Bush, M. F.; Saykally, R. J.; Williams, E. R. *J. Am. Chem. Soc.* **2008**, *130*, 9122-9128.
(148) Bush, M. F.; Saykally, R. J.; Williams, E. R. *Int. J. Mass. Spectrom.* **2006**, *253*, 256-262.
(149) Gao, B.; Wyttenbach, T.; Bowers, M. T. *J. Am. Chem. Soc.* **2009**, *131*, 4695-4701.
(150) Blades, A. T.; Kebarle, P. *J. Phys. Chem. A* **2005**, *109*, 8293-8298.
(151) Peschke, M.; Blades, A. T.; Kebarle, P. *J. Phys. Chem. A* **1998**, *102*, 9978-9985.
(152) Carl, D. R.; Moision, R. M.; Armentrout, P. B. *Int. J. Mass. Spectrom.* **2007**, *265*, 308-325.
(153) Cooper, T. E.; Carl, D. R.; Armentrout, P. B. *J. Phys. Chem. A* **2009**, *113*, 13727-13741.
(154) Rodgers, M. T.; Armentrout, P. B. *J. Phys. Chem. A* **1997**, *101*, 1238-1249.
(155) Carl, D. R.; Armentrout, P. B. *ChemPhysChem* **2013**, *14*, 681-697.
(156) Donald, W. A.; Leib, R. D.; Demireva, M.; Williams, E. R. *J. Am. Chem. Soc.* **2011**, *133*, 18940-18949.
(157) Rodriguez-Cruz, S. E.; Jockusch, R. A.; Williams, E. R. *J. Am. Chem. Soc.* **1999**, *121*, 8898-8906.
(158) Rodriguez-Cruz, S. E.; Jockusch, R. A.; Williams, E. R. *J. Am. Chem. Soc.* **1998**, *120*, 5842-5843.
(159) Wong, R. L.; Paech, K.; Williams, E. R. *Int. J. Mass. Spectrom.* **2004**, *232*, 59-66.
(160) Donald, W. A.; Williams, E. R. *J. Phys. Chem. A* **2008**, *112*, 3515-3522.
(161) Donald, W. A.; Leib, R. D.; Demireva, M.; O'Brien, J. T.; Prell, J. S.; Williams, E. R. *J. Am. Chem. Soc.* **2009**, *131*, 13328-13337.

(162) Richmond, G. L. *Chem. Rev.* **2002**, *102*, 2693-2724.

(163) Torchet, G.; de Feraudy, M. F.; Boutin, A.; Fuchs, A. H. *J. Chem. Phys.* **1996**, *105*, 3671.

(164) Maillet, J.-B.; Boutin, A.; Fuchs, A. H. *J. Chem. Phys.* **1999**, *111*, 2095.

(165) van de Waal, B. W. T., G.; Feraudy, M. F. *Chem. Phys. Lett.* **2000**, *331*, 57-63.

(166) Buch, V.; Sigurd, B.; Paul Devlin, J.; Buck, U.; Kazimirski, J. K. *Int. Rev. Phys. Chem.* **2004**, *23*, 375-433.

(167) Bergman, R.; Swenson, J. *Nature* **2000**, *403*, 283-286.

(168) Delzeit, L.; Devlin, J. P.; Buch, V. *J. Chem. Phys.* **1997**, *107*, 3726.

(169) Delzeit, L.; Devlin, M. S.; Rowland, B.; Devlin, J. P.; Buch, V. *J. Phys. Chem.* **1996**, *100*, 10076-10082.

(170) Buch, V.; Delzeit, L.; Blackledge, C.; Devlin, J. P. *J. Phys. Chem.* **1996**, *100*, 3732-3744.

(171) Pradzynski, C. C.; Forck, R. M.; Zeuch, T.; Slavicek, P.; Buck, U. *Science* **2012**, *337*, 1529-1532.

(172) Torchet, G.; Farges, J.; Deferaudy, M. F.; Raoult, B. *Ann. Phys-Paris* **1989**, *14*, 245-260.

(173) Torchet, G.; Schwartz, P.; Farges, J.; Deferaudy, M. F.; Raoult, B. *J. Chem. Phys.* **1983**, *79*, 6196-6202.

(174) Heiles, S.; Cooper, R. J.; DiTucci, M. J.; Williams, E. R. *Chem. Sci.* **2015**, *6*, 3420-3429.

(175) Donald, W. A.; Williams, E. R. *Pure Appl. Chem.* **2011**, *83*, 2129-2151.

(176) Donald, W. A.; Leib, R. D.; Demireva, M.; Negru, B.; Neumark, D. M.; Williams, E. R. *J. Phys. Chem. A* **2011**, *115*, 2-12.

(177) Donald, W. A.; Williams, E. R. *J. Phys. Chem. B* **2010**, *114*, 13189-13200.

(178) Donald, W. A.; Williams, E. R. *J. Am. Soc. Mass. Spectr.* **2010**, *21*, 615-625.

(179) Donald, W. A.; Demireva, M.; Leib, R. D.; Aiken, M. J.; Williams, E. R. *J. Am. Chem. Soc.* **2010**, *132*, 4633-4640.

(180) Demireva, M.; Williams, E. R. *J. Am. Soc. Mass. Spectr.* **2010**, *21*, 1133-1143.

(181) Donald, W. A.; Leib, R. D.; O'Brien, J. T.; Williams, E. R. *Chemistry* **2009**, *15*, 5926-5934.

(182) Prell, J. S.; O'Brien, J. T.; Holm, A. I. S.; Leib, R. D.; Donald, W. A.; Williams, E. R. *J. Am. Chem. Soc.* **2008**, *130*, 12680-12689.

(183) O'Brien, J. T.; Prell, J. S.; Holm, A. I. S.; Williams, E. R. *J. Am. Soc. Mass. Spectr.* **2008**, *19*, 772-779.

(184) Donald, W. A.; Leib, R. D.; O'Brien, J. T.; Holm, A. I. S.; Williams, E. R. *Proc. Natl. Acad. Sci. U.S.A.* **2008**, *105*, 18102-18107.

(185) Donald, W. A.; Leib, R. D.; O'Brien, J. T.; Bush, M. F.; Williams, E. R. *J. Am. Chem. Soc.* **2008**, *130*, 3371-3381.

(186) Leib, R. D.; Donald, W. A.; O'Brien, J. T.; Bush, M. F.; Williams, E. R. *J. Am. Chem. Soc.* **2007**, *129*, 7716-7.

(187) Leib, R. D.; Donald, W. A.; Bush, M. F.; O'Brien, J. T.; Williams, E. R. *J. Am. Soc. Mass. Spectr.* **2007**, *18*, 1217-1231.

(188) Leib, R. D.; Donald, W. A.; Bush, M. F.; O'Brien, J. T.; Williams, E. R. *J. Am. Chem. Soc.* **2007**, *129*, 4894-4895.

(189) Klots, C. E. *J. Chem. Phys.* **1985**, *83*, 5854-5860.

(190) Nam, S. H.; Park, H. S.; Lee, M. A.; Cheong, N. R.; Song, J. K.; Park, S. M. *J. Chem. Phys.* **2007**, *126*, 224302.

(191) Evans, D. H. *Chem. Rev.* **2008**, *108*, 2113-2144.

Chapter 2

Hydrated Alkali Metal Ions: Spectroscopic Evidence for Clathrates

This chapter is reproduced with permission from
Cooper, R.J.; Chang, T.M.; Williams, E.R.
"Hydrated Alkali Metal Ions: Spectroscopic Evidence for Clathrates"
Journal of Physical Chemistry A **2013**, 117, 6571-6579
© 2013 American Chemical Society

2.1 Introduction

Water-solute interactions are important in a wide range of physical phenomena including molecular structure,[1-5] solubilities of dissolved gases[6] and the partitioning of ions near interfaces.[7-10] Water has a remarkable ability to form hydrogen-bonding (H-bonding) networks that incorporate small guest molecules. At high pressure and low temperature, water can form ice-like crystalline solids known as clathrate hydrates around small, nonpolar gas molecules.[11] The gas molecules are trapped in H-bonded water cages that are fused together resulting in one of three known clathrate crystal structures depending on the size of the entrained guest molecule.[11,12] These gas hydrates are thought to play important roles in global climate change[13-15] and planetary surface chemistry,[16,17] and show promise in applications including greenhouse gas sequestration[18,19] as well as natural gas transportation and storage.[20,21] Clathrate hydrates of small hydrocarbons, such as methane, can block oil and gas flow in pipelines often requiring the use of large volumes of chemical inhibitors that can contaminate crude feedstocks.[11,12] These same gas hydrates are promising for use as an untapped energy source. Deposits of methane clathrates occur in permafrost soils and, to a much larger extent, in oceanic sediments. Although estimates of the total amount of methane trapped in clathrate deposits worldwide vary considerably,[22,23] conservative estimates suggest that the total energy trapped in clathrates is twice the amount in all other sources of natural gas combined.[11,12] Owing to their potential applications and importance in industrial processes, understanding the formation of gas hydrates has been the subject of recent experimental[17,24-26] and computational[27-31] research.

Evidence that some hydrated gas-phase ions adopt clathrate structures has also been reported. A number of groups have noted an anomalously high ion abundance in mass spectra of $H^+(H_2O)_n$ for $n = 21$ generated with a variety of experimental conditions.[32-40] Such peaks of increased intensity in mass spectra are referred to as "magic number" clusters (MNCs). It was proposed over 35 years ago that the high stability of the $H^+(H_2O)_{21}$ cluster arises from the ability of water molecules to form a pentagonal dodecahedral clathrate structure around an encaged water molecule consisting of twelve 5-water rings, with the excess charge either residing at the surface of the water cage network or at the interior water molecule.[33,41] Several computational studies have identified the dodecahedron as a stable, low-energy structure,[34,37,39,42-50] with more recent calculations indicating that the proton resides on the surface.[39,46-50] Castleman and co-workers[51] reacted $H^+(H_2O)_{21}$ with trimethylamine and found that up to 10 trimethylamine molecules attached to this ion, consistent with 10 free O-H groups on the surface of a water dodecahedron. Spectroscopic evidence for a clathrate structure was reported by both Shin *et al.*[39]

and Miyazaki *et al.*,[52] who performed IR studies on size-selected protonated water clusters. These groups observed multiple bands in the free-OH region (~3600 – 3800 cm^{-1}) at smaller cluster sizes ($n \leq 10$) arising from water molecules in different H-bonding environments. The spectra simplify near $n = 11$ to two bands, which persists until $n = 21$ where there is a spectral simplification to one band consistent with the homogeneous H-bonding environment of surface water molecules in a clathrate structure.

The appearance of magic numbers in clusters of gaseous hydrates of other ions, including $H^+(H_2O)_{28}$,[34,40] $O^+(H_2O)_{20}$,[53] doubly protonated gramicidin S,[38] alkylammonium ions,[54] and $NH_4^+(H_2O)_{20}$[55,56] have been attributed to clathrate structures as well, and experimental evidence for such structures from vibrational spectroscopy has been reported for $NH_4^+(H_2O)_{20}$.[56] An abundant MNC for Cs^+, Rb^+ and K^+ occurs at $n = 20$ and there are additional magic numbers near this cluster size as well.[57-60] A MNC for Li^+ at $n = 20$ has been produced under some conditions,[58,59] but not others.[60]

The structures and stabilities of clathrates of alkali metal ions have been extensively investigated with computational methods.[58,61-67] Dodecahedral clusters are calculated to be stable, but other structures can be lower in energy. Smith and Dang reported[62] that the global minimum structure for $Cs^+(H_2O)_{20}$ is a clathrate cage consisting of 4-, 5-, and 6-membered water rings which is more stable than the dodecahedron by ~4 kJ/mol. Clathrate cages were also identified as lowest-energy structures for $Cs^+(H_2O)_{18}$ and $Cs^+(H_2O)_{22}$. Hartke and co-workers investigated structures of $M^+(H_2O)_n$ clusters where M = Na, K, and Cs and $n \leq 24$ using a TIP4P/OPLS model potential.[64,65] They found that the lowest-energy structures for $Cs^+(H_2O)_{20}$ and $K^+(H_2O)_{20}$ are distorted dodecahedra that are essentially isoenergetic with other non-dodecahedral clathrates. Clathrate structures were found to be lowest in energy for other cluster sizes, with complete cages forming for these ions at $n = 18$. In contrast, clathrate structures are not energetically competitive for Na^+, which is located off-center in the droplet,[63-65] consistent with other higher-level *ab inito* calculations[66] and the absence of a MNC in the mass spectra for this ion.[58-60,63]

Here, the first experimental evidence for the formation of clathrate cages in MNCs of alkali metal ions using IRPD spectroscopy is reported. The larger K^+, Rb^+ and Cs^+ ions promote the formation of clathrate cages but Na^+ does not, and Li^+ is intermediate with a significant population of clathrate structures for clusters with 20 water molecules.

2.2 Experimental Methods

All experiments were performed using a home-built 7.0 T Fourier-transform ion cyclotron resonance mass spectrometer coupled to a tunable OPO/OPA laser system. The instrument, formerly with a 2.75 T magnet, and experimental setup are described in detail elsewhere.[68] Briefly, hydrated ions are generated by nanoelectrospray ionization of 3-5 mM aqueous solutions of alkali metal salts using borosilicate capillaries pulled to an inner tip diameter of ~1 μm. A platinum wire is inserted into the capillary so that it is in direct contact with the solution. A potential of ~+600 V relative to the entrance of the mass spectrometer is applied to the wire. The resulting hydrated ions are guided by electrostatic lenses through five stages of differential pumping into an ion cell that is surrounded by a temperature regulated copper jacket,[69] equilibrated to 133 K for at least 8 h prior to each experiment. A pulse of dry nitrogen gas is introduced into the vacuum chamber at a pressure of ~10^{-6} Torr for ~5 s to aid with thermalizing and trapping the ions. This is followed by a ~7 s delay to allow the pressure in the chamber to drop below 10^{-8} Torr. The ion of interest is subsequently isolated using a stored waveform inverse Fourier transform waveform prior to photodissociation.

Blackbody infrared radiative dissociation (BIRD) rate constants are determined from the extent of fragmentation that occurs for up to 3.0 s as a result of the absorption of blackbody photons from the ion cell and copper jacket. Laser photodissociation at specific IR frequencies is achieved by irradiating the isolated precursor ions for ~1 s with tunable IR light from an OPO/OPA laser system (LaserVision, Bellevue, WA, U.S.A.) pumped with the fundamental of a Nd:YAG laser (Continuum, Santa Clara, CA, U.S.A.) at a 10 Hz repetition rate. A first-order photodissociation rate constant is obtained from the relative abundances of the precursor and fragment ions. This rate constant is corrected for fragmentation due to BIRD measured in the absence of laser irradiation, as well as frequency dependent variations in the laser power. The photodissociation rate constants are plotted as a function of incident photon energy yielding IRPD spectra.

Calculated structures for $Cs^+(H_2O)_{20}$ and $Na^+(H_2O)_{20}$ were obtained from a Monte Carlo conformation search using Macromodel 9.1 (Schrödinger, Inc., Portland, Oregon). The lowest-energy conformer for each of these clusters was geometry optimized at the B3LYP/6-31+G** level of theory using Q-Chem 3.1[70] (Q-Chem, Inc., Pittsburgh, PA).

2.3 Results and Discussion

2.3.1 Magic Number Clusters. A broad distribution of hydrated ions, $M^+(H_2O)_n$, where M = Li, Na, K, Rb and Cs, can be readily formed by electrospray ionization (Figure 2.1; mass spectra plotted on an *n* scale for comparisons between different metal ions at the same cluster size). The average cluster size depends on several experimental parameters, but for a given set of conditions, the cluster abundances are reproducible to within a few percent. There are several MNCs in these distributions, with $n = 20$ especially abundant for Cs^+. This cluster size is also abundant in the distributions for Rb^+ and K^+, but not Na^+ and only marginally so for Li^+. Magic numbers in mass spectra of alkali ion hydrates, especially those that occur at $n = 20$, have been reported previously.[57-60] Evidence that $Li^+(H_2O)_{20}$ is a MNC was reported previously under some conditions[58,59] but not others.[60]

Some other cluster sizes also have unusually high abundances. There are magic numbers at $n = 18$ for Cs^+, Rb^+ and K^+, and $n = 16$ is also unusually abundant for K^+. There are additional magic numbers at larger cluster sizes, such as $n = 49, 51, 53$ and 55 for Li^+ and at $n = 41$ and 38 for K^+ and Rb^+, respectively. To our knowledge, these larger magic numbers have not been reported previously for these metal ions. For *n* between 17 and 21, the mass spectra of hydrated alkali metal ions measured here reproduce features reported in previous studies of these hydrates, indicating that these MNCs are produced under a wide variety of conditions.[57-60]

2.3.2 Cluster Stability. The appearance of a MNC depends not only on the thermodynamic stability of the cluster itself, but also on that of both larger and smaller clusters. For example, the high abundance of $K^+(H_2O)_{20}$ could be due to the high stability of this cluster, or it could be due to the significant instability of both $K^+(H_2O)_{19}$ and $K^+(H_2O)_{21}$, i.e., $K^+(H_2O)_{21}$ may be rapidly depleted by evaporation, thereby increasing the population of the next lowest lying cluster. The intrinsic stability of each cluster between $n = 17$ and 21 was determined by measuring BIRD rate constants for these clusters (Figure 2.2). BIRD rate constants for these ions depend on the rates of radiative absorption and emission as well as the binding energies of water molecules to the cluster. The radiative absorption and emission rates for different metal ions at the same cluster size should be similar. Thus, differences in BIRD rate constants at specific cluster sizes predominantly reflect differences in binding energies of water molecules, with smaller BIRD rate constants indicative of more stable structures with higher water molecule binding energies.

BIRD rate constants for Cs^+, Rb^+ and K^+ with $n = 18$ and 20 are much lower than those of neighboring clusters and those for Li^+ and Na^+ at these same sizes. In the absence of structural effects, water molecule binding energies should increase with decreasing cluster size, although differences at these large cluster sizes are expected to be small. There are no distinct magic numbers for sodium with between 17 and 21 water molecules attached and the range of BIRD rate constants for these clusters is small (~0.20 – 0.35 s^{-1}) (Figure 2.2, bottom). Other alkali ion hydrates with BIRD rates that are significantly below or above this range are indicative of especially stable or unstable clusters, respectively. These results indicate that the origin of the high abundances of $M^+(H_2O)_{20}$, M = Cs, Rb and K, is due to both the high stabilities of these specific clusters and the significant instability of the next higher cluster, $M^+(H_2O)_{21}$. The high stability of the $n = 20$ clusters suggests structures in which hydrogen bonding is optimized for each water molecule. The instability of the $n = 21$ clusters for Cs^+, Rb^+ and K^+ compared to that for Na^+ and Li^+ is consistent with an additional water molecule attaching to the stable H-bonded $n = 20$ core. The clusters $M^+(H_2O)_{18}$, M = Cs, Rb and K, also have high stabilities, but the clusters at the next higher size are only slightly less stable than those with Na^+, and all the clusters at $n = 17$ have similar stabilities.

Rate constants for Cs^+ were measured at additional cluster sizes. The BIRD rate constant for $n = 16$ is higher than that at $n = 17$ and 15, indicating that the stabilities of the clusters in this size range are not solely an even/odd number effect. Previous studies suggest that the appearance of even magic numbers starting at $n = 18$ for Cs^+ ends after $n = 24$,[57-60] and our mass spectra show a similar trend with the next magic number at $n = 27$. This likely reflects a transition from hydrogen bonding networks based on the addition of water molecules to the $n = 20$ structure to networks built around other stable geometries.

2.3.3 Free-OH Stretch Region of $M^+(H_2O)_{17-21}$. IRPD spectra between ~3660 – 3760 cm^{-1} of $M^+(H_2O)_n$, where $n = 17 – 21$ and M = Cs or Na are shown in Figure 2.3. Vibrational resonances in this region correspond to free-OH stretches, and these frequencies are sensitive to the local water H-bond network[39,40,52,56,71-75] and the ion charge.[76-78] There is a relatively sharp band at ~3700 cm^{-1} in the spectrum of each ion, which is characteristic of the free-OH stretch of a water molecule that accepts two and donates one H-bond (AAD water molecule).[39,40,52,56] There are no other free-OH stretch bands in the spectra of either $Cs^+(H_2O)_{18}$ or $Cs^+(H_2O)_{20}$, indicating that the H-bonding environment of surface water molecules with a free-OH stretch is homogeneous insofar as they each form three hydrogen bonds. In contrast, there is a band of varying intensity near 3720 cm^{-1} in the spectra of the other Cs^+ clusters. This stretching frequency corresponds to a water molecule that accepts and donates one H-bond (AD water molecule). The appearance of the AD band in these clusters indicates that some water molecules participate in less extensive hydrogen bonding, forming only two H-bonds. The presence of some water molecules with only two H-bonds for $Cs^+(H_2O)_n$, where $n = 17$, 19 and 21 is consistent with the lower stability of these ions compared to those with $n = 18$ and 20, where all water molecules have at least three H-bonds.

Stretching bands in the free-OH region have been used to characterize the structures of a variety of gas-phase hydrated ions,[39,40,52,56,71-79] including small hydrates of alkali metal ions ($n < 10$).[80-82] A dodecahedral clathrate structure for $H^+(H_2O)_{21}$ was deduced from a combination of computed and experimental vibrational predissociation spectra.[39,40,52,83] An intense AAD band, and the disappearance of the AD band at this cluster size indicate the onset of the dodecahedral clathrate structure, which has only one stretching band in the free-OH region corresponding to AAD water molecules. There is a similar spectral simplification in the free-OH region of $Cs^+(H_2O)_n$ to just the AAD band for $Cs^+(H_2O)_{20}$ (Figure 2.3) characteristic of a caged hydration structure, such as the dodecahedral clathrate. The appearance of just an AAD band for $Cs^+(H_2O)_{18}$ differs from $H^+(H_2O)_{19}$, where the AD stretch was also observed, indicating a significant difference in hydration structure between the hydrated proton and hydrated alkali ions. With their larger size and lower surface charge density, it is likely that some alkali ions are more suitable guests for clathrate cages than the small and highly mobile hydrated proton.

The absence of a magic number at $n = 20$ for Na^+ points to a fundamentally different hydration motif for this ion compared to the larger Cs^+. The IRPD spectra for $Na^+(H_2O)_{17\text{-}20}$ are strikingly different from those of Cs^+ over this range of cluster sizes (Figure 2.3). For hydrated Na^+, the AAD band is the most intense, but the AD band is a distinct peak in all spectra except for $n = 17$, for which significant photodissociation is still observed at this frequency. These results indicate that the arrangement of water molecules around Na^+ is much less uniform. The presence of two-coordinate water molecules in these sodium clusters is likely the origin of their higher BIRD rate constants and the absence of MNCs.

The ratio of the AD to AAD signal provides information about the hydration structure in these clusters. The areas under the AD and AAD bands were determined from Gaussian fits of these bands after a baseline subtraction to account for the high-energy tail of the bonded-OH bands. The ratios of the AD to AAD peak areas are given in Table 2.1. For Cs^+, Rb^+ and K^+, this ratio is ≤ 0.01 at $n = 18$ and 20 whereas this ratio is more than five-fold higher at the adjacent cluster sizes. Evidently, the larger alkali ions adopt hydration structures at $n = 18$ and 20 that maximize the extent of hydrogen bonding for water molecules with a free-OH, the most obvious candidates being clathrate cages. For Na^+, the value of 0.24 at $n = 20$ is substantially higher than that for the larger ions, pointing to a less optimal H-bond network containing more two-coordinate water molecules. There is no significant trend with cluster size, consistent with the similar BIRD rate constants obtained for these sodiated clusters. Interestingly, the AD band is far less intense for $Li^+(H_2O)_{20}$ than it is for $Na^+(H_2O)_{20}$ despite the smaller ionic radius of Li^+. Although Na^+ appears to be an unsuitable guest for a clathrate cage, such structures appear to be energetically competitive for Li^+ at $n = 20$.

2.3.4 Comparison to Computed Structures. The origin of MNCs for hydrated alkali metal ions has been investigated previously with various levels of theory.[58,61-67] Hartke and co-workers reported structures for $M^+(H_2O)_{1\text{-}24}$, where M = Cs, K and Na, that were identified with a global geometry optimization procedure using a TIP4P/OPLS empirical potential to model both ion-water and water-water interactions.[63-65] They found that several MNCs can be rationalized by the formation of clathrate hydration structures around a central ion that are stable as a result of each water molecule participating in three H-bonds. For K^+ and Cs^+, they found that clathrate hydration structures begin to be energetically preferred at $n = 16$ and $n = 18$, respectively, and are also lowest energy for $n = 20$. The lowest-energy structure for $Cs^+(H_2O)_{20}$ and $K^+(H_2O)_{20}$ is a distorted dodecahedron, but these structures are nearly isoenergetic with other non-dodecahedral clathrate structures that differ in energy by as little as 1 kJ/mol, consistent with other computational results.[62] For $Na^+(H_2O)_{20}$, Hartke and co-workers found that the cation is not in the center of the droplet in the lowest-energy structure, with ion-water interactions disrupting the formation of a clathrate H-bond network.[63] This structure is 13 kJ/mol more stable than the dodecahedral cage, indicating that clathrate structures are not energetically competitive for this ion. These structures were found to be stable at temperatures between 40 – 150 K.[65] Their results are in agreement with *ab initio* calculations for $Na^+(H_2O)_{19\text{-}21}$, which suggest that there is no special stability associated with the dodecahedral structure.[66]

Low-energy structures of $Cs^+(H_2O)_{20}$ and $Na^+(H_2O)_{20}$ were generated from a Monte Carlo conformational search for illustrative purposes, and the lowest-energy structures were subsequently optimized at the B3LYP/6-31+G** level of theory (Figure 2.4). A clathrate structure identified from these limited calculations is lowest in energy for cesium, with each water molecule participating in three H-bonds (Figure 2.4a). This structure consists of 4-, 5- and 6-membered water rings, consistent with previous computational studies where non-dodecahedral clathrates were found to be energetically competitive with or more stable than dodecahedral clathrates.[62,64,65] In contrast, the hydration structure around Na^+ is significantly less uniform, and includes two, three, and four-coordinate water molecules (Figure 2.4b). The total number of H-bonds in $Cs^+(H_2O)_{20}$ is 30 compared to 28 H-bonds for $Na^+(H_2O)_{20}$, which is consistent with the higher stability of the cesium cluster. The fewer H-bonds for $Na^+(H_2O)_{20}$ indicate that direct ion-water interactions are somewhat more important than water-water interactions at this cluster size.

Our experimental data provide support for the formation of clathrate cages as the origin of MNCs for hydrated alkali metal ions with $17 \leq n \leq 21$. For Cs^+, Rb^+ and K^+ with $n = 18$ and 20, the low BIRD rate constants and the appearance of just the AAD band in the free-OH region are consistent with stable clathrate cages forming around these ions. To our knowledge, Rb^+ has not been studied computationally, but our results indicate that its hydration structure is similar to that for Cs^+ and K^+. It is likely that cluster populations in our experiments consist of many isomers that are energetically competitive. For the $n = 20$ clathrates, both the dodecahedral and non-dodecahedral clathrates consist of only AAD and ADD (accepts one and donates two H-bonds) water molecules. These structures are expected to have virtually indistinguishable spectra in the free-OH region, so the relative contributions of dodecahedral and non-dodecahedral structures cannot be determined. The absence of a trend in BIRD rate constants for Na^+, as well as the persistence of the AD stretch in the spectra, indicate that clathrate structures are not formed for this ion.

Interactions between Li^+ and surrounding water molecules are even stronger than those for Na^+, yet the low BIRD rate constant and diminished AD band for $Li^+(H_2O)_{20}$ are suggestive of contributions of a clathrate-type structure to the ion population. Calculations on lithium hydrates show that at $n = 20$, the lithium ion can occupy a tetrahedral pocket near the water cluster surface where it is surrounded by four water molecules in the first coordination shell.[67] It appears that the smaller size and lower coordination number of Li^+ makes possible the formation of cage-like structures. Unlike the larger alkali metal ions that are centered within the 20 water clathrates, Li^+ occupies a site closer to the surface.[67] At other cluster sizes, however, computed structures of lithium hydrates are more similar to sodium hydrates and no clathrate structures are expected.[67] Based on the AD/AAD band ratios (Table 2.1), there does not appear to be a significant population of clathrate structures for lithium at cluster sizes other than $n = 20$.

2.3.5 Bonded-OH Stretch Region of *n* = 20 Clathrates. Information about clathrate structures of H^+ and NH_4^+ deduced from IR spectra have been primarily based on an analysis of the free-OH region.[39,40,52,56] Although the hydrogen-bonded region (~3000 – 3600 cm^{-1}) contains a wealth of information about the hydration network, spectral congestion and inherently broad bands can complicate detailed analysis. Spectra of $M^+(H_2O)_{20}$ for each of the alkali metal ions over both the free and bonded-OH regions are shown in Figure 2.5. There are three dominant features in the hydrogen-bonded region, with the highest energy band at ~3550 cm^{-1}, which has previously been assigned to the H-bonded stretches of ADD water molecules.[39,52,84] Calculations on $H^+(H_2O)_{21}$ indicate that the ADD symmetric and asymmetric stretches are split into sharp doublets,[39] and our spectra of $M^+(H_2O)_{20}$ show evidence for this splitting. It is difficult to assign the broad peak centered on ~3400 cm^{-1} to a particular normal mode of vibration because there are many coupled modes with resonances near this energy. The lower energy peak near 3200 cm^{-1} likely arises from the H-bonded stretch of AAD water molecules.[84] The photodissociation rate constants are higher for $Na^+(H_2O)_{20}$ than the other alkali ion hydrates at this size, consistent with the lower stability of this ion measured by BIRD as well as possible effects of structure on absorption cross sections.

The intensities of the ADD stretches at ~3550 cm^{-1} in the spectra of Cs^+, Rb^+, and K^+ are similar whereas the intensity of this stretch is slightly lower in the spectrum of Li^+ and much lower in that of Na^+. The signal intensity of the ADD band at 3550 cm^{-1} was evaluated for each ion by integrating both this band and the broad H-bonding feature at 3400 cm^{-1}. The 3550 cm^{-1}/3400 cm^{-1} band ratios for Cs^+(0.53), Rb^+(0.48), and K^+(0.51) are similar and are much higher than that for Na^+(0.35). Thus, the intensity of the ADD band in the bonded-OH region is inversely correlated to the intensity of the AD free-OH band (Table 2.1). For $Na^+(H_2O)_{20}$, the relative intensity of the ADD band is almost 30% lower than that for the larger ions and the AD to AAD ratio in the free-OH region is 24 times higher. The 3550 cm^{-1}/3400 cm^{-1} ratio for $Li^+(H_2O)_{20}$ is 0.44 and is intermediate between that of Na^+ and the larger ions, indicating a significant population of clathrate structures for Li^+. Thus, the appearance of the ADD band in the bonded-OH region appears to be a signature for clathrates with $n = 20$ because it correlates with the disappearance of the AD band in the free-OH region.

A similar correlation between the emerging ADD band at 3550 cm^{-1} and the disappearing AD band at 3720 cm^{-1} was reported for $H^+(H_2O)_{21}$.[39,52] As the water network transitions from a planar to a more cage-like structure, there are fewer two-coordinate water molecules and a greater population of three-coordinate water molecules. In the case of alkali ion clathrates, it appears that a similar trend occurs. A clathrate structure with dodecahedral geometry has 10 ADD water molecules at its vertices.[61] Even for non-dodecahedral clathrate structures, the population of ADD water molecules is the same as a result of the geometry of the cage. Clathrate water networks are made up exclusively of three-coordinate water molecules, and deviations from this structural network lead to a less stable geometry for the larger cations. $Na^+(H_2O)_{20}$ has more two- and four-coordinate water molecules leading to a decreased number of ADD water molecules and a corresponding lowering of the thermal stability of this cluster. The relative intensity of the ADD band in the bonded-OH region is therefore an excellent signature for ions in clathrates consisting of 20 water molecules.

2.3.6 Bonded-OH Region Stretch Region of $K^+(H_2O)_{17\text{-}21}$. The general applicability of the ADD stretching signature in the hydrogen-bonded region to clathrates of sizes other than n = 20 was investigated. IRPD spectra in this region for $K^+(H_2O)_n$ with $17 \leq n \leq 21$ are shown in

Figure 2.6. The intensity of the ADD band compared to the band arising from broad hydrogen-bonding features at 3400 cm^{-1} does not change appreciably between cluster sizes n = 17 and 19. Yet there is spectral simplification in the free-OH region of $K^+(H_2O)_{18}$, strongly suggesting the presence of a clathrate structure. It appears that the intensity of the ADD band in the H-bonding region is not a reliable spectroscopic signature for clathrates at smaller cluster sizes.

Similar results were reported for spectra of protonated water, where the ADD shoulder near 3550 cm^{-1} is only intense starting at the magic number $H^+(H_2O)_{21}$ and the intensity of this band decreases with increasing cluster size. Computational results indicate that the relative populations of ADD and AAD water molecules are the same for both $K^+(H_2O)_{18}$ and $K^+(H_2O)_{20}$.[65] If this is the case, then the greater intensity of the ADD H-bonded stretch at 3550 cm^{-1} for n = 20 may be the result of a larger transition dipole associated with the highly symmetric dodecahedral structure. The persistence of this stretch for the next highest hydrate indicates that water adds on to the clathrate core instead of significantly disrupting the H-bond network for this stable structure, consistent with the anomalously high BIRD rate constant measured for n = 21.

2.4 Conclusions

The structures of MNCs in the mass spectra of $M^+(H_2O)_{17\text{-}21}$, where M = Li, Na, K, Rb and Cs were investigated at 133 K by BIRD and IRPD spectroscopy in the hydrogen-stretch region (~2600 – 3800 cm^{-1}). Clathrate structures for $M^+(H_2O)_{20}$ for M = Cs, Rb, and K are evident from the free-OH stretch of AAD water molecules and the absence of a band for AD water molecules in the IRPD spectra. This result is supported by a corresponding band at 3550 cm^{-1} in the hydrogen bonding OH region that is due to ADD water molecules and is characteristic of clathrate structures at this cluster size. IRPD results indicate that clathrate structures exist for K^+, Rb^+, and Cs^+ with 18 water molecules as well. This is the first direct experimental evidence for clathrate structures for hydrated alkali metal ions. BIRD rate constants indicate that the binding energies of water molecules to $M^+(H_2O)_{20}$ for M = Cs, Rb, and K are unusually high and that the binding energies to the corresponding clusters with 21 water molecules are unusually low, consistent with water attaching onto a clathrate core for the larger cluster.

In contrast to results for the larger alkali metal ions with 20 water molecules, there is significant signal in the free-OH region of the IRPD spectra of $Na^+(H_2O)_{20}$ that corresponds to AD water molecules and a lower signal in the bonded-OH region corresponding to AAD water molecules. There is no enhanced abundance for this cluster in the mass spectrum. These results indicate that clathrate structures are much less significant for Na^+. In contrast, signals in these corresponding regions in the IRPD spectrum for $Li^+(H_2O)_{20}$, as well as the higher abundance of this cluster in the mass spectrum suggests that clathrate structures do exist along with other structures for this small ion. These results indicate that the size of the cation is not the only factor that affects clathrate formation, but rather the combination of cation size and how the ion affects the hydrogen-bonding network of water molecules in the cluster determines clathrate stability.

These results indicate that IRPD spectra measured in both the bonded and free-OH regions in combination with BIRD rate constants can provide a useful indicator of clathrate structures, although the bonded-OH region appears to be most useful for clusters with 20 water molecules. This method should be generally applicable for investigating the structures of other ions that may induce clathrate formation.

2.5 References

(1) Levy, Y.; Onuchic, J. N. *Annu. Rev. Biophys. Biomol. Struct.* **2006**, 35, 389–415.

(2) Bush, M. F.; Prell, J. S.; Saykally, R. J.; Williams, E. R. *J. Am. Chem. Soc.* **2007**, *129*, 13544–13553.

(3) Blom, M. N.; Compagnon, I.; Polfer, N. C.; Helden, von, G.; Meijer, G.; Suhai, S.; Paizs, B.; Oomens, J. *J. Phys. Chem. A* **2007**, *111*, 7309–7316.

(4) Nagornova, N. S.; Rizzo, T. R.; Boyarkin, O. V. *Science* **2012**, *336*, 320–323.

(5) Chang, T. M.; Prell, J. S.; Warrick, E. R.; Williams, E. R. *J. Am. Chem. Soc.* **2012**, 134, 15805–15813.

(6) Chang, R. *Physical Chemistry for the Chemical and Biological Sciences*. University Science Books: Sausalito, CA, 2000; pp. 215–217.

(7) Jungwirth, P.; Tobias, D. J. *Chem. Rev.* **2006**, *106*, 1259–1281.

(8) Ghosal, S.; Hemminger, J. C.; Bluhm, H.; Mun, B. J.; Hebenstreit, E. L.; Ketteler, G.; Ogletree, D. F.; Requejo, F. G.; Salmeron, M. *Science* **2005**, *307*, 563–566.

(9) Petersen, P. B.; Saykally, R. J. *Annu. Rev. Phys. Chem.* **2006**, *57*, 333–364.

(10) Noah-Vanhoucke, J.; Geissler, P. L. *Proc. Natl. Acad. Sci. U.S.A.* **2009**, *106*, 15125–15130.

(11) Sloan, E. D. *Nature* **2003**, *426*, 353–363.

(12) Koh, C. A.; Sloan, E. D.; Sum, A. K.; Wu, D. T. *Annu. Rev. Chem. Biomol. Eng.* **2011**, *2*, 237–257.

(13) Hesselbo, S.; Grocke, D.; Jenkyns, H.; Bjerrum, C.; Farrimond, P.; Morgans Bell, H. S.; Green, O. *Nature* **2000**, *406*, 392–395.

(14) Archer, D.; Buffett, B.; Brovkin, V. *Proc. Natl. Acad. Sci. U.S.A.* **2009**, *106*, 20596–20601.

(15) Dickens, G. R.; O'Neil, J. R.; Rea, D. K.; Owen, R. M. *Paleoceanography* **2010**, *10*, 965–971.

(16) Tobie, G.; Lunine, J. I.; Sotin, C. *Nature* **2006**, *440*, 61–64.

(17) Shin, K.; Kumar, R.; Udachin, K. A.; Alavi, S.; Ripmeester, J. A. *Proc. Natl. Acd. Sci. U.S.A.* **2012**, 109, 14785–14790.

(18) Brewer, P.; Friederich, G.; Peltzer, E.; Orr, F. *Science* **1999**, *284*, 943–945.

(19) Park, Y.; Kim, D. Y.; Lee, J.-W.; Huh, D.-G.; Park, K.-P.; Lee, J.; Lee, H. *Proc. Natl. Acad. Sci. U.S.A.* **2006**, *103*, 12690–12694.

(20) Gudmundsson, J. S.; Andersson, V.; Levik, O. I.; Mork, M. *Ann. N.Y. Acad. Sci.* **2000**, *912*, 403–410.

(21) Stern, L. A.; Circone, S.; Kirby, S. H.; Durham, W. B. *J. Phys. Chem. B* **2001**, *105*, 1756–1762.

(22) Kvenvolden, K. A. *Proc. Natl. Acad. Sci. U.S.A.* **1999**, *96*, 3420–3426.

(23) Boswell, R. Engineering. *Science* **2009**, *325*, 957–958.

(24) Alavi, S.; Udachin, K.; Ripmeester, J. A. *Chem. Eur. J.* **2009**, 16, 1017–1025.

(25) Falenty, A.; Kuhs, W. F. *J. Phys. Chem. B* **2009**, *113*, 15975–15988.

(26) Rauh, F.; Mizaikoff, B. *Anal. Bioanal. Chem.* **2011**, *402*, 163–173.

(27) Walsh, M. R.; Koh, C. A.; Sloan, E. D.; Sum, A. K.; Wu, D. T. *Science* **2009**, *326*, 1095–1098.

(28) Jacobson, L. C.; Molinero, V. *J. Am. Chem. Soc.* **2011**, *133*, 6458–6463.

(29) Knott, B. C.; Molinero, V.; Doherty, M. F.; Peters, B. *J. Am. Chem. Soc.* **2012**, 134, 19544–19547.
(30) Pirzadeh, P.; Kusalik, P. G. *J. Am. Chem. Soc.* **2013**, doi:10.1021/ja400521e.
(31) Fleischer, E. B.; Janda, K. C. *J. Phys. Chem. A* **2013**, doi:10.1021/jp311351j.
(32) Lin, S. S. *Rev. Sci. Instrum.* **1973**, *44*, 516–517.
(33) Searcy, J. Q. *J. Chem. Phys.* **1974**, *61*, 5282–5288.
(34) Hermann, V.; Kay, B. D.; Castleman, A. W., Jr. *Chem. Phys.* **1982**, *72*, 185–200.
(35) Beuhler, R. J.; Friedman, L. *J. Chem. Phys.* **1982**, *77*, 2549–2557.
(36) Echt, O.; Kreisle, D.; Knapp, M.; Recknagel, E. *Chem. Phys. Lett.* **1984**, *108*, 401–407.
(37) Nagashima, U.; Shinohara, H.; Nishi, N.; Tanaka, H. *J. Chem. Phys.* **1986**, *84*, 209–214.
(38) Lee, S.-W.; Freivogel, P.; Schindler, T.; Beauchamp, J. L. *J. Am. Chem. Soc.* **1998**, *120*, 11758–11765.
(39) Shin, J. W.; Hammer, N. I.; Diken, E. G.; Johnson, M. A.; Walters, R. S.; Jaeger, T. D.; Duncan, M. A.; Christie, R. A.; Jordan, K. D. *Science* **2004**, *304*, 1137–1140.
(40) Wu, C.-C.; Lin, C.-K.; Chang, H.-C.; Jiang, J.-C.; Kuo, J.-L.; Klein, M. L. *J. Chem. Phys.* **2005**, *122*, 074315.
(41) Kassner, J. L.; Hagen, D. E. *J. Chem. Phys.* **1976**, *64*, 1860–1861.
(42) Holland, P. M.; Castleman, A. W. *J. Chem. Phys.* **1980**, *72*, 5984–5990.
(43) Buffey, I. P.; Brown, W. B. *Chem. Phys. Lett.* **1984**, *109*, 59–65.
(44) Kozack, R. E.; Jordan, P. C. *J. Chem. Phys.* **1993**, *99*, 2978–2984.
(45) Khan, A. *Chem. Phys. Lett.* **1994**, *217*, 443–450.
(46) Khan, A. *Chem. Phys. Lett.* **2000**, *319*, 440–450.
(47) Hodges, M. P.; Wales, D. J. *Chem. Phys. Lett.* **2000**, *324*, 279–288.
(48) Iyengar, S. S.; Petersen, M. K.; Day, T. J. F.; Burnham, C. J.; Teige, V. E.; Voth, G. A. *J. Chem. Phys.* **2005**, *123*, 084309.
(49) Singh, N. J.; Park, M.; Min, S. K.; Suh, S. B.; Kim, K. S. *Angew. Chem. Int. Ed. Engl.* **2006**, *45*, 3795–3800.
(50) Kuś, T.; Lotrich, V. F.; Perera, A.; Bartlett, R. J. *J. Chem. Phys.* **2009**, *131*, 104313.
(51) Wei, S.; Shi, Z.; Castleman, A. W., Jr. *J. Chem. Phys.* **1991**, *94*, 3268–3270.
(52) Miyazaki, M.; Fujii, A.; Ebata, T.; Mikami, N. *Science* **2004**, *304*, 1134–1137.
(53) Wu, H.-F.; Chin, C.-C.; Liu, B.-M.; Chen, Y.-C.; Lin, C.-H.; Chang, K.-D.; Lee, Y.-H. *Rapid Commun. Mass Spectrom.* **2011**, *25*, 410–414.
(54) Nguyen, V. Q.; Chen, X. G.; Yergey, A. L. *J. Am. Soc. Mass. Spectrom.* **1997**, *8*, 1175–1179.
(55) Shinohara, H.; Nagashima, U.; Tanaka, H.; Nishi, N. *J. Chem. Phys.* **1985**, *83*, 4183–4192.
(56) Diken, E. G.; Hammer, N. I.; Johnson, M. A. *J. Chem. Phys.* **2005**, 123, 164309.
(57) Selinger, A.; Castleman, A. W., Jr. *J. Phys. Chem.* **1991**, 95, 8442–8444.
(58) Steel, E. A.; Merz, K. M.; Selinger, A.; Castleman, A. W. *J. Phys. Chem.* **1995**, *99*, 7829–7836.
(59) Zatula, A. S.; Ryding, M. J.; Andersson, P. U.; Uggerud, E. *Int. J. Mass Spectrom.* **2012**, *330-332*, 191–199.
(60) Sobott, F.; Wattenberg, A.; Barth, H. D.; Brutschy, B. *Int. J. Mass Spectrom.* **1999**, 187, 271–279.
(61) Cioslowski, J.; Nanayakkara, A. *Int. J. Mod. Phys. B* **1992**, *06*, 3687–3693.
(62) Smith, D. E.; Dang, L. X. *J. Chem. Phys.* **1994**, *101*, 7873–7881.

(63) Hartke, B.; Charvat, A.; Reich, M.; Abel, B. *J. Chem. Phys.* **2002**, *116*, 3588–3600.
(64) Schulz, F.; Hartke, B. *ChemPhysChem* **2002**, *3*, 98–106.
(65) Schulz, F.; Hartke, B. A. *Theor. Chem. Acc.* **2005**, *114*, 357–379.
(66) Khan, A. *Chem. Phys. Lett.* **2004**, 388, 342–347.
(67) González, B. S.; Hernández-Rojas, J.; Wales, D. J. *Chem. Phys. Lett.* **2005**, *412*, 23–28.
(68) Bush, M. F.; O'Brien, J. T.; Prell, J. S.; Saykally, R. J.; Williams, E. R. *J. Am. Chem. Soc.* **2007**, 129, 1612–1622.
(69) Wong, R. L.; Paech, K.; Williams, E. R. *Int. J. Mass Spectrom.* **2004**, 232, 59–66.
(70) Shao, Y.; Molnar, L. F.; Jung, Y.; Kussmann, J.; Ochsenfeld, C.; Brown, S. T.; Gilbert, A. T. B.; Slipchenko, L. V.; Levchenko, S. V.; O'Neill, D. P et al. *Phys. Chem. Chem. Phys.* **2006**, *8*, 3172–3191.
(71) Chang, H.-C.; Wang, Y.-S.; Lee, Y. T.; Chang, H.-C. *Int. J. Mass Spectrom.* **1998**, *179/180*, 91–102.
(72) Walters, R. S.; Pillai, E. D.; Duncan, M. A. *J. Am. Chem. Soc.* **2005**, *127*, 16599–16610.
(73) Kamariotis, A.; Boyarkin, O. V.; Mercier, S. R.; Beck, R. D.; Bush, M. F.; Williams, E. R.; Rizzo, T. R. *J. Am. Chem. Soc.* **2006**, *128*, 905–916.
(74) O'Brien, J. T.; Williams, E. R. *J. Phys. Chem. A* **2011**, *115*, 14612–14619.
(75) Demireva, M.; O'Brien, J. T.; Williams, E. R. *J. Am. Chem. Soc.* **2012**, *134*, 11216–11224.
(76) Carnegie, P. D.; Bandyopadhyay, B.; Duncan, M. A. *J. Phys. Chem. A* **2008**, *112*, 6237–6243.
(77) Prell, J. S.; O'Brien, J. T.; Williams, E. R. *J. Am. Chem. Soc.* **2011**, *133*, 4810–4818.
(78) O'Brien, J. T.; Williams, E. R. *J Am Chem Soc* **2012**, *134*, 10228–10236.
(79) Polfer, N. C.; Oomens, J. *Mass Spectrom. Rev.* **2009**, 28, 469-494.
(80) Lisy, J. M. *Int. Rev. Phys. Chem.* **1997**, *16*, 267–289.
(81) Miller, D. J.; Lisy, J. M. *J. Am. Chem. Soc.* **2008**, *130*, 15381–15392.
(82) Miller, D. J.; Lisy, J. M. *J. Am. Chem. Soc.* **2008**, *130*, 15393–15404.
(83) Miyazaki, M.; Fujii, A.; Ebata, T.; Mikami, N. *J. Phys. Chem. A* **2004**, *108*, 10656–10660.
(84) Gruenloh, C. J.; Carney, J. R.; Arrington, C. A.; Zwier, T. S.; Fredericks, S. Y.; Jordan, K. D. *Science* **1997**, *276*, 1678–1681.

2.6 Tables and Figures

Table 2.1. Ratios of AD (~3720 cm^{-1}) to AAD (~3700 cm^{-1}) peak areas determined from Gaussian fits of the bands in the IRPD spectra.

n	Li^+	Na^+	K^+	Rb^+	Cs^+
17	0.36	0.18	0.05	0.06	0.1
18	0.21	0.2	≤ 0.01	≤ 0.01	≤ 0.01
19	0.18	0.29	0.07	0.09	0.06
20	0.03	0.24	≤ 0.01	≤ 0.01	≤ 0.01
21	0.08	0.09	0.05	0.05	0.05

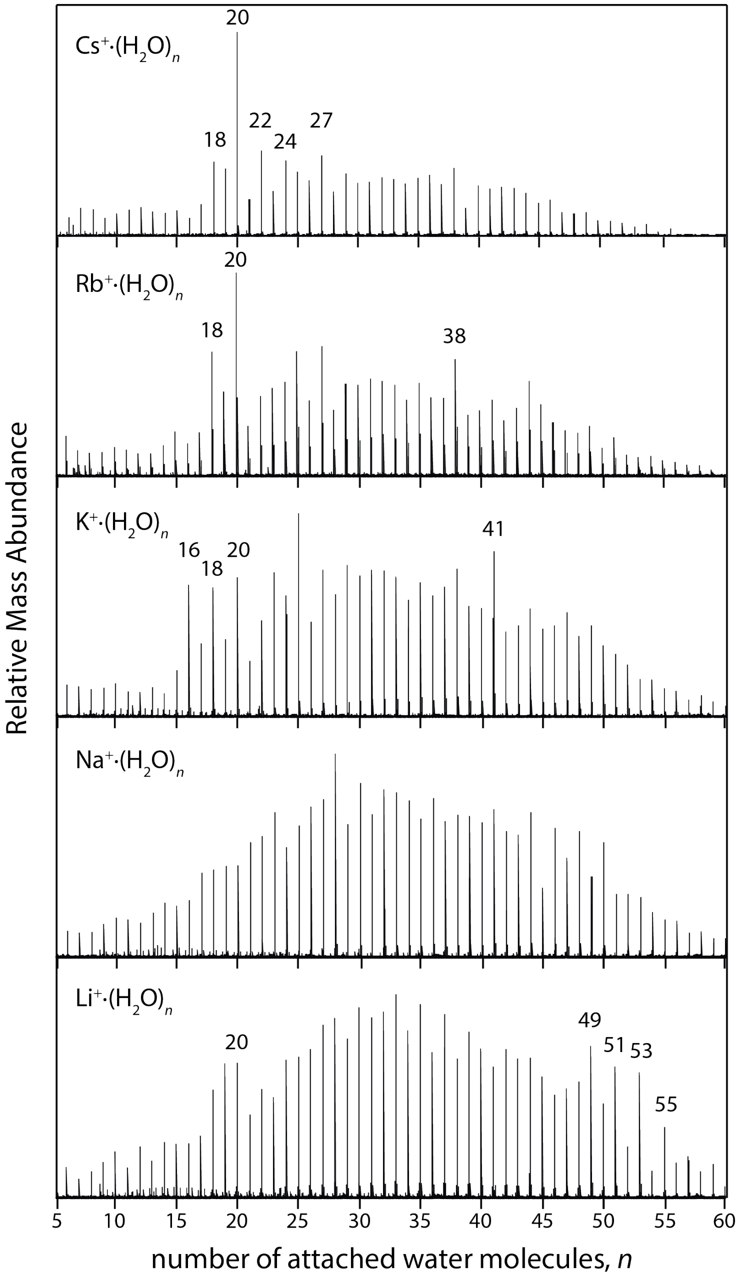

Figure 2.1. Mass spectra of $M^+(H_2O)_n$, where M = Cs, Rb, K, Na and Li, with the abscissa plotted using an *n* scale to facilitate comparison between the different metal ions. Select magic number clusters, corresponding to ions of high abundance relative to adjacent clusters, are labeled.

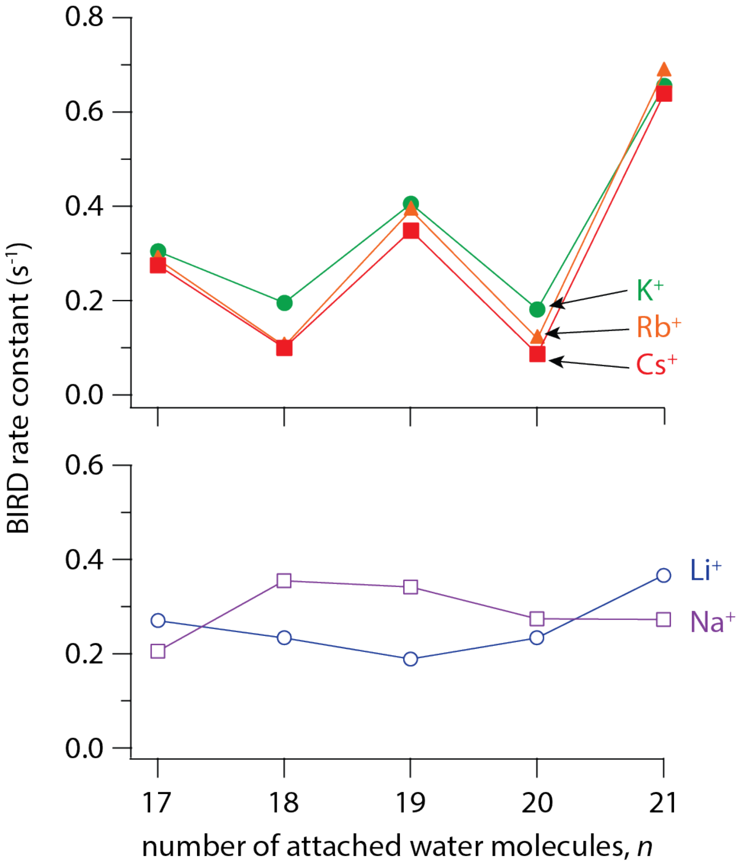

Figure 2.2. BIRD rate constants for $M^+(H_2O)_{17\text{-}21}$, where M = Cs, Rb, K, Na and Li. Low BIRD rate constants reflect high water binding energies characteristic of stable clusters.

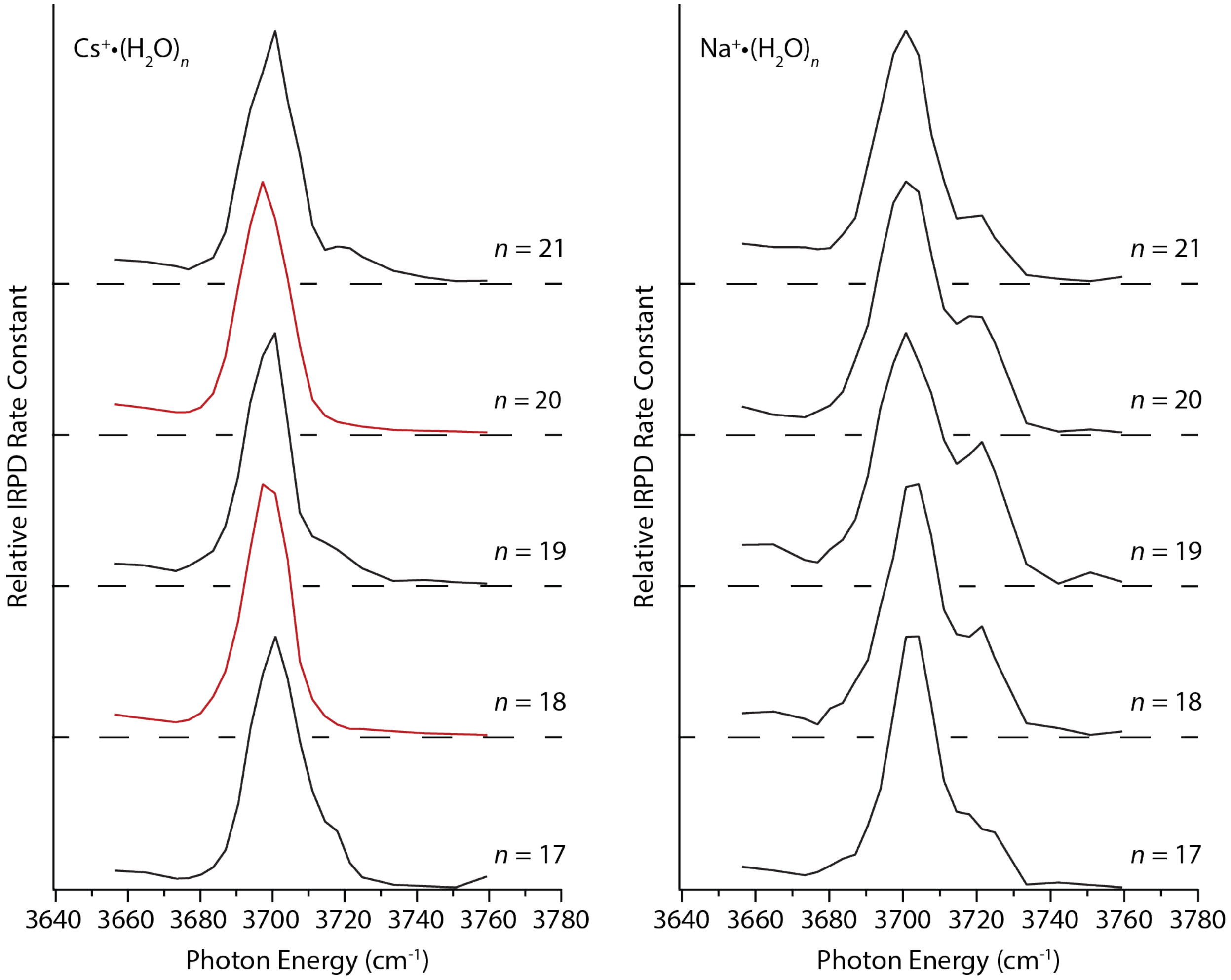

Figure 2.3. IRPD spectra of $Cs^+(H_2O)_{17\text{-}21}$ and $Na^+(H_2O)_{17\text{-}21}$ in the free-OH region. The spectral simplification to only the AAD stretch for $Cs^+(H_2O)_{20}$ and $Cs^+(H_2O)_{18}$ indicates clathrate hydration structures where each water molecule participates in three hydrogen bonds.

a) $Cs^+(H_2O)_{20}$

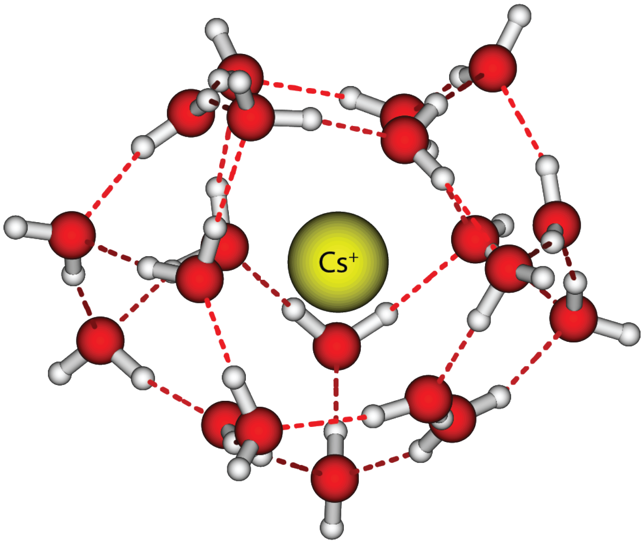

b) $Na^+(H_2O)_{20}$

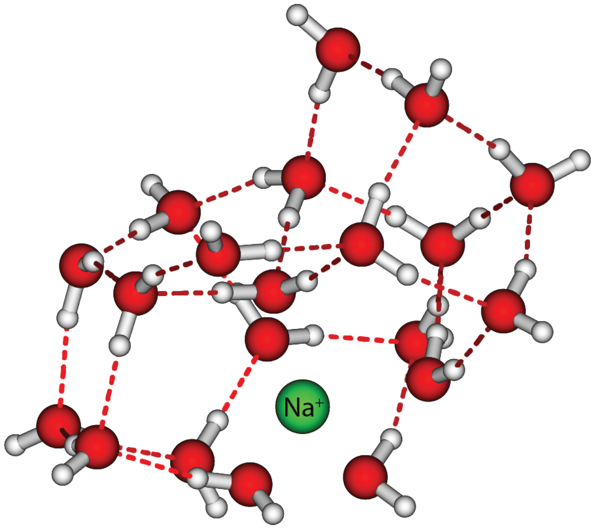

Figure 2.4. Identified lowest-energy structures for (a) $Cs^+(H_2O)_{20}$ and (b) $Na^+(H_2O)_{20}$ optimized at the B3LYP/6-31+G** level of theory.

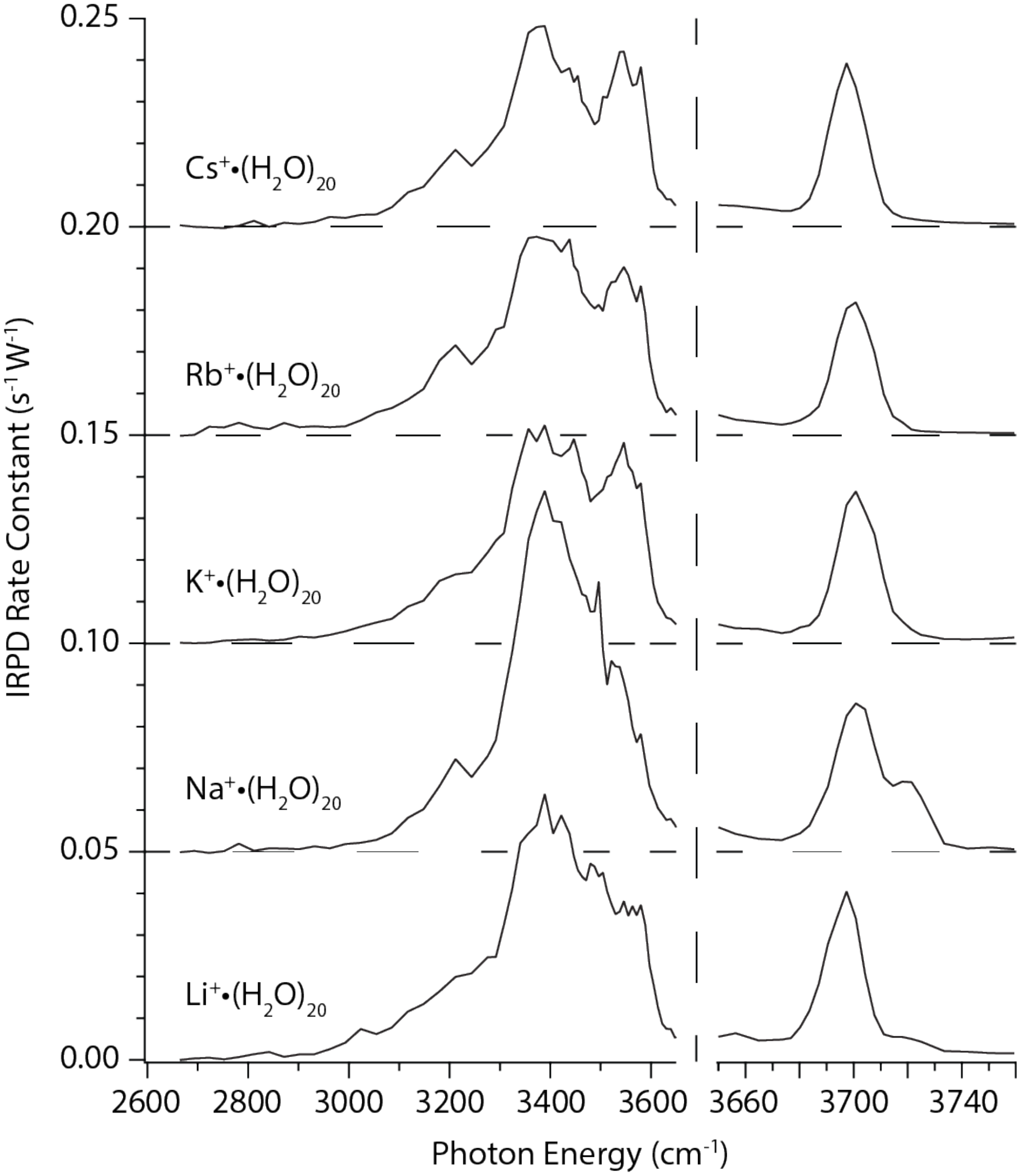

Figure 2.5. IRPD spectra of $M^+(H_2O)_{20}$, where M = Cs, Rb, K, Na and Li in the bonded-OH (~2600 – 3600 cm^{-1}) and free-OH (~3600 – 3800 cm^{-1}) regions.

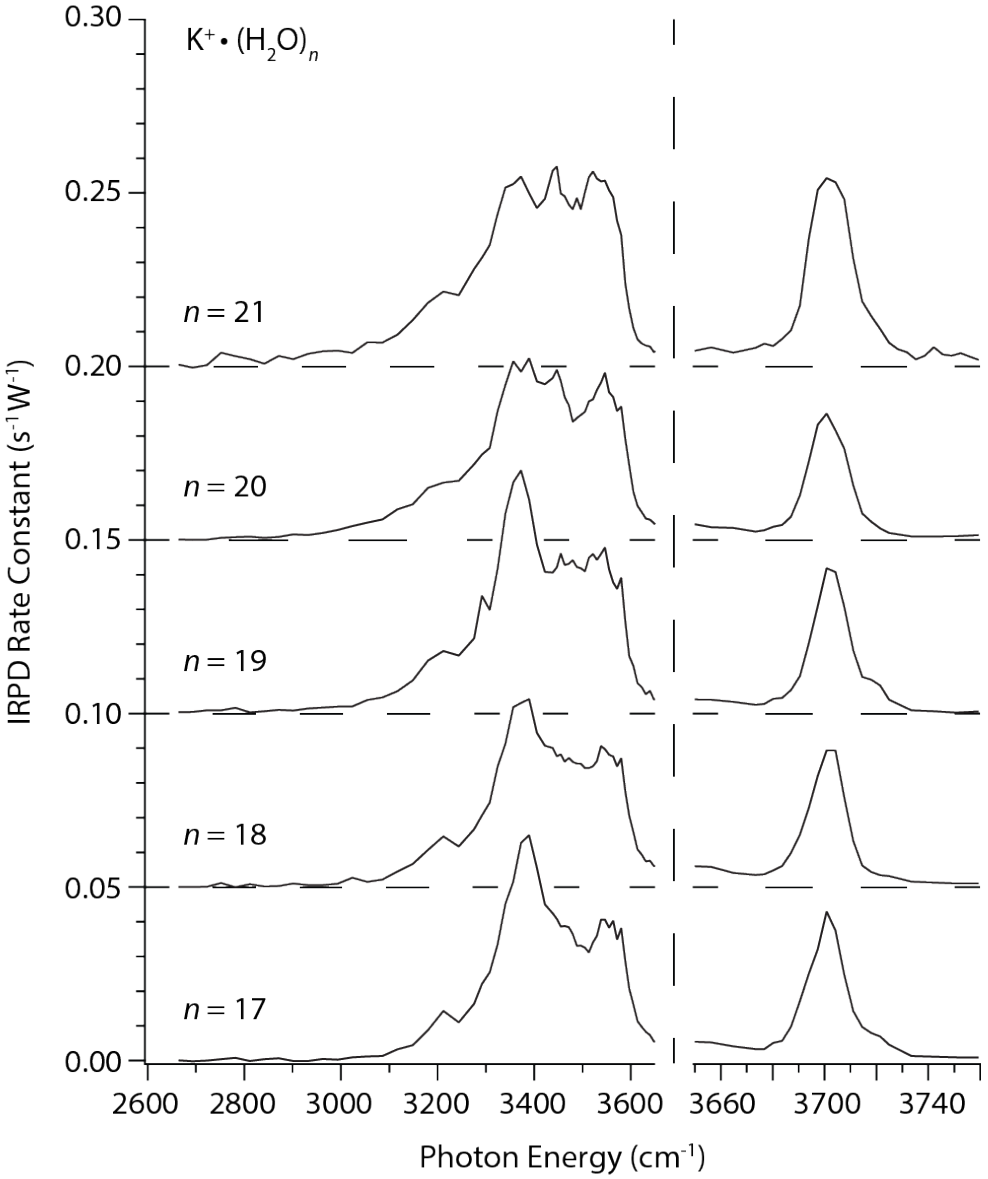

Figure 2.6. IRPD spectra of $K^+(H_2O)_{17\text{-}21}$ in the bonded-OH (~2600 – 3600 cm^{-1}) and free-OH (~3600 – 3800 cm^{-1}) regions.

Chapter 3

Hydration of Guanidinium: Second Shell Formation at Small Cluster Size

This chapter is reproduced with permission from
Cooper, R.J.; Heiles, S.; DiTucci, M.J.; Williams, E.R.
"Hydration of Guanidinium: Second Shell Formation at Small Cluster Size"
Journal of Physical Chemistry A **2014**, 118, 5657-5666
© 2014 American Chemical Society

3.1 Introduction

Many guanidinum salts (Gdm^+X^-) are well known to disrupt native protein structure, and are widely used to investigate various aspects of protein folding and stability.[1-7] The presence of GdmCl and GdmSCN at high concentrations (~6 M) increases the stabilities of unfolded states of most proteins resulting in their denaturation. The effect that ions have on protein structure was first reported over 125 years ago by Franz Hofmeister, who ordered salts on their ability to precipitate or solubilize proteins in aqueous solution.[8,9] The ordering of both cations and anions is referred to as the "Hofmeister series", and the ion effects are more pronounced for the anions.[10] For cations, the series is typically reported[11] as $N(CH_3)_4^+ < NH_4^+ < K^+ < Na^+ < Li^+ < Mg^{2+} < Ca^{2+} < Gdm^+$ with early members of the series "salting out" proteins by stabilizing their native structure and latter members "salting in" proteins by destabilizing the folded state. The Hofmeister series is of fundamental importance to a broad range of fields because of its remarkable correlation to diverse physical properties, such as enzyme activity,[12] bacterial growth,[13] transport through ion channels,[14] and the surface activity of ions.[15] Despite the well-characterized dependence of these physical properties on ion identity, a unifying mechanistic description remains elusive and a topic of debate.[16-18] The effectiveness of guanidinum at the destabilizing end of the Hofmeister series is especially interesting because it does not follow the general trend of increasing charge density established by the other cations in the series.

The effects of ions on protein structure have been attributed to direct ion-protein interactions and also to effects of ions on the structure of water itself, which could influence protein structure. The high concentrations of guanidinium typically necessary to unfold proteins indicate that Gdm^+ is likely present at the protein-water interface.[19] Results from two-dimensional infrared (2D-IR) spectroscopy indicate that Gdm^+ is more effective at disrupting β-sheets than α-helical structure, leading some to suggest that there is specificity in how the ion interacts directly with a protein.[20] Much computational effort has been exerted on unraveling which Gdm^+-protein interactions promote unfolding.[21-37] Molecular dynamics (MD) simulations indicate that guanidinum can interact with proteins in a variety of ways: through an electrostatic interaction with polar or charged side-chain groups,[23,24,31,35] by hydrogen bonding (H-bonding) to the peptide backbone or side-chain groups,[23,27,30,35] and through a "hydrophobic" interaction between the non-polar, weakly hydrated faces of Gdm^+ and aromatic[21,22,26,27,30-32] or aliphatic[22,28] groups. Experimental evidence for these mechanisms is limited and comes primarily from studies of small peptides and other model systems in the presence of denaturants.[26,30,31,35,38-40]

Interestingly, several studies have found that Gdm^+ is particularly effective at denaturing peptides rich in tryptophan residues indicating that the ion can disrupt aromatic stacking interactions.[35,38,40] The ability of Gdm^+ to interface with aromatic groups is consistent with arginine stacking interactions observed in protein crystal structures.[32,41] A perhaps less intuitive interaction mechanism found by several MD simulations is the possibility that Gdm^+ can form homoion contact pairs, thus forming aggregates that aid in stabilizing nonpolar groups.[21,22,32,34,37] Recent experimental results from near-edge X-ray fine structure absorption spectroscopy (NEXFAS) provide some evidence for this association.[42] The relative contribution of each of these interactions to the denaturant properties of Gdm^+ is unknown, but it is likely that many of the ways in which the ion can interact with a protein contribute to its role as a denaturant.

The way in which guanidinium is solvated by surrounding water molecules and influences the H-bonding network of water is also likely to contribute to the efficacy of Gdm^+ as a denaturant. Ions that interact with the protein surface must be able to readily shed solvating water molecules. A consistent description of how Gdm^+ influences surrounding water molecules has begun to emerge from several orthogonal experimental techniques. Results from femtosecond infrared (fs-IR) anisotropy decay experiments that measure the reorientation dynamics of bulk water molecules indicate that the reorientation times of GdmCl solutions and pure water are similar.[43] The small perturbation of Gdm^+ on the reorientation times of water molecules has led the authors to conclude that the ion does not impose long-range structure on water. Results from neutron diffraction experiments[21,44] on the solution phase hydration structure of Gdm^+ indicate that Gdm^+ does not compete effectively for H-bonding interactions with water molecules. The density of water molecules at inner shell distances was found to be similar to that of bulk water leading to the conclusion that Gdm^+ is a weakly hydrated ion. An explicit description of how Gdm^+ is hydrated, however, has thus far primarily been addressed through MD simulations. One such study found that on average, 4.5 water molecules form nearly linear H-bonds with the NH_2 groups in the plane of the ion.[21] The way in which water molecules were organized above and below the plane of the ion was found to be analogous to interactions of water with hydrophobic surfaces, and this behavior has also been observed in higher-level ab initio MD simulations.[34] Results from temperature excursion infrared experiments also indicate that Gdm^+ forms linear H-bonds in solution.[45] These results offer tantalizing clues about how guanidinium is hydrated, but a more direct probe of ion water interactions could provide new structural insights into these interactions.

Herein, we report infrared photodissociation (IRPD) spectra for gaseous $Gdm^+(H_2O)_n$, $n = 1 – 5$. Readily interpretable features in these spectra indicate that Gdm^+ is solvated in the plane of the ion, and for $n = 1 – 3$, the water molecules reside in the interstitial spaces between amino groups, participating in one H-bond with each group. At $n = 4$, there is conclusive evidence for the start of a second hydration shell indicating that Gdm^+ has a small inner shell coordination number. Structural motifs that emerge in the structures of $n = 4$ and 5 reveal that water-water bonding is preferred over ion-water bonding. These results provide the first experimental evidence of the specific manner in which water binds to this unique ion at early stages of hydration.

3.2 Experimental Methods

3.2.1 IRPD Spectroscopy. IRPD spectra of hydrated guanidinium ions were measured using a home-built 7.0 T Fourier-transform ion cyclotron resonance (FT-ICR) mass spectrometer coupled to a tunable OPO/OPA tabletop laser system. The instrument and experimental setup, which previously incorporated a 2.75 T magnet, are described in detail elsewhere.[46] Briefly, hydrated ions are formed by nanoelectrospray ionization (see Appendix A) of 3-5 mM aqueous solutions of guanidinium chloride (Sigma Aldrich, Saint-Louis, MO) using borosilicate capillaries that are pulled to an inner diameter of ~1 μm. A platinum wire is inserted into the capillary so that it is in contact with the solution, and a potential of ~ +600 V relative to the heated capillary entrance of the mass spectrometer is applied to the wire. The resulting hydrated ions are guided through five stages of differential pumping into an ion cell that is surrounded by a temperature-regulated copper jacket,[47] equilibrated to 133 K for at least 8 h prior to each experiment. A pulse of dry nitrogen gas is introduced into the vacuum chamber at a pressure of $\sim 10^{-6}$ Torr for ~5 s to aid with thermalizing and trapping the ions. This is followed by a ~7 s delay to allow the pressure in the chamber to drop below 10^{-8} Torr. The ion of interest is subsequently isolated using a stored inverse Fourier transform waveform prior to photodissociation.

Mass-selected clusters are photodissociated at specific frequencies using tunable IR light from an OPO/OPA laser system (LaserVision, Bellevue, WA) pumped by the 1064 nm fundamental of a Nd:YAG laser (Continuum Surelight I-10, Santa Clara, CA) at a 10 Hz repetition rate. Irradiation times between 1 and 60 s provide substantial, but not complete, fragmentation of the precursor ion. A first-order photodissociation rate constant is obtained from the relative abundances of the precursor and fragment ions. This rate constant is corrected for frequency-dependent variations in laser power as well as blackbody infrared radiative dissociation (BIRD), which occurs as a result of the absorption of blackbody photons from the 133 K ion cell and cell jacket. The IRPD spectrum of $\mathrm{Gdm^+(H_2O)_1}$ was measured at 298 K due to the high stability of this cluster.

3.2.2 Computational Chemistry. Structures of $\mathrm{Gdm^+(H_2O)_{1\text{-}5}}$ were generated by initially positioning water molecules around the ion in Macromodel 9.1 (Schrödinger, Inc., Portland, OR). For $\mathrm{Gdm^+(H_2O)_5}$, a Monte Carlo conformation search for additional structures using a basin-hopping routine was performed using an OPLS2005 force field with an energy cutoff of 15 kcal/mol. A total of 15 low-energy structures were saved and the lowest, mid, and highest-energy structures were selected for further optimization using quantum chemistry. The structures obtained from chemical intuition and the conformational search were then geometry optimized in Q-Chem 4.0[48] (Q-Chem, Inc., Pittsburgh, PA) at the B3LYP/6-31++G** level of theory prior to vibrational frequency and intensity calculations at the same level of theory. For calculated spectra, vibrational frequencies were scaled by 0.954[49] and convolved with a 60 and 15 $\mathrm{cm^{-1}}$ fwhm Gaussian for the 3000 – 3500 $\mathrm{cm^{-1}}$ and 3500 – 3800 $\mathrm{cm^{-1}}$ regions, respectively. Zero-point energies, enthalpy, and entropy corrections at 133 K were calculated for these structures using unscaled B3LYP/6-31++G** harmonic oscillator vibrational frequencies. Additional optimizations on $\mathrm{Gdm^+(H_2O)_{3,5}}$ were performed using the B3LYP functional with both 6-311++G** and aug-cc-pVDZ basis sets. Further, optimizations were performed for $\mathrm{Gdm^+(H_2O)_{1\text{-}5}}$ using the ωB97D functional and for $\mathrm{Gdm^+(H_2O)_{3,5}}$ using the MP2 level of theory, both with the 6-31++G** basis set. Zero-point energy, enthalpy, and entropy calculations for these structures were calculated using unscaled harmonic frequencies obtained at the corresponding level of theory after geometry optimization.

3.3 Results and Discussion

3.3.1 Structural Signatures in IRPD Spectra of $Gdm^+(H_2O)_{1-5}$. The hydration of guanidinium was investigated by measuring IRPD spectra of $Gdm^+(H_2O)_{1-5}$ in the hydrogen stretch region (~3000 – 3800 cm^{-1}) (Figure 3.1). The stretching frequencies of O–H and N–H oscillators are sensitive to their local environments and shift with ion charge state, proximity and orientation to the charge, and the extent to which they participate in H-bonding. These frequencies can be broadly divided into two regions depending on whether or not the oscillator is directly involved in H-bonding. Vibrational resonances at higher frequencies (~3500 – 3800 cm^{-1}) correspond to N–H and O–H stretches that are not H-bonded and are thus "free" to oscillate. Stretches that occur at lower frequencies (~3000 – 3500 cm^{-1}) are characterized by comparatively broader linewidths and arise from O–H and N–H bonds that directly participate in H-bonding.

The evolution of bands in the free O–H region (~3600 – 3800 cm^{-1}) for $Gdm^+(H_2O)_{1-5}$ indicates that a transition occurs between $n = 3$ and 4. For the smaller guanidinium hydrates, there are two bands in this region corresponding to the symmetric and asymmetric stretches of water molecules.[50,51] Starting at $n = 4$, the degeneracy of the asymmetric stretch is lifted resulting in three distinct asymmetric stretch bands. Although free O–H oscillators are not involved in a H-bond, their stretching frequencies are sensitive to the local H-bonding environment. For example, the free O–H stretch of a water molecule that accepts two H-bonds and donates one (AAD water) is different enough from that of a water molecule that accepts and donates one H-bond (AD water) that these separate resonances can typically be resolved.[50,52-55] This dependence of the O–H frequency on the H-bonding environment of water has been exploited to derive structural information about a variety of hydrated ions.[49,50,52-57] In the case of guanidinium, these data suggest that for cluster sizes between $n = 1$ and 3, the hydrogen bonding environment of each water molecule is the same. For $n = 4$ and 5, the presence of multiple free O–H bands is consistent with water molecules residing in different H-bonding environments, thereby signaling a breaking of symmetry in the structure.

Also apparent in these spectra is the disappearance of the free N–H band for $Gdm^+(H_2O)_3$ that is prominent for the two smaller cluster sizes between 3520-3560 cm^{-1}. This indicates that for the majority of the ion population, solvation by only three water molecules quenches all six of the free N–H stretches in the plane of the guanidinium ion. The only feasible way that these water molecules can be arranged to satisfy this constraint is if each water molecule sits in the interstitial spaces between the three NH_2 groups in guanidinium, thereby accepting two H-bonds, each contributed by a different amino group.

The disappearance of the free N–H stretch coincides with an increase in the intensity of the broad band centered on 3480 cm^{-1} which is attributable to bonded N–H stretches. The extensive photodissociation in this region starting at $n = 3$ is also consistent with a symmetric hydration structure for $Gdm^+(H_2O)_3$. For $n \geq 4$, a prominent band centered at 3440 cm^{-1} appears, corresponding to bonded O–H stretches. These stretches correspond to water molecules that are H-bonding to each other, suggesting that water-water H-bonds are preferentially formed over a bond between the positively charged carbon atom and water. Such an interpretation is consistent with the multiplicity of bands observed in the free O–H region at these cluster sizes, which also indicates that there is H-bonding between water molecules.

3.3.2 Calculated Structures for $Gdm^+(H_2O)_{1-5}$. Low-energy structures identified for $Gdm^+(H_2O)_{1-5}$ are shown in Figure 3.2 along with their relative Gibbs free energies at 133 K.

Only one stable structure was identified for $Gdm^+(H_2O)_1$ (**1a**) where the water molecule is between two amino groups, accepting one H-bond from each group. The N–H•••O bond angle is ~147° at the B3LYP/6-31++G** level of theory indicating that these H-bonds are strained. Structures in which the water molecule was initially directly above the carbon atom, which has a calculated net atomic Mulliken charge of +0.356 a.u., minimized to structure **1a**.

Two local minimum structures were identified for $Gdm^+(H_2O)_2$. In the lowest-energy isomer (**2a**), both water molecules are H-bonded to the amino groups, occupying two of the three available sites between these groups. In the higher energy structure (+8.7 kJ/mol, **2b**), one water molecule accepts two H-bonds from the amino groups and forms one H-bond with the other water molecule, initiating a second solvation shell.

Three stable low-energy structures were identified for $Gdm^+(H_2O)_3$. Structure **3a**, in which all three water molecules are H-bonded to the NH_2 groups, is lowest in energy and has D_{3h} symmetry. In structure **3b** (+4.8 kJ/mol), two water molecules H-bond with the amino groups and the third water molecule forms a water-water H-bond with one of these inner shell water molecules. The third structure (**3c**, +16.4kJ/mol) consists of one amino-bound water molecule in the first shell forming water-water H-bonds with two outer shell water molecules. Isomers **3b** and **3c** are structures where the formation of one water-water H-bond displaces the formation of two N–H•••O H-bonds. Remarkably, structure **3b** is only ~5 kJ/mol higher in energy at this level of theory despite having one less H-bond, indicating that a single water-water H-bond is nearly as strong as two H-bonds between a water molecule and the ion at this cluster size.

Four stable isomers that are within ~17 kJ/mol of each other were identified for $Gdm^+(H_2O)_4$. In the lowest-energy structure (**4a**), three inner shell water molecules H-bond with the amino groups and one water molecule forms a water-water H-bond with one of these inner shell water molecules thereby establishing the start of a second solvation shell. In structure **4b**, all four water molecules reside in the plane of the ion, with two of the water molecules each accepting a single H-bond and the other two in the remaining interstitial sites. Such a structure clearly precludes optimal H-bonding and is the highest-energy isomer (+17.4 kJ/mol). Structures **4c** (+10.6 kJ/mol) and **4d** (+3.9 kJ/mol) are similar insofar as two water molecules H-bond directly to the amino groups whilst the other two water molecules form water-water H-bonds in the second solvation shell.

Although there are many stable isomers for $Gdm^+(H_2O)_5$, four isomers were identified that are within ~22 kJ/mol of each other. Lowest-energy structure **5a** is a continuation of the established pattern of lowest-energy structures **1a**–**4a**: three inner shell water molecules H-bond directly with guanidinium and the two outer shell water molecules each form one water-water H-bond with different inner shell water molecules. Structure **5d** is similar to structure **5a**, but both outer shell water molecules coordinate to the same inner shell water molecule in **5d** resulting in a structure that is +3.9 kJ/mol higher in energy. In structure **5b** (+5.8 kJ/mol), only two water molecules H-bond with guanidinium and the remaining water molecules form water-water H-bonds with these inner shell water molecules. Structure **5c** is the highest energy isomer considered (+22.2 kJ/mol), and has a four-membered water ring that includes one of the two inner shell water molecules. The water molecule in the ring that accepts two H-bonds from Gdm^+ imposes strain in the water ring structure making it less energetically favorable.

For the guanidinium hydrates with *n* between 1 and 5, structures were generated where a water molecule was placed over the central carbon atom, which is calculated to have a net atomic Mulliken charge between ~+0.200 and +0.356 a.u. depending upon the number of attached water molecules. Upon geometry optimization, all such structures relaxed to one of the identified isomers where the water molecule preferentially forms H-bonds with either one of the NH_2 groups or with another water molecule. To investigate the origin of this effect, the molecular orbitals of $Gdm^+(H_2O)_1$ were calculated at the B3LYP/6-31++G** level of theory and the lowest unoccupied molecular orbital (LUMO) for this cluster is shown in Figure 3.3a. There is no orbital density around the carbon atom in the LUMO explaining why structures where a water molecule is placed over this carbon are unstable. Most of the orbital density is instead concentrated in the two remaining spaces between amino groups where water binding is calculated to be most favored. An electrostatic potential surface of $Gdm^+(H_2O)_1$ was generated at the same level of theory (Figure 3.3b), and shows that most of the excess positive charge is localized primarily on the hydrogen atoms and not the carbon atom, consistent with the observed water binding motif.

The dependence of these calculations on both the level of theory and basis set was investigated and the results are shown in Table 3.1. Single-point energies at different levels of theory were calculated for all low-energy structures after geometry optimization using the 6-31++G** basis set. These calculations were performed with two different functionals, B3LYP and ωB97D, and second order Møller-Plesset perturbation theory (MP2). There is no effect on the energetic ordering of isomers with any of these types of theory with this basis set, although there are small differences in energy between isomers. The effects of basis set were evaluated by running single point calculations on optimized structures of $Gdm^+(H_2O)_3$ and $Gdm^+(H_2O)_5$ using a single density functional (B3LYP) but with different basis sets (6-31++G**, 6-311++G** and aug-cc-pVDZ; Table 3.1). The ordering of the isomers for these two cluster sizes does depend somewhat on the basis set. For $Gdm^+(H_2O)_3$, a different isomer (**3b**) is lowest in energy with the larger basis sets. The magnitude of this energetic reordering is quite modest, and the energy difference between structures **3a** and **3b** is within 5 kJ/mol for all basis sets.

3.3.3 Comparison of IRPD and Calculated Spectra for $Gdm^+(H_2O)_1$. Experimental and calculated infrared spectra for $Gdm^+(H_2O)_1$ are shown in Figure 3.4. There are bands in the free O–H region of both the IRPD spectrum (3711 cm^{-1} and 3625 cm^{-1}) and the calculated spectrum (3705 cm^{-1} and 3611 cm^{-1}) corresponding to the asymmetric and symmetric stretches of water, respectively. These resonances are red-shifted compared to those of water vapor which occur at 3756 cm^{-1} and 3657 cm^{-1}.[58] The red-shifting of these frequencies can be attributed to H-bonding with the NH_2 groups, as well as a Stark shift from the ion's electric field which also lowers the oscillator frequency.[59] H-bonding also redshifts the asymmetric and symmetric N–H stretches. Calculations indicate that the H-bonding in $Gdm^+(H_2O)_1$ results in a redshift of these N-H stretches of 29 cm^{-1} and 95 cm^{-1}, respectively, compared to those in the bare ion (see Appendix A). The free and bonded asymmetric N–H stretches for structure **1a** are at 3554 cm^{-1} and 3525 cm^{-1}, respectively, whereas there is only a single broad peak between 3500–3580 cm^{-1} in the IRPD spectrum which is likely due to the overlap of these bands. The symmetric free N–H stretch is calculated at 3442 cm^{-1} and there is a broad feature in the experimental spectrum in this region. There is poorer agreement between the measured and calculated resonances of the symmetric bonded N–H stretch, calculated at 3347 cm^{-1}. One broad feature is observed between 3100–3300 cm^{-1} in the IRPD spectrum that corresponds to this stretch. N–H stretches involved in H-bonding are expected to have considerable anharmonic character, and the harmonic calculations employed in this study do not adequately describe the effects of anharmonicity on these vibrational frequencies.

The measured intensities of bands below ~3500 cm^{-1} are systematically lower than the calculated intensities for $Gdm^+(H_2O)_{1-5}$. IRPD action spectra may not reflect true linear absorption spectra. This can be attributed in part to the lower energy deposited per photon and lower laser power in this spectral range which may necessitate the sequential absorption of multiple photons to induce photodissociation. Uncertainty in calculated intensities and broadening of these bands also contribute to the discrepancy between measured and calculated intensities.[60]

3.3.4 Comparison of IRPD and Calculated Spectra for $Gdm^+(H_2O)_2$. The IRPD spectrum of $Gdm^+(H_2O)_2$ is shown in Figure 3.5, along with calculated IR spectra for the two low-energy isomers. A second water molecule added to **1a** can either attach directly to guanidinium (**2a**) or form a H-bond with the first water molecule (**2b**). The free O–H region of the spectrum clearly distinguishes these two possibilities. The measured spectrum has only two resonances in this region corresponding to the symmetric and asymmetric stretches of water molecules that accept two H-bonds (AA water molecules), which align well with these calculated frequencies for **2a**. If isomer **2b** were present, there should be two well-resolved asymmetric free O–H stretches corresponding to water molecules that accept two and donate one H-bond (AAD water molecules) and those that accept one H-bond (A water molecules). The absence of contributions from AAD and A bands in this spectrum rule out any significant population of isomer **2b** in our experiment.

There is also good agreement between the calculated and measured spectrum for structure **2a** throughout the rest of the spectral region. There is an asymmetric free N–H stretch in both spectra just below 3540 cm^{-1}. The calculated asymmetric bonded N–H stretch occurs at 3459 cm^{-1} and there is significant dissociation attributable to this vibration observed at ~3475 cm^{-1}. The symmetric stretches of the free and bonded N–H oscillators appear as a broad region of dissociation centered on ~3400 cm^{-1}, which is blue-shifted about 60 cm^{-1} from their calculated values. The anharmonicity of these lower frequency vibrations likely accounts for this difference. For this reason, the higher frequency region of the spectra is more diagnostic of structure.

3.3.5 Comparison of IRPD and Calculated Spectra for $Gdm^+(H_2O)_3$. The IRPD spectrum for $Gdm^+(H_2O)_3$ (Figure 3.6) is simpler than those of the smaller two hydrates, suggesting a highly symmetric hydration structure. In the free O–H region of the IRPD spectrum, only the AA asymmetric and symmetric stretching bands are observed, which is consistent with structure **3a**. This indicates that isomers where water-water H-bonds are formed (**3b** and **3c**) do not contribute significantly to the experimental population of $Gdm^+(H_2O)_3$. A broad, intense band corresponding to the asymmetric bonded N–H stretch is calculated to occur at 3472 cm^{-1} for isomer **3a** and such a band occurs in the experimental spectrum at 3485 cm^{-1}. The low-energy tail of this band observed in the IRPD spectrum likely arises from symmetric bonded N–H stretches. These bands are significantly higher in frequency than those measured for $NH_4^+(H_2O)_3$ (~2900-3200 cm^{-1}),[61] consistent with the non optimal hydrogen bonding orientation in $Gdm^+(H_2O)_3$. Of note in the spectrum of $Gdm^+(H_2O)_3$ is the absence of any free N–H stretches, which is consistent with isomer **3a** where all N–H bonds are involved in H-bonding with water molecules.

Our results for $Gdm^+(H_2O)_{1-3}$ establish a definitive pattern for the hydration of guanidinium at these small cluster sizes. The sequential addition of water molecules in the interstitial spaces between NH_2 groups is favored over the formation of water-water H-bonds or a direct interaction between water and the carbon atom that carries a partial positive charge. The resulting planar hydration structure differs substantially from the more isotropic hydration motifs typical for metal ions.[60,62-65] Interestingly, the correct lowest-energy structure for $Gdm^+(H_2O)_3$ (**3a**) is predicted using the B3LYP functional in conjunction with the smallest basis set (6-31++G**) whereas isomer **3b** is incorrectly identified as lowest in energy with both of the larger basis sets.

3.3.6 Comparison of IRPD and Calculated Spectra for $Gdm^+(H_2O)_4$. Shown in Figure 3.7 are the IRPD and calculated spectra for $Gdm^+(H_2O)_4$. The free O–H region is the most diagnostic region for distinguishing between isomers **4a-d** where multiple types of asymmetric stretching bands are observed for the first time. Comparing the number and frequency of these stretches with those of the calculated spectra shows that isomer **4a** is in best agreement with the measured data. A small band near 3741 cm^{-1} from an A water molecule lies closely to the calculated resonance at 3743 cm^{-1}. Bands from AA and AAD water molecules occur in the IRPD spectrum at 3721 cm^{-1} and 3693 cm^{-1}, respectively, with their calculated counterparts predicted to occur at these same frequencies. Similar to $Gdm^+(H_2O)_3$, there is a broad, intense peak centered at 3484 cm^{-1} in the experimental spectrum associated with asymmetric bonded N–H stretches that are calculated to occur between 3452-3478 cm^{-1} for this isomer. Additionally, there is a new resonance in the IRPD spectrum centered at 3432 cm^{-1} consistent with strong bonded O–H stretches.[66] Both these stretches and the symmetric N–H stretches for isomer **4a** occur between 3353–3367 cm^{-1} and 3298–3317 cm^{-1}, respectively.

The appearance of H-bonded stretches between water molecules in $Gdm^+(H_2O)_4$ in both the free and bonded O–H regions heralds the beginning of a second hydration shell. Once three water molecules fully occupy the pockets between amino groups, additional water molecules form water-water H-bonds to these inner shell water molecules. Calculated sequential water binding energies for the first five water molecules to guanidinium are given in Table 3.2. There is a large decrease in binding energy between the $n = 3$ and 4 hydrates, consistent with the measured BIRD rate constants, which more than double from $n = 3$ (0.016 s^{-1}) to $n = 4$ (0.038 s^{-1}). Several factors influence BIRD rate constants,[67] including differences in water molecule binding energies. These results indicate that a very stable inner solvation shell is established with three water molecules, and that the second shell water molecules are bound much less strongly.

Inner shell coordination numbers have been measured with infrared action spectroscopy for a variety of hydrated cations in the gas phase, including alkali metal ions[65] and transition metals.[52,68-74] The completion of the first hydration shell by $n = 3$ for Gdm^+ is one of the smallest coordination numbers measured in the gas phase; both Cu^+ and Au^+ have a coordination number of $n = 2$.[68,73] Results from MD simulations of guanidinum in bulk solution suggest that the ion is weakly solvated above and below the central carbon atom,[21,34] and our data are consistent with this finding. The emergence of water-water H-bonds at $n = 4$ indicates that interactions between water molecules are favored over ion-water interactions starting at this cluster size. The solution phase hydration structure of guanidinum has been previously studied by Mason et al. via neutron diffraction where they found only a slight modulation in the radial distribution function of this ion at distances characteristic of inner shell water molecules.[44] These results show that guanidinium weakly interacts with water in solution, but it was not possible to obtain an explicit coordination number for Gdm^+ in solution from these measurements. The small coordination number of guanidinium measured here is consistent with the weak hydration of this ion in solution.

3.3.7 Comparison of IRPD and Calculated Spectra for Gdm$^+$(H$_2$O)$_5$. The IRPD spectrum of Gdm$^+$(H$_2$O)$_5$ along with calculated spectra for four low-energy isomers are shown in Figure 3.8. There are three resonances in the free O–H region at 3742 cm^{-1}, 3725 cm^{-1}, and 3697 cm^{-1} corresponding to the asymmetric free O–H stretches of A, AA, and AAD water molecules respectively. The spectrum of isomer **5a** agrees most closely with experiment in this region with these same resonances calculated at 3746 cm^{-1}, 3724 cm^{-1} and 3692 cm^{-1}. Structures **5b-c** have a different number of resonances in this region indicating that they do not contribute significantly to the ion population. Additionally, isomers **5b** and **5c** are predicted to have free N–H stretches between 3520–3580 cm^{-1} due to the incomplete coordination of water to guanidinium, but significant dissociation in this region is not observed.

The relative intensities of the free O–H stretches in the IRPD spectrum and the calculated spectrum for isomer **5a** are sufficiently different that some contributions from other isomers in our experimental population cannot be ruled out, although uncertainties in calculated intensities also likely contribute to this difference. To investigate whether there are other isomers present, IRPD kinetic data was measured at each of the asymmetric stretch resonances (3742 cm^{-1}, 3725 cm^{-1}, and 3697 cm^{-1}) in the free O–H region. Briefly, the experimental population is irradiated with IR photons of a fixed wavelength that is resonant with a specific isomer and off resonant with others.[75-77] Irradiation of Gdm$^+$(H$_2$O)$_5$ at each of these three wavelengths leads to first order dissociation kinetics ($R^2 > 0.99$) to at least 85% depletion of the precursor ion (see Appendix A). These results indicate that there is substantial overlap of the laser beam with the ion cloud, and are consistent with a single isomer or rapidly interconverting isomers. The deviation from first-order kinetics when the precursor is depleted below 85% could be a result of non-ideal overlap of the laser beam with the ion cloud or the presence of a small population of off-resonant isomers.

The relative intensity of the bonded O–H band (~3440 cm^{-1}) increases significantly between $n = 4$ and 5, consistent with the formation of additional water-water H-bonds for Gdm$^+$(H$_2$O)$_5$. The hydration motif that starts for Gdm$^+$(H$_2$O)$_4$ continues at this cluster size where water molecules prefer to form H-bonds with each other as opposed to a direct electrostatic interaction with guanidinium. Spectra of larger guanidinium hydrates indicate that this trend continues for $n > 5$, although both the large number of possible isomers and computational accuracy at larger clusters sizes obfuscates the elucidation of explicit hydration structures for these clusters.

3.4 Conclusions

The structures of small guanidinium hydrates, Gdm$^+$(H$_2$O)$_{1-5}$, were elucidated by IRPD spectroscopy in the hydrogen-stretch region (~3000-3800 cm^{-1}) in conjunction with computational methods. Water molecules interact with Gdm$^+$ through H-bonding to the amino groups from the interstitial spaces between these groups in the plane of the ion. The disappearance of the free N–H band in the spectrum of Gdm$^+$(H$_2$O)$_3$ indicates that with only three water molecules attached, these sites are completely filled. The H-bonding motif of these inner shell water molecules to Gdm$^+$ in the gas phase is different from that reported in solution where MD simulations and condensed phase measurements suggest that linear H-bonds are formed. These differences are likely a result of the presence of surrounding water molecules in solution that can compete for H-bonding with inner shell water molecules, providing the necessary energetic impetus to drive their expulsion from the pockets. Hydrogen bonding between water molecules is indicated in the IRPD spectrum of $Gdm^+(H_2O)_4$ by both the presence of multiple bands in the free O–H region as well as additional photodissociation in the bonded O–H region. This heralds the start of a second hydration shell. Remarkably, Gdm^+ has an unusually small coordination number ($n = 3$) for a monovalent ion despite its relatively large ionic radius (~0.21 nm).[78] Water-water bonding is preferred over ion-water bonding for $Gdm^+(H_2O)_{4-5}$. The calculated sequential binding energies of water molecules to guanidinium are consistent with this transition. The water-guanidinium binding energies are significantly lower than those of other protein denaturing cations in the Hofmeister series.[79,80] The destabilizing effect of these other ions on protein structure has been attributed to ion pair formation with strongly hydrated carboxylate groups.[16] Ion pairing is favored for ions with a similar affinity for water.[81] The low charge density and lower hydration energy of guanidinium compared to these other ions should make ion-pair formation with carboxylate less favorable, suggesting that other mechanisms, including H-bonding, homoion pairing, and nonpolar interactions with proteins, may contribute to the denaturant activity of this ion.

The apparent hydrophobicity of Gdm^+ above and below the plane of the ion despite the partial positive charge on the carbon atom is a result of little orbital density around this atom. These hydrophobic surfaces may allow Gdm^+ to interact favorably with aromatic and nonpolar groups in proteins, as has been suggested elsewhere.[21] In contrast, the propensity of Gdm^+ to form hydrogen bonds with water in the plane of the ion gives this ion surfactant-like qualities that may aid in its ability to denature proteins. The unusual asymmetric hydration properties of this ion likely account for its similar position to high charge density ions in the Hofmeister series that solvate symmetrically. Our results for these small guanidinium hydrates indicate that the ion does not strongly interact with water, and that any long-range structural effects of Gdm^+ on the hydrogen-bonding network of water molecules should be significantly less than that of many other ions investigated previously. Experiments with larger Gdm^+ hydrates may provide additional insights into the interesting properties of this ion.

3.5 References

(1) Tanford, C. *Adv. Protein. Chem.* **1970**, *24*, 1-95.

(2) Arakawa, T.; Timasheff, S. N. *Biochemistry* **1984**, *23*, 5924-5929.

(3) Mayo, S. L.; Baldwin, R. L. *Science* **1993**, *262*, 873-876.

(4) Pappenberger, G.; Aygun, H.; Engels, J. W.; Reimer, U.; Fischer, G.; Kiefhaber, T. *Nat. Struct. Biol.* **2001**, *8*, 452-458.

(5) Lipman, E. A.; Schuler, B.; Bakajin, O.; Eaton, W. A. *Science* **2003**, *301*, 1233-1235.

(6) Rashid, F.; Sharma, S.; Bano, B. *Protein J.* **2005**, *24*, 283-292.

(7) Lo Nostro, P.; Ninham, B. W. *Chem. Rev.* **2012**, *112*, 2286-2322.

(8) Hofmeister, F. *Arch. Exp. Pathol. Pharmacol.* **1887**, *24*, 247-260.

(9) Kunz, W.; Henle, J.; Ninham, B. W. *Curr. Opin. Colloid. In.* **2004**, *9*, 19-37.

(10) Zhang, Y. J.; Cremer, P. S. *Curr. Opin. Chem. Biol.* **2006**, *10*, 658-663.

(11) Cacace, M. G.; Landau, E. M.; Ramsden, J. J. *Q. Rev. Biophys.* **1997**, *30*, 241-277.

(12) Zhao, H. *J. Mol. Catal. B-Enzym.* **2005**, *37*, 16-25.

(13) Lo Nostro, P.; Ninham, B. W.; Lo Nostro, A.; Pesavento, G.; Fratoni, L.; Baglioni, P. *Phys. Biol.* **2005**, *2*, 1-7.

(14) Grigorjev, P. A.; Bezrukov, S. M. *Biophys. J.* **1994**, *67*, 2265-2271.

(15) Petersen, P. B.; Saykally, R. J. *Annu. Rev. Phys. Chem.* **2006**, *57*, 333-364.

(16) Collins, K. D. *Methods* **2004**, *34*, 300-311.

(17) O'Brien, J. T.; Prell, J. S.; Bush, M. F.; Williams, E. R. *J. Am. Chem. Soc.* **2010**, *132*, 8248-8249.

(18) Marcus, Y. *Chem. Rev.* **2009**, *109*, 1346-1370.

(19) England, J. L.; Haran, G. *Annu. Rev. Phys. Chem.* **2011**, *62*, 257-277.

(20) Huerta-Viga, A.; Woutersen, S. *J. Phys. Chem. Lett.* **2013**, *4*, 3397-3401.

(21) Mason, P. E.; Neilson, G. W.; Enderby, J. E.; Saboungi, M. L.; Dempsey, C. E.; MacKerell, A. D.; Brady, J. W. *J. Am. Chem. Soc.* **2004**, *126*, 11462-11470.

(22) Mason, P. E.; Brady, J. W.; Neilson, G. W.; Dempsey, C. E. *Biophys. J.* **2007**, *93*, L4-L6.

(23) O'Brien, E. P.; Dima, R. I.; Brooks, B.; Thirumalai, D. *J. Am. Chem. Soc.* **2007**, *129*, 7346-7353.

(24) Camilloni, C.; Rocco, A. G.; Eberini, I.; Gianazza, E.; Broglia, R. A.; Tiana, G. *Biophys. J.* **2008**, *94*, 4654-4661.

(25) England, J. L.; Pande, V. S.; Haran, G. *J. Am. Chem. Soc.* **2008**, *130*, 11854-11855.

(26) Mason, P. E.; Dempsey, C. E.; Neilson, G. W.; Kline, S. R.; Brady, J. W. *J. Am. Chem. Soc.* **2009**, *131*, 16689-16696.

(27) Mason, P. E.; Dempsey, C. E.; Vrbka, L.; Heyda, J.; Brady, J. W.; Jungwirth, P. *J. Phys. Chem. B* **2009**, *113*, 3227-3234.

(28) Godawat, R.; Jamadagni, S. N.; Garde, S. *J. Phys. Chem. B* **2010**, *114*, 2246-2254.

(29) Graziano, G. *Phys. Chem. Chem. Phys.* **2011**, *13*, 12008-12014.

(30) Heyda, J.; Kozisek, M.; Bednarova, L.; Thompson, G.; Konvalinka, J.; Vondrasek, J.; Jungwirth, P. *J. Phys. Chem. B* **2011**, *115*, 8910-8924.

(31) Kubickova, A.; Krizek, T.; Coufal, P.; Wernersson, E.; Heyda, J.; Jungwirth, P. *J. Phys. Chem. Lett.* **2011**, *2*, 1387-1389.

(32) Vazdar, M.; Vymetal, J.; Heyda, J.; Vondrasek, J.; Jungwirth, P. *J. Phys. Chem. A* **2011**, *115*, 11193-11201.

(33) Weiss, A. K. H.; Hofer, T. S.; Randolf, B. R.; Rode, B. M. *Phys. Chem. Chem. Phys.* **2012**, *14*, 7012-7027.

(34) Vazdar, M.; Uhlig, F.; Jungwirth, P. *J. Phys. Chem. Lett.* **2012**, *3*, 2021-2024.
(35) Xu, X.; Wu, P.; Xu, W.; Shao, Q.; An, L.; Zhang, H.; Cai, C.; Zhao, B. *Phys. Chem. Chem. Phys.* **2012**, *14*, 5824-5836.
(36) Koishi, T.; Yasuoka, K.; Willow, S. Y.; Fujikawa, S.; Zeng, X. C. *J. Chem. Theory Comput.* **2013**, *9*, 2540-2551.
(37) Mandal, M.; Mukhopadhyay, C. *Phys. Rev. E* **2013**, *88,* 052708.
(38) Dempsey, C. E.; Piggot, T. J.; Mason, P. E. *Biochemistry* **2005**, *44*, 775-781.
(39) Zarrine-Afsar, A.; Mittermaier, A.; Kay, L. E.; Davidson, A. R. *Protein Sci.* **2006**, *15*, 162-170.
(40) Dempsey, C. E.; Mason, P. E.; Bracly, J. W.; Neilson, G. W. *J. Am. Chem. Soc.* **2007**, *129*, 15895-15902.
(41) Flocco, M. M.; Mowbray, S. L. *J. Mol. Biol.* **1994**, *235*, 709-717.
(42) Shih, O.; England, A. H.; Dallinger, G. C.; Smith, J. W.; Duffey, K. C.; Cohen, R. C.; Prendergast, D.; Saykally, R. J. *J. Chem. Phys.* **2013**, *139*, 035104.
(43) van der Post, S. T.; Tielrooij, K. J.; Hunger, J.; Backus, E. H. G.; Bakker, H. J. *Faraday Discuss.* **2013**, *160*, 171-189.
(44) Mason, P. E.; Neilson, G. W.; Dempsey, C. E.; Barnes, A. C.; Cruickshank, J. M. *Proc. Natl. Acad. Sci. U.S.A.* **2003**, *100*, 4557-4561.
(45) Scott, J. N.; Nucci, N. V.; Vanderkooi, J. M. *J. Phys. Chem. A* **2008**, *112*, 10939-10948.
(46) Bush, M. F.; O'Brien, J. T.; Prell, J. S.; Saykally, R. J.; Williams, E. R. *J. Am. Chem. Soc.* **2007**, *129*, 1612-1622.
(47) Wong, R. L.; Paech, K.; Williams, E. R. *Int. J. Mass. Spectrom.* **2004**, *232*, 59-66.
(48) Shao, Y.; Molnar, L. F.; Jung, Y.; Kussmann, J.; Ochsenfeld, C.; Brown, S. T.; Gilbert, A. T. B.; Slipchenko, L. V.; Levchenko, S. V.; O'Neill, D. P et al. *Phys. Chem. Chem. Phys.* **2006**, *8*, 3172–3191.
(49) Chang, T. M.; Prell, J. S.; Warrick, E. R.; Williams, E. R. *J. Am. Chem. Soc.* **2012**, *134*, 15805-15813.
(50) Shin, J. W.; Hammer, N. I.; Diken, E. G.; Johnson, M. A.; Walters, R. S.; Jaeger, T. D.; Duncan, M. A.; Christie, R. A.; Jordan, K. D. *Science* **2004**, *304*, 1137-1140.
(51) Jiang, L.; Wende, T.; Bergmann, R.; Meijer, G.; Asmis, K. R. *J. Am. Chem. Soc.* **2010**, *132*, 7398-7404.
(52) Walters, R. S.; Pillai, E. D.; Duncan, M. A. *J. Am. Chem. Soc.* **2005**, *127*, 16599-16610.
(53) Diken, E. G.; Hammer, N. I.; Johnson, M. A.; Christie, R. A.; Jordan, K. D. *J. Chem. Phys.* **2005**, 123, 164309.
(54) Headrick, J. M.; Diken, E. G.; Walters, R. S.; Hammer, N. I.; Christie, R. A.; Cui, J.; Myshakin, E. M.; Duncan, M. A.; Johnson, M. A.; Jordan, K. D. *Science* **2005**, *308*, 1765-1769.
(55) Cooper, R. J.; Chang, T. M.; Williams, E. R. *J. Phys. Chem. A* **2013**, *117*, 6571-6579.
(56) Kamariotis, A.; Boyarkin, O. V.; Mercier, S. R.; Beck, R. D.; Bush, M. F.; Williams, E. R.; Rizzo, T. R. *J. Am. Chem. Soc.* **2006**, *128*, 905-916.
(57) Heine, N.; Fagiani, M. R.; Rossi, M.; Wende, T.; Berden, G.; Blum, V.; Asmis, K. R. *J. Am. Chem. Soc.* **2013**, *135*, 8266-8273.
(58) Herzberg, G. *Infrared and Raman Spectra of Polyatomic Molecules*; Molecular Structure and Molecular Spectra *II*; Van Nostrad and Co., Inc.: Princeton, NJ, 1945.
(59) Prell, J. S.; O'Brien, J. T.; Williams, E. R. *J. Am. Chem. Soc.* **2011**, *133*, 4810-4818.
(60) Bush, M. F.; Saykally, R. J.; Williams, E. R. *ChemPhysChem* **2007**, *8*, 2245-2253.

(61) Wang, Y. S.; Chang, H. C.; Jiang, J. C.; Lin, S. H.; Lee, Y. T.; Chang, H. C. *J. Am. Chem. Soc.* **1998**, *120*, 8777-8788.

(62) Miller, D. J.; Lisy, J. M. *J. Chem. Phys.* **2006**, *124*, 024319.

(63) Kolaski, M.; Lee, H. M.; Choi, Y. C.; Kim, K. S.; Tarakeshwar, P.; Miller, D. J.; Lisy, J. M. *J. Chem. Phys.* **2007**, *126*, 074302.

(64) Miller, D. J.; Lisy, J. M. *J Am. Chem. Soc.* **2008**, *130*, 15381-15392.

(65) Miller, D. J.; Lisy, J. M. *J. Am. Chem. Soc.* **2008**, *130*, 15393-15404.

(66) Prell, J. S.; Williams, E. R. *J. Am. Chem. Soc.* **2009**, *131*, 4110-4119.

(67) Price, W. D.; Schnier, P. D.; Williams, E. R. *J. Phys. Chem. B* **1997**, *101*, 664-673.

(68) Iino, T.; Ohashi, K.; Mune, Y.; Inokuchi, Y.; Judai, K.; Nishi, N.; Sekiya, H. *Chem. Phys. Lett.* **2006**, *427*, 24-28.

(69) Iino, T.; Ohashi, K.; Inoue, K.; Judai, K.; Nishi, N.; Sekiya, H. *J. Chem. Phys.* **2007**, *126*, 194302.

(70) Cooper, T. E.; O'Brien, J. T.; Williams, E. R.; Armentrout, P. B. *J. Phys. Chem. A* **2010**, *114*, 12646-12655.

(71) Carnegie, P. D.; Bandyopadhyay, B.; Duncan, M. A. *J. Phys. Chem. A* **2011**, *115*, 7602-7609.

(72) O'Brien, J. T.; Williams, E. R. *J. Phys. Chem. A* **2011**, *115*, 14612-14619.

(73) Li, Y.; Wang, G.; Wang, C.; Zhou, M. *J. Phys. Chem. A* **2012**, *116*, 10793-10801.

(74) Bandyopadhyay, B.; Reishus, K. N.; Duncan, M. A. *J. Phys. Chem. A* **2013**, *117*, 7794-7803.

(75) Prell, J. S.; Chang, T. M.; O'Brien, J. T.; Williams, E. R. *J. Am. Chem. Soc.* **2010**, *132*, 7811-7819.

(76) Prell, J. S.; Correra, T. C.; Chang, T. M.; Biles, J. A.; Williams, E. R. *J. Am. Chem. Soc.* **2010**, *132*, 14733-14735.

(77) Prell, J. S.; Chang, T. M.; Biles, J. A.; Berden, G.; Oomens, J.; Williams, E. R. *J. Phys. Chem. A* **2011**, *115*, 2745-2751.

(78) Marcus, Y. *J. Chem. Thermodyn.* **2012**, *48*, 70-74.

(79) Kebarle, P. *Annu. Rev. Phys. Chem.* **1977**, *28*, 445-476.

(80) Peschke, M.; Blades, A. T.; Kebarle, P. *J. Phys. Chem. A* **1998**, *102*, 9978-9985.

(81) Collins, K. D. *Biophys. J.* **1997**, *72*, 65-76.

3.6 Tables and Figures

Table 3.1. Relative Gibbs free energies in kJ/mol of the isomers for $Gdm^+(H_2O)_{2\text{-}5}$ calculated at the indicated level of theory at 133 K.

Structure	B3LYP/ 6-31++G**	B3LYP/ 6-311++G**	B3LYP/ aug-cc-pVDZ	omegaB97D/ 6-31++G**	MP2/ 6-31++G**
2a	0.0			0.0	
2b	+8.7			+12.3	
3a	0.0	0.0	0.0	0.0	0.0
3b	+4.8	-1.5	-3.1	+2.8	+5.8
3c	+16.4	+13.5	+8.2	+17.2	+22.8
4a	0.0			0.0	
4b	+17.4			+4.0	
4c	+10.6			+10.2	
4d	+3.9			+2.4	
5a	0.0	0.0	0.0	0.0	0.0
5b	+5.8	+6.5	+7.5	+11.0	+14.8
5c	+22.2	+23.2	+22.2	+20.6	+26.9
5d	+3.9	+7.4	+4.4	+1.5	+2.9

Table 3.2. Calculated binding energies (ΔH kJ/mol) at the B3LYP/6-31++G** level of theory for the reaction $Gdm^+\bullet(H_2O)_n \rightarrow Gdm^+\bullet(H_2O)_{n-1} + H_2O$ corrected for the basis set superposition error.

n	ΔH at 0 K
1	76.1
2	68.7
3	62.0
4	50.9
5	49.1

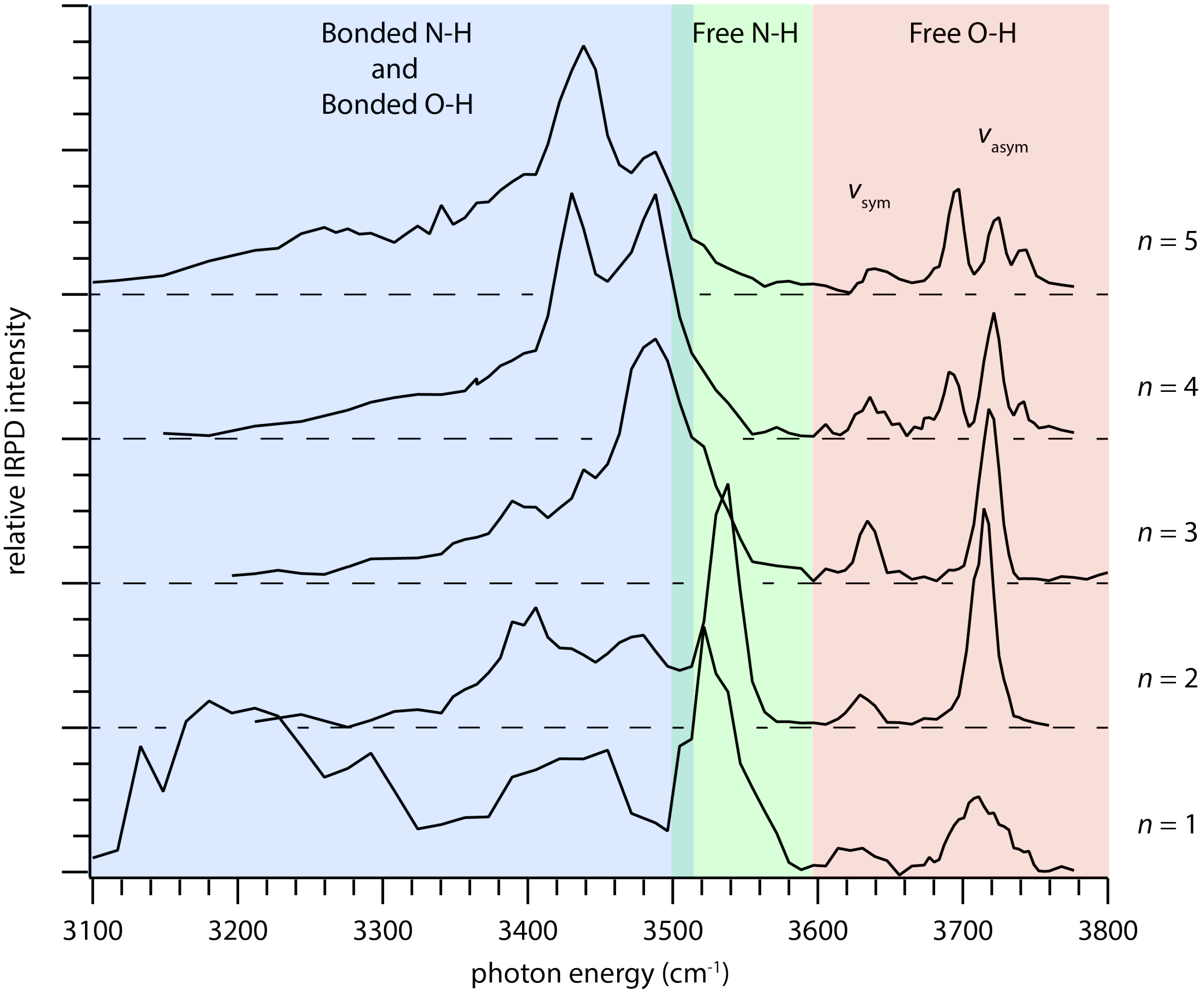

Figure 3.1. IRPD spectra of $Gdm^+(H_2O)_{1-5}$ measured at 298 K for $Gdm^+(H_2O)_1$ and 133 K for $Gdm^+(H_2O)_{2-5}$.

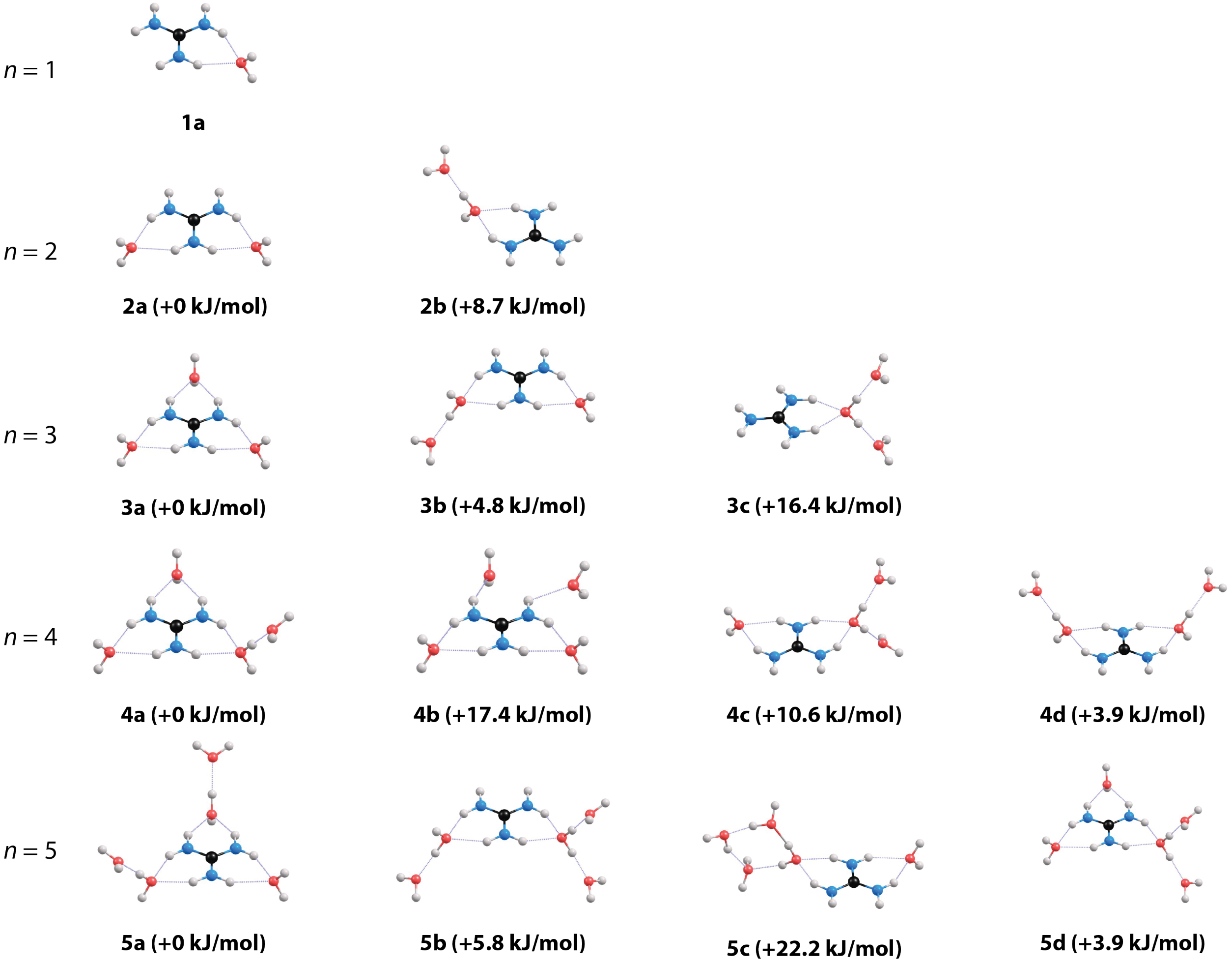

n = 1

1a

n = 2

2a (+0 kJ/mol) **2b (+8.7 kJ/mol)**

n = 3

3a (+0 kJ/mol) **3b (+4.8 kJ/mol)** **3c (+16.4 kJ/mol)**

n = 4

4a (+0 kJ/mol) **4b (+17.4 kJ/mol)** **4c (+10.6 kJ/mol)** **4d (+3.9 kJ/mol)**

n = 5

5a (+0 kJ/mol) **5b (+5.8 kJ/mol)** **5c (+22.2 kJ/mol)** **5d (+3.9 kJ/mol)**

Figure 3.2. Calculated isomers for $Gdm^+(H_2O)_{1\text{-}5}$ at the B3LYP/6-31++G** level of theory and their relative Gibbs free energies at 133 K.

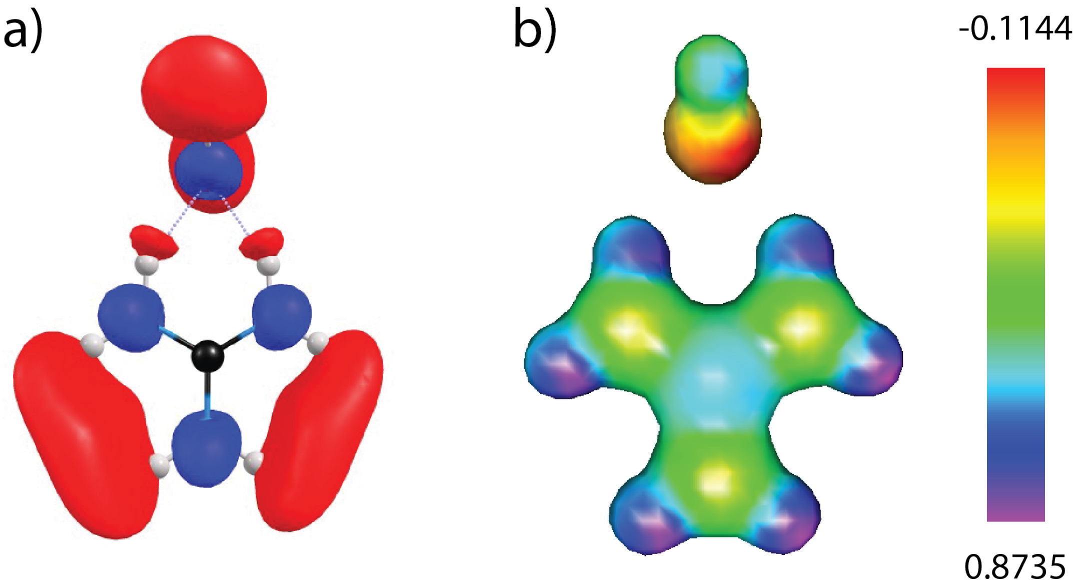

Figure 3.3. (a) LUMO of Gdm$^+$(H$_2$O)$_1$ calculated at the B3LYP/6-31++G** level of theory, (b) electrostatic potential map of Gdm$^+$(H$_2$O)$_1$ at the same level of theory using an isosurface value of 0.500 e/Å^3.

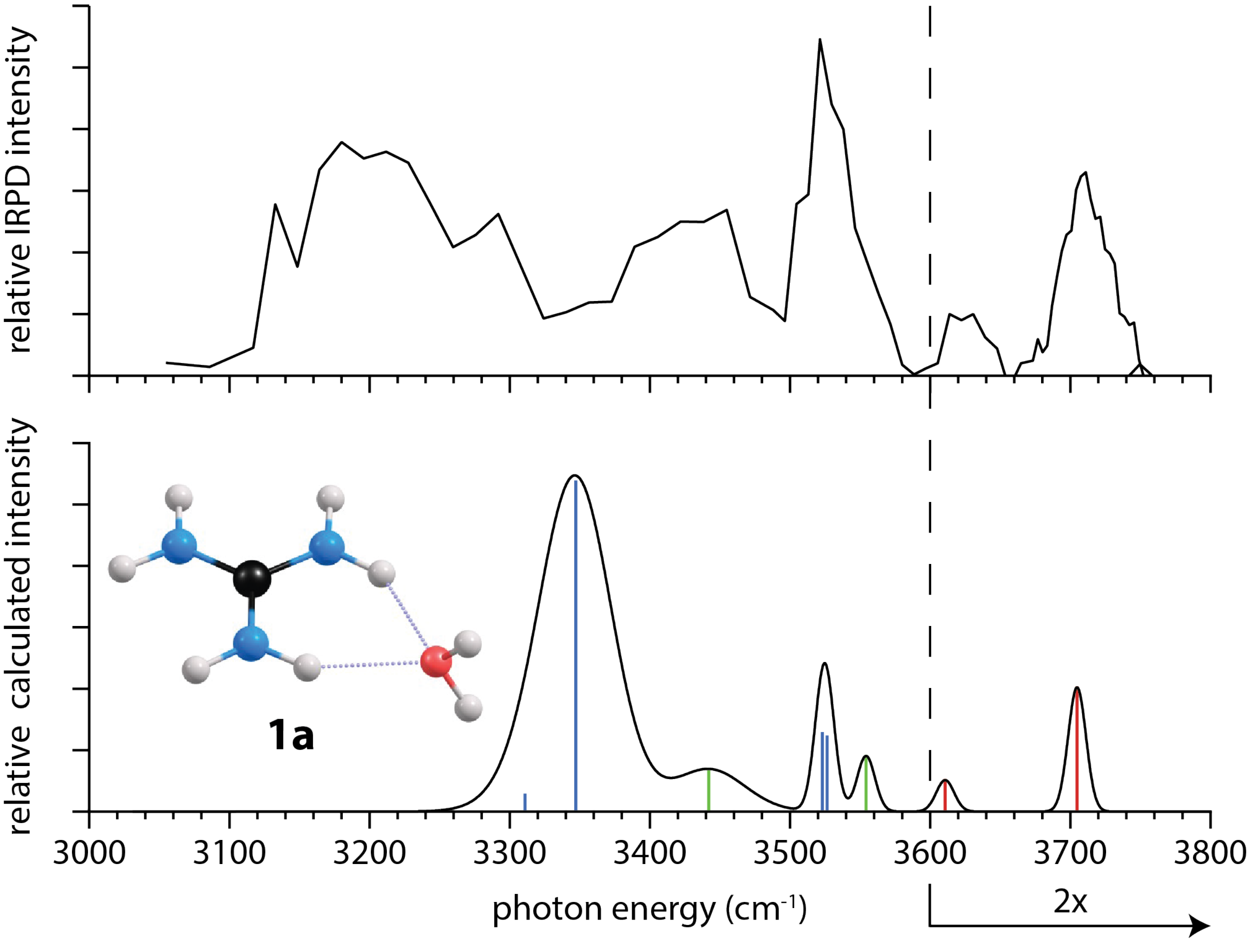

Figure 3.4. IRPD spectrum and calculated spectrum of the low-energy isomer at the B3LYP/6-31++G** level of theory for $Gdm^+(H_2O)_1$. Color-coding is by oscillator type: free O–H (red), free N–H (green), bonded N–H (blue).

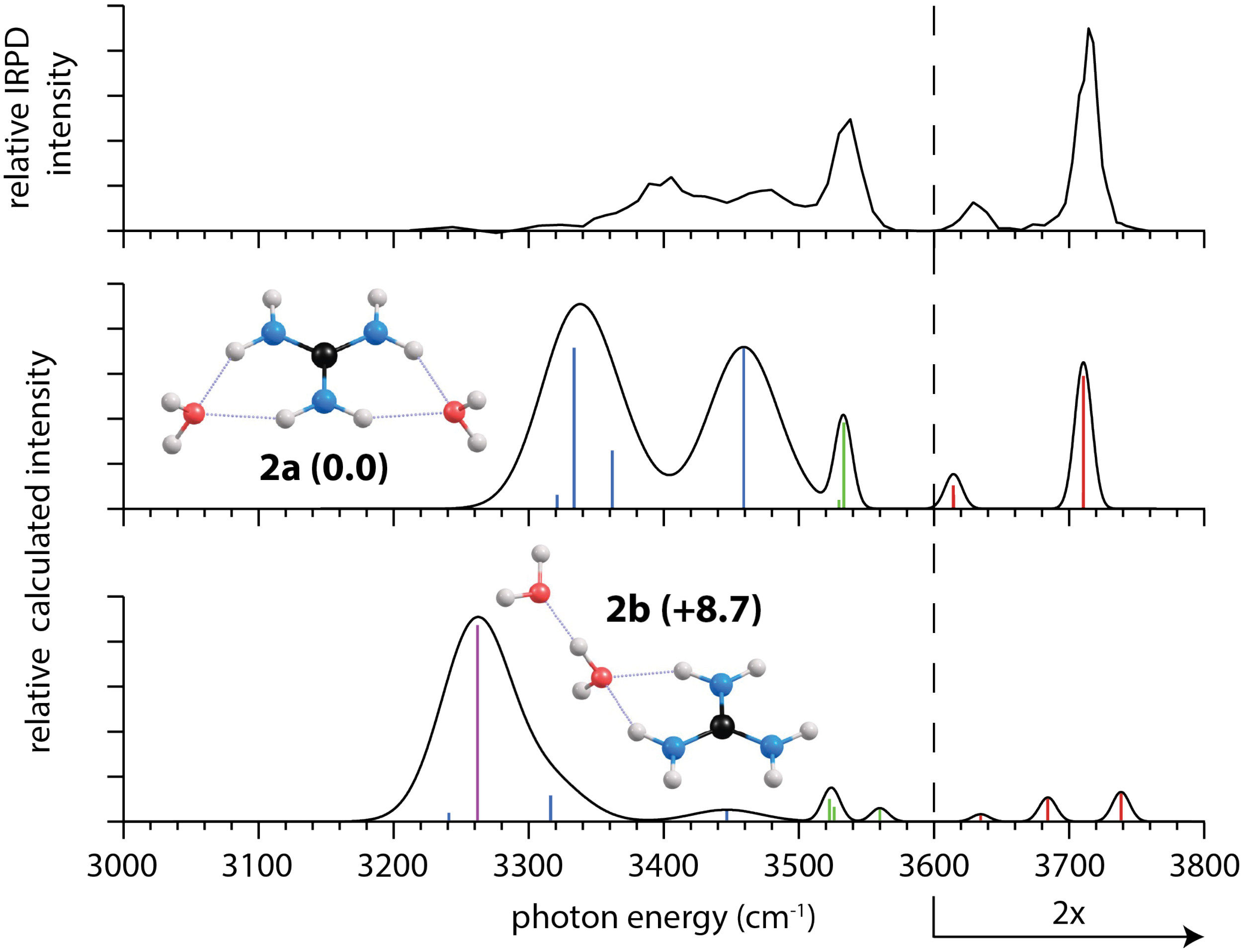

Figure 3.5. IRPD spectrum and calculated spectra of low-energy isomers at the B3LYP/6-31++G** level of theory for $Gdm^+(H_2O)_2$. Relative Gibbs free energies in kJ/mol of the isomers are calculated at the above level of theory at 133 K. Color-coding is by oscillator type: free O–H (red), free N–H (green), bonded N–H (blue), bonded O–H (purple).

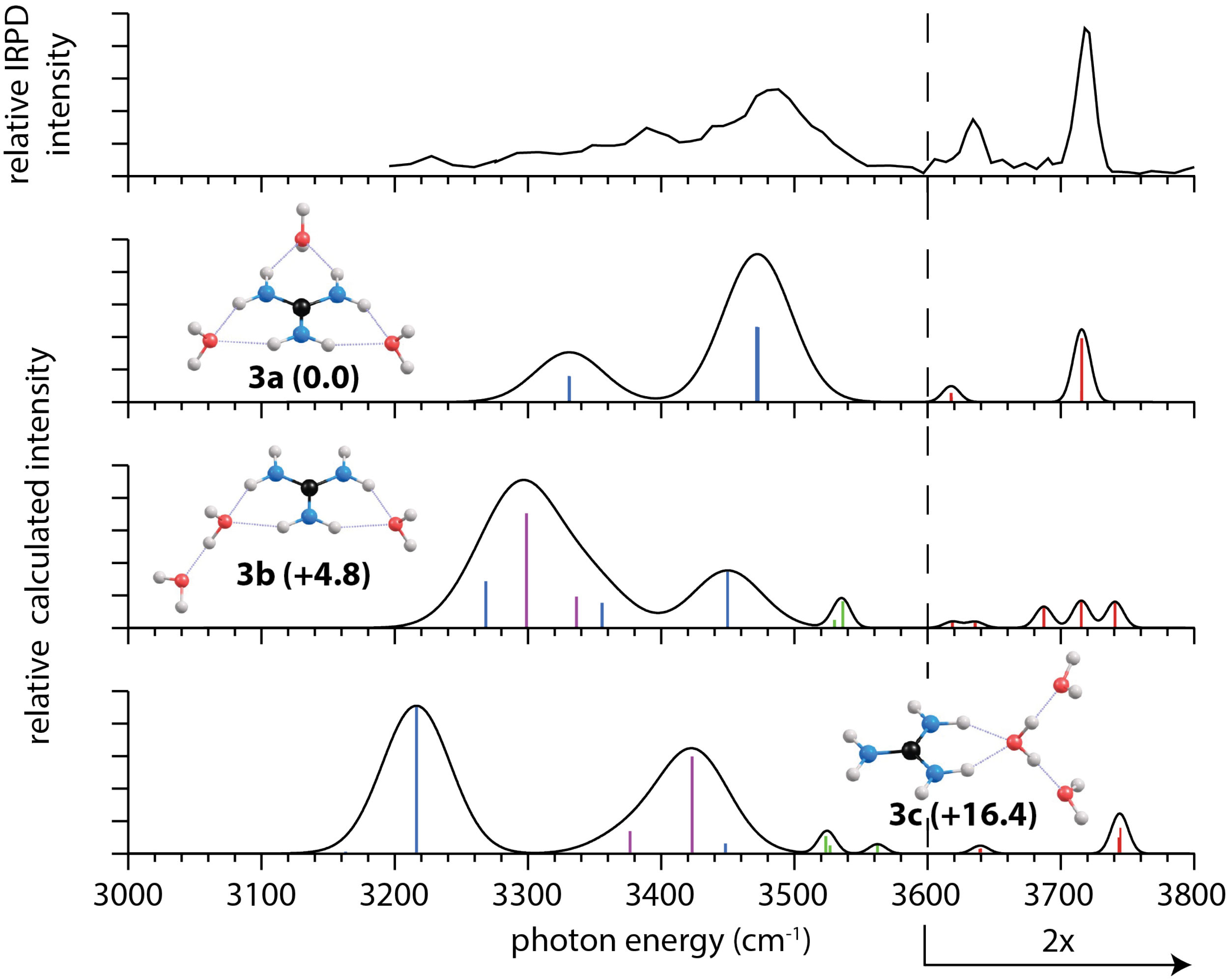

Figure 3.6. IRPD spectrum and calculated spectra of low-energy isomers at the B3LYP/6-31++G** level of theory for $Gdm^+(H_2O)_3$. Relative Gibbs free energies in kJ/mol of the isomers are calculated at the above level of theory at 133 K. Color-coding is by oscillator type: free O–H (red), free N–H (green), bonded N–H (blue), bonded O–H (purple).

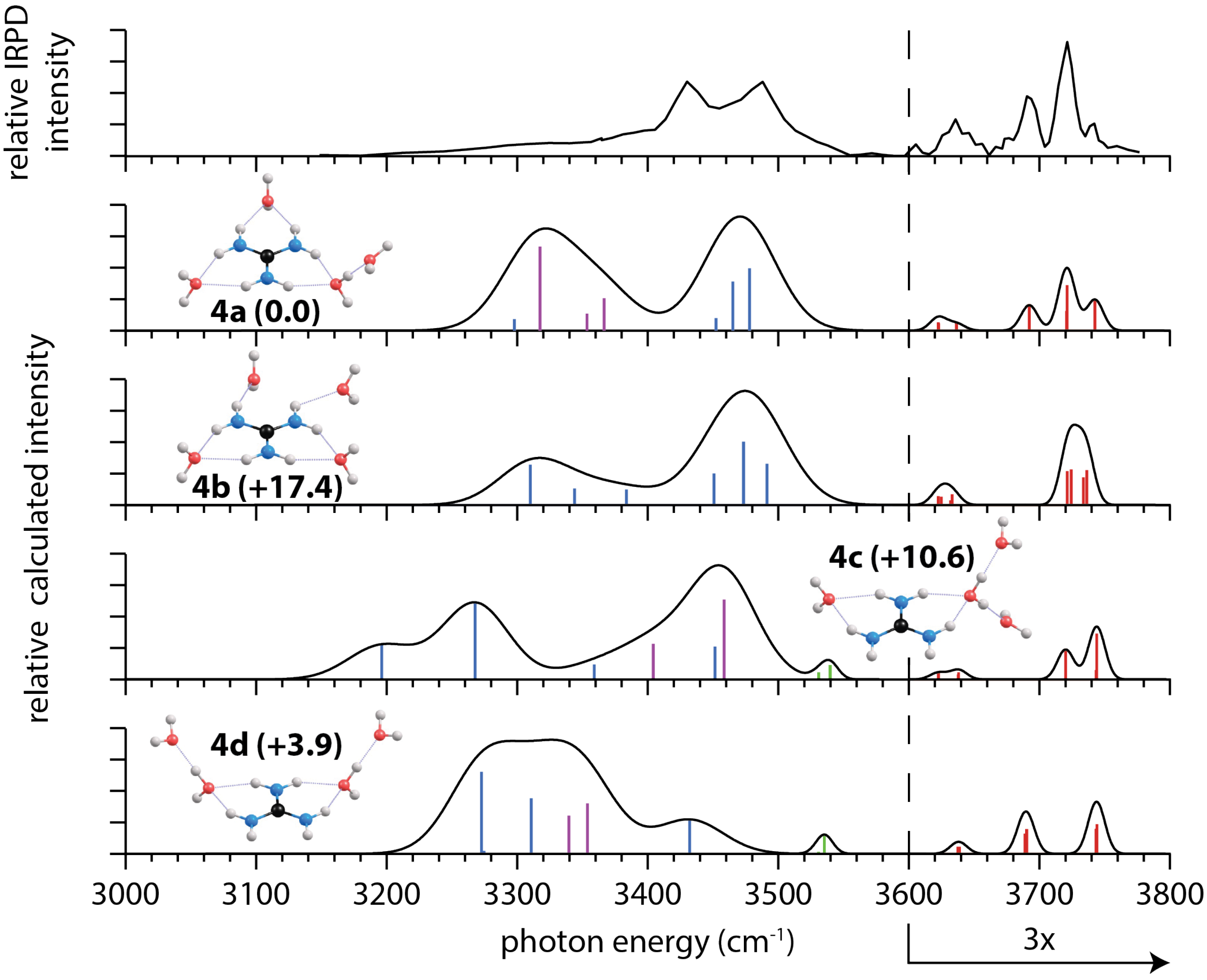

Figure 3.7. IRPD spectrum and calculated spectra of low-energy isomers at the B3LYP/6-31++G** level of theory for $Gdm^+(H_2O)_4$. Relative Gibbs free energies in kJ/mol of the isomers are calculated at the above level of theory at 133 K. Color-coding is by oscillator type: free O–H (red), free N–H (green), bonded N–H (blue), bonded O–H (purple).

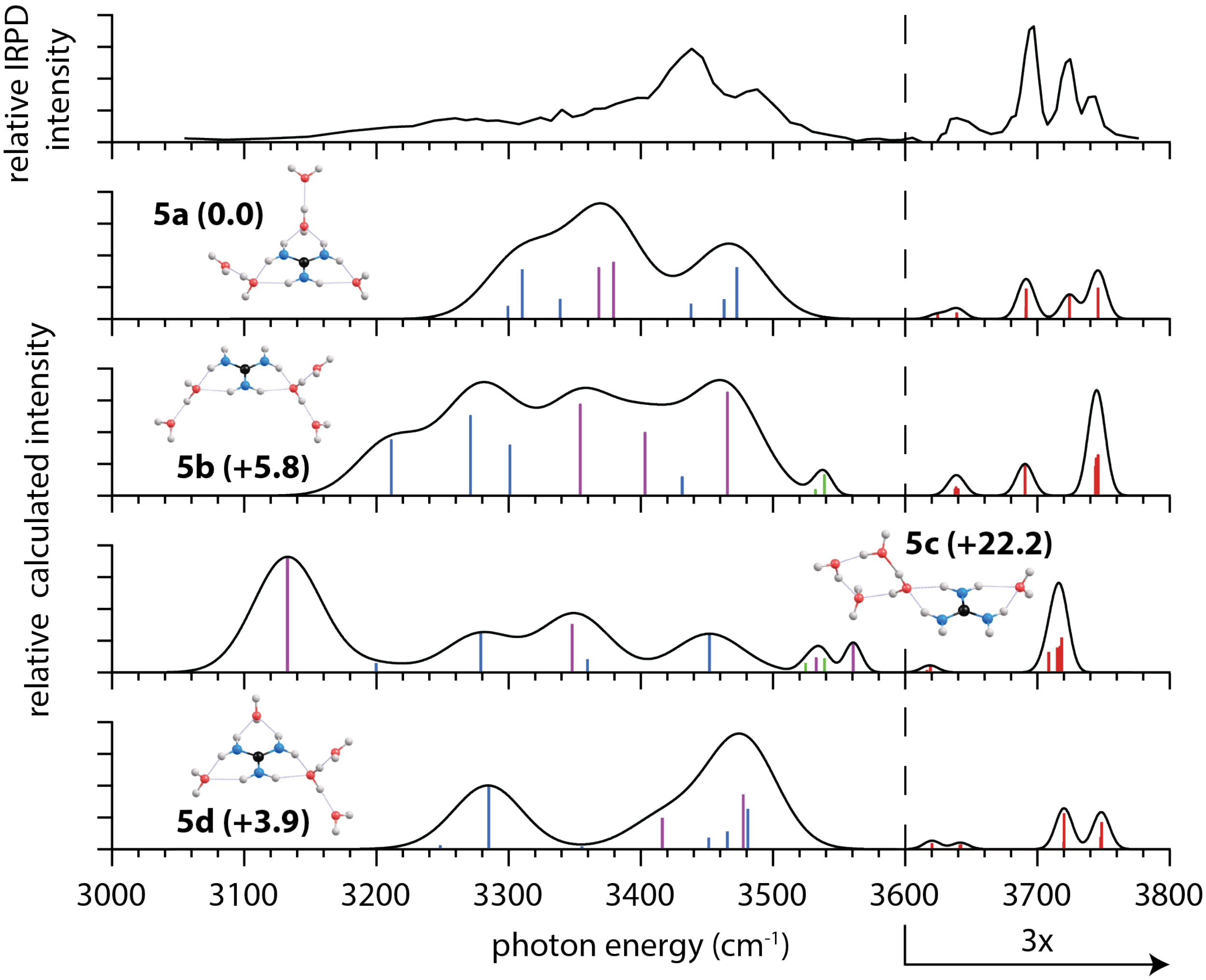

Figure 3.8. IRPD spectrum and calculated spectra of low-energy isomers at the B3LYP/6-31++G** level of theory for $Gdm^+(H_2O)_5$. Relative Gibbs free energies in kJ/mol of the isomers are calculated at the above level of theory at 133 K. Color-coding is by oscillator type: free O–H (red), free N–H (green), bonded N–H (blue), bonded O–H (purple).

Chapter 4

Effects of Electronic Structure on the Hydration of $PbNO_3^+$ and $SrNO_3^+$ Ion Pairs

This chapter is reproduced with permission from
Cooper, R.J.; Heiles, S.; Williams, E.R.
"Effects of Electronic Structure on the Hydration of $PbNO_3^+$ and
$SrNO_3^+$ Ion Pairs"
Physical Chemistry Chemical Physics **2015**, 17, 15963-15975
© 2015 Royal Society of Chemistry

4.1 Introduction

Lead is one of the most widely dispersed toxins in the environment, and its deleterious effects on human health have been recognized since the 1960s.[1-3] Once ingested, lead deposits into tissues in the central nervous system[4,5] and various organs throughout the body,[6] disrupting their function. Divalent lead in particular inhibits the function of regulatory metalloproteins by acting as a heavy-metal substitute for metal ion cofactors. Pb(II) can bind to the Ca(II)-regulated calmodulin messenger protein[7,8] thereby falsely activating cell signaling processes.[9,10] Other calcium-dependent enzymes are affected by Pb(II), including protein kinase C, whose activity can be stimulated by picomolar concentrations of lead.[11] Similarly, Pb(II) has been found to inhibit the function of Zn(II) and Fe(II) metalloenzymes involved in heme biosynthesis,[2,12] resulting in anemia. Lead binding depends both on its specific interaction with proteins but also its interactions with water. Knowledge of the coordination chemistry of divalent lead is thus important for understanding its biological activity.

The stability of lead in an oxidation state two less than the group valency is a characteristic shared amongst the heavier *p*-block elements, the so-called "inert pair effect".[13] This property has been explained by a relativistic contraction of the 6*s* orbital, which stabilizes the electrons against oxidation and confers chemical inertness.[14,15] Although these inert electrons do not participate in chemical bonding, crystal structures of Pb(II)-containing complexes indicate that they can be categorized into two broad families depending on the apparent stereochemical activity of the inert pair.[16,17] In holodirected complexes, electron density is evenly distributed around the metal ion, as are ligands in the coordination sphere. Just the opposite is the case in hemidirected Pb(II)-complexes, where asymmetric electron density on the ion results in voids in the coordination sphere. Shimony-Livny and co-workers conducted a survey of the binding preferences of lead by analyzing 329 crystal structures of lead-containing compounds.[16] They reported that Pb(II) can adopt coordination numbers (CN) ranging from 2–10, with the exclusive formation of hemidirected structures for CN = 2–5, the exclusive formation of holodirected structures for CN = 9–10, and the presence of both structures for CN = 6–8. It was initially postulated that the asymmetric electron density on Pb(II) arises from a mixing of the occupied atomic 6*s* orbital with unoccupied 6*p* orbitals, creating directional *s*–*p* hybrid orbitals.[18] *Ab inito* calculations on solid-state Pb(II) complexes indicate that the 6*s* electrons remain largely unhybridized, and that asymmetric electron density on the ion is due to charge transfer between the ligands and vacant 6*p* orbitals on Pb(II).[19] These findings better explain the presence of both holo- and hemidirected structures for the intermediate CNs of Pb(II), where there is a dependence on the identity of the ligand.

Although there is much data for solid-state Pb(II) complexes, there is little experimental data on the hydration of lead in aqueous solution.[17] An early proton magnetic resonance measurement indicated that the primary hydration number for Pb(II) is 5.7,[20] although this value has been called into question.[21] Persson et al. measured an extended X-ray absorption fine structure spectrum of a 0.1 M solution of $Pb(ClO_4)_2$, and from the broad distribution of Pb—O bond distances concluded that Pb(II) is hemidirected in aqueous solution.[17] *Ab inito* calculations on $Pb^{2+}(H_2O)_n$ clusters indicate that hemidirected structures are favored for $n < 6$, with holodirected structures becoming energetically competitive at $n = 6$.[22,23] In contrast, molecular dynamics simulations of aqueous Pb(II) indicate predominantly holodirected structures.[21,24] Even less is known about solvated lead complexes.

Solvated ions can be readily formed by electrospray ionization and probed using infrared photodissociation spectroscopy in conjunction with quantum computational chemistry to obtain information about the structures of ions solvated by water[25-45] as well as other ligands.[46-48] Stace and co-workers showed that many complexes of Pb(II) with organic ligands are stable in the gas phase,[49,50] but that gaseous clusters of $Pb^{2+}(H_2O)_n$ are unstable to hydrolysis for $n < 11$ and consequently are not present in electrospray ionization (ESI) mass spectra.[51] However, they report that hydrates of the contact ion pair $[PbNO_3]^+(H_2O)_n$ are stable at small cluster sizes, and Raman measurements indicate that ion pairing between metal ions and nitrate can occur in solution.[52] IRPD studies of ion pair hydrates have so far been limited to two reports on the first hydration shell of metal hydroxides,[53,54] and a report on $[MgNO_3]^+(H_2O)_{1\text{-}4}$.[55] How the hydration of an ion pair evolves past the completion of an inner shell around the metal ion has hitherto not been studied.

Here, the hydration of $[PbNO_3]^+(H_2O)_n$ and $[SrNO_3]^+(H_2O)_n$ is probed with IRPD spectroscopy, with the latter species serving as a reference for an ion pair incorporating a metal ion with a closed shell of electrons. IRPD spectra of $[MNO_3]^+(H_2O)_n$ with $2 \leq n \leq 8$ show that the onset of hydrogen bonding (H-bonding) begins at $n = 5$ for $PbNO_3^+$ and $n = 6$ for $SrNO_3^+$ indicating differences in their inner hydration shells. Comparisons between IRPD and calculated spectra of $[PbNO_3]^+(H_2O)_{2\text{-}5}$ and $[SrNO_3]^+(H_2O)_{3\text{-}6}$ show that hemidirected structures are energetically favorable for $PbNO_3^+$. We attribute this structural preference to charge transfer between the nitrate and water ligands and unoccupied 6*p* orbitals on Pb(II). IRPD spectra of larger hydrates of these ion pairs show that differences in their hydration persist up to $n = 25$, well past the first hydration shell.

4.2 Experimental Methods

4.2.1 IRPD Spectroscopy. IRPD spectra of hydrated $PbNO_3^+$ and $SrNO_3^+$ were acquired using a 7.0 T Fourier-transform ion cyclotron resonance mass spectrometer coupled to a tunable OPO/OPA tabletop laser system. A detailed description of the apparatus and experiment can be found elsewhere.[56] Briefly, hydrated ions are generated from nanoelectrospray ionization of 3–5 mM aqueous solutions of $Pb(NO_3)_2$ (J.T. Baker, Phillipsburg, NJ) and $Sr(NO_3)_2$ (Mallinckrodt, Paris, KY) using borosilicate glass capillaries that are pulled to an inner tip diameter of ~1 μm. A platinum wire is inserted into the capillary tube so that it is in contact with the solution, and a ~+600 V potential relative to the heated capillary entrance of the mass spectrometer is applied to the wire to initiate electrospray. Ions are directed from atmosphere through five stages of differential pumping into the ion cell using electrostatic lenses. The cell is surrounded by a temperature-regulated copper jacket[57] that is equilibrated to 133 K for 8 h prior to experiments. A pulse of dry nitrogen gas is introduced into the vacuum chamber at a pressure of ~10^{-6} Torr for ~5 s to aid with thermalizing and trapping the ions. This is followed by a ~7 s delay to reduce the pressure in the cell to < 10^{-8} Torr. Precursor ions are selected using stored waveform inverse Fourier transforms.

Mass-selected clusters are photodissociated at specific frequencies using an OPO/OPA laser system (LaserVision, Bellevue, WA) pumped by the 1064 nm fundamental of a Nd:YAG laser (Continuum Surelight I-10, Santa Clara, CA) at a 10 Hz repetition rate with pulse energies between ~1–4 mJ between 3000–3800 cm^{-1}. Irradiation times between 1 to 10 s are used to produce substantial, but not complete, fragmentation of the isolated precursor ions which dissociate by the sequential loss of water molecules. First-order photodissociation rate constants are determined from the relative abundances of the precursor and fragment ions, and are corrected for frequency-dependent variations in laser power as well as blackbody infrared radiative dissociation (BIRD), which occurs as a result of the absorption of blackbody photons from the 133 K ion cell and cell jacket.

4.2.2 Computational Chemistry. Low-energy structures of $PbNO_3^+$ and $SrNO_3^+$ with between 2 and 10 water molecules attached were generated in Macromodel 9.1 (Schrodinger, Inc., Portland, OR) by a Monte Carlo conformational search using an OPLS2005 force field with an energy cutoff of 40 kJ/mol. Anywhere between tens to hundreds of geometries were identified depending on the cluster size. From the resulting pool of low-energy structures, structures representing different isomers and water molecule binding sites were selected for geometry optimization in Q-Chem 4.1[58] (Q-Chem, Inc., Pittsburgh, PA) at the B3LYP/aug-cc-pVDZ level of theory (using the CRENBL effective core potential for Sr and Pb) prior to vibrational frequency and intensity calculations at the same level of theory. For calculated spectra, vibrational frequencies were scaled by 0.958 and convolved with a 60 and 15 cm^{-1} fwhm Gaussian for the 3000–3510 cm^{-1} and 3510–3800 cm^{-1} regions, respectively. Zero-point energies, enthalpy, and entropy corrections at 133 K were calculated for these structures using unscaled B3LYP/aug-cc-pVDZ harmonic oscillator vibrational frequencies. Additional optimizations on $[PbNO_3]^+(H_2O)_{4\text{-}5}$ and $[SrNO_3]^+(H_2O)_{4\text{-}5}$ were performed using the B3LYP functional with the 6-31++G** basis set, and the MP2 level of theory with both aug-cc-pVDZ and 6-31++G** basis sets. Zero-point energy, enthalpy, and entropy corrections for these structures were calculated using unscaled harmonic frequencies obtained at the corresponding level of theory after geometry optimization. The wave functions of $PbNO_3^+$ and $SrNO_3^+$ with 5 water molecules attached were analyzed by the natural bond orbital (NBO) package of Reed and Weinhold, NBO 5.0,[59] that is incorporated in Q-Chem 4.1.

4.3 Results and Discussion

4.3.1 IRPD Spectra of Small $PbNO_3^+$ and $SrNO_3^+$ Hydrates. The structures of $[PbNO_3]^+(H_2O)_n$ and $[SrNO_3]^+(H_2O)_n$ with n between 2 and 8 were investigated by measuring IRPD spectra in the hydrogen stretch region (~3000–3800 cm^{-1}) at 133 K (Figure 4.1). Vibrational resonances in this region arise from both hydrogen-bonded (H-bonded) and “free” O—H stretches of water molecules. The frequencies of these oscillators are influenced by their local environment within the cluster, the ion charge state,[31-33] proximity to the charge,[32] and participation in hydrogen bonding.[34-38] The overlaid spectra of $PbNO_3^+$ and $SrNO_3^+$ hydrates shown in Figure 4.1 can be delineated into two principal spectral regions. Resonances in the higher-frequency free O—H region (~3550–3800 cm^{-1}) arise from O—H oscillators that are not involved in H-bonding and are relatively sharp bands. The broad bands of dissociation observed in the lower-frequency region (~3000-3600 cm^{-1}) are a result of bonded O—H stretches, including both water-water and water-nitrate hydrogen bonds.

The IRPD spectra of the size selected $PbNO_3^+$ and $SrNO_3^+$ clusters are significantly different, especially in the bonded O—H region, indicating that the solvation of these two ion pairs by water is also significantly different. The onset of dissociation in the bonded O—H region indicates the formation of a second shell of water molecules in the hydration of various cations, including alkali and alkaline metal ions,[25,26,39] transition metal ions,[28,29,40-42,60] and polyatomic ions.[30,61] In the IRPD spectrum of $[PbNO_3]^+(H_2O)_5$, there is a broad region of dissociation with a maximum near 3475 cm^{-1} that extends down to 3000 cm^{-1}, indicating H-bonding within the cluster. By comparison, evidence of H-bonding in the IRPD spectra of $[SrNO_3]^+(H_2O)_n$ occurs at $n \geq 6$, indicating that Sr(II) can accommodate an additional water molecule in its inner hydration shell. It is intriguing that the formation of a second hydration shell begins at a smaller cluster size for $PbNO_3^+$ than $SrNO_3^+$ considering that both Pb(II) and Sr(II) have nearly identical crystallographic ionic radii (133 and 132 pm, respectively).[62] This difference in the onset of second shell formation suggests that the hydration of these ions is significantly affected by the differences in the electronic structures of lead and strontium. For the $n = 6$ and 8 cluster sizes, the intensity in the bonded O—H region of $[SrNO_3]^+(H_2O)_n$ is less than that of $[PbNO_3]^+(H_2O)_n$, consistent with the $[SrNO_3]^+(H_2O)_n$ clusters containing fewer H-bonds, although other factors also influence the intensities of these bands.

Features in the free O—H region of the $[PbNO_3]^+(H_2O)_n$ and $[SrNO_3]^+(H_2O)_n$ spectra also provide structural information. The free O—H region can be subdivided into two regions arising from the antisymmetric and symmetric stretches of water molecules, which appear between 3650–3750 cm^{-1} and 3550–3650 cm^{-1}, respectively (Figure 4.1). The onset of H-bonding in the bonded O—H region is accompanied by changes in the free O—H band structure. There are two distinct symmetric stretching bands in the spectrum of $[PbNO_3]^+(H_2O)_5$, whereas the symmetric stretching bands near 3600 cm^{-1} are degenerate for the smaller $PbNO_3^+$ hydrates. This indicates that water molecules in $[PbNO_3]^+(H_2O)_5$ reside in different environments, as would be expected of inner shell versus outer shell water molecules. Changes in the free O—H band structure of $[SrNO_3]^+(H_2O)_n$ spectra also accompany the onset of H-bonding in the $n = 6$ cluster. Most apparent is the broadening of the antisymmetric stretching band centered on 3715 cm^{-1} in IRPD spectrum of $[SrNO_3]^+(H_2O)_5$ upon the addition of a water molecule, indicating the greater diversity of water molecule binding sites in $[SrNO_3]^+(H_2O)_6$.

4.3.2 Calculated Lowest-Energy Structures for $[MNO_3]^+(H_2O)_n$. Calculated lowest-energy isomers of $[PbNO_3]^+(H_2O)_n$ and $[SrNO_3]^+(H_2O)_n$ for $n = 2$–10 at the B3LYP/aug-cc-pVDZ level of theory are shown in Figure 4.2. There are differences between the calculated structures of $PbNO_3^+$ and $SrNO_3^+$ hydrates at the smallest cluster size ($n = 2$) that persist up to the largest calculated hydrates at $n = 10$. There is an energetic preference for hemidirected coordination complexes of $PbNO_3^+$, where there is a void in the coordination sphere around Pb(II). The directed electron density on Pb(II) apparently repels water molecules from the ion on the side opposite to the nitrate ligand. The structural effects of this repulsive domain are made evident by comparing lowest-energy structures of $[PbNO_3]^+(H_2O)_2$ and $[SrNO_3]^+(H_2O)_2$. Water molecules reside above and below the plane of the nitrate ion in $[PbNO_3]^+(H_2O)_2$, aligning an O—H bond along the Pb—O axis of the ion pair. The structure for $[SrNO_3]^+(H_2O)_2$ has the ligands distributed in such a way that repulsion between them is minimized.

The anisotropic hydration of $PbNO_3^+$ relative to the more isotropic hydration of $SrNO_3^+$ is a motif that persists in the calculated structures of the larger hydrates of these ions, qualitatively explaining some of the features in the IRPD spectra (Figure 4.1). Although the lowest-energy structures of the hydrated ion pairs are similar at $n = 3$, those of $PbNO_3^+$ and $SrNO_3^+$ with four water molecules attached are significantly different. For $[PbNO_3]^+(H_2O)_4$, lead is hemidirected and the water molecules hydrate the ion pair anisotropically whereas the water molecules are more isotropically arranged around $[SrNO_3]^+(H_2O)_4$. As a consequence of their quasi-spherical distribution in $[SrNO_3]^+(H_2O)_4$, water molecules reside in substantially different binding sites around the strontium ion, consistent with the presence of multiple symmetric stretching bands in the IRPD spectrum of $[SrNO_3]^+(H_2O)_4$ (Figure 4.1). Structural differences are even more apparent for the $n = 5$ clusters. The lowest-energy structure identified for $[PbNO_3]^+(H_2O)_5$ is hemidirectional, with water-water H-bonds preferentially forming over direct solvation of Pb(II). The presence of a second shell water molecule in this structure is consistent with the photodissociation observed in the bonded O—H region of the IRPD spectrum of $[PbNO_3]^+(H_2O)_5$. In contrast, water molecules in the structure of $[SrNO_3]^+(H_2O)_5$ form a complete inner solvation shell around Sr(II), consistent with the absence of H-bonded stretches in the IRPD spectrum of this cluster.

The hemidirected nature of Pb(II) is calculated to be energetically favorable in structures of $[PbNO_3]^+(H_2O)_n$ for the larger $n = 6$, 8, and 10 cluster sizes as well. A comparison of the structures of $[SrNO_3]^+(H_2O)_n$ and $[PbNO_3]^+(H_2O)_n$ at these cluster sizes shows that the steric repulsion from the directional electron density on Pb(II) plays an important role in the difference in the hydration of these two ions. In general, water molecules coordinate isotropically to Sr(II), filling out the inner shell of the cation. Subsequent water molecules that attach to the $SrNO_3^+$ ion pair form a bridge between this inner shell and the nitrate anion, accepting H-bonds from inner shell water molecules and donating H-bonds to nitrate. In contrast, a full inner shell around Pb(II) in $PbNO_3^+$ does not form in this range of cluster sizes, leading to structures where the ion pair is not isotropically solvated by water. The directional distribution of electron density on Pb establishes a “hydrophobic” surface that repels water molecules away from part of the ion so they preferentially form water-water H-bonds, eschewing short-range ion-dipole interactions with the cation. It is interesting to note that for both $[SrNO_3]^+(H_2O)_n$ and $[PbNO_3]^+(H_2O)_n$, these calculations predict that the nitrate ligand transitions from being bidentate to monodentate between the $n = 8$ and 10 cluster sizes, presumably to maximize the number of H-bonds formed between water molecules and nitrate.

4.3.3 Structures of $[MNO_3]^+(H_2O)_{2\text{-}3}$. To obtain more detailed information about structures, the IRPD spectra are compared to calculated spectra of low-energy isomers. The IRPD spectra of $[PbNO_3]^+(H_2O)_{2\text{-}3}$ and $[SrNO_3]^+(H_2O)_3$ shown in Figure 4.1 have simple band structures, and a detailed comparison between experiment and theory can be found in the supporting information. An IRPD spectrum of $[SrNO_3]^+(H_2O)_2$ was not acquired at 133 K because photodissociation for this stable complex was not observed for up to 60 s of laser irradiation. Calculations indicate that the water molecule binding energy for $[SrNO_3]^+(H_2O)_2$ (~103 kJ/mol) is significantly higher than that for $[PbNO_3]^+(H_2O)_2$ (~77 kJ/mol), consistent with the absence of observable photodissociation for the former ion under these conditions (Table S1). The two bands appearing at 3595 cm^{-1} and 3685 cm^{-1} in the IRPD spectrum of $[PbNO_3]^+(H_2O)_2$ correspond to the symmetric and antisymmetric stretches of water molecules, which are substantially red-shifted from their neutral values in water vapor of 3657 cm^{-1} and 3756 cm^{-1}, respectively.[63] The calculated spectrum of the lowest-energy isomer of $[PbNO_3]^+(H_2O)_2$ matches closely with the IRPD spectrum (See Appendix B1). Similarly, the IRPD spectra of $[PbNO_3]^+(H_2O)_3$ and $[SrNO_3]^+(H_2O)_3$ have resonances associated with the symmetric and antisymmetric stretching motions of water molecules, and match most closely with the calculated spectra of the lowest-energy isomers (Figures S2 and S3). The broadened symmetric stretching band in the IRPD spectrum of $[SrNO_3]^+(H_2O)_3$ may arise from the existence of low-lying isomers where water molecules are distributed more evenly around the strontium ion (See Appendix B3). The maximum infrared photodissociation rate constant for $[SrNO_3]^+(H_2O)_3$ is about four times lower than that for $[PbNO_3]^+(H_2O)_3$ indicating that water molecules in this complex are more tightly bound and that the absorption of multiple photons may be required to induce observable laser-induced photodissociation on the timescale of the experiment.

4.3.4 Structures of $[MNO_3]^+(H_2O)_4$. The IRPD spectrum of $[SrNO_3]^+(H_2O)_4$ along with calculated infrared spectra of four low-energy isomers are shown in Figure 4.3. The most intense band in the experimental spectrum is the antisymmetric stretch at 3708 cm^{-1} that is closely reproduced in the calculated spectra of isomers **4a–4c**. The positions of water molecules around the strontium ion in these three isomers differ substantially, yet the antisymmetric stretching bands are similar, indicating that the antisymmetric stretching frequencies of these inner shell water molecules are not sensitive to their position around the ion pair. The two well-defined bands in this region near 3585 cm^{-1} and 3635 cm^{-1} do not unequivocally correspond to the symmetric stretching bands in the calculated spectrum of any single isomer. The spectrum of isomer **4c** (+2.5 kJ/mol) is arguably the best fit with experiment, reproducing the measured number of resonances, although the lowest-energy symmetric stretch is calculated to be ~60 cm^{-1} lower than that in the IRPD spectrum. These calculations indicate that the frequencies of the symmetric stretching bands are sensitive to the positions of water molecules within the cluster, and discrepancies between experiment and theory could arise from uncertainties in harmonic oscillator frequencies and intensities[64] as well as the presence of energetically competitive isomers. For ions where there are many interconverting isomers or that have vibrations that are significantly anharmonic, calculated harmonic spectra of low-energy isomers can differ from the experimental infrared spectra.[65,66] Uncertainties as a result of the harmonic frequency approximation can also affect calculated Gibbs free energies, which may affect the relative energetic ordering of isomers presented here. Structure **4d** (+25.1 kJ/mol) is the lowest-energy isomer identified that includes a hydrogen bond and is significantly higher in energy than all the isomers without H-bonding (**4a**–**4c**). The poor match between its calculated spectrum and the IRPD spectrum, most notably the calculated H-bonded stretch centered on 3182 cm^{-1} that is absent in the experiment, indicate that it does not constitute a significant fraction of the experimental population.

The experimental and calculated infrared spectra for $[PbNO_3]^+(H_2O)_4$ are shown in Figure 4.4. The lowest-energy isomer (**4a**) reproduces the water antisymmetric and symmetric stretching bands in the IRPD spectrum near 3705 cm^{-1} and 3612 cm^{-1}, respectively, but there are additional features in the experimental spectrum of $[PbNO_3]^+(H_2O)_4$ that cannot be explained by isomer **4a** alone. An intense band at 3684 cm^{-1} is present in the antisymmetric stretching region, as well as two broad regions of low intensity in the bonded O—H region near 3460 cm^{-1} and 3100 cm^{-1}. Collectively, these resonances may arise from a minor population of structures in which there is hydrogen bonding, such as isomer **4b** (+8.1 kJ/mol). This structure has a resonance at 3686 cm^{-1} corresponding to the antisymmetric free O—H stretch of a water molecule donating one H-bond. The bonded O—H stretch of this water molecule is calculated to occur at 3052 cm^{-1}, which could account for the small recorded resonance near 3100 cm^{-1}. The experimentally observed dissociation between 3300–3500 cm^{-1} is not reproduced in any of the calculated spectra, and we postulate that this band may arise from an O—H oscillator forming a weak H-bond with nitrate. Isomers **4c** and **4d** have calculated spectra in poor agreement with the IRPD spectrum in the free O—H region, and it is unlikely that they contribute significantly to the experimental population.

4.3.5 Structures of $[MNO_3]^+(H_2O)_5$. The IRPD and calculated spectra of $[SrNO_3]^+(H_2O)_5$ are shown in Figure 4.5. There is good agreement between the IRPD spectrum and the calculated spectrum for lowest-energy isomer **5a**. In this structure, there is no H-bonding and water molecules spherically solvate the strontium ion. There is no spectroscopic evidence for a substantial population of isomers with H-bonded structures, such as isomers **5b–5e**, which are > 14 kJ/mol higher in energy.

The IRPD spectrum of $[PbNO_3]^+(H_2O)_5$ (Figure 4.6) differs significantly from that of $[SrNO_3]^+(H_2O)_5$ (Figure 4.5). In striking contrast to $[SrNO_3]^+(H_2O)_5$, there is substantial dissociation in the bonded O—H region of $[PbNO_3]^+(H_2O)_5$ signifying the onset of H-bonding in this cluster. The water molecule binding energies of these ions differ, and this difference affects the relative dissociation efficiencies of these ions which is a complicating factor in comparing spectral intensities in the bonded O—H region. The water molecule binding energies decrease with increasing cluster size (Table S1), and at $n = 5$, the water molecule binding energies of these two ions are within 20 kJ/mol. The maximum infrared rate constant for $SrNO_3^+$ is within a factor of ~2 of that for $PbNO_3^+$ at $n = 5$. This indicates that the differences in the relative binding energies of water to these ions has a relatively small effect on the ability to observe photodissociation, and that the differences in the spectra of these two ions in the H-bonding region are significant.

The best matches between experiment and theory for $[PbNO_3]^+(H_2O)_5$ are isomer **5b** (+1.7 kJ/mol) and lowest-energy isomer **5c,** indicating the presence of both isomers in the experiment (Figure 4.6). The broad antisymmetric stretching band between 3660–3740 cm^{-1} in the IRPD spectrum is consistent with a combination of the antisymmetric stretches calculated for **5b** and **5c**. There are two free O—H symmetric stretching bands centered on 3620 cm^{-1} and 3585 cm^{-1} in the IRPD spectrum. These resonances are closely matched by the calculated symmetric stretches of isomer **5b** at 3611 cm^{-1} and 3570 cm^{-1}. The greater relative intensity of the higher-energy symmetric stretch in the experimental spectrum is consistent with the presence of isomer **5c**, which is calculated to have a symmetric stretching band centered on 3605 cm^{-1}.

Resonances in the bonded O—H region of the $[PbNO_3]^+(H_2O)_5$ spectrum can also be attributed to a combination of isomers **5b** and **5c**. The experimental band that has a maximum near 3475 cm^{-1} corresponds to the O—H stretch of the second shell water molecule in isomer **5c** that weakly H-bonds with nitrate and is predicted to occur at 3504 cm^{-1}. The broad region of dissociation in the lowest-energy region of the experimental spectrum can be attributed to isomer **5b**, which has a water-water H-bond calculated to have a resonance near 3134 cm^{-1}. In general, the agreement between experimental and calculated frequencies and intensities is poorer in the bonded O—H region. Such discrepancies have been observed in the calculated spectra of a variety of hydrated gaseous ions investigated by IRPD spectroscopy.[25,30,34,67-69] and can be attributed to uncertainties associated with using the harmonic approximation, as well as effects of basis set and level of theory used.[64] IRPD action spectra can also differ from computed spectra owing to fragmentation efficiencies that depend on the photon energy.[70,71]

For larger hydrates of $SrNO_3^+$ and $PbNO_3^+$, a comparison between experiment and theory is more challenging owing to the increasing number of possible isomers and increasing computational difficulty with increasing cluster size. Our results for $[SrNO_3]^+(H_2O)_6$, however, indicate that the outer shell water molecule accepts a H-bond from an inner shell water molecule and donates a weak H-bond to nitrate, thus forming a bridge between the hydration shell around Sr(II) and nitrate (See Appendix B4). The effects of basis set and type of theory on the energetic ordering of isomers was evaluated from single point calculations on optimized structures of the hydrated ions with $n = 4$ and 5 using two types of theory (MP2 and DFT/B3LYP) in conjunction with two different basis sets (aug-cc-pVDZ and 6-31++G**). There is no significant energetic reordering of the isomers for any of the ions investigated, and in all cases, the same lowest-energy structure was identified (Tables S2 and S3).

4.3.6 NBO Analysis of $[PbNO_3]^+(H_2O)_5$. A NBO analysis[72] of the lowest-energy isomer of $[PbNO_3]^+(H_2O)_5$ was performed to elucidate the relationship between the apparent hemidirected nature of Pb(II) in this complex and its electronic structure. The filled NBOs ϕ_i that represent the natural Lewis structure of a molecule commonly account for > 99.9% of the total electron density.[73] The remaining electron density is described by non-Lewis NBOs ϕ_j of lower occupancy that describe portions of the molecular valence space not associated with the localized Lewis structure. Occupancy of these non-Lewis NBOs thus accounts for irreducible delocalization effects in the description of the total electron density and leads to a lowering of the electronic energy. The resonance delocalization of electron density from filled (donor) ϕ_i NBOs to unfilled (acceptor) ϕ_j NBOs constitutes charge transfer between the orbitals, and can be calculated from second order perturbation theory.[74] Analyses of these stabilizing donor-acceptor interactions have led to chemically intuitive descriptions of hyperconjugative effects,[75] H-bonded systems,[76,77] and ion-molecule complexes.[73]

Results from an NBO analysis of $[PbNO_3]^+(H_2O)_5$ indicates that the electron density is strongly resonance delocalized, with the occupancy of Lewis NBOs accounting for only 99.16% of the total electron density. Shown in Figure 4.7a is a set of three unfilled, non-Lewis NBOs that are primarily responsible for this delocalization, accepting charge from filled Lewis NBOs on the water and nitrate ligands (Figure 4.7b). These acceptor orbitals are localized 6*p* atomic orbitals on Pb(II). The orientation of the $6p_1$ orbital in particular is consistent with a region of repulsive electron density that could partially explain the hemidirected character of Pb(II).

Calculated stabilization energies due to charge transfer between donor NBOs on the water and nitrate ligands and the acceptor 6*p* NBOs on Pb are shown in Table 4.1. The most stabilizing interaction (91.6 kJ/mol) occurs between a lone pair on an oxygen atom of nitrate (LP_1) and the $6p_1$ orbital on Pb. These orbitals are relatively close in energy and have good spatial overlap (Figure 4.7) making this the most favorable charge transfer interaction. The next most stabilizing interaction occurs between a lone pair on the second coordinating oxygen atom of the nitrate ligand (LP_2) and the $6p_1$ orbital on Pb(II). Significant charge transfer also occurs between the four inner shell water molecules and the $6p_2$ and $6p_3$ NBOs on Pb(II). The high occupancies of these 6*p* orbitals (Table 4.1), especially the $6p_1$ orbital that accepts charge from nitrate, indicate that they play an essential role in accurately describing the electronic structure of $[PbNO_3]^+(H_2O)_5$. Charge transfer from nitrate to lead slightly shortens the average nitrate-cation distance to 2.56 Å in this complex as compared to 2.63 Å for $[SrNO_3]^+(H_2O)_5$. Conversely, average cation-oxygen bond lengths for inner shell water molecules are somewhat greater for lead (2.68 Å) than strontium (2.62 Å) for $n = 5$ as a result of the reduced positive charge on the lead cation (Table 4.2). An analysis of the net atomic Mulliken charges on Pb and Sr in the lowest-energy structures for the $n = 2$–10 hydrates (Table 4.2) shows that the net atomic charge on lead is ~ +0.5 less than strontium for these cluster sizes, indicating that the charge transfer efficiency does not depend strongly on the extent of hydration within this range of cluster sizes.

Interestingly, the steric influence of lead's 6*s* electrons (i.e., the "inert pair") appears to be minor. Figure 4.7c shows that the valence NBO associated with these electrons is largely unhybridized, having predominately *s* character – the amount of *p* character is calculated to be only 1.47%. These results suggest that the hemidirected nature of the $[PbNO_3]^+(H_2O)_5$ complex can mostly be attributed to a charge transfer effect from the nitrate ligand into an unoccupied 6*p* orbital on lead. This is consistent with *ab initio* calculations performed on structures of lead solvated by water[22] as well as other ligands.[78] Several groups have found that the calculated hybridization of the inert pair is sensitive to the size of the effective core potential used to describe lead,[22,23] potentially explaining an earlier finding where the 6*s* electrons were calculated to be more significantly hybridized.[16]

4.3.7 Structural Signatures in IRPD Spectra of Larger $PbNO_3^+$ and $SrNO_3^+$ Hydrates. The extent to which the structural differences in nascent hydrates of $PbNO_3^+$ and $SrNO_3^+$ persist at larger cluster sizes was investigated by measuring IRPD spectra of $[PbNO_3]^+(H_2O)_n$ and $[SrNO_3]^+(H_2O)_n$, where $n = 10, 15, 20, 25, 30$ (Figure 4.8). The IRPD spectra of both ion pairs with up to 25 water molecules attached are distinguishable in the free O—H and bonded O—H regions but are indistinguishable at $n = 30$ (Figure 4.8). Low-energy structures of these ion pairs with 25 water molecules attached generated using molecular mechanics indicate that there are several water molecules in the third solvation shell (See Appendix B5). This indicates that differences in the electronic structures of $PbNO_3^+$ and $SrNO_3^+$ influence their hydration past the first and even the second solvation shell.

The overall intensity of the bonded O—H stretch region is greater for $[PbNO_3]^+(H_2O)_{10}$ than $[SrNO_3]^+(H_2O)_{10}$, which reflects the more extensive H-bond network in hydrates of $PbNO_3^+$ as a result of the onset of H-bonding at smaller cluster size. At this cluster size, the differences in water molecule binding energies between these clusters is calculated to be ~6 kJ/mol (Table S1) and this difference should only have a minor effect on relative dissociation efficiencies in this spectral region. The intensity of this band becomes similar for both ions with increasing cluster size, indicating that the relative differences in the number of H-bonded oscillators and binding energies diminish. It is also apparent that the shape of the bonded O—H feature is more symmetrical for $[PbNO_3]^+(H_2O)_n$, with the maximum dissociation at ~3475 cm^{-1} for the $n = 10$ and 15 clusters and slightly red-shifting to ~3450 cm^{-1} in the spectra of the larger hydrates. The H-bonded features in the spectra of the larger clusters closely resemble both the bulk infrared spectrum of neutral water[79] and IRPD spectra of hydrated ions that weakly interact with water,[61] indicating optimal water-water H-bonding within the interior of the nanodrops. In contrast, the bonded O—H regions in the IRPD spectra of $[SrNO_3]^+(H_2O)_n$ with up to 25 water molecules are blue-shifted up to ~50 cm^{-1}. This suggests that the H-bond networks in these $SrNO_3^+$ nanodrops are more strained as a result of the stronger interaction between Sr(II) and water compared to

Pb(II) and water where delocalization of electron density from nitrate reduces the net charge on the ion. This interpretation is consistent with condensed phase measurements of hydrated cations measured by vibrational sum frequency generation,[80,81] where the H-bonded stretches of water molecules are shifted towards higher frequencies for ions with greater charge densities.

The most striking difference in the bonded O—H region of these larger $PbNO_3^+$ and $SrNO_3^+$ clusters is the band centered near ~3550 cm^{-1} in the IRPD spectra of the $SrNO_3^+$ hydrates for $n = 15, 20$, and 25. There are resonances at this frequency in IRPD spectra of hydrated ions that form clathrate structures with ~20 water molecules attached, including the hydrated proton,[43-45] alkali metal ions,[82] ammonium,[83,84] and alkylammonium ions[84] corresponding to water molecules that accept one H-bond and donate two H-bonds ("ADD" water molecules) that are integral to forming cage-like, three-dimensional H-bond networks. Results from Fujii and co-workers indicate that an intense ADD band is a general feature of small water clusters (n ~20–50), where the dominant structural motif is calculated to be "centered cage" structures wherein several water molecules are entrained in a three-dimensional water cage.[85] The larger size of these ion pairs precludes structures where an ion pair is completely encapsulated by a water cage with only 20 water molecules or so, but it is possible that partial cage-like structures with a high percentage of three-coordinate water molecules can form around the ion pair. Indeed, the lowest-energy structures of $[SrNO_3]^+(H_2O)_{2-10}$ in Figure 4.2 suggests such a hydration motif, where water molecules first nucleate around Sr(II) and subsequently align along the approximately dipolar electric field of $SrNO_3^+$, forming H-bonds with each other and the nitrate anion. This leads to the beginnings of a cage-like hydration network in the calculated lowest-energy structure of $[SrNO_3]^+(H_2O)_{10}$.

Two distinct bands appear in the free O—H region of these larger $PbNO_3^+$ and $SrNO_3^+$ clusters (Figure 4.8): an intense band near 3700 cm^{-1} associated with water molecules accepting two H-bonds and donating one H-bond (AAD water molecule), and a small band near 3720 cm^{-1} arising from water molecules that accept and donate only one H-bond (AD water molecule). The free O—H stretches of water molecules in $[PbNO_3]^+(H_2O)_n$ are red-shifted by 5.6–7.6 cm^{-1} compared to those in $[SrNO_3]^+(H_2O)_n$ for $n = 10$, 15 and 20, but they are closer in frequency at $n = 25$ (3.3 cm^{-1}) and are indistinguishable at $n = 30$. The centroid frequencies of the AAD free O—H bands were determined by fitting each peak with a Gaussian function, and the frequencies for all cluster sizes are shown in Appendix B. The frequencies of free O—H oscillators depend on the charge of the ion and, to a lesser extent, the size of the ion.[32] Sr(II) and Pb(II) have the same ionic radii[62] indicating that the red-shift in the frequency of surface water stretches in hydrates of $PbNO_3^+$ is due to higher charge transfer between water molecules and lead. This is consistent with findings by Duncan and co-workers, who reported that charge transfer can red-shift the O–H stretch frequencies in IRPD spectra of water molecules bound to singly charged cations.[86] As our NBO analysis of $[PbNO_3]^+(H_2O)_5$ suggests, the unfilled 6p orbitals of Pb(II) can readily accept charge from donating water and nitrate ligands. Charge transfer from water molecules that are located in outer solvation shells will decrease with increasing cluster size because of poorer overlap with the atomic orbitals on the metal ion. The number of water molecules in the second and higher hydration shells increases relative to the number of water molecules in the first hydration shell and the IRPD spectra increasingly reflect absorption of these outer shell water molecules with increasing cluster size. Thus, the IRPD spectra of these clusters are expected to converge at some cluster size where the contributions to the spectra from water molecules that are significantly perturbed by these ions becomes negligible.

4.4 Conclusions

The structures of $[PbNO_3]^+(H_2O)_n$ and $[SrNO_3]^+(H_2O)_n$ were investigated with IRPD spectroscopy and with theory. Although these ions are the same size, they differ significantly in their hydration. H-bonded stretches in the IRPD spectra indicate the onset of second shell formation at $n = 5$ for $PbNO_3^+$ (and a minor population of second shell structures at $n = 4$) and $n = 6$ for $SrNO_3^+$. Calculated structures of $PbNO_3^+$ and $SrNO_3^+$ with 10 and fewer water molecules indicate that hemidirected structures are favored for Pb(II) where there is a noticeable void in its coordination sphere, and these results are consistent with the IRPD spectra. The asymmetric solvation for hydrates of $PbNO_3^+$ is due to the asymmetric electron density on Pb(II) that repels water molecules away from the portion of its coordination sphere opposite to the nitrate ligand, constraining the available binding site for water molecules. Results from an NBO analysis of $[PbNO_3]^+(H_2O)_5$ indicate that the asymmetric charge density on Pb(II) is a result of charge transfer from the nitrate and water ligands into vacant 6*p* orbitals on the ion. In contrast, Sr(II) in $SrNO_3^+$ is isotropically solvated by water.

The IRPD spectra of $PbNO_3^+$ and $SrNO_3^+$ with up to 25 water molecules attached differ. The maximum intensity of the H-bonded stretches of $SrNO_3^+$ are blue-shifted compared to those of $PbNO_3^+$, indicating a greater perturbation of the water H-bond network by strontium than lead. This is consistent with the higher net atomic Mulliken charges of $[SrNO_3]^+(H_2O)_n$ compared to $[PbNO_3]^+(H_2O)_n$. The intense band at 3550 cm^{-1} in the spectra of $SrNO_3^+$ with 15, 20, and 25 waters attached suggests that partial clathrate-like structures may form around this ion pair. The free O—H stretches of AAD water molecules in hydrates of $PbNO_3^+$ are red-shifted by up to ~8 cm^{-1} compared to those in hydrates of $SrNO_3^+$ for $n = 10, 15, 20$ but are the same by $n = 30$. The red-shifting of surface water molecules in $[PbNO_3]^+(H_2O)_n$ is consistent with the transfer of electron density from their O—H bonds to the lead ion. Collectively, the spectral differences between the larger hydrates of $PbNO_3^+$ and $SrNO_3^+$ demonstrate that the electronic structure of an ion can play an important role in how it is solvated past the first and even second solvent shells.

4.5 References

(1) Patterson, C. C. *Arch. Environ. Health.* **1965**, *11*, 344-360.
(2) Vallee, B. L.; Ulmer, D. D. *Annu. Rev. Biochem.* **1972**, *41*, 91-128.
(3) Mahaffey, K. R. *Environ. Health Persp.* **1977**, *19*, 285-295.
(4) Finkelstein, Y.; Markowitz, M. E.; Rosen, J. F. *Brain. Res. Rev.* **1998**, *27*, 168-176.
(5) Lidsky, T. I.; Schneider, J. S. *Brain* **2003**, *126*, 5-19.
(6) Goyer, R. A.; Rhyne, B. C. *Int. Rev. Exp. Pathol.* **1973**, *12*, 1-77.
(7) Wilson, M. A.; Brunger, A. T. *Acta Crystallogr D* **2003**, *59*, 1782-1792.
(8) Kursula, P.; Majava, V. *Acta. Crystallogr. F* **2007**, *63*, 653-656.
(9) Simons, T. J. B. *Neurotoxicology* **1993**, *14*, 77-86.
(10) Marchetti, C. *Neurotox. Res.* **2003**, *5*, 221-235.
(11) Markovac, J.; Goldstein, G. W. *Nature* **1988**, *334*, 71-73.
(12) Ku, W. W.; Slowiejko, D.; Bestervelt, L. L.; Buroker, M. R.; Piper, W. N. *Toxicol. In Vitro* **1990**, *4*, 763-769.
(13) Sidgwick, N. V. *The Electronic Theory of Valency*; Oxford University Press: Clarendon, 1927.
(14) Pitzer, K. S. *Accounts Chem. Res.* **1979**, *12*, 272-276.
(15) Pyykko, P. *Chem. Rev.* **1988**, *88*, 563-594.
(16) Shimoni-Livny, L.; Glusker, J. P.; Bock, C. W. *Inorg. Chem.* **1998**, *37*, 1853-1867.
(17) Persson, I.; Lyczko, K.; Lundberg, D.; Eriksson, L.; Placzek, A. *Inorg. Chem.* **2011**, *50*, 1058-1072.
(18) Orgel, L. E. *J. Chem. Soc.* **1959**, 3815-3819.
(19) Walsh, A.; Watson, G. W. *J. Solid State Chem.* **2005**, *178*, 1422-1428.
(20) Swift, T. J.; Sayre, W. G. *J. Chem. Phys.* **1966**, *44*, 3567-&.
(21) Hofer, T. S.; Rode, B. M. *J. Chem. Phys.* **2004**, *121*, 6406-6411.
(22) Wander, M. C. F.; Clark, A. E. *Inorg. Chem.* **2008**, *47*, 8233-8241.
(23) Devereux, M.; van Severen, M. C.; Parisel, O.; Piquemal, J. P.; Gresh, N. *J. Chem. Theory Comput.* **2011**, *7*, 138-147.
(24) Gourlaouen, C.; Gerard, H.; Parisel, O. *Chemistry* **2006**, *12*, 5024-5032.
(25) Bush, M. F.; Saykally, R. J.; Williams, E. R. *ChemPhysChem* **2007**, *8*, 2245-2253.
(26) Miller, D. J.; Lisy, J. M. *J. Am. Chem. Soc.* **2008**, *130*, 15393-15404.
(27) Goebbert, D. J.; Garand, E.; Wende, T.; Bergmann, R.; Meijer, G.; Asmis, K. R.; Neumark, D. M. *J. Phys. Chem. A* **2009**, *113*, 7584-7592.
(28) O'Brien, J. T.; Williams, E. R. *J. Phys. Chem. A* **2011**, *115*, 14612-14619.
(29) Li, Y.; Wang, G.; Wang, C.; Zhou, M. *J. Phys. Chem. A* **2012**, *116*, 10793-10801.
(30) Cooper, R. J.; Heiles, S.; DiTucci, M. J.; Williams, E. R. *J. Phys. Chem. A* **2014**, *118*, 5657-5666.
(31) Carnegie, P. D.; Bandyopadhyay, B.; Duncan, M. A. *J. Phys. Chem. A* **2008**, *112*, 6237-6243.
(32) Prell, J. S.; O'Brien, J. T.; Williams, E. R. *J. Am. Chem. Soc.* **2011**, *133*, 4810-4818.
(33) O'Brien, J. T.; Williams, E. R. *J. Am. Chem. Soc.* **2012**, *134*, 10228-10236.
(34) Headrick, J. M.; Diken, E. G.; Walters, R. S.; Hammer, N. I.; Christie, R. A.; Cui, J.; Myshakin, E. M.; Duncan, M. A.; Johnson, M. A.; Jordan, K. D. *Science* **2005**, *308*, 1765-1769.

(35) Heine, N.; Fagiani, M. R.; Rossi, M.; Wende, T.; Berden, G.; Blum, V.; Asmis, K. R. *J. Am. Chem. Soc.* **2013**, *135*, 8266-8273.

(36) Leon, I.; Cocinero, E. J.; Rijs, A. M.; Millan, J.; Alonso, E.; Lesarri, A.; Fernandez, J. A. *Phys. Chem. Chem. Phys.* **2013**, *15*, 568-575.

(37) Inokuchi, Y.; Ebata, T.; Rizzo, T. R.; Boyarkin, O. V. *J. Am. Chem. Soc.* **2014**, *136*, 1815-1824.

(38) Heine, N.; Yacovitch, T. I.; Schubert, F.; Brieger, C.; Neumark, D. M.; Asmis, K. R. *J. Phys. Chem. A* **2014**, *118*, 7613-7622.

(39) Inokuchi, Y.; Ohshimo, K.; Misaizu, F.; Nishi, N. *J. Phys. Chem. A* **2004**, *108*, 5034-5040.

(40) Walters, R. S.; Pillai, E. D.; Duncan, M. A. *J. Am. Chem. Soc.* **2005**, *127*, 16599-16610.

(41) Iino, T.; Ohashi, K.; Inoue, K.; Judai, K.; Nishi, N.; Sekiya, H. *J. Chem. Phys.* **2007**, *126*, 194302.

(42) Cooper, T. E.; O'Brien, J. T.; Williams, E. R.; Armentrout, P. B. *J. Phys. Chem. A* **2010**, *114*, 12646-12655.

(43) Shin, J. W.; Hammer, N. I.; Diken, E. G.; Johnson, M. A.; Walters, R. S.; Jaeger, T. D.; Duncan, M. A.; Christie, R. A.; Jordan, K. D. *Science* **2004**, *304*, 1137-1140.

(44) Miyazaki, M.; Fujii, A.; Ebata, T.; Mikami, N. *Science* **2004**, *304*, 1134-1137.

(45) Fournier, J. A.; Johnson, C. J.; Wolke, C. T.; Weddle, G. H.; Wolk, A. B.; Johnson, M. A. *Science* **2014**, *344*, 1009-1012.

(46) Brathwaite, A. D.; Duncan, M. A. *J. Phys. Chem. A* **2013**, *117*, 11695-11703.

(47) Shishido, R.; Kawai, Y.; Fujii, A. *J. Phys. Chem. A* **2014**, *118*, 7297-7305.

(48) Reishus, K. N.; Brathwaite, A. D.; Mosley, J. D.; Duncan, M. A. *J. Phys. Chem. A* **2014**, *118*, 7516-7525.

(49) Akibo-Betts, G.; Barran, P. E.; Puskar, L.; Duncombe, B.; Cox, H.; Stace, A. J. *J. Am. Chem. Soc.* **2002**, *124*, 9257-9264.

(50) Puskar, L.; Barran, P. E.; Duncombe, B. J.; Chapman, D.; Stace, A. J. *J. Phys. Chem. A* **2005**, *109*, 273-282.

(51) McQuinn, K.; Hof, F.; McIndoe, J. S.; Chen, X. J.; Wu, G. H.; Stace, A. J. *Chem. Commun.* **2009**, 4088-4090.

(52) McCoustra, M. R. *Phys. Chem. Chem. Phys.* **2008**, *10*, 4676-4677.

(53) Marsh, B. M.; Zhou, J.; Garand, E. *J. Phys. Chem. A* **2014**, *118*, 2063-2071.

(54) Johnson, C. J.; Dzugan, L. C.; Wolk, A. B.; Leavitt, C. M.; Fournier, J. A.; McCoy, A. B.; Johnson, M. A. *J. Phys. Chem. A* **2014**, *118*, 7590-7597.

(55) Jiang, L.; Wende, T.; Bergmann, R.; Meijer, G.; Asmis, K. R. *J. Am. Chem. Soc.* **2010**, *132*, 7398-7404.

(56) Bush, M. F.; O'Brien, J. T.; Prell, J. S.; Saykally, R. J.; Williams, E. R. *J. Am. Chem. Soc.* **2007**, *129*, 1612-1622.

(57) Wong, R. L.; Paech, K.; Williams, E. R. *Int. J. Mass. Spectrom.* **2004**, *232*, 59-66.

(58) Shao, Y.; Molnar, L. F.; Jung, Y.; Kussmann, J.; Ochsenfeld, C.; Brown, S. T.; Gilbert, A. T. B.; Slipchenko, L. V.; Levchenko, S. V.; O'Neill, D. P.; DiStasio, R. A.; Lochan, R. C.; Wang, T.; Beran, G. J. O.; Besley, N. A.; Herbert, J. M.; Lin, C. Y.; Van Voorhis, T.; Chien, S. H.; Sodt, A.; Steele, R. P.; Rassolov, V. A.; Maslen, P. E.; Korambath, P. P.; Adamson, R. D.; Austin, B.; Baker, J.; Byrd, E. F. C.; Dachsel, H.; Doerksen, R. J.; Dreuw, A.; Dunietz, B. D.; Dutoi, A. D.; Furlani, T. R.; Gwaltney, S. R.; Heyden, A.; Hirata, S.; Hsu, C. P.; Kedziora, G.; Khalliulin, R. Z.; Klunzinger, P.; Lee, A. M.; Lee,

M. S.; Liang, W.; Lotan, I.; Nair, N.; Peters, B.; Proynov, E. I.; Pieniazek, P. A.; Rhee, Y. M.; Ritchie, J.; Rosta, E.; Sherrill, C. D.; Simmonett, A. C.; Subotnik, J. E.; Woodcock, H. L.; Zhang, W.; Bell, A. T.; Chakraborty, A. K.; Chipman, D. M.; Keil, F. J.; Warshel, A.; Hehre, W. J.; Schaefer, H. F.; Kong, J.; Krylov, A. I.; Gill, P. M. W.; Head-Gordon, M. *Phys. Chem. Chem. Phys.* **2006**, *8*, 3172-3191.
(59) Glendening, E. D.; Badenhoop, J. K.; Reed, A. E.; Carpenter, J. E.; Bohman, J. A.; Morales, C. M.; Weinhold, F. Theoretical Chemistry Institute, University of Wisconsin, Madison, WI, 2001.
(60) O'Brien, J. T.; Williams, E. R. *J. Phys. Chem. A* **2008**, *112*, 5893-5901.
(61) Prell, J. S.; Williams, E. R. *J. Am. Chem. Soc.* **2009**, *131*, 4110-4119.
(62) Shannon, R. D. *Acta. Crystallogr. A* **1976**, *32*, 751-767.
(63) Herzberg, G. *Infrared and Raman Spectra of Polyatomic Molecules*; Van Nostrand and Co., Inc.: Princeton, NJ, 1945; Vol. Molecular Structure and Molecular Spectra II.
(64) Cramer, C. J. *Essentials of Computational Chemistry Theories and Models*; 2 ed.; John Wiley & Sons, Ltd: West Sussex, England, 2004.
(65) Jiang, L.; Sun, S. T.; Heine, N.; Liu, J. W.; Yacovitch, T. I.; Wende, T.; Liu, Z. F.; Neumark, D. M.; Asmis, K. R. *Phys. Chem. Chem. Phys.* **2014**, *16*, 1314-1318.
(66) Brites, V.; Lisy, J. M.; Gaigeot, M. P. *J. Phys. Chem. A* **2015**, *119*, 2468-2474.
(67) Mizuse, K.; Mikami, N.; Fujii, A. *Angew. Chem. Int. Edit.* **2010**, *49*, 10119-10122.
(68) Prell, J. S.; Chang, T. M.; O'Brien, J. T.; Williams, E. R. *J. Am. Chem. Soc.* **2010**, *132*, 7811-7819.
(69) Chang, T. M.; Prell, J. S.; Warrick, E. R.; Williams, E. R. *J. Am. Chem. Soc.* **2012**, *134*, 15805-15813.
(70) Polfer, N. C. *Chem. Soc. Rev.* **2011**, *40*, 2211-2221.
(71) Prell, J. S.; Correra, T. C.; Chang, T. M.; Biles, J. A.; Williams, E. R. *J. Am. Chem. Soc.* **2010**, *132*, 14733-14735.
(72) Foster, J. P.; Weinhold, F. *J. Am. Chem. Soc.* **1980**, *102*, 7211-7218.
(73) Reed, A. E.; Curtiss, L. A.; Weinhold, F. *Chem. Rev.* **1988**, *88*, 899-926.
(74) Weinhold, F. *J. Comput. Chem.* **2012**, *33*, 2363-2379.
(75) Cramer, C. J.; Kelterer, A. M.; French, A. D. *J. Comput. Chem.* **2001**, *22*, 1194-1204.
(76) Vallejos, M. A.; Angelina, E. L.; Peruchena, N. M. *J. Phys. Chem. A* **2010**, *114*, 2855-2863.
(77) Wendler, K.; Thar, J.; Zahn, S.; Kirchner, B. *J. Phys. Chem. A* **2010**, *114*, 9529-9536.
(78) Gourlaouen, C.; Gerard, H.; Piquemal, J. P.; Parisel, O. *Chem-Eur. J.* **2008**, *14*, 2730-2743.
(79) Freda, M.; Piluso, A.; Santucci, A.; Sassi, P. *Appl. Spectrosc.* **2005**, *59*, 1155-1159.
(80) Nihonyanagi, S.; Yamaguchi, S.; Tahara, T. *J. Am. Chem. Soc.* **2014**, *136*, 6155-6158.
(81) Covert, P. A.; Jena, K. C.; Hore, D. K. *J. Phys. Chem. Lett.* **2014**, *5*, 143-148.
(82) Cooper, R. J.; Chang, T. M.; Williams, E. R. *J. Phys. Chem. A* **2013**, *117*, 6571-6579.
(83) Diken, E. G.; Hammer, N. I.; Johnson, M. A.; Christie, R. A.; Jordan, K. D. *J. Chem. Phys.* **2005**, *123*.
(84) Chang, T. M.; Cooper, R. J.; Williams, E. R. *J. Am. Chem. Soc.* **2013**, *135*, 14821-14830.
(85) Hamashima, T.; Mizuse, K.; Fujii, A. *J. Phys. Chem. A* **2011**, *115*, 620-625.
(86) Bandyopadhyay, B.; Reishus, K. N.; Duncan, M. A. *J. Phys. Chem. A* **2013**, *117*, 7794-7803.

4.6 Tables and Figures

Table 4.1. Resonance delocalization energies between donor NBO ϕ_i and acceptor NBO ϕ_j calculated by second order perturbation theory. The occupancies of the acceptor orbitals as well as their difference in energy from the donor orbitals are also shown.

Donor(i)	Acceptor(j)	Stabilization Energy (kJ/mol)	Occupancy of Acceptor	ε_j-ε_i (hartrees)
NO_3-LP_1	$6p_1$	91.6	0.123	0.39
NO_3-LP_2	$6p_1$	68.2		0.39
H_2O (1)	$6p_2$	60.1	0.098	0.63
H_2O (2)	$6p_3$	53.6	0.087	0.55
H_2O (3)	$6p_3$	47.7		0.64
H_2O (4)	$6p_2$	35.0		0.65
Pb-6*s*	$6p_1$	5.0		0.46

Table 4.2. Net atomic Mulliken charges on Pb and Sr in the calculated lowest-energy isomers of $[PbNO_3]^+(H_2O)_{2\text{-}6,8,10}$ and $[SrNO_3]^+(H_2O)_{2\text{-}6,8,10}$ at the B3LYP/aug-cc-pVDZ level of theory.

Ion	n = 2	n = 3	n = 4	n = 5	n = 6	n = 8	n = 10
$[PbNO_3]^+(H_2O)_n$	+1.34	+1.40	+1.43	+1.41	+1.46	+1.54	+1.43
$[SrNO_3]^+(H_2O)_n$	+1.97	+1.88	+1.87	+1.82	+1.76	+1.92	+2.00

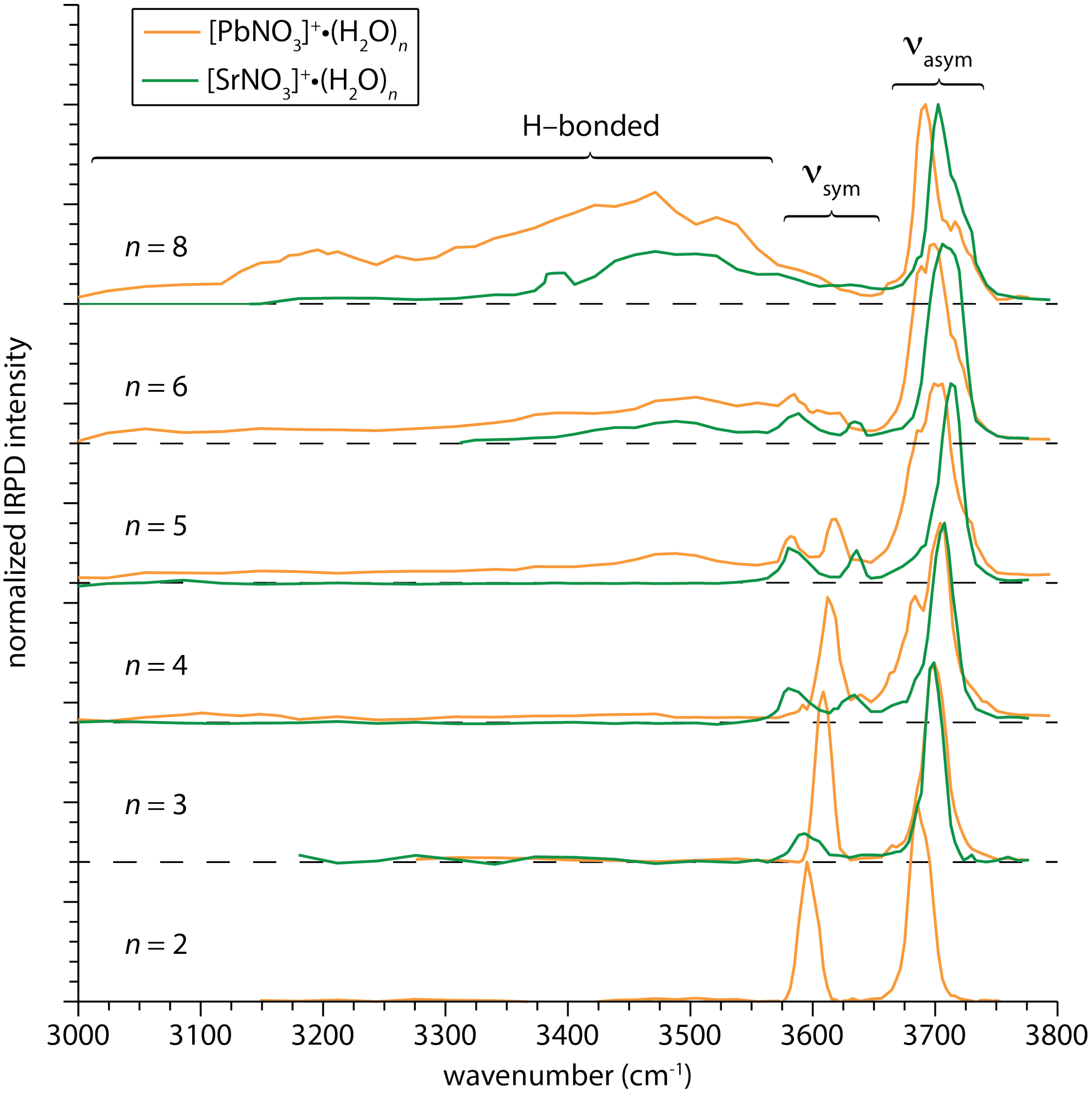

Figure 4.1. IRPD spectra of $[PbNO_3]^+(H_2O)_{2\text{-}6,8}$ and $[SrNO_3]^+(H_2O)_{3\text{-}6,8}$ measured at 133 K.

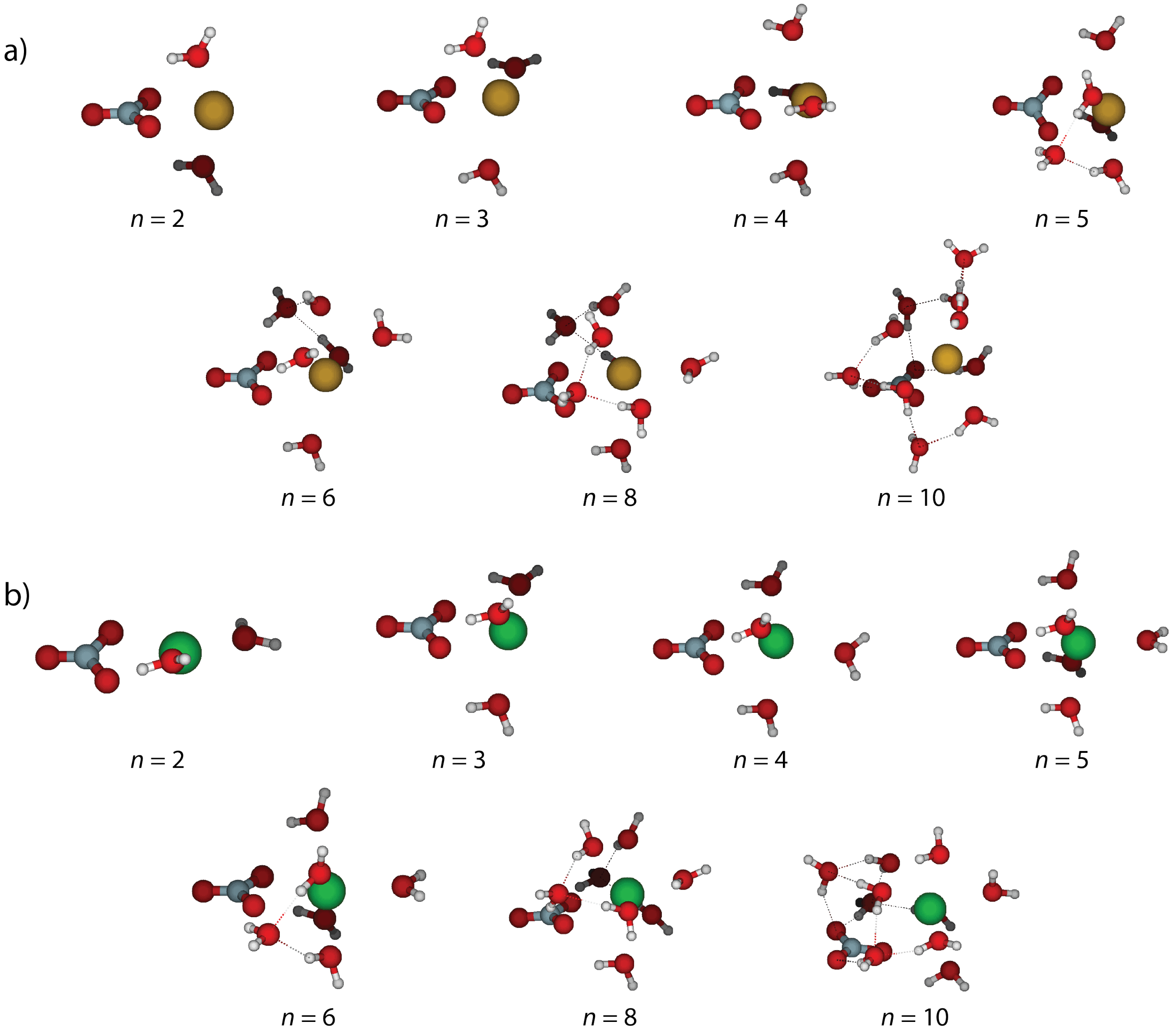

Figure 4.2. (a) Calculated lowest-energy structures at 133K of (a) $[PbNO_3]^+(H_2O)_{2\text{-}6,8,10}$ and (b) $[SrNO_3]^+(H_2O)_{2\text{-}6,8,10}$ at the B3LYP/aug-cc-pVDZ level of theory.

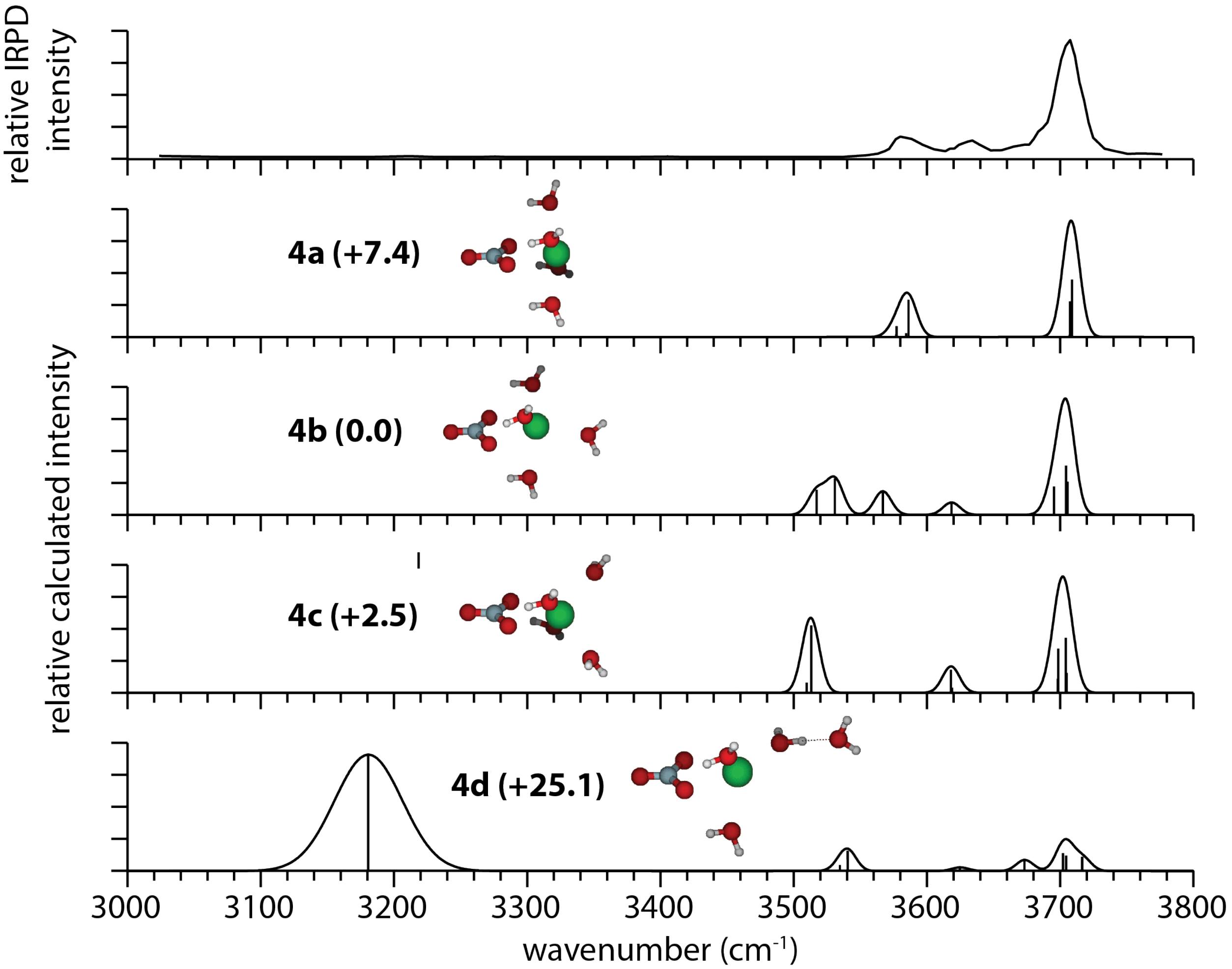

Figure 4.3. IRPD spectrum of $[SrNO_3]^+(H_2O)_4$ and calculated spectra of low-energy isomers at the B3LYP/aug-cc-pVDZ level of theory, along with their relative Gibbs free energies in kJ/mol at 133 K.

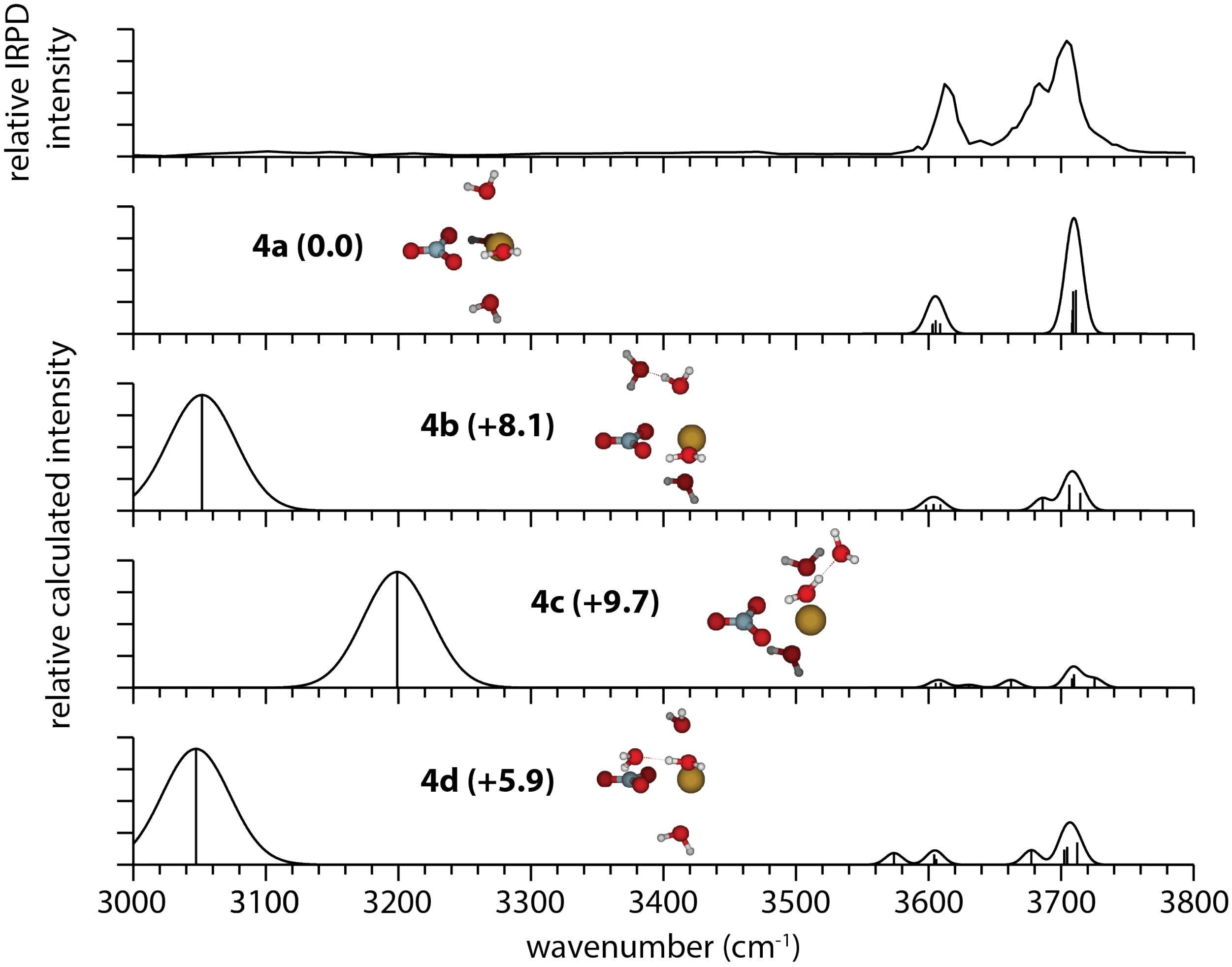

Figure 4.4. IRPD spectrum of $[PbNO_3]^+(H_2O)_4$ and calculated spectra of low-energy isomers at the B3LYP/aug-cc-pVDZ level of theory, along with their relative Gibbs free energies in kJ/mol at 133 K.

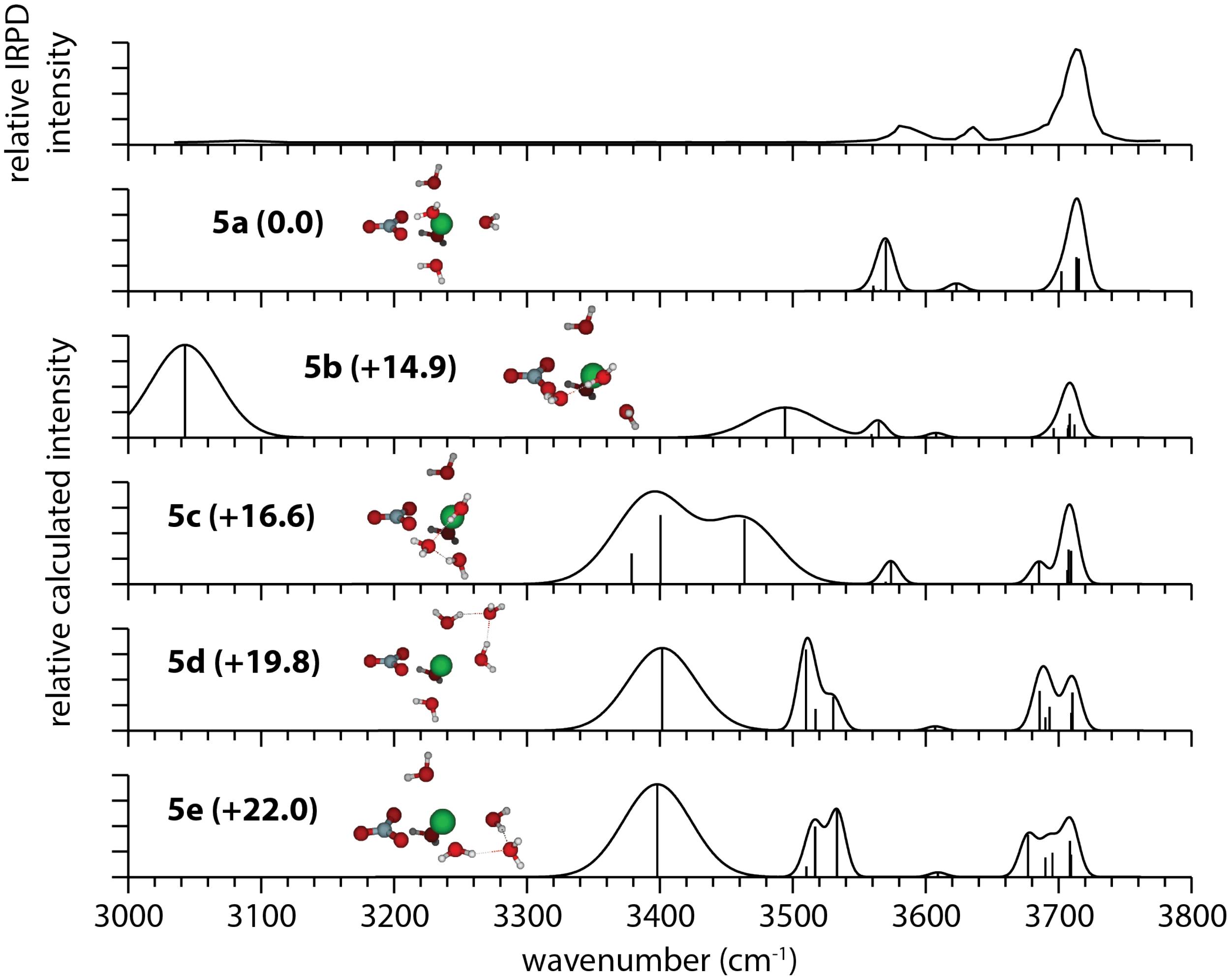

Figure 4.5. IRPD spectrum of $[SrNO_3]^+(H_2O)_5$ and calculated spectra of low-energy isomers at the B3LYP/aug-cc-pVDZ level of theory, along with their relative Gibbs free energies in kJ/mol at 133 K.

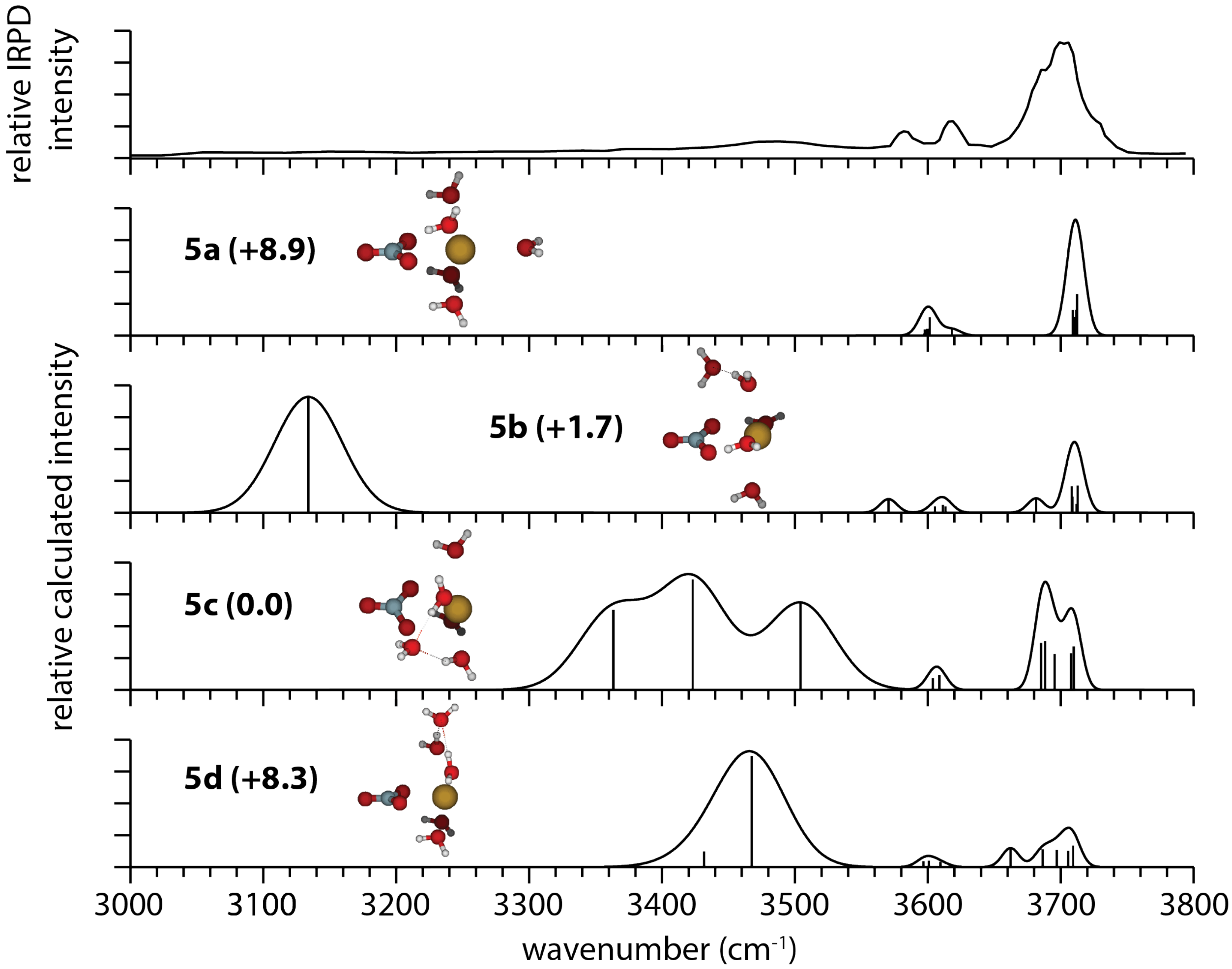

Figure 4.6. IRPD spectrum of $[PbNO_3]^+(H_2O)_5$ and calculated spectra of low-energy isomers at the B3LYP/aug-cc-pVDZ level of theory, along with their relative Gibbs free energies in kJ/mol at 133 K.

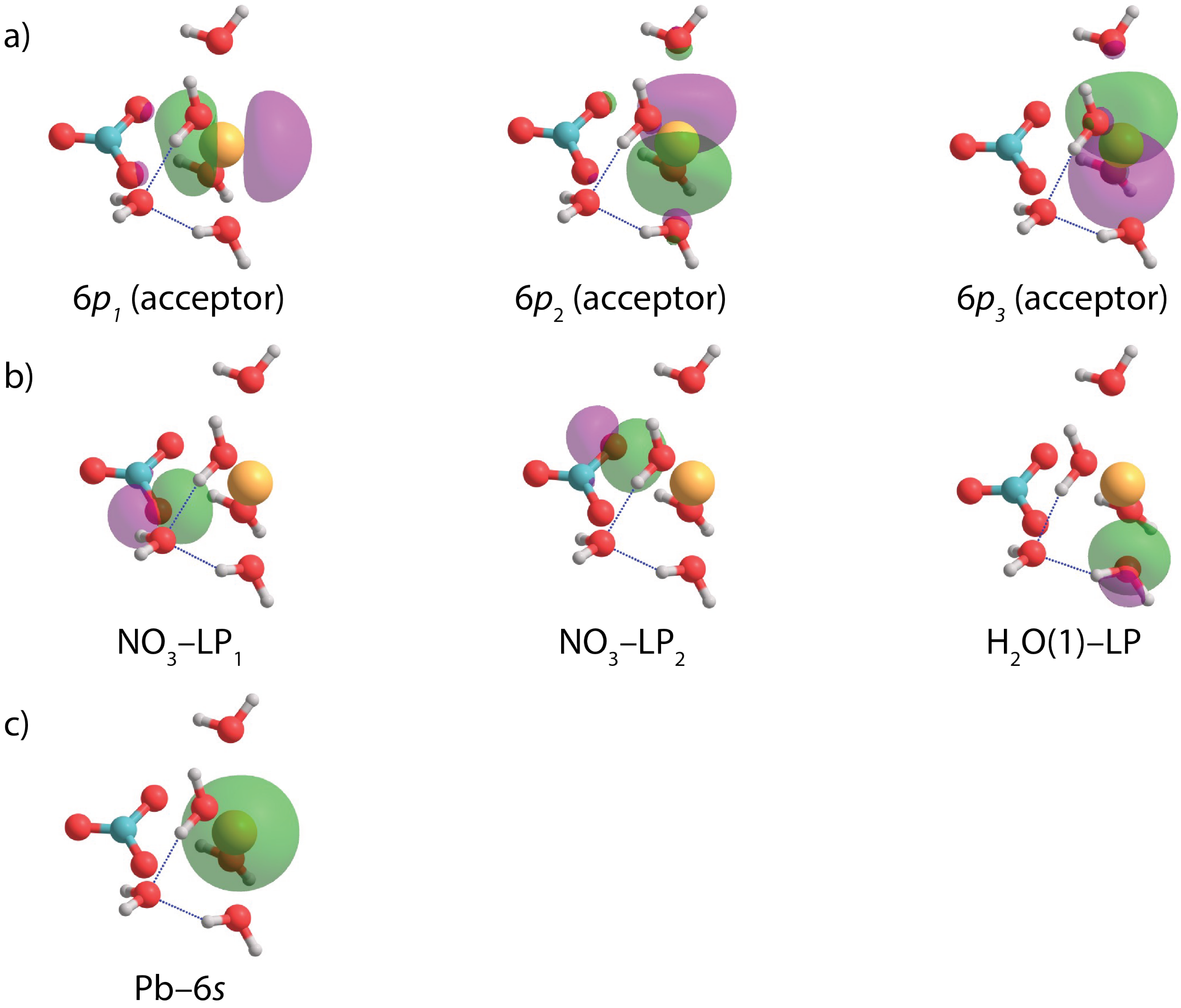

Figure 4.7. (a) Unfilled NBOs centered on Pb(II) that accept charge. (b) Filled NBOs on the nitrate and water ligands that donate charge. (c) NBO of valence 6*s* electrons on Pb(II) that has almost pure *s* character. All orbitals are plotted using an isosurface value of 0.05 e/Å^3.

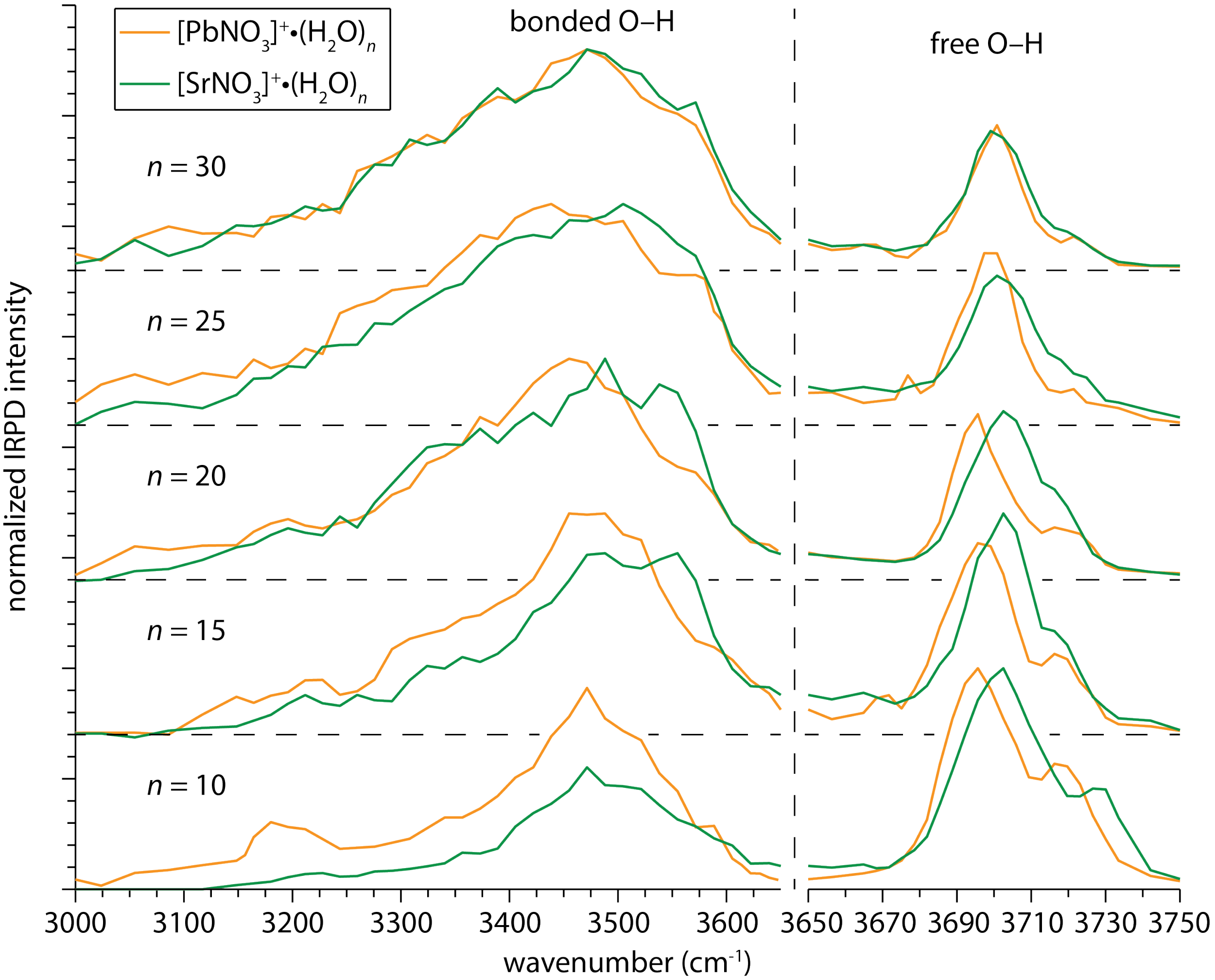

Figure 4.8. IRPD spectra of $[PbNO_3]^+(H_2O)_n$ and $[SrNO_3]^+(H_2O)_n$ for n = 10, 15, 20, 25, 30 in the free O—H (~3650–3750 cm^{-1}) and bonded O—H (~3000–3650 cm^{-1}) regions. The abscissa in the free O—H region is expanded to make the differences between these bands more clear.

Chapter 5

Delayed Onset of Crystallinity in Ion-Containing Aqueous Nanodrops

This chapter is reproduced with permission from
Cooper, R.J.; Change, T.M.; DiTucci, M.J.; Williams, E.R.
"Delayed Onset of Crystallinity in Ion-Containing Aqueous Nanodrops"
Journal of the American Chemical Society **2016**, 138, 96-99
© 2016 American Chemical Society

5.1 Introduction

Water clusters containing charged particles are involved in numerous phenomena central to atmospheric and space sciences. Ion-induced nucleation is a major pathway to the formation of aerosol particles because electrostatic forces can stabilize embryonic particles with diameters between 1–2 nm and accelerate their growth rates.[1] Upon further growth, such particles drive diverse processes ranging from ion-enhanced chemical reactions on sea spray droplets[2] to the production of ozone-depleting chlorine species on the surfaces of ice nanoparticles.[3] When confined to nanometer-sized spaces, the properties of water differ significantly from those in bulk solution owing to the large interfacial area that disrupts optimal hydrogen bonding (H-bonding).[4] In small water clusters cooled well below the solvent's bulk freezing point, the formation of crystalline ice is inhibited by the tendency for dangling O–H bonds at the surface to optimize H-bonding interactions.[5] The minimum number of water molecules needed to support crystallization within a neutral water cluster has been the subject of experimental and theoretical studies. Electron diffraction experiments[6] on water clusters formed in a free jet expansion indicate that the onset of crystallization occurs between $n = 200–1000$, and FT-IR spectra of ice nanoparticles along with calculations by Buch *et al.* are in agreement with this size range.[5a,b] A complicating factor in interpreting these experiments is that the cluster size must be estimated. This obstacle was recently surmounted by Pradzynski *et al.* who measured infrared spectra of neutral water clusters doped with sodium atoms.[7] The clusters were separated and mass analyzed after infrared-modulated photoionization. They reported that the onset of crystallization occurs at $n = 275 \pm 25$ and that the clusters are predominately crystalline by $n = 475$, the largest size investigated. The temperature of the water clusters in this experiment was estimated to be 90–115 K and the onset of crystallization may occur at smaller cluster sizes for higher temperatures.[8]

Ions are well known to reduce the freezing point of water, but the extent to which ion-induced patterning of the water molecule network disrupts crystallization within a cold nanodrop has not been previously investigated. Infrared photodissociation (IRPD) spectroscopy is a sensitive structural probe of hydrated gaseous ions, and IR spectroscopies of hydrated ions have yielded detailed structural information about how H-bond networks are arranged around ions.[9] IRPD results indicate that both the charge state[10] and size[10a] of an ion affect its hydration and that the H-bonding network of water molecules is minimally perturbed by some ions,[9d] but can be affected past the first solvation shell by others.[9e,f] Thus, one might expect that in aqueous nanodrops where an ion is internally solvated, the crystallization of water will be hindered and that this effect will be more pronounced for high valency ions. The extent to which an ion can disrupt the H-bonding network of water molecules located remotely from the ion has implications for a wide variety of phenomena, most notably Hoffmeister series effects of ions on protein solubilities.[11] Our laboratory has developed an experimental technique (see Appendix C) for studying extensively hydrated ions[9e,f,10b] in isolation at a well-defined temperature without the complicating presence of counterions. Herein, we use IRPD spectroscopy to characterize how La^{3+} perturbs the H-bonding network in $(H_2O)_n$ clusters with $n = 50–550$. La^{3+} was chosen because of its high valency and single dominant isotope, which results in improved signal-to-noise ratios for these measurements.

5.2 Results and Discussion

The electrospray-generated $La^{3+}(H_2O)_n$ clusters are trapped in the ion cell of a 7.0 T Fourier-transform ion cyclotron resonance mass spectrometer where they are thermalized at 133 K, size-selected, and photodissociated with a tunable infrared laser (for more experimental details, see Appendix C). The IRPD spectra of $La^{3+}(H_2O)_n$ (Figure 5.1) can be divided into two distinct regions. The relatively sharp resonances in the spectra between ~3650–3750 cm^{-1} arise from dangling “free” O—H oscillators on the surface of the nanodrop that are not H-bonded. The much broader bands between ~3000–3650 cm^{-1} are due to H-bonded O—H oscillators throughout the nanodrop. The ratio of the intensities of the free O—H to bonded O—H bands decreases with increasing cluster size because the fraction of water molecules on the surface of the nanodrops decreases relative to those in the interior. There is also a shift in the frequency of the free O—H band. In the spectrum of $La^{3+}(H_2O)_{50}$, this band is centered on 3683 cm^{-1}, and blue-shifts with increasing cluster size up to $n = 250$ where it has a value of 3696 cm^{-1}, close to that obtained from SFG measurements at the air-water interface.[12] The frequency shift of the free O—H band is attributable to a Stark shift from the ion’s electric field, which is more pronounced for smaller cluster sizes.[10]

Changes in the bonded O—H region with cluster size reflect size-dependent structural changes that occur in the H-bonding networks. The IRPD spectrum of $La^{3+}(H_2O)_{50}$ has a broad band centered on ~3410 cm^{-1} that is consistent with similar bands in infrared and Raman spectra of amorphous ice and liquid water that have a maximum near 3400 cm^{-1}.[13] Crystalline ice has an absorption maximum near 3200 cm^{-1},[13] a region with little intensity in the spectrum of $La^{3+}(H_2O)_{50}$. This suggests that water molecules in this cluster adopt a phase that is close to that of liquid water or amorphous ice. The intensity between 3000–3400 cm^{-1} increases with cluster size, and for $200 \leq n \leq 350$, the spectra contain one very broad (~400 cm^{-1}) symmetric band with a maximum near 3350 cm^{-1}. Studies of neutral ice nanoparticles indicate that strained subsurface crystalline ice has a spectroscopic signature similar to crystalline ice,[5a,b] and the emergence of strained ice-like water may contribute to the increased intensity between 3000–3400 cm^{-1} with increasing cluster size. At $n = 400$, there is a significant spectral change where a distinct band centered on 3220 cm^{-1} appears that is the most intense feature in the spectrum. This band, which is attributed to crystalline ice,[7] continues to grow in intensity relative to the amorphous ice band up through the largest cluster size measured at $n = 550$. The emergence of a distinct crystalline ice band at 3200 cm^{-1} was used to identify the onset of crystallinity in neutral droplets.[7] Accordingly, we conclude that the onset of crystallinity occurs at $n \approx 375$ in these ion-doped aqueous nanodrops, 100 water molecules greater than the onset of crystallinity reported for neutral water clusters at a comparable temperature.[7]

The spectral red-shift of ~200 cm^{-1} accompanying the onset of crystallinity in these $La^{3+}(H_2O)_n$ clusters is remarkably similar to that measured in temperature-dependent infrared and Raman spectra of bulk water,[13] and temperature-dependent SFG spectra at the air/water interface.[14] A similar red-shift also occurs in FT-IR spectra of ice nanoparticles as the size distribution increases from tens to thousands of water molecules.[5a] The delayed onset of crystallinity in the lanthanum-containing nanodrops relative to neutral nanodrops can be rationalized as a result of the perturbation induced by the internally solvated ion that disrupts the formation of crystalline ice in the interior of the nanodrop. The extent to which ions affect the H-bonding network of water molecules located remotely from the ion is hotly debated with reports based on femtosecond infrared,[15] terahertz absorption,[16] and Raman[17] measurements concluding that the structuring effect is limited to the first solvation shell. Our present results show that a single La^{3+} ion exerts a long-range influence on water molecules that extends well beyond the first solvation shell, consistent with IRPD studies of hydrated polyatomic anions and anionic complexes,[9e,f] dielectric relaxation spectroscopy of aqueous salt solutions,[18] and X-ray scattering measurements of long-range solvent ordering around colloidal nanoparticles.[19] The extent of ion-induced patterning of water will decrease with increasing temperature,[9f] and this may explain some of the discrepancies between conclusions drawn from our experiments and those performed near room temperature.

For a spherical nanodrop, the ratio of the area of the free O—H band (3650–3750 cm^{-1}) to the area of the bonded O—H band (3000–3650 cm^{-1}) should decrease linearly with 1/r provided that the fraction of surface water molecules with a free O—H bond remains constant. These data as a function of $n^{-1/3}$ ($\propto 1/r$) for $La^{3+}(H_2O)_n$ clusters are shown in Figure 5.2. This ratio of spectral intensities is linear for $n \geq 100$ indicating that these nanodrops are approximately spherical, consistent with transmission electron microscopy images of larger ice nanoparticles ($r \approx 15$–30 nm).[20] The exception to the linear trend is $La^{3+}(H_2O)_{50}$ for which the area under the free O—H band is anomalously large. The higher intensity of the free O—H band for this ion is attributed to the strong influence of the ion's electric field on the surface of the cluster that orients additional O—H bonds outwards.[10] The effect of the ion on the orientations of surface water molecules may also affect their spectral intensities.

In order to estimate the distance to which La^{3+} patterns the H-bonding network of water molecules located remotely from the ion, molecular dynamics simulations were performed on $Mo^{3+}(H_2O)_{550}$ at 133 K. Mo^{3+} is the largest trivalent ion parameterized in the OPLS 2005 force field and is slightly smaller than La^{3+} (see Appendix C for further computational details). From a 60 ns trajectory, 1000 structures were generated and the effect of the ion on the orientations of water molecules located at a distance *d* from the ion was evaluated by calculating the angle θ between the dipole vector of each water molecule and the vector defined by the metal–oxygen displacement (Figure 5.3, inset) for every structure. A histogram of $\langle\theta\rangle$ values as a function of distance from the metal ion for the 1000 structures is shown in Figure 5.3. Water molecules in the inner hydration shell are strongly oriented "outwards" by the ion, with $\langle\theta\rangle$ near 170°. This orientation bias decays exponentially with increasing distance from the ion up until ~14 Å where the angles becomes larger again near the surface of the nanodrop. At the surface, under-coordinated "dangling" water molecules are oriented with their O—H bonds pointing away from the ion. *Ab inito* dynamics simulations would result in a more accurate description of H-bonding interactions in these clusters, and may predict the onset of a crystalline phase, but are prohibitively expensive for clusters of this size. The initial decrease to ~14 Å is attributed to ion-induced patterning of the H-bond network in the nanodrop that decreases with distance from the ion. To characterize the spatial extent of ion-induced patterning in these nanodrops, the data for *d* < 13.5 Å were fit with an exponential function thereby excluding surface effects. The decay constant τ from the fit is 3.19 Å. When adjusted for the 2.25 Å offset between the first shell water molecules and the ion, the τ value indicates that the orientation bias of water molecules drops to ~37 % of its maximal value at a distance of 5.4 Å from the ion. This distance corresponds to the third hydration shell, as shown in the calculated radial distribution function for a representative structure of $Mo^{3+}(H_2O)_{550}$ (Figure 5.4).

The results from this dynamics simulation predict that trivalent metal ions can pattern the H-bonding network strongly out to *at least* the third hydration shell which, for Mo^{3+}, includes ~60 water molecules. The strength of this patterning effect diminishes exponentially with distance from the ion, and competition between ion-water patterning and crystallization may result in less extensive patterning than our calculations suggest. These calculations are consistent with the delayed onset of crystallinity in the $La^{3+}(H_2O)_n$ clusters deduced from the IRPD data.

Our combined experimental and theoretical results indicate that La^{3+} exerts a strong influence on the H-bonding network of water molecules located remotely from the ion, thereby frustrating crystallization in aqueous nanodrops. The extent of solvent patterning will depend on the ion charge state and to a lesser extent ion size.[10] There is some experimental evidence indicating that divalent ions can affect the structure of water outside the first solvation shell.[9e,10,18] Future investigations should provide new insights into how the crystallization process in confined nanoscale systems depends on temperature, and ion charge state and size.

5.3 References

(1) (a) Lee, S. H.; Reeves, J. M.; Wilson, J. C.; Hunton, D. E.; Viggiano, A. A.; Miller, T. M.; Ballenthin, J. O.; Lait, L. R. *Science* **2003**, *301*, 1886. (b) Yu, F. Q.; Turco, R. P. *J. Geophys. Res-Atmos.* **2001**, *106*, 4797.

(2) Knipping, E. M.; Lakin M. J.; Foster K. L. Jungwirth, P.; Tobias, D. J.; Gerber, R. J.; Dabdub, D.; Finlayson-Pitts, B. J. *Science* **2000**, *288*, 301.

(3) Gertner, B. J.; Hynes, J. T. *Science* **1996**, *271*, 1563.

(4) (a) Algara-Siller, G.; Lehtinen, O.; Wang, F. C.; Nair, R. R.; Kaiser, U.; Wu, H. A.; Geim, A. K.; Grigorieva, I. V. *Nature* **2015**, *519*, 443. (b) Levinger, N. E. *Science* **2002**, 298, 1722.

(5) (a) Buch, V.; Sigurd, B.; Paul Devlin, J.; Buck, U.; Kazimirski, J. K. *Int. Rev. Phys. Chem.* **2004**, *23*, 375. (b) Devlin, J. P.; Joyce, C.; Buch, V. *J. Phys. Chem. A* **2000**, *104*, 1974. (c) Buch, V.; Delzeit, L.; Blackledge, C.; Devlin, J. P. *J. Phys. Chem.* **1996**, *100*, 3732.
(6) (a) Torchet, G.; Schwartz, P.; Farges, J.; Deferaudy, M. F.; Raoult, B. *J. Chem. Phys.* **1983**, *79*, 6196. (b) Torchet, G., Farges, J., Deferaudy, M. F. & Raoult, B. *Ann. Phys-Paris* **1989**, *14*, 245.

(7) Pradzynski, C. C.; Forck, R. M.; Zeuch, T.; Slavicek, P.; Buck, U. *Science* **2012**, *337*, 1529.

(8) Buck, U.; Pradzynski, C. C.; Zeuch, T.; Dieterich, J. M.; Hartke, B. *Phys. Chem. Chem. Phys.* **2014**, *16*, 6859.

(9) (a) Fournier, J. A.; Johnson, C. J.; Wolke, C. T.; Weddle, G. H.; Wolk, A. B.; Johnson, M. A. *Science* **2014**, *344*, 1009. (b) Tielrooij, K. J.; Garcia-Araez, N.; Bonn, M.; Bakker, H. J. *Science* **2010**, *328*, 1006. (c) Shishido, R.; Li, Y. C.; Tsai, C. W.; Bing, F.; Fujii, A.; Kuo, J. L. *Phys. Chem. Chem. Phys.* **2015**, 17, 25863. (d) Prell, J. S.; Williams, E. R. *J. Am. Chem. Soc.* **2009**, *131*, 4110. (e) O'Brien, J. T.; Prell, J. S.; Bush, M. F.; Williams, E. R. *J. Am. Chem. Soc.* **2010**, *132*, 8248. (f) DiTucci, M. J.; Heiles, S.; Williams, E. R. *J. Am. Chem. Soc.* **2015**, *137*, 1650.

(10) (a) Prell, J. S.; O'Brien, J. T.; Williams, E. R. *J. Am. Chem. Soc.* **2011**, *133*, 4810. (b) O'Brien, J. T.; Williams, E. R. *J. Am. Chem. Soc.* **2012**, *134*, 10228.

(11) Marcus, Y. *Chem. Rev.* **2009**, *109*, 1346
(12) Ji, N.; Ostroverkhov, V.; Tian, C. S.; Shen, Y. R. *Phys. Rev. Lett.* **2008**, *100*, 096102.

(13) (a) Brubach, J. B.; Mermet, A.; Filabozzi, A.; Gerschel, A.; Roy, P. *J. Chem. Phys.* **2005**, *122*, 184509. (b) D'Arrigo, G.; Maisano, G.; Mallamace, F.; Migliardo, P.; Wanderlingh, F. *J. Chem. Phys.* **1981**, *75*, 4264.

(14) Wei, X.; Miranda, P. B.; Zhang, C.; Shen, Y. R. *Phys. Rev. B* **2002**, *66*, 085401.

(15) Omta, A. W.; Kropman, M. F.; Woutersen, S.; Bakker, H. J. *Science* **2003**, *301*, 347.

(16) (a) Funkner, S.; Niehues, G.; Schmidt, D. A.; Heyden, M.; Schwaab, G.; Callahan, K. M.; Tobias, D. J.; Havenith, M. *J. Am. Chem. Soc.* **2012**, *134*, 1030. (b) Sharma, V.; Bohm, F.; Seitz, M.; Schwaab, G.; Havenith, M. *Phys. Chem. Chem. Phys.* **2013**, *15*, 8383.

(17) Smith, J. D.; Saykally, R. J.; Geissler, P. L. *J. Am. Chem. Soc.* **2007**, *129*, 13847.

(18) Buchner, R. *Pure Appl. Chem.* **2008**, *80*, 1239.

(19) Zobel, M.; Neder, R. B.; Kimber, S. A. *Science* **2015**, *347*, 292.

(20) Delzeit, L.; Blake, D. *J. Geophys. Res.* **2001**, *106*, 33371.

5.4 Figures

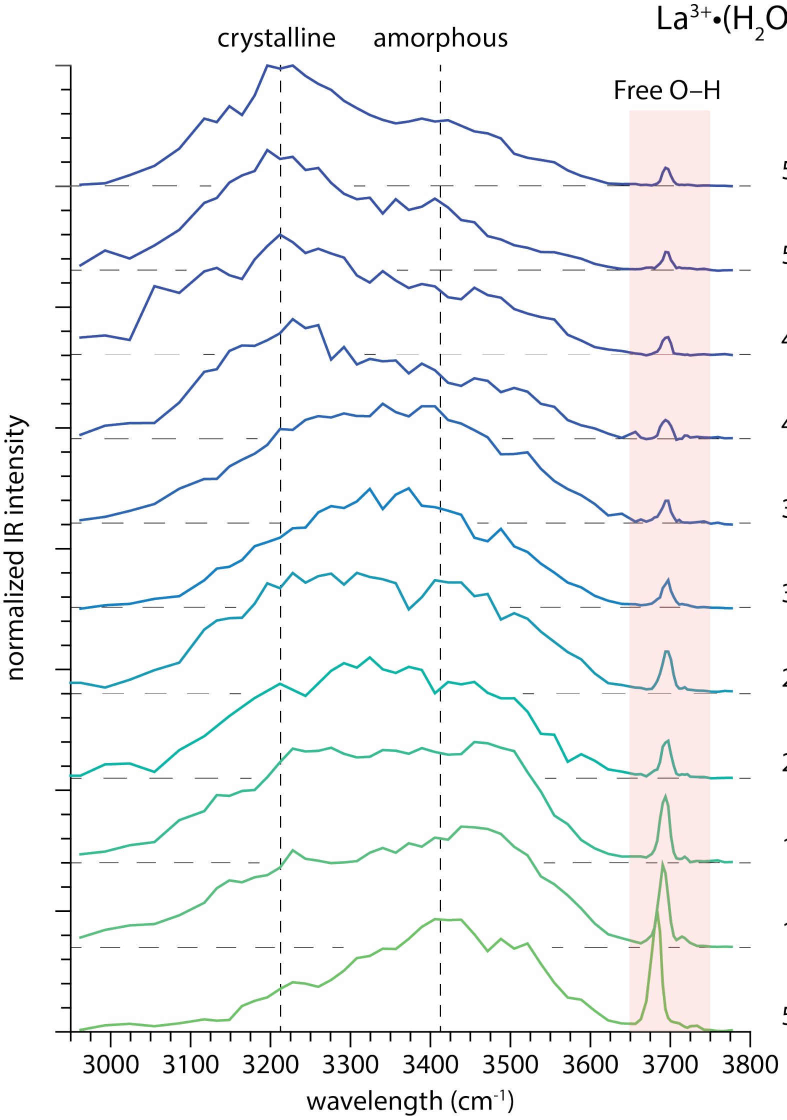

Figure 5.1. IRPD spectra of La^{3+}(H$_2$O)$_n$ for $50 \leq n \leq 550$ measured at 133 K. The sharp bands between 3650–3750 cm^{-1} correspond to free O—H stretches of water molecules located exclusively on the surface of the nanodrops, whereas the broader resonances between 3000 and 3650 cm^{-1} arise from hydrogen bonded O—H stretches throughout the clusters. Crystalline and amorphous ice bands are marked with vertical dashed lines.

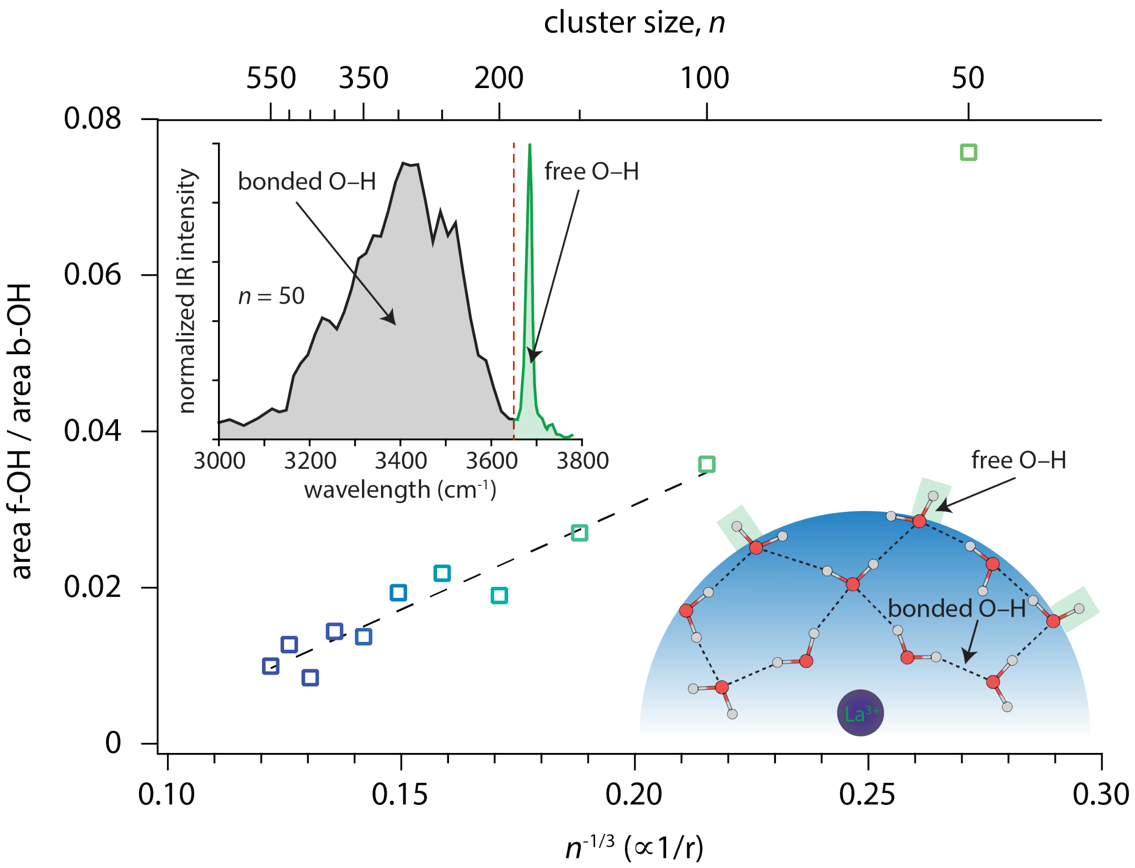

Figure 5.2. Ratio of integrated band intensities of the free O—H stretches (3650–3750 cm^{-1}) to bonded O—H stretches (3600–3650 cm^{-1}) in each $La^{3+}(H_2O)_n$ IRPD spectrum as a function of $n^{-1/3}$, which is proportional to $1/r$. The two spectral bands that are integrated are shown in the top left inset, and the bottom right inset depicts the different types of O—H stretches that give rise to these bands. The average cluster size, *n*, is indicated in the top abscissa. A linear least-squares fit ($R^2 = 0.93$) for clusters with *n* between 100 and 550 is shown by the dashed line.

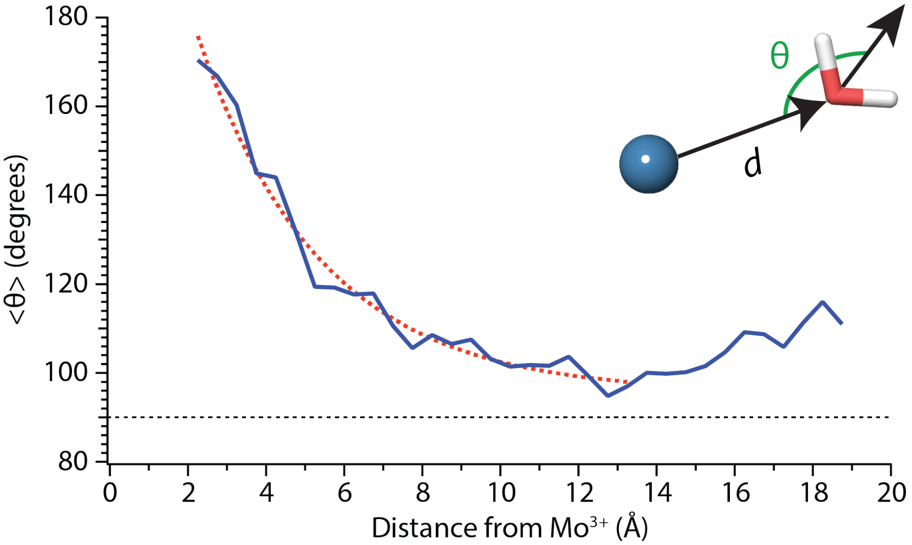

Figure 5.3. Average angle θ (shown in inset) calculated from 1000 structures of $Mo^{3+}(H_2O)_{550}$ as a function of distance from the metal ion in bin sizes of 0.5 Å. The dotted red line is an exponential fit to these data between 2.25 and 13.5 Å and the horizontal dotted black line marks <θ> = 90°.

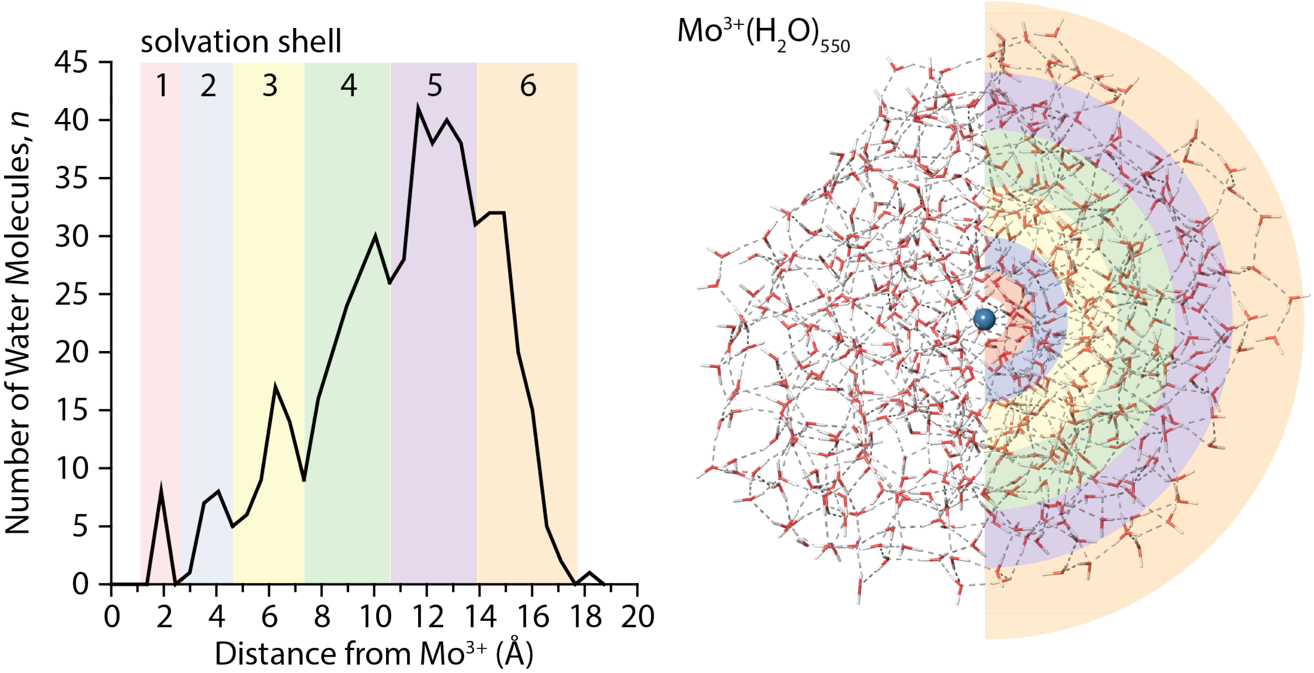

Figure 5.4. Radial distribution function of Mo^{3+}–O distances binned in 0.5 Å increments (left) for the lowest-energy structure of $Mo^{3+}(H_2O)_{550}$ (right). Minima in the distribution function indicate transitions between solvation shells, which are numbered and color-coded.

Chapter 6

Structural and Electrostatic Effects at the Surfaces of Size- and Charge-Selected Aqueous Nanodrops

This chapter is reproduced with permission from
Cooper, R.J.; O'Brien, J.T.; Chang, T.M.; Williams, E.R.
"Structural and Electrostatic Effects at the Surface of Size- and
Charge-Selected Aqueous Nanodrops"
Manuscript in preparation for submission

6.1 Introduction

Hydrated ions are ubiquitous in nature and play fundamental roles in biological and environmental phenomena. In confined nanoscale environments, interactions between ions and water molecules influence complex physicochemical processes. For example, ion channel proteins that regulate signal transduction in cells transport specific ions through cell membranes and this selectivity is based upon the size of the hydrated ion.[1-3] In the atmosphere, ion-mediated particle nucleation is a major pathway to aerosol formation.[4-6] The electrostatic forces between ions, water vapor, and other gaseous species stabilize small embryonic particles with diameters between 1–2 nm that seed the growth of aerosols which influence the climate[7,8] and human health.[9] Ion hydration also dictates many of the fundamental properties of aqueous electrolyte solutions. Perhaps the most well known example is the Hofmeister series where ions are ranked by their ability to precipitate out proteins in solution. Hofmeister orderings of ions have also been implicated in other solution phenomena, including salt solubilities[10,11] and the aqueous surface activity of ions.[12-15] Although the first reports of this ordering are over 120 years old,[16] the molecular origins of the Hofmeister series remain debated. The effects of ions on protein stability have been attributed to direct ion-protein interactions[10,17-21] as well as ion-water interactions that can alter the H-bonding network of water,[22-27] and it is unclear to what extent these proposed mechanisms contribute to the observed phenomena. Thus, an understanding of how ions affect the H-bonding network of water molecules is a prerequisite for rationalizing Hofmeister effects.

While there is consensus that ions can significantly alter the structure and dynamics of water molecules in the first hydration shell from those in bulk solution, the spatial extent of this effect remains contentiously debated. Reports based on femtosecond infrared,[28-30] X-ray absorption,[31,32] and static vibrational spectroscopy[33,34] experiments indicate that ions do not significantly affect the hydrogen bond (H-bond) network of water molecules outside the first hydration shell. In contrast, results from dielectric relaxation spectroscopy,[35] 2D IR,[36] and X-ray scattering[37] measurements suggest perturbations of solvent structure and dynamics that extent into at least the second shell. Directly comparing the results of these studies is complicated by the wide ranges of concentrations employed (~0.5–6 M) as well as the obfuscating presence of counterions.[31] Information about how ions affect the H-bond structure of water at the air-water interface has been obtained by comparing sum-frequency generation (SFG) spectra of pure water[38-41] and ionic solutions.[42-47] The signal intensity in SFG spectra of aqueous salt solutions changes with the identity and concentration of the dissolved ions, from which information about how ions affect interfacial water can be deduced. A joint experimental and theoretical study of aqueous ammonium sulfate and ammonium chloride solutions found that the structure of interfacial water depends strongly upon the charge density of the anion. The SFG signal of aqueous $(NH_4)_2SO_4$ solutions is greater than that of NH_4Cl solutions.[45] This enhancement in signal was attributed to differences in the hydration of SO_4^{2-} and Cl^-, where the strongly hydrated sulfate ion lies at one extreme end of the Hofmeister series. MD simulations indicate that SO_4^{2-} strongly interacts with water molecules in solution and is consequently depleted from the interface. This has the net effect of increasing the depth of the interfacial region, leading to an enhancement in SFG signal. In contrast, the comparatively weakly hydrated ion Cl^- is present at the interface in concentrations similar to that in bulk. SFG measurements indicate that the larger, more polarizable halides have enhanced concentrations at air-water interfaces, linking the Hofmeister behavior of these ions to their surface activity.[48] These studies demonstrate that intrinsic ion-water interactions can lead to substantial changes in the structure of aqueous interfaces.

An alternative approach to studying ion hydration is through measurements on gaseous hydrated ions where counterion effects can be studied explicitly[49,50] or can be eliminated. The effect of a single ion or electron on water structure can be investigated as a function of hydration extent ranging from a single water molecule up to hundreds of water molecules, and information about ion solvation can be obtained in the limit of infinite dilution.[51-57] Infrared photodissociation (IRPD) spectroscopy can probe the structures of numerous gas-phase hydrates, including metal ions,[58-64] anions[22,24,65-68] and protonated/ionized amino acids and peptides.[69-72] Heteroatom-hydrogen stretching frequencies are sensitive to their local H-bonding environment, and IRPD measurements have been used to elucidate detailed hydration structures of ions with up to ~20 water molecules attached. IRPD spectra can be compared under readily achievable experimental conditions to calculated absorption spectra of candidate structures to identify populations of distinct isomers in the experimental ensemble.[73-75] For more extensively hydrated ions, identifying single isomers is generally not feasible, but information about how ions affect the H-bonding network of water in nanometer-sized droplets can still be deduced from spectral signatures. On account of the large surface area-to-volume ratios of these nanodrops, their IRPD spectra contain sharp resonances from surface water molecules with hydrogen atoms that do not participate in H-bonding ("free" OH bonds) similar to those observed in SFG spectra at the air-water interface.[38-41] Free OH stretches act as antennas whose frequencies (typically ~3650–3750 cm^{-1}) are sensitive to the H-bonding environment of each water molecule as well as the electric field at a nanodrop's surface. Evidence that the multiply charged ions SO_4^{2-} and $Fe(CN)_6^{3-}$ can perturb the structure of water molecules into the second and third solvation shells has been deduced from IRPD spectra in the free OH region.[22,24] Results from IRPD spectroscopy of hydrated ions at fixed cluster size (n = 36 and 250) indicate that ion-water patterning can extend to the surface of the nanodrop leading to spectral changes in the free OH band.[23,76] The free OH stretch frequencies in these clusters depend on the electric field of the ion, and this Stark shift has been used to deduce the stretching frequencies of free OH oscillators in corresponding neutral droplets. However, a fully size-resolved investigation of how nanodrop structure evolves as a function of cluster size, ion charge state, and ion polarity has not been previously reported.

Here, we present results from IRPD spectroscopy in the free OH stretch region of $M(H_2O)_n$ where M = La^{3+}, Ca^{2+}, Na^+, Li^+, I^-, and SO_4^{2-} and n ranges from 20 water molecules up to a maximum of 550 water molecules, recorded at 133 K. The spectra show that ion charge state and polarity strongly influence H-bonding motifs of water molecules at the surfaces of the smaller nanodrops consistent with results from supporting MD simulations. For the multivalent cations, there are pronounced Stark shifts for free OH stretches of hydrates with less than ~100 water molecules which we attribute to a perturbation of solvent structure by the ion. These size-resolved measurements reveal surface curvature effects in smaller droplets that provide insights on the inherent structure of surface water in confined environments. By extrapolating our results to infinite dilution we are able to establish a precise value for the free OH stretch frequency of a neutral water molecule at the surface of water.

6.2 Experimental Methods

6.2.1 IRPD Spectroscopy. Experiments were performed using a 7.0 T Fourier transform ion cyclotron resonance (FT-ICR) mass spectrometer coupled to a tunable infrared laser. The instrument, recently upgraded from a 2.7 T magnet, is described elsewhere.[77] Briefly, hydrated ions are formed by nanoelectrospray ionization of ~5 mM solutions of $LaCl_3$, $CaCl_2$, NaCl, KI, (Sigma-Aldrich, Saint-Louis, MO) and $CuSO_4$ (Fischer Scientific, Fair Lawn, NJ) dissolved in ultrapure water (Millipore, Billerica, MA). The hydrated ions are guided by electrostatic lenses through five stages of differential pumping into the FT-ICR cell. A pulse of dry nitrogen gas (~10^{-6} Torr) is introduced into the high vacuum chamber through a piezoelectric valve to aid with the trapping and thermalization of the ions to the temperature of a copper jacket[78] surrounding the cell. The jacket is maintained at a temperature of 133 K by a regulated flow of liquid nitrogen. After accumulating ions for 5–7 s, there is a pump down delay of similar length to allow the pressure in the cell to return to $< 10^{-8}$ Torr. Precursor ions are selected using stored waveform inverse Fourier transforms. An ensemble averaging technique[79] is used for improving the signal-to-noise ratios of the spectra by mass selecting multiple precursor ions that have adjacent hydration states. For small clusters containing less than ~150 water molecules, ensembles containing 1-3 precursor ions are selected whereas for $150 \leq n < 300$ and $300 \leq n \leq 550$, ensembles containing 3-5 and 7-11 neighboring cluster sizes are used, respectively. A weighted-average cluster size is reported throughout.

The mass selected precursor ions are subsequently irradiated at specific frequencies between 3650–3750 cm^{-1} with infrared light from an OPO/OPA tabletop laser system (LaseVision, Bellevue, WA) pumped by the 1064 nm fundamental of a Nd:YAG laser (Continuum Surelight I-10, Santa Clara, CA) at a 10 Hz repetition rate. Irradiation times between 0.5–2 s are chosen to induce substantial, but not complete, fragmentation of the precursor ions that dissociate by the sequential loss of single water molecules. First-order photodissociation rate constants are calculated from the relative abundances of precursor and fragment ions and are corrected for frequency-dependent variations in laser power as well as dissociation due to blackbody radiation from the cell and copper jacket.[79]

6.2.2 Computational Chemistry. Molecular dynamics (MD) simulations of $(H_2O)_n$ and $M(H_2O)_n$ where $M = Mo^{3+}$, Ca^{2+}, Na^+, I^- and SO_4^{2-} and $20 \leq n \leq 300$ were performed using the OPLS_2005 force field implemented in MacroModel 11.2 (Schrödinger, Inc., Portland, OR). After an initial geometry relaxation with molecular mechanics, the systems were allowed to equilibrate for 10 ns using canonical ensemble stochastic dynamics at 133 K. Integration time steps of 1.5 fs were used and the SHAKE algorithm was applied to all hydrogen atoms. The final equilibrated geometries were used to run 50 ns dynamics trajectories, from which 1000 structures were saved for each ion. An in-house routine written in MATLAB (The Mathworks, Inc., Natick, MA) was used to characterize the H-bonding environments within the identified structures. From the saved .xyz coordinates, O–H•••O distances and angles were calculated for every OH bond in a given structure in order to discern free and H-bonded OH stretches. The distance cutoff for a H-bond was chosen to be 2.6 Å, and the maximum angular deviation of the O–H•••O angle from linearity was set to 60°. Identified free OH bonds were categorized according to the H-bonding environment of the parent water molecule based on the number of H-bonds it accepted and donated. For the $M(H_2O)_n$ structures where $n = 250$, the program was also used to calculate the angle θ between the dipole vector of each water molecule located at a distance d from the ion and the radial vector defined by the ion-oxygen displacement. In the case of the polyatomic ion SO_4^{2-}, the location of the ion was chosen to be its center of mass. Similar data was also calculated for $(H_2O)_{250}$ clusters using the center of mass to calculate the radial vector. The resulting distance and angle data (d, θ) from each of the 1000 structures in three trajectories was binned in 0.5 Å increments, and the average angle $<\theta>$ in each bin was calculated.

At present, infrared spectra calculated from *ab inito* methods are prohibitively expensive for the majority of cluster sizes investigated here. An alternative approach is to calculate OH stretch spectra directly from cluster geometries identified by molecular dynamics trajectories.[34,80,81] This approach, originally devised to calculate the vibrational spectrum of bulk water, is based on the proportionality between the frequency shift of an OH oscillator and the component of the local electric field projected along the OH bond vector. For each of the 1000 structures identified for a given cluster, each hydrogen and oxygen atom is assigned a charge of +0.41 and -0.82 *e*, respectively, and the ion is assigned its formal charge. From these assigned point charges, the electric field at each hydrogen atom H_i arising from the ion and all the hydrogen and oxygen atoms of *other* water molecules in the cluster is calculated. The resulting electric field vector at each H_i is then projected along the OH_i bond unit vector to yield the component of the field along the bond, E_i, in atomic units. Local OH stretch frequencies f_i (in cm^{-1}) are calculated from the mapping $f_i = 3762 - 5060 \times E_i - 86225 \times E_i^2$ where the coefficients are empirical parameters determined by fitting frequencies from *ab initio* calculations on neutral water clusters.[80,81] These uncoupled frequencies along with the intramolecular coupling constants described in ref 78 are used to calculated the coupled OH stretch frequencies for water molecule. The distribution of absorption frequencies is plotted as a histogram of the coupled OH frequencies from all 1000 structures. Relative infrared intensities are calculated from the square magnitude of the frequency-dependent transition dipole moment found in ref 78.

6.3 Results and Discussion

6.3.1 Spectral Progression of Free OH Bands. Photodissociation spectra in the free OH stretch region (3650–3750 cm^{-1}) of size-selected clusters of $M(H_2O)_n$, where M = La^{3+}, Ca^{2+}, Na^+, Li^+, I^-, and SO_4^{2-} are shown in Figures 1-4. The interpretation of these spectra is guided by two principles. First, the number of distinguishable bands is related to the heterogeneity of H-bonding environments of water molecules at the surfaces of these clusters. The frequencies of free OH stretches are exquisitely sensitive to a water molecule's H-bonding environment,[58-64,73,82,83] and the free OH stretch of a water molecule red-shifts as the water molecule's participation in H-bonding increases. Using the nomenclature where "A" denotes a H-bond accepted by a water molecule and "D" denotes a H-bond donated by a water molecule, free OH bands appear in increasing frequency following the order AAD < AD ≈ AA < A. This ordering refers to antisymmetric free OH bands that are significantly more intense and sharper than the corresponding symmetric stretches and thus more useful for structural characterization.[73] Second, the frequencies of these bands are affected by the charge, size and polarity of the ion[23,76,84] as well as the proximity of the OH oscillator to the ion.[76] Highly charged cations induce the greatest red-shift whereas anions cause these stretches to blue-shift. For ions that have the same charge state but differ in size, the magnitude of the Stark shift is greatest for the smaller ions.[76]

The spectra of $La^{3+}(H_2O)_n$ clusters for $20 \leq n \leq 550$ exhibit significant changes in both H-bonding motifs and Stark shifting as a function of cluster size (Figure 6.1). For the smallest cluster, $La^{3+}(H_2O)_{20}$, three distinct bands appear in the spectrum centered on 3665 cm^{-1}, 3685 cm^{-1} and 3720 cm^{-1}. This spectrum strongly resembles previously reported IRPD spectra of $La^{3+}(H_2O)_{17\text{-}20}$,[85] from which the lowest-energy band is assigned to AAD stretches whereas the broader band from ~3675—3700 cm^{-1} arises from AD and AA stretches that have similar frequencies at this cluster size. The highest energy band reflects a population of under-coordinated A water molecules, indicating that H-bonding between water molecules is not optimized in this cluster on account of strong interactions with La^{3+} that orient water molecules in the interior resulting in sub-optimal H-bonding at the surface. At $n = 25$, the splitting between the lower energy bands decreases resulting in one broad resonance between 3660—3680 cm^{-1} with a small shoulder at 3700 cm^{-1}. The high energy A band near 3725 cm^{-1} is still clearly visible and is in fact slightly more intense. With increasing cluster size, the spectra of these La^{3+} hydrates simplify indicating the onset of more optimal H-bonding between water molecules. The band for dangling A water molecules disappears by $n = 38$ and on the low energy side, the AAD band dominates the spectrum by $n = 48$. For larger clusters, the spectra consist of an intense AAD band with hints of a weak AD band lying about 20 cm^{-1} higher in frequency. The Stark shift of the AAD band is particularly striking in these spectra; there is ~30 cm^{-1} red-shift going from $n = 102$ to $n = 20$. This signals that the electric field of La^{3+} strongly perturbs the frequencies of free OH stretches located remotely from the ion. The Stark shift with increasing cluster size is more gradual for larger clusters, and is on the order of only a few cm^{-1}.

Similar trends, although less pronounced, are apparent in the IRPD spectra of $Ca^{2+}(H_2O)_n$ for n between 20 and 300 (Figure 6.2). The spectrum of the $n = 20$ cluster contains one broad resonance spanning 3660—3720 cm^{-1} that encompasses AAD, AD, and AA stretches. There is very weak dissociation in the region between 3725—3750 cm^{-1} consistent with a minor population of A water molecules, but clearly not to the extent observed in the small La^{3+} hydrates. This indicates that water-water interactions are more optimal in Ca^{2+} hydrates than La^{3+} hydrates, as one might expect based on the lower charge on the ion. The spectra quickly simplify with increasing cluster size and contain a dominant AAD band as well as a small AD band. The Stark shift of the AAD band is ~10 cm^{-1} for n between 20 and 100, significantly smaller than the 30 cm^{-1} Stark shift for the La^{3+} hydrates. This difference in the magnitude of the Stark shift suggests that the charge state of the hydrated ion is an important factor in Stark shifting, but that other factors, such as solvent structuring, charge transfer, and ion size also contribute to this effect.

Compared to the multivalent cations, the IRPD spectra of $Na^+(H_2O)_n$ and $Li^+(H_2O)_n$ show different size-dependent changes (Figure 6.3). For $Na^+(H_2O)_{20}$, there are two distinct bands centered on 3701 cm^{-1} and 3720 cm^{-1} corresponding to AAD and AD water molecules, respectively. The AD band decreases with cluster size, becoming only a small shoulder in spectra of clusters larger than $n = 30$. Interestingly, the AAD band blue-shifts with decreasing cluster size in striking contrast to the trends observed in the spectra of La^{3+} and Ca^{2+} hydrates. The magnitude of this Stark shift is quite small; approximately 4 cm^{-1} between $n = 30$ and 250. The simple band structure in these spectra signify that Na^+ weakly perturbs the H-bonding structure of water. Thus, the blue-shifting of the AAD band with decreasing cluster size is likely due to the surface electric field established by intrinsic structure of water in these small nanodrops. Spectra of $Li^+(H_2O)_n$ were also recorded to investigate how an ion's size affects Stark shifting and droplet structure. Li^+ has an ionic radius of 90 pm compared to 116 pm for Na^+. The lower intensity of the AD band in the spectrum $Li^+(H_2O)_{20}$ relative to that of $Na^+(H_2O)_{20}$ is on account of Li^+ forming partial clathrate structures at this "magic number" cluster size.[86] The AAD band in the spectra of $Li^+(H_2O)_n$ for $n = 20$ and 30 is red-shifted by ~ 4 cm^{-1} compared to the corresponding Na^+ spectra, consistent with the smaller ionic radius and higher charge density of Li^+. Differences between the two singly charged ions diminish with increasing cluster size; the band frequencies differ by ~ 2 cm^{-1} for $n = 50$ and < 1 cm^{-1} for $n = 80$ and 120. Thus, the identity of an ion can affect droplet structure and Stark shifting particularly at small cluster sizes and these effects become less pronounced with increasing cluster size.

Electrostatic interactions between anions and solvating water molecules lead to inherently different hydration motifs in anionic clusters, which are manifest in the IRPD spectra of $SO_4^{2-}(H_2O)_n$ and $I^-(H_2O)_n$ (Figure 6.4). For example, the spectral progression for $SO_4^{2-}(H_2O)_n$ begins at $n = 50$ because clusters smaller than $n \sim 47$ do not contain a free OH band in their IRPD spectra.[24] Water molecules in these clusters have both OH bonds oriented inwards towards the sulfate ion thereby establishing a H-bonding network that is oriented in the opposite direction to the hydration motif for nanodrops containing cations wherein the OH bonds are directed outwards away from the solvated ion. In fact, the appearance of a free OH stretching band in photodissociation spectra of hydrated multiply charged anions has been taken as a metric of the spatial extent of ion-induced patterning of the H-bond network.[22,24] This structuring effect can extend into the third solvation shell and beyond. The AAD band in the spectrum of $SO_4^{2-}(H_2O)_{50}$ appears as a broad band superimposed on the high-energy tail of dissociation from H-bonded OH stretches and grows in relative intensity with increasing cluster size. The Stark shift of this band with decreasing cluster size is clearly in the opposite direction of the multivalent cations and is similar in magnitude to the $Ca^{2+}(H_2O)_n$ clusters for $50 \leq n \leq 300$ (4 cm^{-1} for Ca^{2+} and 6 cm^{-1} for SO_4^{2-}). A similar trend is observed in the IRPD spectra of $I^-(H_2O)_n$, although for this singly charged anion, there is already a free OH band by $n = 25$ owing to weaker ion-water interactions. At common cluster sizes where spectra were recorded ($n = 70$, 140, and 250), the blue-shift in the free OH band of $I^-(H_2O)_n$ is less than that of $SO_4^{2-}(H_2O)_n$, consistent with the lower charge of the former ion.

6.3.2 Stark Shifting of Surface OH Stretches. To obtain a better understanding of how the frequencies of surface-bound free OH stretches change with cluster size, the AAD bands in the IRPD spectra in Figures 1-4 were fit with Gaussian line shapes. The resulting centroid frequencies from these fittings are shown in Figure 6.5 as a function of $n^{-2/3}$, which is proportional to $1/r^2$ where r is the radius of the droplet. This relationship between cluster size and radius holds for spherical nanodrops and there is experimental[51] and computational[22,51,76] evidence that indicates these nanodrops are approximately spherical. Within first-order perturbation theory, the Stark shift of an OH oscillator relative to its gas phase value is linearly proportional to the local electric field at the H atom projected along the OH bond.[87,88] The observed trend that free OH stretches of nanodrops containing highly charged cations redshift with decreasing cluster size (and increasing proximity to the ion) whereas nanodrops containing anions blue-shift is characteristic of Stark shifting due to the electric field of the solvated ion. However, considering that the electric field of an atomic ion drops off as $1/r^2$ one might expect a linear relationship between the frequency of surface OH oscillators and the inverse square of the cluster radius. Our results indicate that this is not necessarily the case; the measured Stark shifts of free OH stretches exhibit varying degrees of non-linear behavior as a function of $1/r^2$. This is especially apparent for hydrates of the multiply charged cations La^{3+} and Ca^{2+}. For these ions it appears that there are two regimes delimited by cluster size. Pronounced Stark shifting is observed for the smaller clusters ($n < \sim100$) followed by a transition to a regime where the Stark shifts are significantly reduced in magnitude.

For each ion besides iodide, an optimal least-squares fitting of the Stark shift data in Figure 6.5 using two lines was performed. The data for iodide are highly linear ($R^2 = 0.997$) and therefore only a single line was used for the fitting. In order to select the cluster size marking the transition between the two regimes in an unbiased way, a MATLAB script was written that evaluates all possible ways of fitting the Stark shifting data for a given ion with two lines. The best fitting was chosen to be the one that gave the smallest residuals. These linear fittings are shown in Figure 6.5 where the break in the fittings is denoted by a dashed line for smaller cluster sizes and a solid line for larger cluster sizes. The identified transition cluster size is correlated to the ion's charge ($n = 102$ for La^{3+}, $n = 100$ and 80 for Ca^{2+} and SO_4^{2-}, respectively, and $n = 36$ and 30 for Li^+ and Na^+, respectively). This suggests that the different Stark shifting regimes are related to the ion's ability to pattern the H-bonding network of water within the nanodrop. Water is a polarizable medium with a large molecular dipole moment and its structure is thus susceptible to the influence of an ion's electric field. As we will show, this patterning effect can propagate to a nanodrop's surface thereby affecting the orientations of free OH bonds at the surface. Free OH bonds that are better aligned with the radial electric field of the ion will have a greater Stark shift owing to the improved overlap, as is the case for La^{3+} and Ca^{2+} hydrates. Conversely, in nanodrops where there is poorer alignment between free OH bonds and the ion's electric field, the magnitude of the Stark shift will be smaller. This may explain why the measured Stark shifts in smaller $SO_4^{2-}(H_2O)_n$ clusters are less pronounced; structures obtained from MD simulations indicate that OH bonds in these cluster are directed more tangentially to the nanodrop's surface (*vide infra*). Interestingly, the Stark shift data for $La^{3+}(H_2O)_n$ transitions at $n = 102$ and it has previously been reported that the onset of crystallinity in size-selected La^{3+}–doped aqueous nanodrops is delayed by ~100 water molecules compared to neutral water clusters.[51] The frustration of crystallinity was attributed La^{3+} disrupting optimal H-bonding of water molecules located remotely from the ion. Our present results for La^{3+} are consistent with this finding and indicate a relationship between Stark shifting and the ability of an ion to perturb the H-bonding network of water.

The precise control of nanodrop size and charge made possible by mass-selection also precludes measurements on neutral droplets with this technique. However, some properties of neutral droplets and bulk water can be inferred from the linear fit parameters of the Stark shifting data. For example, the slopes of the fits to the larger clusters of the monovalent cations (m = 51.2 and m = 8.4 for Na^+ and Li^+, respectively) are positive, indicating a blue-shift with decreasing cluster size despite the positive charge on these ions. There is a much larger blue-shift in the slope of the linear fit to iodide (m = 111.6). Interpolation between the measured slopes for Na^+ and I^- at large cluster size yields a positive slope (m = 81.4) that indicates the free

OH stretches of neutral water clusters blue-shift with decreasing cluster size (Figure 6.5, dotted line). In the absence of an ion, a Stark shift could arise from electric fields generated by the intrinsic structure of interfacial water. At the bulk air-water interface, the electric field can have a non-zero component directed in the surface normal direction owing to the net dipolar orientation of water molecules. This establishes a surface potential at the interface, where a positive value indicates a net orientation of water molecule hydrogen atoms towards the bulk and a negative value indicates that water molecules tend to orient their hydrogen atoms towards the vapor phase.[89] Although the surface potential of liquid water cannot be measured directly, experiments on dilute ionic solutions indicate that it has a small positive value (~0.1 V).[90,91] Our Stark shift data suggest that the electric fields at the surfaces of neutral nanodrops become increasingly negative with decreasing cluster size, which corresponds to an increasingly positive surface potential. As the nanodrops decrease in size, the surface area-to-volume ratio sharply increases and OH bonds at the surface may be reoriented to optimize H-bonding. It is therefore reasonable that the surface potential of water appears to vary with the surface curvature.

Extrapolation of the linear fits of the Stark shift data for large clusters to infinite cluster size yields AAD free OH stretch frequencies that range from 3696.5 – 3701.0 cm^{-1}. This narrow range of frequencies should bracket the frequencies of the corresponding surface OH stretch in bulk water. Previous extrapolations of the neutral AAD free OH stretch from IRPD data of hydrated ions at fixed cluster size yielded estimates of 3704.9–3709.7 cm^{-1} for clusters with 36 water molecules[76] and 3699.3–3700.1 cm^{-1} for clusters with 250 water molecules.[23] Because these estimates pertain to the free OH stretches of water molecules in a neutral droplet of corresponding size they include surface curvature effects. The range of frequencies reported here (3696.5–3701.0 cm^{-1}) is therefore the first measurement of the AAD free OH stretch frequency of neutral bulk water from IRPD spectroscopy, which under these conditions should be similar to a linear spectroscopy. This range of values agrees well with those from SFG measurements of bulk aqueous interfaces near room temperature (3690–3705 cm^{-1}).[38,39,41,45,46] The free OH band in SFG spectra appears as a broad feature (~50 cm^{-1} fwhm) and its frequency and line shape is dependent upon the polarization and orientations of the incident laser beams resulting in a greater uncertainty in determining free OH stretching frequencies. Under the cold conditions of our experiment, the phase of water in the interior of the droplet begins to resemble crystalline ice for $n \geq 375$.[51] Thus, for the larger $La^{3+}(H_2O)_n$ clusters, the free OH band should more closely correspond to bulk ice although there is no significant change in the frequency or line shape of the free OH bands for these cluster sizes. This is consistent with temperature dependent SFG studies reporting that the free OH stretch frequency is insensitive to temperature suggesting a strong resemblance between the surfaces of ice and liquid water.[39,92,93]

6.3.3 Modeled Stark Shifting. Simulated infrared spectra of $M(H_2O)_n$ for M = Mo^{3+}, Ca^{2+}, Na^+, I^-, and SO_4^{2-} with n ranging between 20 and 300 water molecules were calculated directly from cluster geometries generated by dynamics simulations. Spectra of cluster sizes larger than $n \sim 300$ could not be calculated due to MATLAB memory restrictions and Mo^{3+} was substituted for La^{3+} because it is the largest trivalent ion parameterized in the software used for the dynamics simulations. The electrostatic model used to calculate these spectra, originally implemented in simulations of bulk water, is based on the relationship between the stretching frequency of an OH oscillator and the local electric field it experiences.[80,81] This model was previously adapted by our group to calculate infrared spectra of various hydrated gaseous ions at fixed cluster size ($n = 36$).[76] Here, we use the simulated spectra to investigate the physical origins of the frequency shifts of the free OH bands as a function of cluster size. For each cluster simulated, the resulting infrared spectra have resonances arising from both free and bonded OH stretches. The AAD bands in the free OH region were fit with a Gaussian line shape and centroid frequencies extracted from these fits are plotted as a function of $n^{-2/3}$, which is proportional to $1/r^2$ (Figure 6.6). Results from this model reproduce several of the experimental trends. The direction of Stark shifting is clearly correlated to ion polarity with the free OH stretching frequencies of cationic clusters red-shifting and anionic clusters blue-shifting with decreasing cluster size. The free OH frequencies of the neutral water cluster do not change significantly with cluster size, but for the smaller $(H_2O)_{50}$ and $(H_2O)_{20}$ clusters are blue-shifted by ~3 cm^{-1} and 6 cm^{-1}, respectively, compared to the larger water clusters. In ion-containing clusters, the extent of Stark shifting is dependent upon the charge state of the ion where the largest frequency shifts are calculated for the multivalent ions (Mo^{3+}, Ca^{2+}, and SO_4^{2-}). These results provide further evidence that OH stretching frequencies are sensitive to the local electric field experienced by the hydrogen atoms in these clusters. The magnitude of the Stark shifts calculated for these clusters is greater than what is observed in experiment. For example, the experimental frequency shift of the AAD band in $La^{3+}(H_2O)_n$ clusters between $n = 20$ and 300 is ~30 cm^{-1} whereas the calculated shift for this size range is ~60 cm^{-1}. Overall, the calculated frequencies agree fairly closely with the experimental frequencies and on average deviate by ~14 cm^{-1}. Extrapolations of the IRPD data to infinite cluster size give free OH stretch frequencies centered on ~3698 cm^{-1} whereas the modeled data is centered on ~3715 cm^{-1}. Thus, this simple electrostatic model can account for the major experimental trends in Stark shifting with ion charge state.

There are also significant differences between the simulated and experimental Stark shifting data. For Mo^{3+} and Ca^{2+}, the calculated Stark shifting is overall more linear as a function of $1/r^2$ than what is observed in experiment. The calculated frequency shifts are overall much more linear than the experimental data, and do not replicate the pronounced Stark shifting at small cluster size for La^{3+} and Ca^{2+}. Additionally, the slope of the simulated $Na^+(H_2O)_n$ data is opposite in sign to what is observed in experiment suggesting that the models used in these simulations do not accurately account for H-bonding and other noncovalent interactions in these clusters. The limitations of the point charge model used to simulate infrared spectra have been described in detail elsewhere.[76] Briefly, because all atoms are considered as fixed point charges, neither charge transfer nor polarization effects are accounted for. Although this model includes the effects of intramolecular coupling between OH stretches, it does not explicitly include intramolecular coupling to the H_2O bend or intermolecular coupling between water molecules. The insights gained from this model, despite its shortcomings, calls for the development of more sophisticated electrostatic models that take into account vibrational coupling/polarization effects.

6.3.4 Hydration Motifs and Droplet Composition. MD simulations were used to investigate how ions affect the H-bonding network of water in aqueous nanodrops. Representative low energy structures identified from MD simulations at 133 K for $M(H_2O)_{50}$ where M = Mo^{3+}, Ca^{2+}, Na^+, Li^+, I^- and SO_4^{2-} show significant differences in ion hydration motifs (Figure 6.7). The structure of $Mo^{3+}(H_2O)_{50}$ is highly puckered due to strong Mo^{3+}–water interactions that result in under-coordinated water molecules at the surface of the cluster, including three dangling A water molecules. The large number of free OH bonds (29) indicates that H-bonding between water molecules is not optimized. As the charge state of the solvated cation decreases, so too does the ion's effect on the solvent. The calculated structures of

$Ca^{2+}(H_2O)_{50}$ and $Na^{+}(H_2O)_{50}$ have 21 and 17 free OH bonds, respectively, with the latter structure being more compact in shape as H-bonding between water molecules is better optimized in clusters with lower charge. Fundamentally different hydration motifs are apparent in the structures of the anions $I^{-}(H_2O)_{50}$ and $SO_4^{2-}(H_2O)_{50}$ where OH bonds are directed inwards towards the solvated ion resulting in fewer free OH bonds at the surfaces of the clusters (7 and 2, respectively) and more optimized water-water H-bonding. The small number of free OH oscillators for $SO_4^{2-}(H_2O)_{50}$ is consistent with the very weak free OH band in the IRPD spectrum of this cluster. Additionally, the tangential orientation of these free OH bonds with respect to the cluster surface is consistent with a decrease in the magnitude of Stark shifting for smaller $SO_4^{2-}(H_2O)_n$ clusters on account of poorer overlap with the ion's electric field.

A more comprehensive view of how nanodrop composition changes with ion charge state and extent of hydration for $M(H_2O)_n$ where M = Mo^{3+}, Ca^{2+}, Na^{+}, I^{-}, and SO_4^{2-} and n = 50, 100, and 250 is given in Table 6.1, which shows the relative populations of different types free OH stretches taken from averages over 1000 calculated structures. Free OH stretches are categorized according to the H-bonding environment of the associated water molecule as either AAD, AD, or "UC" where the last category encompasses all types of under-coordinated water molecules (A, AA, D). There are two general trends in these data. First, for a fixed cluster size, the droplets containing high valency ions have the greatest percentage of under-coordinated surface water molecules. Second, for a given ion, as the droplet size increases, H-bonding at the surface of the cluster becomes more optimal as indicated by the greater percentage of AAD and AD stretches. This trend is most striking for the $Mo^{3+}(H_2O)_n$ hydrates where for n = 50, nearly 30% of free OH stretches arise from dangling A and AA water molecules. As the size of the nanodrop increases, the solvated ion's influence on the surface structure diminishes and by n = 250, there are virtually no under-coordinated water molecules. This is qualitatively consistent with the IRPD spectra of $La^{3+}(H_2O)_n$ insofar as the spectra of smaller cluster sizes ($n \leq 38$) have A and AA bands that are not observed in the spectra of the larger clusters. We note that the populations of different free OH stretches taken from these calculations cannot be used to directly predict band intensities because the transition dipole moments of the stretches are not taken into account. For the anionic clusters, the hydration motif is reversed and even at the smallest cluster size (n = 50), there are no under-coordinated water molecules. Yet the surfaces are still strained; $SO_4^{2-}(H_2O)_{50}$ has on average only 1.1 free OH bonds owing to the strong effect of SO_4^{2-} on surface waters. For both cationic and anionic clusters with 250 water molecules attached, the relative populations of AAD and AD stretches become nearly equal as the effect of an ion on nanodrop surface structure diminishes. Interestingly, although the H-bonding environments of free OH stretches become similar at n = 250 the percentage of OH groups that are free OH stretches remains dependent upon the identity of the ion (La^{3+}: 11%, Ca^{2+}: 9%, Na^{+}: 8%, I^{-}: 8%, SO_4^{2-}: 4%) consistent with a previous IRPD study that compared band intensities in detail at this cluster size.[23] These results provide further evidence that ion-water interactions established in the interior of the nanodrop give rise to hydration patterns that propagate out to the nanodrop's surface.

Perturbations of surface water structure must ultimately arise from the effects of solvated ions on the H-bonding network of water in the interior of the nanodrop. Information about the extent of ion-induced patterning was estimated from MD simulations of the n = 250 clusters for Mo^{3+}, Ca^{2+}, Na^{+}, I^{-}, and SO_4^{2-}, as well as $(H_2O)_{250}$ clusters. The average orientations of the dipole moments of water molecules, $<\theta>$, are shown a function of distance d from the ion in Figure 6.8 as solid lines. For the neutral water clusters, the orientation data is plotted as a function of distance from the center-of -mass of the cluster. These data show that the orientations of water molecules within the nanodrop are strongly influenced by both ion charge state and polarity. In the cationic nanodrops, water molecules are oriented "outwards" away from the ion and this patterning effect is strongest for water molecules located closest to the ion. Similar trends are observed for the anions, but in these nanodrops water molecules are oriented "inwards" such that the OH bonds point towards the anion. For the neutral nanodrops, the orientations of water molecules in the interior of the droplet are more randomly distributed. In order to characterize the spatial extent of ion-induced patterning within the nanodrops, these data were fit with exponential functions for $d \leq 12$ Å (dashed lines), where the cutoff distance was chosen to exclude surface effects on water orientation.[51] The fits of the Na^+ and I^- data indicate that the influence of these ions on the orientations of water molecules decays quickly with distance and is weak beyond distances corresponding to the first hydration shell, consistent with reports that these ions minimally perturb the structure of water.[23,76] In contrast, the patterning effect for Mo^{3+} as well as Ca^{2+} and SO_4^{2-} is significantly stronger and can extend up to ~1 nm into the nanodrop. These findings are consistent with changes in Stark shifting arising from a solvent patterning effect. For all of the ions, the simulations suggest that hydration motifs established around the solvated ion can propagate out to the nanodrop's surface.

6.4 Conclusions

The confined environments of aqueous nanodrops serve as ideal systems in which to study the effect of a single ion on the H-bond network of water. Structural changes in size- and charge-selected nanodrops were investigated with IRPD spectroscopy on $M(H_2O)_n$ clusters for M = La^{3+}, Ca^{2+}, Na^+, Li^+, I^-, and SO_4^{2-} with up to 550 water molecules attached. Spectral signatures in the free OH region originating from surface-bound water molecules show that multiply charged ions can significantly influence hydration motifs in these nanodrops. For hydrates of La^{3+} and Ca^{2+}, there are bands corresponding to under-coordinated A and AA water molecules in spectra of the smaller clusters ($n <$ ~40) indicating that strong ion-water interactions disrupt optimal H-bonding between water molecules. Intrinsically different interactions between anions and water molecules leads to the suppression of free OH stretches in the smaller anionic clusters. The dependence of nanodrop structure on ion charge state and polarity is supported by molecular dynamics simulations, which indicate that hydration motifs established around the ion in the interior of the nanodrop can propagate to the nanodrop's surface even for distances exceeding 1 nm.

The frequency shift of the AAD band in the IRPD spectra of these clusters depends upon ion charge state, ion polarity, and droplet size. This is consistent with a Stark shift due to the electric field generated by the ion. Free OH bands red-shift in aqueous nanodrops containing multiply charged cations and blue-shift in nanodrops containing anions, and this trend is reproduced by a computationally inexpensive electrostatic model for simulating infrared spectra of these clusters. The magnitude of Stark shifting becomes greater with increasing ion charge and decreasing ionic radius. The small blue shift of the free OH bands in IRPD spectra of $Na^+(H_2O)_n$ and $Li^+(H_2O)_n$ clusters with decreasing cluster size despite the positive charge of the ions suggests that the intrinsic structure of water in small nanodrops generates a negative electric field at the nanodrop surface. The interpolated Stark shifts for neutral water clusters indicate that the surface potential of water becomes increasingly positive with decreasing cluster size. To our knowledge, this is the first evidence that water clusters containing tens to hundreds of water molecules have established surface potentials, which is a topic that has recently been debated.[91]

In addition, extrapolations of the Stark shifting data to infinite cluster size and thus infinite dilution yield to our knowledge the most precise assignment of the free OH stretching frequency at the surface of liquid water (3696.5 – 3701.0 cm^{-1}). This method accounts for surface curvature effects in nanodrops of finite size and is significantly more precise than values derived from SFG measurements.

The experimental Stark shifting data exhibit varying degrees of non-linearity that is more pronounced for ions with a greater charge density and are best fit by two lines. This effect is especially prominent for smaller $La^{3+}(H_2O)_n$ and $Ca^{2+}(H_2O)_n$ clusters, where the slope of Stark shifting is greater in clusters with less than ~100 water molecules. We attribute this effect to the polarization of water molecules surrounding the solvated ion, which leads to structural changes at the nanodrop surface. Surface free OH bonds that are oriented along the ion's electric field will exhibit more pronounced Stark shifting, as is the case for hydrates of La^{3+} and Ca^{2+}. Our data suggests that multiply charged cations can affect the H-bond network of water molecules at distances corresponding to at least the third hydration shell. This long-range pattering effect has previously been demonstrated for a variety of multiply charged anions where the appearance of a free OH band at large cluster size indicates the weakening of ion-water interactions. For cations, free OH bonds are intrinsically directed away from the ion even at small cluster size and so this observable cannot be used to deduce solvent patterning effects. The pronounced changes in Stark shifting for cations reported here provide a distinct spectroscopic signature for the spatial extent of ion-water interactions in these nanodrops.

Our results reveal that the charge, polarity, and size of an ion can induce hydration motifs in aqueous nanodrops that extend out to the droplets' surfaces. These findings provide new insights into ion hydration and the structure of water in confined environments, which are important for a variety of physical properties including Hofmeister effects. The experimental results also provide stringent benchmarks for theoretical modeling of ion hydration, and our limited success in using simple electrostatic models to simulate Stark shifting in these clusters calls for the development of more sophisticated electrostatic models that can reproduce phenomena related to ion solvation with greater accuracy.

6.5 References

(1) Payandeh, J.; Scheuer, T.; Zheng, N.; Catterall, W. A. *Nature* **2011**, *475*, 353-359.

(2) Zhou, Y. F.; Morais-Cabral, J. H.; Kaufman, A.; MacKinnon, R. *Nature* **2001**, *414*, 43-48.

(3) Doyle, D. A.; Cabral, J. M.; Pfuetzner, R. A.; Kuo, A. L.; Gulbis, J. M.; Cohen, S. L.; Chait, B. T.; MacKinnon, R. *Science* **1998**, *280*, 69-77.

(4) Lee, S. H.; Reeves, J. M.; Wilson, J. C.; Hunton, D. E.; Viggiano, A. A.; Miller, T. M.; Ballenthin, J. O.; Lait, L. R. *Science* **2003**, *301*, 1886-1889.

(5) Kulmala, M. *Science* **2003**, *302*, 1000-1001.

(6) Yu, F. Q.; Turco, R. P. *J. Geophys. Res-Atmos.* **2001**, *106*, 4797-4814.

(7) Ramanathan, V.; Crutzen, P. J.; Kiehl, J. T.; Rosenfeld, D. *Science* **2001**, *294*, 2119-2124.

(8) Charlson, R. J.; Schwartz, S. E.; Hales, J. M.; Cess, R. D.; Coakley, J. A., Jr.; Hansen, J. E.; Hofmann, D. J. *Science* **1992**, *255*, 423-430.

(9) Davidson, C. I.; Phalen, R. F.; Solomon, P. A. *Aerosol Sci. Tech.* **2005**, *39*, 737-749.

(10) Collins, K. D. *Methods* **2004**, *34*, 300-311.

(11) Collins, K. D. *Biophys. J.* **1997**, *72*, 65-76.

(12) Jubb, A. M.; Hua, W.; Allen, H. C. *Annu. Rev. Phys. Chem.* **2012**, *63*, 107-130.

(13) Jungwirth, P.; Winter, B. *Annu. Rev. Phys. Chem.* **2008**, *59*, 343-366.

(14) Petersen, P. B.; Saykally, R. J. *Annu. Rev. Phys. Chem.* **2006**, *57*, 333-364.

(15) Jungwirth, P.; Tobias, D. J. *Chem. Rev.* **2006**, *106*, 1259-1281.

(16) Kunz, W.; Henle, J.; Ninham, B. W. *Curr. Opin. Colloid. In.* **2004**, *9*, 19-37.

(17) Jungwirth, P.; Cremer, P. S. *Nat. Chem.* **2014**, *6*, 261-263.

(18) Freire, M. G.; Neves, C. M. S. S.; Silva, A. M. S.; Santos, L. M. N. B. F.; Marrucho, I. M.; Rebelo, L. P. N.; Shah, J. K.; Maginn, E. J.; Coutinho, J. A. P. *J. Phys. Chem. B* **2010**, *114*, 2004-2014.

(19) Uejio, J. S.; Schwartz, C. P.; Duffin, A. M.; Drisdell, W. S.; Cohen, R. C.; Saykally, R. J. *Proc. Natl. Acad. Sci. U.S.A.* **2008**, *105*, 6809-6812.

(20) Chen, X.; Yang, T.; Kataoka, S.; Cremer, P. S. *J. Am. Chem. Soc.* **2007**, *129*, 12272-12279.

(21) Zhang, Y. J.; Cremer, P. S. *Curr. Opin. Chem. Biol.* **2006**, *10*, 658-663.

(22) DiTucci, M. J.; Heiles, S.; Williams, E. R. *J. Am. Chem. Soc.* **2015**, *137*, 1650-1657.

(23) O'Brien, J. T.; Williams, E. R. *J. Am. Chem. Soc.* **2012**, *134*, 10228-10236.

(24) O'Brien, J. T.; Prell, J. S.; Bush, M. F.; Williams, E. R. *J. Am. Chem. Soc.* **2010**, *132*, 8248-8249.

(25) Marcus, Y. *Chem. Rev.* **2009**, *109*, 1346-1370.

(26) Scott, J. N.; Nucci, N. V.; Vanderkooi, J. M. *J. Phys. Chem. A* **2008**, *112*, 10939-10948.

(27) Nucci, N. V.; Vanderkooi, J. M. *J. Mol. Liq.* **2008**, *143*, 160-170.

(28) Tielrooij, K. J.; van der Post, S. T.; Hunger, J.; Bonn, M.; Bakker, H. J. *J. Phys. Chem. B* **2011**, *115*, 12638-12647.

(29) Omta, A. W.; Kropman, M. F.; Woutersen, S.; Bakker, H. J. *Science* **2003**, *301*, 347-349.

(30) Omta, A. W.; Kropman, M. F.; Woutersen, S.; Bakker, H. J. *J. Chem. Phys.* **2003**, *119*, 12457-12461.

(31) Schwartz, C. P.; Uejio, J. S.; Duffin, A. M.; Drisdell, W. S.; Smith, J. D.; Saykally, R. J. *Chem. Phys. Lett.* **2010**, *493*, 94-96.

(32) Cappa, C. D.; Smith, J. D.; Messer, B. M.; Cohen, R. C.; Saykally, R. J. *J. Phys. Chem. B* **2006**, *110*, 5301-5309.
(33) Lin, Y. S.; Auer, B. M.; Skinner, J. L. *J. Chem. Phys.* **2009**, *131*, 144511.
(34) Smith, J. D.; Saykally, R. J.; Geissler, P. L. *J. Am. Chem. Soc.* **2007**, *129*, 13847-13856.
(35) Buchner, R. *Pure Appl. Chem.* **2008**, *80*, 1239-1252.
(36) Fournier, J. A.; Carpenter, W.; De Marco, L.; Tokmakoff, A. *J. Am. Chem. Soc.* **2016**, *138*, 9634-9645.
(37) Zobel, M.; Neder, R. B.; Kimber, S. A. *Science* **2015**, *347*, 292-294.
(38) Ji, N.; Ostroverkhov, V.; Tian, C. S.; Shen, Y. R. *Phys. Rev. Lett.* **2008**, *100*, 096102.
(39) Shen, Y. R.; Ostroverkhov, V. *Chem. Rev.* **2006**, *106*, 1140-1154.
(40) Richmond, G. L. *Chem. Rev.* **2002**, *102*, 2693-2724.
(41) Du, Q.; Superfine, R.; Freysz, E.; Shen, Y. R. *Phys. Rev. Lett.* **1993**, *70*, 2313-2316.
(42) Covert, P. A.; Jena, K. C.; Hore, D. K. *J. Phys. Chem. Lett.* **2014**, *5*, 143-148.
(43) Jubb, A. M.; Hua, W.; Allen, H. C. *Accounts Chem. Res.* **2012**, *45*, 110-119.
(44) Gopalakrishnan, S.; Liu, D. F.; Allen, H. C.; Kuo, M.; Shultz, M. J. *Chem. Rev.* **2006**, *106*, 1155-1175.
(45) Gopalakrishnan, S.; Jungwirth, P.; Tobias, D. J.; Allen, H. C. *J. Phys. Chem. B* **2005**, *109*, 8861-8872.
(46) Raymond, E. A.; Richmond, G. L. *J. Phys. Chem. B* **2004**, *108*, 5051-5059.
(47) Shultz, M. J.; Schnitzer, C.; Simonelli, D.; Baldelli, S. *Int. Rev. Phys. Chem.* **2000**, *19*, 123-153.
(48) Liu, D. F.; Ma, G.; Levering, L. M.; Allen, H. C. *J. Phys. Chem. B* **2004**, *108*, 2252-2260.
(49) Donald, W. A.; Leib, R. D.; Demireva, M.; Williams, E. R. *J. Am. Chem. Soc.* **2011**, *133*, 18940-18949.
(50) Cooper, R. J.; Heiles, S.; Williams, E. R. *Phys. Chem. Chem. Phys.* **2015**, *17*, 15963-15975.
(51) Cooper, R. J.; DiTucci, M. J.; Chang, T. M.; Williams, E. R. *J. Am. Chem. Soc.* **2016**, *138*, 96-99.
(52) Servage, K. A.; Fort, K. L.; Silveira, J. A.; Shi, L.; Clemmer, D. E.; Russell, D. H. *J. Am. Chem. Soc.* **2015**, *137*, 8916-8919.
(53) Servage, K. A.; Silveira, J. A.; Fort, K. L.; Russell, D. H. *J. Phys. Chem. Lett.* **2014**, *5*, 1825-1830.
(54) Mizuse, K.; Fujii, A. *Chem. Phys.* **2013**, *419*, 2-7.
(55) Griffin, G. B.; Young, R. M.; Ehrler, O. T.; Neumark, D. M. *J. Chem. Phys.* **2009**, *131*, 194302.
(56) Asmis, K. R.; Santambrogio, G.; Zhou, J.; Garand, E.; Headrick, J.; Goebbert, D.; Johnson, M. A.; Neumark, D. M. *J. Chem. Phys.* **2007**, *126*.
(57) Lee, S. W.; Freivogel, P.; Schindler, T.; Beauchamp, J. L. *J. Am. Chem. Soc.* **1998**, *120*, 11758-11765.
(58) Ke, H.; van der Linde, C.; Lisy, J. M. *J. Phys. Chem. A* **2015**, *119*, 2037-2051.
(59) Sweeney, A. F.; O'Brien, J. T.; Williams, E. R.; Armentrout, P. B. *Int. J. Mass. Spectrom.* **2015**, *378*, 270-280.
(60) Marsh, B. M.; Voss, J. M.; Zhou, J.; Garand, E. *Phys. Chem. Chem. Phys.* **2015**, *17*, 23195-23206.
(61) O'Brien, J. T.; Williams, E. R. *J. Phys. Chem. A* **2011**, *115*, 14612-14619.

(62) Carnegie, P. D.; Bandyopadhyay, B.; Duncan, M. A. *J. Phys. Chem. A* **2011**, *115*, 7602-7609.

(63) Cooper, T. E.; O'Brien, J. T.; Williams, E. R.; Armentrout, P. B. *J. Phys. Chem. A* **2010**, *114*, 12646-12655.

(64) Bush, M. F.; O'Brien, J. T.; Prell, J. S.; Wu, C. C.; Saylkally, R. J.; Williams, E. R. *J. Am. Chem. Soc.* **2009**, *131*, 13270-13277.

(65) Wolke, C. T.; Menges, F. S.; Totsch, N.; Gorlova, O.; Fournier, J. A.; Weddle, G. H.; Johnson, M. A.; Heine, N.; Esser, T. K.; Knorke, H.; Asmis, K. R.; McCoy, A. B.; Arismendi-Arrieta, D. J.; Prosmiti, R.; Paesani, F. *J. Phys. Chem. A* **2015**, *119*, 1859-1866.

(66) Roscioli, J. R.; Diken, E. G.; Johnson, M. A.; Horvath, S.; McCoy, A. B. *J. Phys. Chem. A* **2006**, *110*, 4943-4952.

(67) Robertson, W. H.; Johnson, M. A. *Annu. Rev. Phys. Chem.* **2003**, *54*, 173-213.

(68) Wende, T.; Heine, N.; Yacovitch, T. I.; Asmis, K. R.; Neumark, D. M.; Jiang, L. *Phys. Chem. Chem. Phys.* **2016**, *18*, 267-277.

(69) Schmidt, J.; Kass, S. R. *J. Phys. Chem. A* **2013**, *117*, 4863-4869.

(70) Nagornova, N. S.; Rizzo, T. R.; Boyarkin, O. V. *Science* **2012**, *336*, 320-323.

(71) Bush, M. F.; Prell, J. S.; Saykally, R. J.; Williams, E. R. *J. Am. Chem. Soc.* **2007**, *129*, 13544-13553.

(72) Blom, M. N.; Compagnon, I.; Polfer, N. C.; von Helden, G.; Meijer, G.; Suhai, S.; Paizs, B.; Oomens, J. *J. Phys. Chem. A* **2007**, *111*, 7309-7316.

(73) Cooper, R. J.; Heiles, S.; DiTucci, M. J.; Williams, E. R. *J. Phys. Chem. A* **2014**, *118*, 5657-5666.

(74) Inokuchi, Y.; Ebata, T.; Rizzo, T. R.; Boyarkin, O. V. *J. Am. Chem. Soc.* **2014**, *136*, 1815-1824.

(75) Fournier, J. A.; Johnson, C. J.; Wolke, C. T.; Weddle, G. H.; Wolk, A. B.; Johnson, M. A. *Science* **2014**, *344*, 1009-1012.

(76) Prell, J. S.; O’Brien, J. T.; Williams, E. R. *J. Am. Chem. Soc.* **2011**, *133*, 4810-4818.

(77) Bush, M. F.; O'Brien, J. T.; Prell, J. S.; Saykally, R. J.; Williams, E. R. *J. Am. Chem. Soc.* **2007**, *129*, 1612-1622.

(78) Wong, R. L.; Paech, K.; Williams, E. R. *Int. J. Mass. Spectrom.* **2004**, *232*, 59-66.

(79) Prell, J. S.; O'Brien, J. T.; Williams, E. R. *J. Am. Soc. Mass. Spectr.* **2010**, *21*, 800-809.

(80) Yang, M.; Skinner, J. L. *Phys. Chem. Chem. Phys.* **2010**, *12*, 982-991.

(81) Auer, B. M.; Skinner, J. L. *J. Chem. Phys.* **2008**, *128*.

(82) Fournier, J. A.; Wolke, C. T.; Johnson, M. A.; Odbadrakh, T. T.; Jordan, K. D.; Kathmann, S. M.; Xantheas, S. S. *J. Phys. Chem. A* **2015**, *119*, 9425-9440.

(83) Shin, J. W.; Hammer, N. I.; Diken, E. G.; Johnson, M. A.; Walters, R. S.; Jaeger, T. D.; Duncan, M. A.; Christie, R. A.; Jordan, K. D. *Science* **2004**, *304*, 1137-1140.

(84) Carnegie, P. D.; Bandyopadhyay, B.; Duncan, M. A. *J. Phys. Chem. A* **2008**, *112*, 6237-6243.

(85) Bush, M. F.; Saykally, R. J.; Williams, E. R. *J. Am. Chem. Soc.* **2008**, *130*, 9122-9128.

(86) Cooper, R. J.; Chang, T. M.; Williams, E. R. *J. Phys. Chem. A* **2013**, *117*, 6571-6579.

(87) Fecko, C. J.; Eaves, J. D.; Loparo, J. J.; Tokmakoff, A.; Geissler, P. L. *Science* **2003**, *301*, 1698-1702.

(88) Eaves, J. D.; Tokmakoff, A.; Geissler, P. L. *J. Phys. Chem. A* **2005**, *109*, 9424-9436.

(89) Sokhan, V. P.; Tildesley, D. J. *Mol. Phys.* **1997**, *92*, 625-640.

(90) Randles, J. E. B. *Phys. Chem. Liq.* **1977**, *7*, 107-179.
(91) Fawcett, W. R. *Langmuir* **2008**, *24*, 9868-9875.
(92) Nagata, Y.; Hasegawa, T.; Backus, E. H.; Usui, K.; Yoshimune, S.; Ohto, T.; Bonn, M. *Phys. Chem. Chem. Phys.* **2015**, *17*, 23559-23564.
(93) Wei, X.; Miranda, P. B.; Zhang, C.; Shen, Y. R. *Phys. Rev. B* **2002**, *66*, 085401.

6.6 Tables and Figures

	Mo^{3+}	Ca^{2+}	Na^{+}	I^{-}	SO_4^{2-}
$M(H_2O)_{50}$					
% AAD	61	76	76	93	43
% AD	10	17	24	7	57
% UC	29	7	0	0	0
$M(H_2O)_{100}$					
% AAD	71	84	89	87	59
% AD	9	15	11	13	41
% UC	20	1	0	0	0
$M(H_2O)_{250}$					
% AAD	85	84	86	88	78
% AD	15	16	14	12	22
% UC	0	0	0	0	0

Table 6.1. Relative populations of different types of free OH stretches in calculated structures of $M(H_2O)_n$ where M = Mo^{3+}, Ca^{2+}, Na^+, I^-, and SO_4^{2-} for n = 50, 100, and 250. The category of stretches labeled as "UC" includes A, AA, and D stretches arising from under-coordinated water molecules.

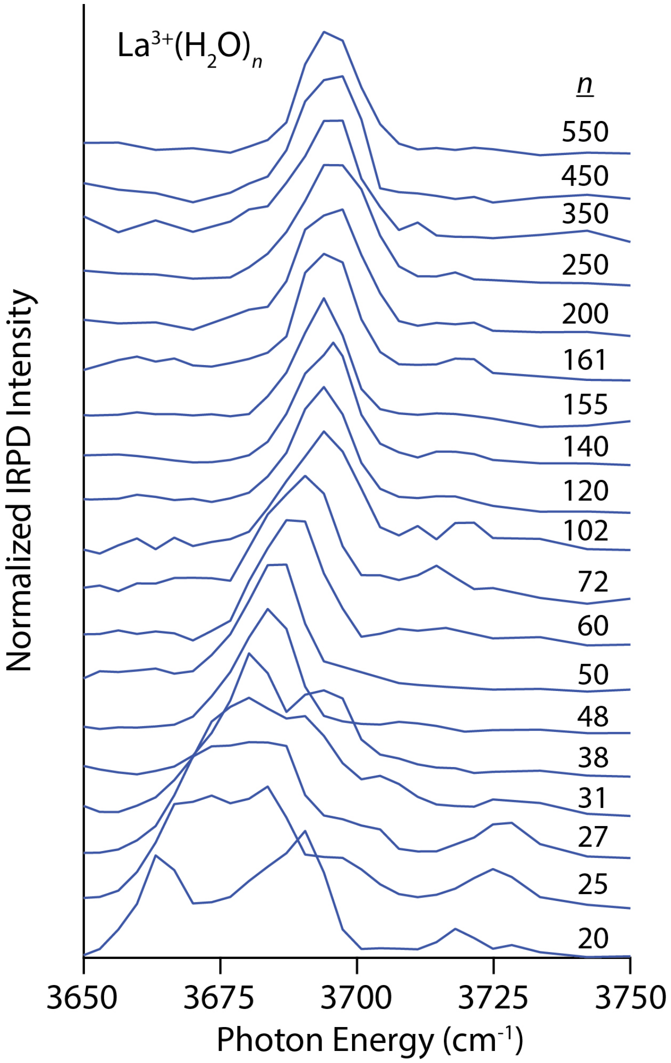

Figure 6.1. IRPD spectra of $La^{3+}(H_2O)_n$ for $23 \leq n \leq 550$ measured at 133 K.

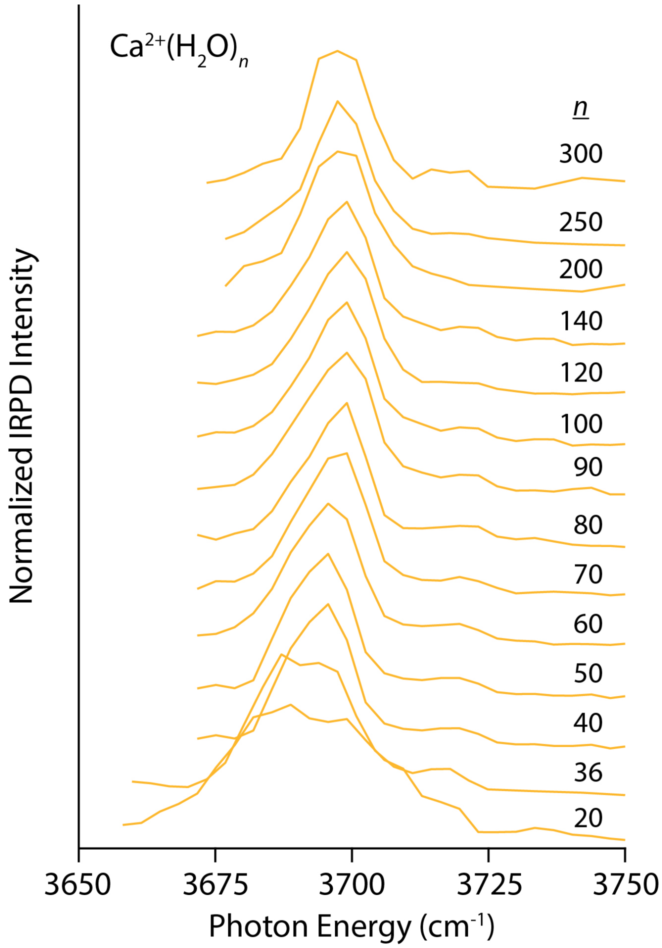

Figure 6.2. IRPD spectra of $Ca^{3+}(H_2O)_n$ for $20 \leq n \leq 300$ measured at 133 K.

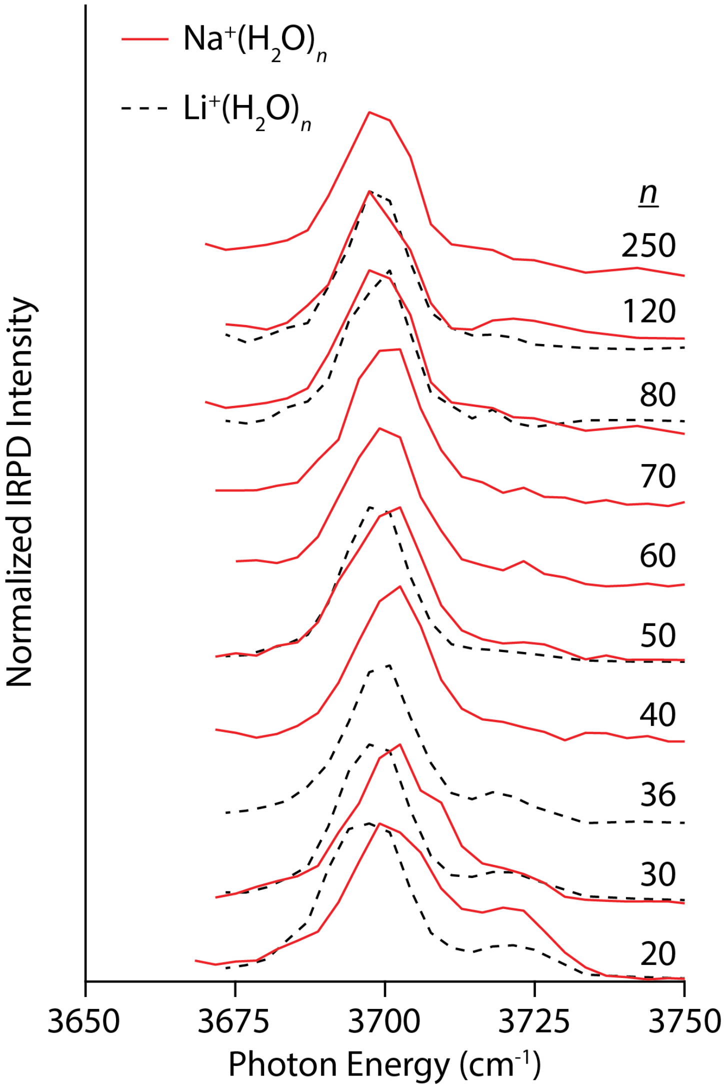

Figure 6.3. IRPD spectra of $Na^+(H_2O)_n$ (solid red lines) and $Li^+(H_2O)_n$ (dashed black lines) for $20 \leq n \leq 250$ and $20 \leq n \leq 120$, respectively, measured at 133 K.

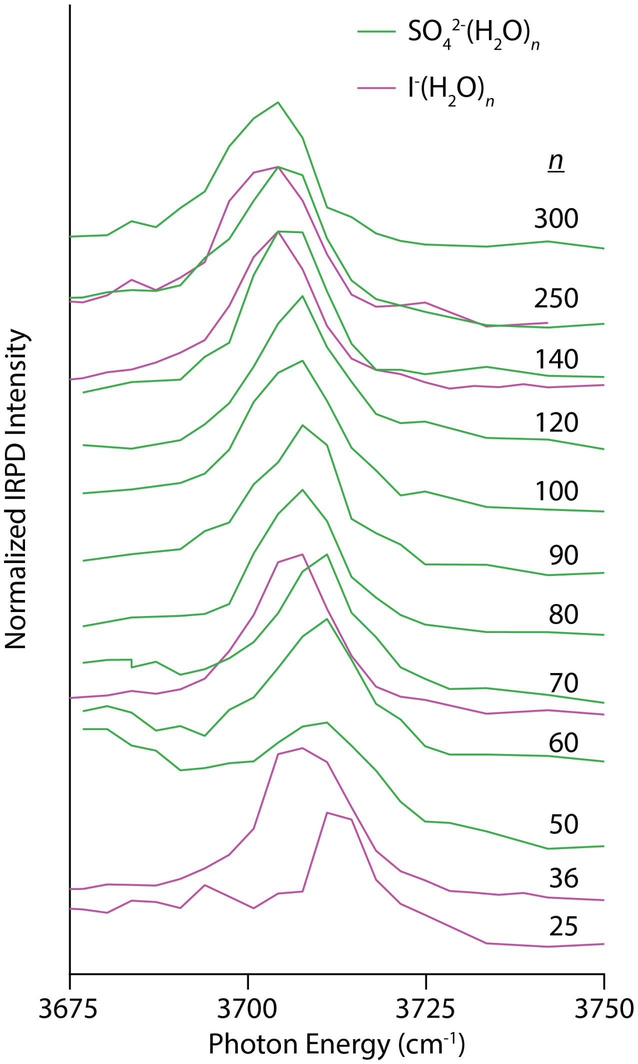

Figure 6.4. IRPD spectra of SO4^{2-}(H_2O)$_n$ (solid green lines) and I$^-$(H_2O)$_n$ (solid magenta lines) for 50 ≤ n ≤ 250 and 25 ≤ n ≤ 250, respectively, measured at 133 K.

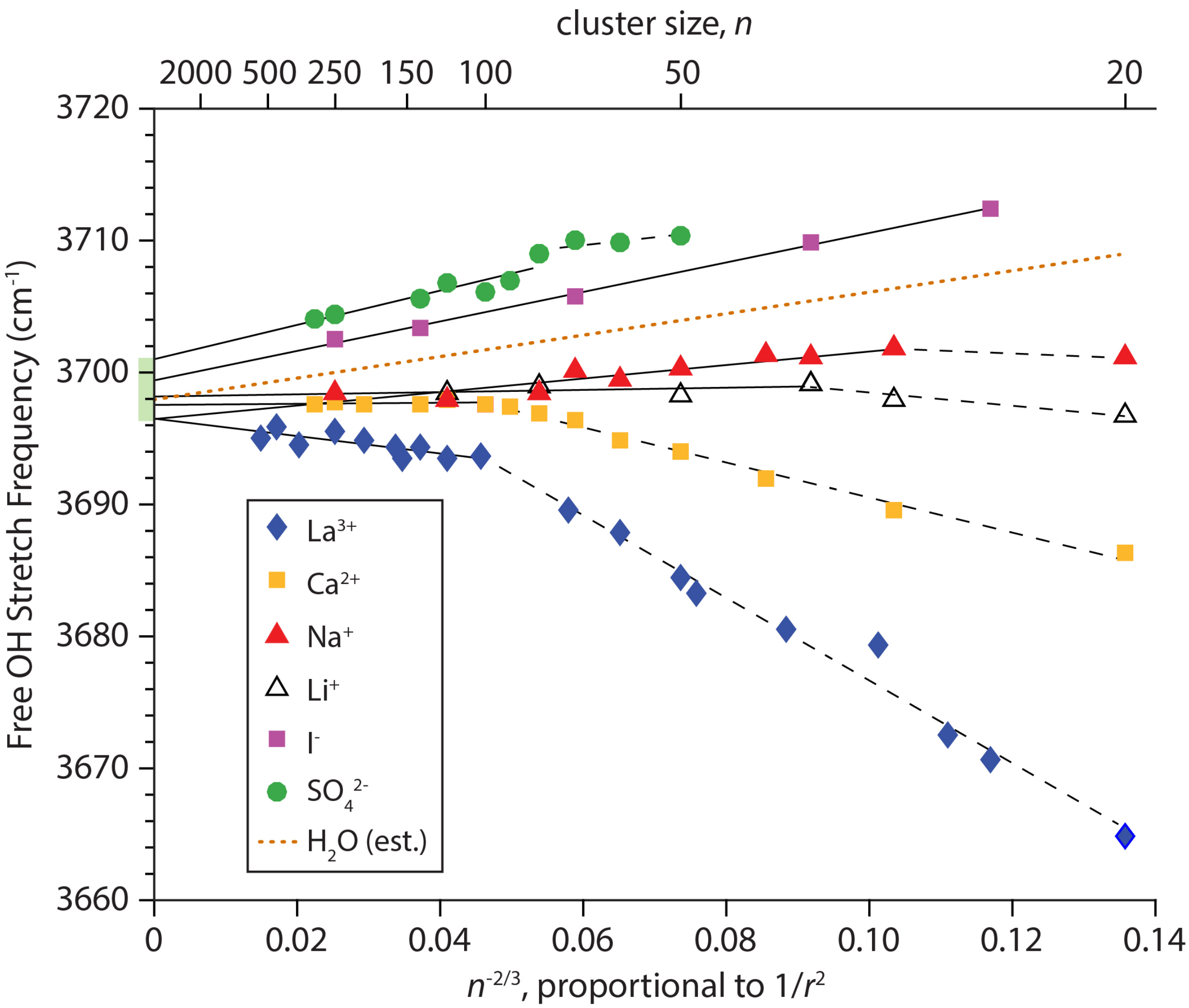

Figure 6.5. Fitted centroid frequencies of the AAD free OH bands for $M(H_2O)_n$ where M = La^{3+}, Ca^{2+}, Na^+, Li^+, I^- and SO_4^{2-} as a function of $n^{-2/3}$, which is proportional to $1/r^2$ where r is the droplet radius. For ions where the observed Stark shift does not linearly depend on the ion's electric field strength, separate linear fits are shown for the larger and smaller cluster sizes as solid and dashed lines, respectively. The extrapolated range of free OH frequencies at infinite cluster size spans 4.5 cm^{-1} and is shown as a green shaded rectangle. Free OH stretching frequencies of neutral $(H_2O)_n$ clusters interpolated from the measured Na^+ and I^- data are shown as a dotted brown line.

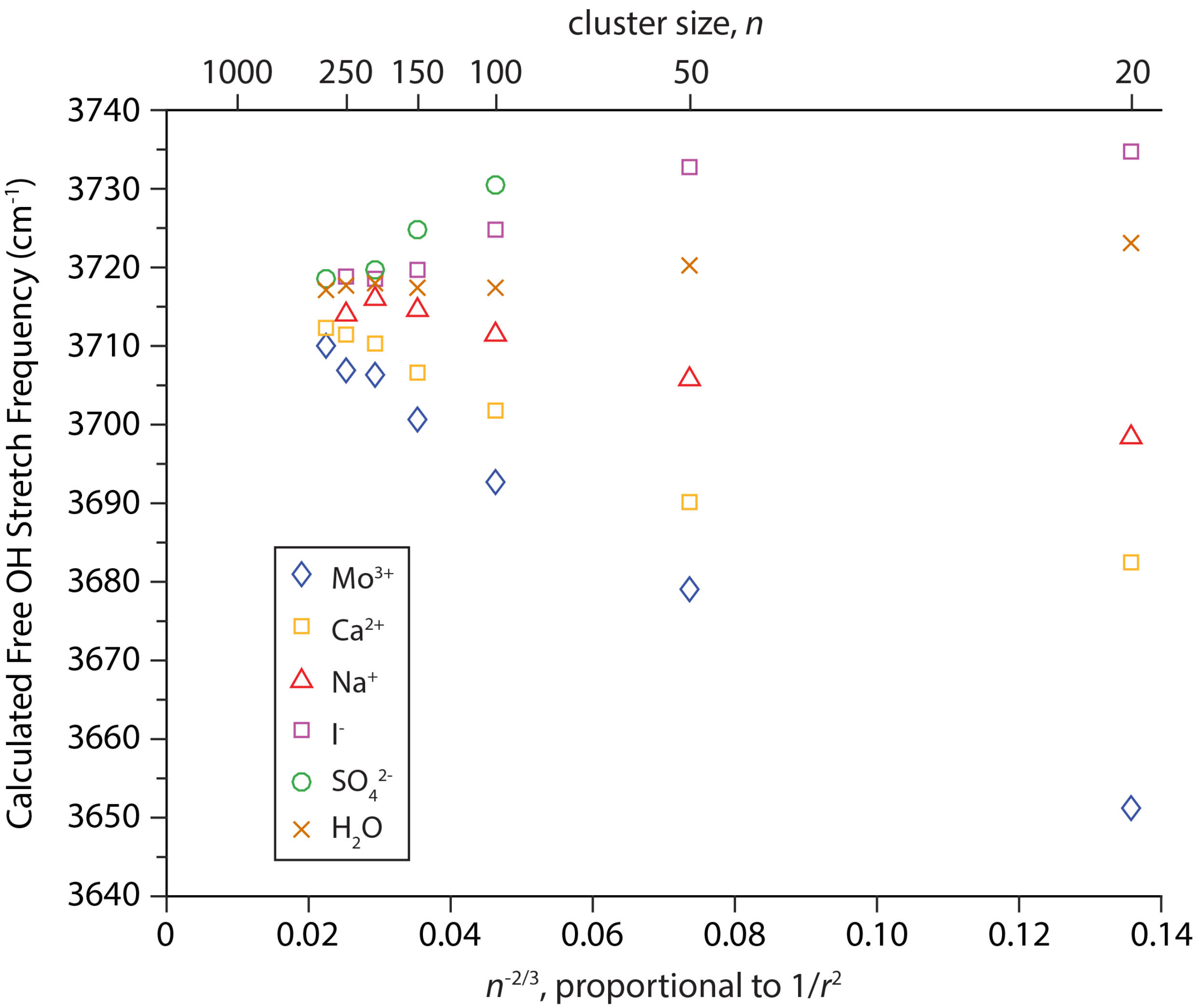

Figure 6.6. Centroid frequencies of the AAD free OH bands from simulated spectra of $(H_2O)_n$ and $M(H_2O)_n$ where M = Mo^{3+}, Ca^{2+}, Na^+, I^- and SO_4^{2-} as a function of $n^{-2/3}$, which is proportional to $1/r^2$ where r is the droplet radius.

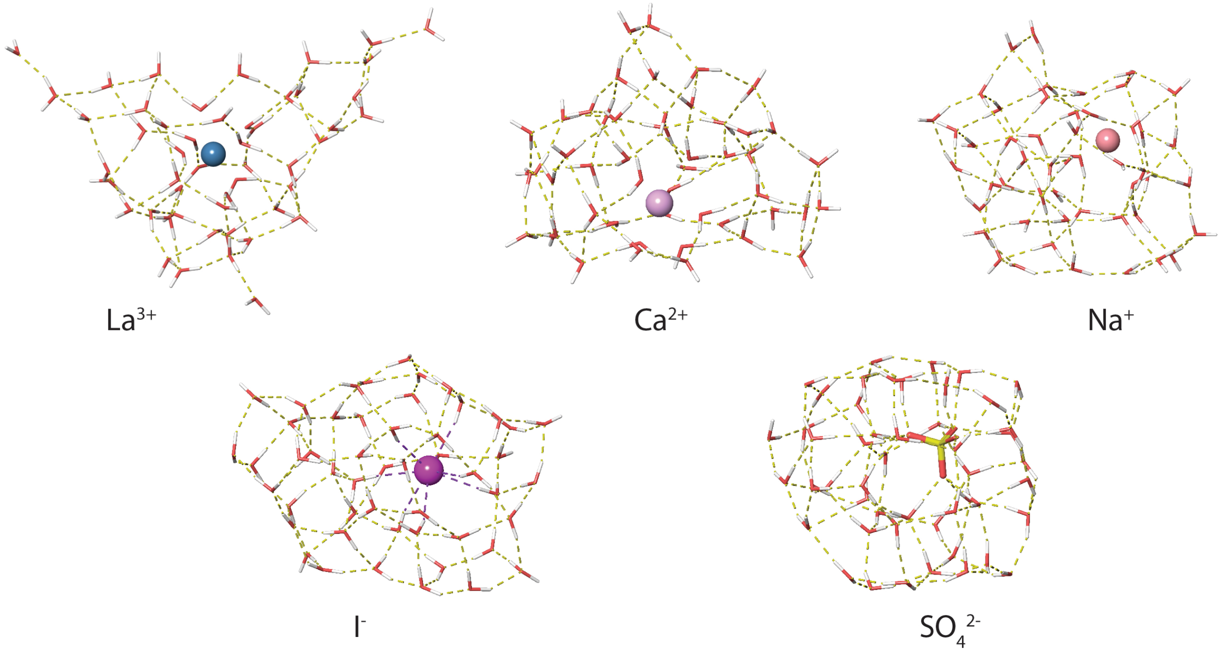

Figure 6.7. Representative low-energy structures of M$(H_2O)_{50}$ where M = La^{3+}, Ca^{2+}, Na^{+}, Li^{+}, I^{-} and SO$_4^{2-}$ identified from molecular dynamics simulations at 133 K.

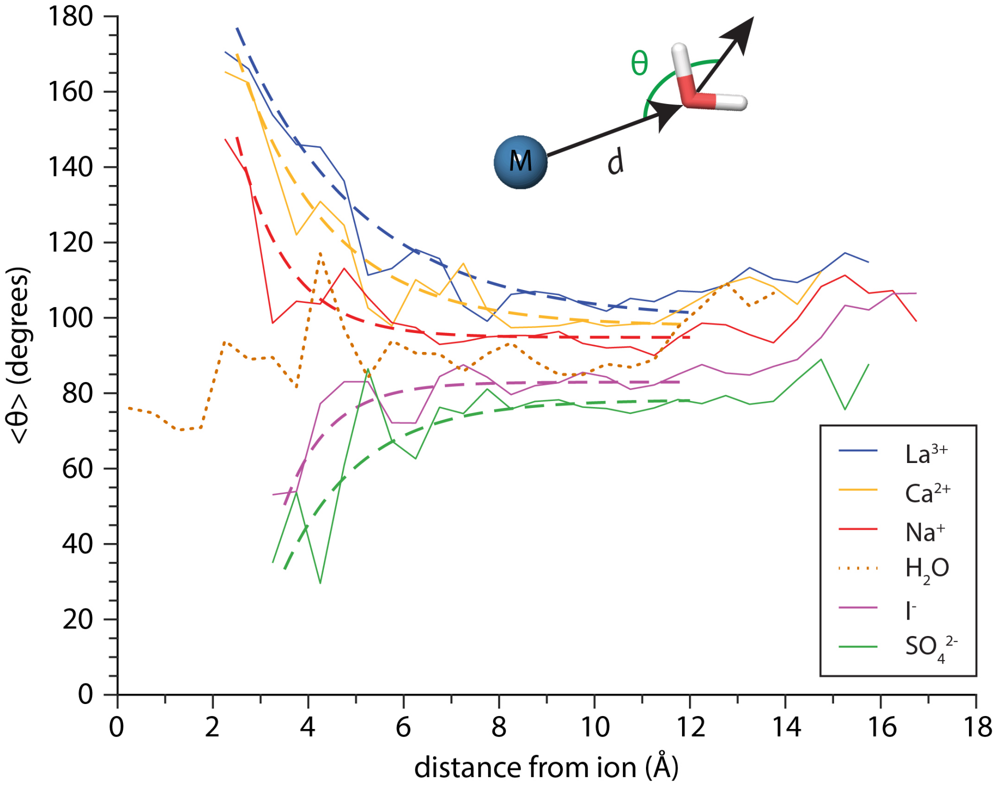

Figure 6.8. Average angular orientation of the water molecule dipole (<θ>) as a function of distance *d* from the ion calculated from MD simulations of $M(H_2O)_{250}$ where M = Mo^{3+}, Ca^{2+}, Na^+, I^-, and SO_4^{2-} binned in 0.5 Å increments. The dashed lines are exponential fits to these data for $d \leq 12$ Å. Results from simulations of $(H_2O)_{250}$ are shown as a dotted brown line, and distances are reported with respect to the center-of-mass of these clusters.

Chapter 7

Absolute One-Electron Reduction Potentials of Cu^{2+}, Ni^{2+}, Co^{2+}, and Zn^{2+} from Laser-Calibrated Nanocalorimetry Experiments

This chapter is reproduced with permission from
Cooper, R.J.; Williams, E.R.
"Absolute One-Electron Reduction Potentials of Cu^{2+}, Ni^{2+}, Co^{2+} and Zn^{2+}
from Laser-Calibrated Nanocalorimetry Experiments"
Manuscript in preparation for submission

7.1 Introduction

The rich reduction-oxidation chemistry of the first-row transition metals governs many processes essential for life. Active sites in metalloenzymes incorporate transition metals that catalyze electrochemical reactions involving hydrogen uptake and storage,[1-3] electron transport[4-6] and carbon rearrangements.[7,8] These catalytic cycles often include reversible one-electron redox events where changes in the oxidation state of the metal ion drive structural changes in the active site, imparting reactivity. An understanding of the energy involved in individual redox reactions is therefore crucial for rationalizing complex electrochemical transformations. Information about the redox behavior of metal ions comes primarily from solution-phase experiments where electron transfer is controlled by electrical potentials applied to electrodes submerged in solution. For species that undergo multiple electron transfer processes, a redox potential for each electron transfer event can be measured if the addition or removal of the sequential electron requires more energy than the previous one. This is the normal ordering of redox potentials. In cases where it is energetically more favorable to add or remove a subsequent electron, rapid sequential or concerted electron transfer occurs such that the concentration of the species resulting from the first redox event is negligible.[9] This phenomenon, known as potential inversion, occurs for many of the first row transition metal ions including Ni^{2+}, Co^{2+} and Zn^{2+}, which consequently do not have measured one-electron reduction potentials in solution.

In solution, redox potentials of half-cells are measured in reference to other half-cells, i.e., reference electrodes, resulting in a ladder of relative thermochemical values. The universally accepted reference point for this relative scale is the standard hydrogen electrode (SHE), $H^+ + e^- \rightarrow \frac{1}{2} H_2(g)$, which is arbitrarily assigned a redox potential of exactly 0 V. Because relative potentials between half-cells have already been accurately measured, if the absolute potential of a single half-cell were determined, it could be used to establish an absolute electrochemical scale. This has captured the attention of many researchers, and considerable effort and debate has gone into assigning an absolute value for the SHE.[10-14] A widely accepted definition of the absolute SHE is the reduction of an aqueous proton referenced to a gaseous electron at rest in vacuum.[11,12] Absolute potentials of the SHE ranging from 4.2–4.7 V have been estimated from numerous methods that rely on data obtained from both theory and experiment.[12-19] One approach to the absolute SHE is through a thermocycle that combines the atomization and ionization energies of hydrogen with the real proton hydration energy.[12] The latter value, however, has been the subject of controversy owing to difficulties in determining the surface potential of water.[20-23] An alternative strategy is to relate gas-phase ionization energies of isolated atoms and ions to both absolute and relative solution phase redox potentials through thermodynamic relations that include the solvation energies of the reduced and oxidized species.[24-35] The main difficulty with this approach is accurately accounting for the absolute solvation energies of single ions, which cannot be measured directly in solution and are thus obtained from calculations. Interactions between ions and water molecules the first few hydration shells are difficult to model due to the anomalous behavior of water molecules in inner hydration shells compared to those in bulk.[25,36,37] Accordingly, increasing the number of solvent molecules treated explicitly in these calculations increases the accuracy of this approach.[24-26] More detailed discussions of the various pathways to an absolute electrochemical scale, and the assumptions and sources of uncertainty associated with each approach, can be found elsewhere.[38-40]

Our group has introduced a gas-phase electrochemistry method called ion nanocalorimetry where the reduction of single ions confined in nanometer-sized aqueous "nanodrops" is used to obtain absolute half-cell potentials in solution.[38-52] When a free electron is captured by an ion-containing nanodrop, the recombination energy (RE) results in fast heating of the cluster, and this energy is dissipated by the evaporation of water molecules. The RE is related to the number of water molecules that evaporate from the nanodrop, their binding energies, and the energy that partitions into the departing water molecules. The RE is an adiabatic value because solvent reorganization around the reduced ion occurs on a timescale that is much faster than that of the experiment.[53-55] The absolute REs obtained from these measurements can then be related to absolute half-cell reduction potentials for metal ions in solution. One key advantage of this technique is that the reduction of the ion depends on the low-probability capture of a low energy electron[47] and is not controlled by a potential as in solution-phase experiments. Ion nanocalorimetry can thus be used to measure one-electron reduction potentials of species where the reduced ion is stable but potential inversion occurs. This is the case for the transition metals Ni^{2+}, Co^{2+} and Zn^{2+} where pulse radiolysis experiments indicate that the corresponding singly charged ions can be formed in solution through reactions with the hydrated electron.[56-58] Our technique can also be used to investigate species for which the reduced ion is inherently unstable and does not exist in water, such as for La^{3+} and Ca^{2+}. For these species, solvent-separated ion-electron pairs are formed upon electron capture by $La^{3+}(H_2O)_n$ and $Ca^{2+}(H_2O)_n$ clusters,[43,49] and from these experiments, the bulk hydration enthalpy of the hydrated electron can be obtained.

Ion nanocalorimetry experiments can also be performed on species for which the relative one-electron reduction potential is known from standard electrochemical measurements such as Cu^{2+}/Cu^{+}. The absolute reduction potentials determined for such species, along with their potentials relative to the SHE, can be used to obtain an absolute reduction potential for the SHE. Values of 4.0–4.3 V have been determined from three largely independent implementations of the nanocalorimetry technique.[39,40,45] The most recent approach extrapolates recombination enthalpies (obtained from REs) of $Eu^{3+}(H_2O)_n$ clusters to infinite cluster size to obtain the absolute reduction enthalpy of the infinitely dilute solution, which was used to determine the absolute half-cell potentials of Eu^{3+}/Eu^{2+} and the SHE.[39] The extrapolation method is potentially the most accurate nanocalorimetry technique because it does not require modeling of cluster solvation enthalpies. However, the cluster dissociation process for $Eu^{3+}(H_2O)_n$ was modeled in order to relate the water loss measured in electron capture experiments to the REs deposited in the nanodrops. The amount of energy deposited in a cluster was calculated using the theoretical binding energy of each departing water molecule and an energy partitioning model for the products. More recently, laser photodissociation experiments[59,60] on hydrated ions have provided an alternative route to obtaining REs without relying on theoretical models. Many hydrated ions absorb light in the ultraviolet region, which results in electronic-to-vibrational energy conversion and cluster heating analogously to the EC experiments. We proposed that by calibrating water loss to energy deposition using photons with known energies, more accurate REs and half-cell potentials could be obtained.[39,59,60]

Here, one-electron recombination enthalpies for $M^{2+}(H_2O)_n$ where M = Cu, Ni, Co and Zn are measured for $36 \leq n \leq 240$. Energy deposition in these clusters is experimentally calibrated with laser photodissociation experiments, and the resulting cluster recombination enthalpies are extrapolated to infinite cluster size to obtain absolute reduction enthalpies for these ions in solution. The measured absolute enthalpies are used to determine absolute reduction potentials for each of these metal ions. An absolute reduction potential for the SHE is obtained from the absolute reduction potential of Cu^{2+} reported here and its relative potential to the SHE measured in solution. Relative one-electron reduction potentials for Ni^{2+}, Co^{2+} and Zn^{2+} referenced to the SHE potential are determined, and to our knowledge are the first experimentally measured values.

7.2 Experimental Methods

All nanocalorimetry experiments were performed using a home-built 7.0 T Fourier-transform ion cyclotron resonance (FT-ICR) mass spectrometer that is described in detail elsewhere.[61] Briefly, hydrated ions are formed by nanoelectrospray ionization[62] (nESI) of ~5 mM aqueous solutions of MCl_2 salts where M = Cu, Ni, Co, and Zn (Sigma-Aldrich, Saint Louis, MO). To form hydrates of protonated aniline and phenylalanine (PheAla), 5 mM solutions in 90/10 water/methanol are acidified by 1% (v/v) acetic acid. The ions are gently guided by electrostatic lenses through five stages of differential pumping into the FT-ICR cell. A pulse of dry nitrogen gas (10^{-6} Torr) is introduced through a piezoelectric valve to aid in the trapping and thermalization of ions to the temperature of a copper jacket[63] surrounding the cell. The temperature of the copper jacket is regulated to 133 K by a controlled flow of liquid nitrogen. Ions are accumulated in the cell for ~5-8 s followed by a pump down delay of similar length to allow the instrument pressure to return to $< 10^{-8}$ Torr. Precursor ions are isolated using SWIFT techniques.[64]

For electron capture (EC) experiments on $M^{2+}(H_2O)_n$, a single precursor ion is isolated for $n < 100$ and distributions consisting of 5 adjacent precursor cluster sizes are isolated for $n \geq 100$. The ensemble method makes it possible to acquire data for larger clusters with improved S/N.[65] Following a 40 ms delay, electrons are introduced into the cell from a heated dispenser cathode (HeatWave Laboratories, Watsonville, CA) mounted axially 20 cm from the center of the cell. A copper wire mesh is mounted 0.5 cm from the cathode and held at a potential of +9.0 V. Electrons are introduced into the cell by applying a negative potential to the cathode housing for 80–120 ms that ranges from ~2.0 – 4.0 V in order to maximize product ion abundances. At all other times, a potential of +10 V is applied to prevent electrons from entering the cell. A delay step of 0.5 or 1.0 s for n less than or greater than ~100, respectively, is introduced after electron irradiation but before ion detection to ensure that dissociation of the reduced clusters is complete.

In the ultraviolet photodissociation (UVPD) experiments on $PheAlaH^+(H_2O)_n$ and $Anilinium(H_2O)_n$, precursor ion distributions consisting of 3 adjacent cluster sizes are isolated for all *n*. After a 40 ms delay, an EX50 Excimer laser (GAM Laser Inc., Orlando, FL) is triggered with a voltage switch for irradiation times between 0.25–1.0 s. The length of the irradiation time is chosen to maximize product ion intensities while minimizing the broadening of precursor and product ion distributions by blackbody infrared radiative dissociation (BIRD). The laser is operated at 250 Hz with ~5 W of power for 193.3 ± 0.5 nm (6.41 ± 0.02 eV) and ~10 W of power for 248.4 ± 0.2 nm (4.991 ± 0.004 eV). The laser light is directed by two aluminum-coated mirrors through a CaF_2 lens with a 1.0 m focal length, and then introduced into the mass spectrometer through a CaF_2 window. A delay time of 0.5 or 1.0 s for $n < 100$ and $n \geq 100$, respectively, is introduced after UV irradiation but before ion detection to ensure that complete dissociation is observed.

7.3 Results and Discussion

7.3.1 Electron Capture by $M^{2+}(H_2O)_n$ for M = Cu, Ni, Co and Zn. Extensively hydrated transition metal ions are formed by nESI resulting in broad distributions of hydrated ions that contain tens to hundreds of water molecules (Figure 7.1a-b). The cluster size distribution can be shifted continuously from small (Figure 7.1a) to large (Figure 7.1b) sizes by changing various instrument parameters including the inlet capillary temperature and voltages on the electrospray interface.[66] Electron capture (EC) experiments can then be performed on specific cluster sizes isolated in the trap of the mass spectrometer (Figure 7.1c). In these experiments, hydrated metal ions are irradiated with thermally generated electrons for 80–120 ms resulting in their reduction. The recombination of an electron and the nanodrop releases energy into the nanodrop resulting in cluster heating and dissociation by the sequential loss of water molecules. For ions with $n > 100$, distributions of precursor ions consisting of five adjacent hydration states are isolated to improve the precision of the measurements of water loss.[65] An example of a typical EC experiment is shown in Figure 7.1c for $Co^{2+}(H_2O)_{118\text{-}122}$. The distribution of clusters at lower *m*/z are unreacted precursor ions and the other distribution of ions at higher *m*/z are ions that have captured one electron and have been reduced. Both distributions are broadened by dissociation due to BIRD. The average number of water molecules lost due to electron capture, $\langle x \rangle$, is obtained from the difference in average cluster size between the precursor and product ion distributions, which for $Co^{2+}(H_2O)_{118\text{-}122}$ corresponds to 9.7 water molecules.

The product ions resulting from EC of $M^{2+}(H_2O)_n$ clusters where M = Cu, Ni, Co, and Zn are shown for $n = 36$, 110 and 210 in Figure 7.2. A single precursor ion was isolated for the $n = 36$ clusters (Figure 7.2a-d), whereas for the $n = 110$ and 210 clusters, distributions of 5 precursor ions centered on these nominal sizes were used (Figure 7.2e-h and Figure 7.2i-l, respectively). The abscissas in these mass spectra are plotted on an *n* scale to facilitate comparisons between product ions. For all cluster sizes, the extent of water loss depends upon the identity of the metal ion and follows the order Cu > Ni > Co > Zn. In the EC experiment for $Cu^{2+}(H_2O)_{108\text{-}112}$, for example, the average precursor ion cluster size, $\langle n \rangle$, is 108.45 water molecules and the average product ion cluster size, $\langle m \rangle$, is 94.53 water molecules corresponding to $\langle x \rangle = 13.92$ water molecules. For the other metal ions, $\langle x \rangle$ at this cluster size is 11.53, 9.86, and 8.73 water molecules for Ni, Co, and Zn, respectively. These differences in water loss reflect significantly different amounts of energy deposited into the clusters from ion-electron recombination events. The amount of energy deposited into a cluster can be roughly approximated from the number of water molecules that evaporate and the binding energy of each departing water molecule. This approximation neglects energy that partitions into the translational, rotational, and vibrational modes of the dissociated water molecules and is therefore a lower bound to the actual energy deposited. High-precision UVPD experiments indicate that water molecule binding energies near this cluster size are ~0.42 eV, [reference BE manuscript] and the observed differences in water loss for nanodrops containing Cu^{2+}, Ni^{2+}, Co^{2+} and Zn^{2+} are thus consistent with recombination energies that differ by ~0.5–2.2 eV. Such differences in water loss persist at larger cluster size (Figure 7.2i–l), which indicates that reduction of the metal ion occurs even for extensively hydrated ions.

In contrast, capture of an electron and formation of a solvated ion-electron pair within the nanodrop lends to water loss that does not depend on the identity of the metal ion. This has previously been observed for alkaline earth metal ions, where for $M^{2+}(H_2O)_{32}$, M = Mg, Ca, Sr and Ba, the measured water loss upon EC was identical within the accuracy of the experiment.[49] Ion-electron pairs have also been observed in EC experiments on some hydrated trivalent lanthanides.[43] Neither the alkaline earth metals nor the lanthanides undergo one-electron reductions in solution, which is consistent with the reduced ions being unstable due to solvent effects. In contrast, the direct reduction of metal ions has been reported for nanodrops containing $[M(NH_3)_6]^{3+}$ for M = Ru, Co, Os, Cr and Ir[40] where, as is the case in the present study, the extent of water loss depends on the metal identity.

7.3.2 Factors that Affect Water Loss. The average number of water molecules lost as a result of EC is shown in Figure 7.3 for $M^{2+}(H_2O)_n$ clusters, where M = Cu, Ni, Cu and Zn, and $36 \leq n \leq 240$. The extent of water loss is different for all of the species and decreases with increasing cluster size. This latter effect can be attributed predominately to improved ion stabilization with increasing solvation, which reduces the energy released upon EC. Additionally, surface effects may also contribute to this phenomenon where the binding energy of a water molecule to a cluster increases slightly with increasing cluster size owing to improved hydrogen bonding at the surfaces of larger nanodrops.[48] It is interesting to note that the number of water molecules lost from $Zn^{2+}(H_2O)_n$ clusters is only greater than previous measurements on $Ca^{2+}(H_2O)_n$ clusters by ~1 water molecule over the size range where comparisons can be made (n = 36–62).[49] Electron capture experiments on $Ca^{2+}(H_2O)_n$ clusters and other alkaline earth metal ions indicate that the formation of a solvated ion-electron pair is preferred over reduction of the metal ion. Thus, for $Zn^{2+}(H_2O)_n$ clusters, the formation of an ion-electron pair may be energetically competitive with reduction, especially at larger cluster sizes (n > ~50) where difference in water loss are on the order of ~0.5 water molecules. At smaller cluster sizes, the number of water molecules lost upon EC for the two ions is less similar. For example, $Zn^{2+}(H_2O)_{36}$ and $Ca^{2+}(H_2O)_{36}$ lose 11.1 and 9.7 water molecules, respectively. This suggests that $Zn^{2+}(H_2O)_n$ clusters are likely reduced at small cluster size.

In these EC experiments, a kinetic shift may arise if the time scale for cluster dissociation is shorter than the time scale of the experiment. For a fixed amount of deposited energy, the time required for complete evaporative water loss from these nanodrops as a result of EC depends on the number of degrees-of-freedom over which the energy is distributed, and consequently the cluster size. Statistical modeling of cluster internal energies in EC experiments indicates that the effective temperature to which a cluster is heated decreases with increasing cluster size.[39,40,42] Thus, the rate of evaporative water loss will be greatest for smaller "hot" clusters and will decrease for larger, cooler clusters. In our experiments, the kinetic shift is measured by varying the length of the delay step after electron irradiation but before ion detection. Measurements of the kinetic shift in EC experiments on $Eu^{3+}(H_2O)_{110}$ indicate that a reaction delay of 40.4 ms is sufficient to observe complete fragmentation of the cluster resulting from EC.[39] In order to assess the effects of the kinetic shift on $\langle x \rangle$ in the larger nanodrops investigated herein, measurements of $\langle x \rangle$ from EC of $Co^{2+}(H_2O)_{198\text{-}202}$ were made using delay times after EC ranging from 0.05–1.5 s (Figure 7.4a). Our results indicate that between 50 ms and 0.5 s, there is a kinetic shift of 0.2 water molecules but that for longer reaction delay times the shift is not significant. To ensure that kinetic shift effects did not impact our measurements, a reaction delay of 0.5 s or 1.0 s was used for cluster sizes below and above $n \sim 100$, respectively.

The initial electron kinetic energy is determined by the potential applied to the cathode housing and the cathode temperature. Previous EC measurements on $Ca^{2+}(H_2O)_{32}$ and $Ca^{2+}(H_2O)_{15}$ indicate that $\langle x \rangle$ does not depend on the cathode voltage. The effects of the cathode voltage on $\langle x \rangle$ were investigated for larger $Co^{2+}(H_2O)_{108\text{-}112}$ clusters that are reduced upon EC (Figure 7.4b). There is no dependence of $\langle x \rangle$ on the applied potential over the entire 4 V range between -1.25 and -4.25 V, which clearly shows that the initial kinetic energy of the electron is not deposited into the cluster. An extrapolated linear least-squares fit of these data to a potential of 0 V results in 9.9 ± 0.1 water molecules lost, which is an indication of the precision of these measurements and in good agreement with prior results. The observation that the initial electron kinetic energy is not deposited into the cluster is attributed to EC having a high cross section when the relative velocity between an ion and electron approaches zero, and this cross section drops off quickly for non-zero relative velocities.[47] The spread of electron velocities in these nanocalorimetry experiments is broadened by several factors including thermal effects, electron-electron repulsion, and inelastic ion-electron collisions that do not result in EC. These factors may result in a small fraction of electrons with the near-zero relative kinetic energies inside the cell, which will be efficiently captured by the positive ions.

7.3.3 Laser-Calibrated Recombination Energies. The recombination energy (RE) deposited into a cluster by EC can be determined from the number of water molecules that evaporate from the cluster. A greater number of water molecules lost after EC reflects a larger RE because more water evaporation is required to cool the cluster close to its initial temperature. One way of approximating REs is by evaluating both the water molecule binding energies, E_o, and the energy partitioned the translational, rotational and vibrational modes of the products. Our group has previously devised a method for calculating REs in this manner where cluster effective temperatures are modeled statistically by solving for cluster internal energies that give the observed average water loss.[40,42] The RE can be written as

$$RE = \sum_{i=1}^{x} E_{o,i} + \frac{5}{2} k_B \sum_{i=1}^{x} T_i^* \qquad (1)$$

where i is an index that runs over each water molecule lost, $E_{o,i}$ is the dissociation energy of the i^{th} water molecule, k_b is Boltzmann's constant, and T_i^* is the effective temperature of the product ion after the loss of i water molecules. Values for both E_o and the energy partitioned into products are obtained from models. A discrete implementation of the Thomson liquid drop model (TLDM) is used to obtain values for E_o,[48] and the expression for the product energy release on the RHS of equation (1) is taken from the Klot's cluster evaporation model.[67]

The accuracies of REs obtained using this method have been difficult to assess due to uncertainties in the accuracies of the various models employed. By far, the largest component of the RE is the sum of the sequential water molecule binding energies. Recent high-precision UVPD experiments on hydrated ions with +1 to +3 charge states and for cluster sizes between 20–500 water molecules have offered insights into the accuracies of E_o values derived from the TLDM.[68] Significant differences between measured water molecule binding enthalpies and those calculated using the TLDM were found for all charge states, with discrepancies between the modeled and experimental enthalpies increasing with increasing cluster size. The magnitude of these discrepancies depends on the bulk water parameters used in the TLDM. For example, the root-mean-square-deviation between experimental and calculated binding enthalpies for monovalent ions was found on average to be 1.12 kcal/mol and 0.59 kcal/mol using liquid water parameters at 313 K and 298 K, respectively. While these differences may seem small, any uncertainties in E_o are compounded in nanocalorimetry experiments where many water molecules are lost. For the $Cu^{2+}(H_2O)_n$ clusters, for example, EC results in the loss of up to 16 water molecules which, taking into account the uncertainties listed above, would shift the REs by ~0.4–0.8 eV.

An alternative approach to determining REs that obviates the need for modeling is by experimentally calibrating the relationship between energy deposition and water loss using laser photodissociation experiments at multiple wavelengths (Figure 7.5). This approach exploits the physical property that ion-containing nanodrops with a suitable chromophore can absorb ultraviolet light at multiple wavelengths. This is illustrated in Figure 7.5a for distributions of hydrated protonated phenylalanine ($PheAlaH^+$) ions centered on $n \sim 100$ (top and middle mass spectra). Upon absorption of a 248 nm photon (top spectrum), which has 5.0 eV of energy, the ion is promoted to an excited electronic state and then relaxes by internal conversion resulting in cluster heating and the appearance of product ions that have lost on average 10.9 water molecules. When 193 nm laser light is used (middle spectrum), 6.4 eV is deposited into the cluster resulting in $\langle x \rangle = 13.9$. In this way, a functional relationship between energy deposited and $\langle x \rangle$ is established that can be used to infer energy deposition that occurs in EC for clusters of similar size. In Figure 7.5a (bottom spectrum), an EC experiment on $Cu^{2+}(H_2O)_{\sim100}$ clusters is shown where the amount of energy deposited is unknown, but the extent of water loss is measured ($\langle x \rangle = 14.3$). The energy deposited into the cluster, which corresponds to the RE, can thus be obtained from the laser photodissociation calibration data. Because dissociation occurs from the *reduced ions* in EC experiments, the referenced laser calibration data must be for an ion with a charge state that is the same as that of the reduced products ions in the EC experiments.

In practice, the laser calibration data is measured for both $PheAlaH^+(H_2O)_n$ and $Anilinium^+(H_2O)_n$ ions as a function of cluster size at both 193 nm and 248 nm with up to 200 water molecules attached (Figure 7.5b). A similar number of water molecules is lost for each of these ions, and the combined data set is fit with a biexponential function (dashed lines). The fits to data measured at both wavelengths indicate that the number of water molecules lost is greatest for $n \sim 50$–60 and then monotonically decreases with increasing cluster size as water molecule binding energies begin to increase due to surface curvature effects.[48] Additional measurements at 248 nm for $n < 30$ show that $\langle x \rangle$ decreases dramatically for these smaller ions as the influence of the ion on water molecule binding energies becomes more pronounced. The functional fits to these data are used to obtain values of $\langle x \rangle$ at different cluster sizes and wavelengths. An example of how these laser calibration data are used to determine a RE for $Cu^{2+}(H_2O)_{\sim100}$ is shown in Figure 7.5c. Water loss measured for the monovalent ions is plotted as a function of photon energy for $\lambda = 193$ and 248, and these data define a linear relationship between energy deposition and water loss. The average number of water molecules lost from the EC experiment is measured, and consequently, the RE can be solved for using this value and the equation of the line, yielding a RE of 6.68 eV. This procedure was repeated using all the EC water loss data for $Cu^{2+}(H_2O)_n$, $Ni^{2+}(H_2O)_n$, $Co^{2+}(H_2O)_n$ and $Zn^{2+}(H_2O)_n$ to determine RE values at each cluster size. Because a separate calibration curve is made for every cluster size, the effects of cluster size on the water molecule binding energies, effective droplet temperatures, and energy partitioned into products are all accounted for experimentally. This is the key advantage of the laser calibration method.

There are two principal sources of uncertainty in obtaining REs using this laser calibration method. First, the calibrant ions used are different species than the reduced precursor ions in the EC experiments. Ideally, the same ions would be used in both experiments (e.g the RE deposited into $Cu^{2+}(H_2O)_n$ clusters would be calibrated with photodissociation experiments on $Cu^{+}(H_2O)_n$ clusters of the same size). M(I) compounds are uncommon for M = Ni, Co, and Zn and do not exist as simple salts. Cu(I) disproportionates in solution.[69,70] Thus, $M^{+}(H_2O)_n$ clusters cannot be formed directly by electrospray ionization in our experimental setup. Another possibility is calibrating with hydrates of the alkali metal ions, but we found that these species do not absorb light at 193 and 248 nm. In contrast, both $PheAlaH^{+}$ and Anilinium contain aryl groups that absorb light at these wavelengths making them suitable reference ions. Is difficult to evaluate the errors associated with the use of molecular calibrant ions, but we note that many properties of hydrated ions depend primarily on the charge state of the ion rather than ion identity, especially for larger clusters. Measured water molecule binding energies of mono and divalent metals ions show a strong dependence on ion identity for water molecules in the first hydration shell, and can differ by more than 10 kcal/mol, but these values quickly converge with increasing cluster size to within 1 kcal/mol for $n > \sim 10$.[48,60] Additionally, there is spectroscopic evidence that monovalent ions do not strongly affect the H-bonding network of water molecules outside of the first hydration shell.[71-75] On this basis, for the extensively hydrated ions probed in these experiments, we expect that the effects of ion identity will not be significant. The second source of uncertainty in obtaining REs with the laser calibration method arises from using two wavelengths of light and modeling the relationship between energy deposition and water loss with a linear fit. The functional dependence of water loss on energy deposited may deviate from linearity. As the deposited photon energy increases, the clusters will heat up to higher effective temperatures and a larger fraction of the total energy deposited will partition into the departing water molecules, resulting in fewer water molecules lost. This effect manifests in a positive y-intercept when the linear fit is extrapolated to 0 eV (Figure 7.5c). The magnitude of this error, however, is quite small; extrapolated y-intercepts are on average 0.33 eV over the range of measured cluster sizes. This represents an upper limit to the error involved in this approximation because the extrapolated REs are much closer to the range of measured photon energies and accordingly this error should be significantly less than 0.33 eV. Further evidence for the nearly linear relationship between energy deposition and water loss comes from laser photodissociation experiments on $Aniline^{+}(H_2O)_n$ clusters that used ~10 different wavelengths of light generated by a visible OPO to measure water loss over a broad range of photon energies (1.65 to 4.66 eV).[76] For $n \geq 12$, it was found that water loss depends linearly on the incident photon energy.

7.3.4 Obtaining ΔH_{abs} from Cluster Measurements. The gas-phase recombination enthalpy of a hydrated metal ion cluster, $\Delta H_R(n)$, is related to the absolute reduction enthalpy of the metal ion in solution, ΔH_{abs}, by the relation:

$$\Delta H_R(n) = \Delta H_{abs} + \Delta\Delta H_{solv}(n) \qquad (2)$$

where $\Delta\Delta H_{\mathrm{solv}}(n)$ is the difference between the solvation enthalpies of the precursor and product cluster ions.[39] Gas-phase recombination enthalpies at a specific cluster size can be obtained directly from the measured REs according to the relation $\Delta H_{\mathrm{R}}(n)$ = -RE(n) - c_{el}, where c_{el} is the integrated heat capacity of the electron from Fermi–Dirac statistics.[77] To obtain a value for ΔH_{abs} without relying on solvation models, the cluster measurements of $\Delta H_{\mathrm{R}}(n)$ can be extrapolated to infinite cluster size to obtain the reduction enthalpy of an ion at the limit of infinite dilution in water. The solvation enthalpy of a cluster ion is inversely proportional to the cluster radius (R) for sufficiently large clusters that are spherical and for which solvation in outer shells depends only on ion charge. Thus, the $\Delta\Delta H_{\mathrm{solv}}(n)$ term in equation 2 will have a 1/R dependence. The volume of a spherical cluster is proportional to n so it follows that the radii of the clusters should be proportional to $n^{1/3}$, and 1/R is proportional to $n^{-1/3}$. Equation 2 can then be rewritten as

$$\Delta H_R(n) = \Delta H_{abs} + Cn^{-1/3} \qquad (3)$$

where C is a constant. A plot of $\Delta H_{\mathrm{R}}(n)$ versus $n^{-1/3}$ should result in a line with a vertical intercept that corresponds to ΔH_{abs}.

The negative of the recombination enthalpies for $M^{2+}(H_2O)_n$ are plotted in Figure 7.6 as a function of $n^{-1/3}$ for M = Cu, Ni, Co and Zn. Linear fits to these data for $36 \le n \le 240$ are shown as dashed lines, and the good quality of these fits (R^2 = 0.95–0.99) indicates that improved ion solvation primarily accounts for the decreasing recombination enthalpies with increasing cluster size. The y-intercepts of these fits correspond to the absolute reduction enthalpy of each ion at infinite cluster size, i.e. infinitely dilute aqueous solutions with unit activity (Table 7.1). The extrapolated values of $-\Delta H_{\mathrm{abs}}$ are 4.67 ± 0.13 (Cu^{2+}), 3.46 ± 0.10 (Ni^{2+}), 2.50 ± 0.06 (Co^{2+}) and 1.36 ± 0.11 (Zn^{2+}). The extrapolations are performed on nanodrops that range from ~0.6–2.4 nm in diameter and extend over a larger range of cluster sizes than previous EC measurements on $Eu^{3+}(H_2O)_n$ clusters (n_{max} = 124) that were performed on an instrument with a lower field strength magnet.[39]

7.3.5 Absolute Reduction Potentials and the SHE. The absolute reduction potential of a metal ion (E^o_{abs}) can be obtained if both the absolute enthalpy and entropy of reduction are known based on the Faraday relation between the Gibbs energy (ΔG_{abs}) and E^o_{abs}:

$$\Delta G_{abs} = \Delta H_{abs} - T\Delta S_{abs} = -nFE^o_{abs} \qquad (4)$$

where n is the number of electrons transferred and F is Faraday's constant. As we have shown, values of ΔH_{abs} can be obtained from the extrapolation of cluster measurements presented herein. Absolute entropies of reduction are obtained from electrochemical measurements of isothermal temperature coefficients ($\partial E^o/\partial T$). For the one-electron reduction of Cu^{2+}, an isothermal temperature coefficient of 0.776 mV/K has been measured[78] that, when added the nonisothermal temperature coefficient of the SHE reaction,[79] yields an absolute entropy term of $T\Delta S_{\mathrm{abs}}$ = 0.49 eV at 298 K. Because these temperature coefficients have been measured with high precision, the uncertainty in the entropy term is less than 0.01 eV, which is negligible in comparison to the uncertainty in the ΔH_{abs} term. Absolute reduction entropies have not been measured for the one-electron reductions of Ni^{2+}, Co^{2+} and Zn^{2+} and so the entropy term for Cu^{2+} is used for these ions.

Reduction entropies depend primarily on the oxidation state of the metal ion and the identity of the coordinated ligands,[40,78,80] such that the approximation made here should not significantly affect the absolute reduction potentials calculated for these other ions.

Values of E_{abs}^{o} for the one-electron reductions of Cu^{2+}, Ni^{2+}, Co^{2+} and Zn^{2+} obtained from these gas-phase nanocalorimetry experiments are shown in Table 7.1. Larger positive values of E_{abs}^{o} indicate a metal ion's greater affinity for electrons and tendency to be reduced in solution. Of all the transition metal ions investigated here, Cu^{2+} undergoes the most energetic reaction with an electron. The standard reduction potential for the one-electron reduction of Cu^{2+} in solution relative to the SHE has been determined from measurements of the equilibrium constant for the reaction $Cu^{2+} + Cu(s) \rightleftharpoons 2Cu^{+}$ extrapolated to infinite dilution, and corresponds to a value of 0.17 V[69], which agrees to within 0.01V of other reported values.[78] This relative potential, combined with the value of E_{abs}^{o} for Cu^{2+} obtained from these nanocalorimetry experiments (5.16 V), indicates that the absolute reduction potential of the SHE is 4.99 V. This value is significantly higher than the previously reported value of 4.11 V obtained using the cluster extrapolation method on the Eu^{3+}/Eu^{2+} couple. This difference, however, is not unexpected. The absolute SHE value determined from the Eu^{3+} data is based on REs that were calculated from modeling the cluster dissociation process (vide supra), including water molecule binding energies, effective cluster temperatures and the energy partitioned into products. To evaluate the accuracy with which energy deposition can be modeled in this manner, the energy deposited into $PheAlaH^{+}(H_2O)_n$ and $Anilinium(H_2O)_n$ clusters upon the absorption of a 193 nm or 248 nm photon was calculated from the water loss data for precursor ions with an average cluster size $\langle n \rangle$ (Figure 7.7). Because the actual energy deposition is known for these clusters (either 6.41 eV or 4.99 eV for the absorption of 193 nm and 248 nm photons, respectively), the calculated values can be directly compared with experiment. Our results show that the calculated amount of energy deposited is, on average, 0.50 ± 0.16 eV and 0.37 ± 0.13 eV lower than the energy of the absorbed photons at 6.41 and 4.99 eV, respectively. Furthermore, the error in the calculated amount of energy deposited increases with increasing cluster size, and for larger clusters, energy deposition is underestimated by as much as ~12%. UVPD experiments indicate that water molecule binding enthalpies predicted by the TLDM increasingly underestimate the actual binding enthalpies in these nanodrops for larger cluster sizes, and the magnitude of this error can exceed 1 kcal/mole.[68] Thus, the predominant source of error in calculating energy deposition is due to the TLDM. The laser calibration method used here to determine REs for Cu^{2+} is significantly more accurate than modeling, resulting in a more accurate absolute reduction potential for the SHE. In addition, owing to the recently upgraded magnetic field strength of our instrument, EC was measured for Cu^{2+} hydrates up to sizes of $n = 240$, which is twice as large as the maximum cluster size investigated for Eu^{3+}. The extrapolated value of ΔH_{abs} for Cu^{2+} was therefore performed over a larger range of cluster sizes, which should also increase the accuracy of this value and hence the absolute SHE potential.

The absolute SHE potential can be used to calculate the "real" solvation energy of the proton, $\alpha(H^{+},aq)$, using a thermochemical cycle that includes the atomization and ionization energies of hydrogen.[38] The real proton solvation energy differs from the absolute solvation energy in that it includes the surface potential of water. The absolute SHE potential obtained from the laser-calibration method (4.99 V) corresponds to a value of -247.4 kcal/mol for $\alpha(H^{+},aq)$. This value is significantly more positive than that reported by Farrell and McTigue (-260.0 kcal/mol),[81] which was obtained by extrapolating high-resistance voltaic cell electrochemical measurements to infinite dilution using an electrostatic model. The accuracy of their value is unknown because it relies on a theoretical model for the surface potential dependence on ion concentration.[82] There is little consensus on the sign and magnitude of the surface potential of water itself, with a broad range of reported values (-1.1 to +0.5 V).[20-23]

7.3.6 Relative Reduction Potentials. Relative one-electron reduction potentials for Ni^{2+}, Co^{2+} and Zn^{2+} have not been measured in solution, presumably because reduction of the singly charged ion occurs at a more positive potential. However, relative reduction potentials for these ions can be obtained by referencing the absolute reduction potentials reported here for these ions to the value of the absolute SHE potential (4.99 V). Doing so results in the following *relative* reduction potentials of -1.05 V, -2.00 V and -3.15 V for Ni^{2+}, Co^{2+} and Zn^{2+}, respectively (Table1). These relative values are expected to have accuracies close to that of the experiment (1 SD = ±0.1 V) because any systematic errors in determining REs will be similar for these transition metal ions, and should largely cancel when subtracting the absolute reduction potential of the SHE obtained from the Cu^{2+} data.

Although relative one-electron redox potentials for Ni^{2+}, Co^{2+} and Zn^{2+} have not been previously measured, the existence of the corresponding singly charged metal ions has been observed with spectrophotometric techniques combined with pulse radiolysis, which produces reactive hydrated electrons, $e^-(aq)$. The chemical potential of $e^-(aq)$ relative to the SHE has been reported to be between -2.7 V and -2.9 V.[83,84] Any species with a more positive potential than this range of values will thus be reduced by the hydrated electron. The relative reduction potentials reported here for Ni^{2+}/Ni^+ (-1.05) and Co^{2+}/Co^+ (-2.00) are well above the chemical potential of $e^-(aq)$, consistent with their reduction in solution. Recent first principles calculations of the reduction potential for the Ni^{2+}/Ni^+ half-cell predict a range of values between -1.05 to -1.28 V depending on the level of theory used,[35] in excellent agreement with our results. To our knowledge, calculated one-electron reductions potentials for Co^{2+} and Zn^{2+} have not been reported, and the values herein should serve as benchmarks for such calculations. The relative potential we report for zinc (-3.15 V) is slightly more negative than that of the hydrated electron, although the values are likely with error. Measurements of bimolecular rate constants between M^{2+} ions and $e^-(aq)$ indicate that rate constants for Cu^{2+}, Ni^{2+} and Co^{2+} are 8–19 times larger than that of Zn^{2+}.[56] These results indicate that reduction of Zn^{2+} is not very favorable and may be energetically competitive with the formation of a solvated ion-electron pair in our experiments.

7.4 Conclusions

We have demonstrated that ion nanocalorimetry can be used to study electrochemical reactions difficult to probe using traditional solution-phase techniques. These experiments are conducted in an electron-limited regime where reduction of the metal ion depends on the low-probability capture of a free electron. This is in stark contrast to solution-phase measurements where reduction is controlled by a potential applied to a submersed electrode. In such experiments, it is impossible to measure one-electron reduction potentials for species where potential inversion occurs. This is because it is energetically more favorable for the reduced ion to undergo a subsequent reduction and it is thus immediately reduced at the electrode surface. The absolute and relative one-electron reduction potentials for Ni^{2+}, Co^{2+} and Zn^{2+} reported here are the first experimentally determined values for these species. The relative potential we find for Ni^{2+} (-1.05 V) agrees well with values recently derived from *ab initio* calculations,[35] and the relative potentials for the other ions should serve as benchmarks for theory. Our data indicate that Cu^+, Ni^+ and Co^+ are stable species in these aqueous nanodrops. However, the low relative potential for Zn^{2+} (-3.15 V) indicates that electron capture and the formation of solvent-separated ion-electron pairs may be energetically competitive upon EC by $Zn^{2+}(H_2O)_n$ clusters. Similarities in water loss between $Zn^{2+}(H_2O)_n$ and $Ca^{2+}(H_2O)_n$ clusters for $n > \sim 50$ also hint at this competitiveness because for the latter ion, EC results in an ion-electron pair. Future ion nanocalorimetry experiments should offer additional insights into the rich redox chemistry of other transition metal ions, and for species where one-electron reductions have not been measured, may be able to determine whether this occurs on account of potential inversion or the inherent instability of the reduced ion.

The laser calibration method described herein provides a pathway to an absolute electrochemical scale that does not rely on modeling. By experimentally calibrating the relationship between the amount of energy deposited in a cluster ion and the resulting water loss, the need to model ion-electron recombination energies is eliminated. Comparisons between the known amount of energy deposited into $PheAlaH^+(H_2O)_n$ and Anilinium$(H_2O)_n$ clusters by 5.0 eV and 6.41 eV photons and the calculated amount of energy deposited indicates that the modeling underestimates energy deposition by ~8% on average and becomes systematically less accurate with increasing cluster size. We attribute the majority of the error in the modeling to errors in the TLDM used to calculate water molecule binding energies. It has recently been reported that the TLDM does not accurately reproduce experimental trends in water molecule binding energies for these nanodrops, especially at large cluster size. The value of the SHE that we obtain from the absolute reduction potential of Cu^{2+} (4.99 V) is significantly higher than values obtained by previous nanocalorimetry methods as well as the range of values reported from other measurements. From this absolute SHE potential, a value of -247.4 kcal/mol is obtained for the real solvation energy of the proton. The precision of these values can ultimately be assessed by using the method delineated here to measure half-cell potentials of several species with known one-electron reduction potentials, and by comparing the value of the absolute SHE potential derived from each one. For reductions involving trivalent metal ions such as Eu^{3+}, the laser calibration must be performed on hydrated divalent ions. The accuracy of the laser calibration method itself could be improved by using a visible OPO to generate a broader range of photon energies. Efforts towards these goals are underway in our laboratory.

7.5 References

(1) Volbeda, A.; Charon, M. H.; Piras, C.; Hatchikian, E. C.; Frey, M.; Fontecillacamps, J. C. *Nature* **1995**, *373*, 580-587.

(2) Fontecilla-Camps, J. C.; Volbeda, A.; Cavazza, C.; Nicolet, Y. *Chem. Rev.* **2007**, *107*, 4273-4303.

(3) Ogata, H.; Lubitz, W.; Higuchi, Y. *Dalton Trans.* **2009**, 7577-7587.

(4) Tsukihara, T.; Aoyama, H.; Yamashita, E.; Tomizaki, T.; Yamaguchi, H.; ShinzawaItoh, K.; Nakashima, R.; Yaono, R.; Yoshikawa, S. *Science* **1996**, *272*, 1136-1144.

(5) Yoshikawa, S.; Shinzawa-Itoh, K.; Nakashima, R.; Yaono, R.; Yamashita, E.; Inoue, N.; Yao, M.; Fei, M. J.; Libeu, C. P.; Mizushima, T.; Yamaguchi, H.; Tomizaki, T.; Tsukihara, T. *Science* **1998**, *280*, 1723-1729.

(6) Gray, H. B.; Winkler, J. R. *Annu. Rev. Biochem.* **1996**, *65*, 537-561.

(7) Drennan, C. L.; Huang, S.; Drummond, J. T.; Matthews, R. G.; Ludwig, M. L. *Science* **1994**, *266*, 1669-1674.

(8) Matthews, R. G.; Smith, A. E.; Zhou, Z. H. S.; Taurog, R. E.; Bandarian, V.; Evans, J. C.; Ludwig, M. *Helv. Chim. Acta.* **2003**, *86*, 3939-3954.

(9) Evans, D. H. *Chem. Rev.* **2008**, *108*, 2113-2144.

(10) Bockris, J. O.; Khan, S. U. M. *Appl. Phys. Lett.* **1984**, *45*, 913-913.

(11) Trasatti, S. *Electrochim Acta.* **1990**, *35*, 269-271.

(12) Trasatti, S. *Pure Appl. Chem.* **1986**, *58*, 955-966.

(13) Reiss, H. *J. Electrochem. Soc.* **1988**, *135*, C247-C258.

(14) Reiss, H.; Heller, A. *J. Phys. Chem.* **1985**, *89*, 4207-4213.

(15) Fawcett, W. R. *Langmuir* **2008**, *24*, 9868-9875.

(16) Kelly, C. P.; Cramer, C. J.; Truhlar, D. G. *J. Phys. Chem. B* **2006**, *110*, 16066-16081.

(17) Hansen, W. N.; Hansen, G. J. *Phys. Rev. A Gen. Phys.* **1987**, *36*, 1396-1402.

(18) Hansen, W. N. K., D. M. *J. Electroanal. Chem.* **1979**, *100*, 493-500.

(19) Gomer, R.; Tryson, G. *J. Chem. Phys.* **1977**, *66*, 4413.

(20) Cendagorta, J. R.; Ichiye, T. *J. Phys. Chem. B* **2015**, *119*, 9114-9122.

(21) Kathmann, S. M.; Kuo, I. F.; Mundy, C. J.; Schenter, G. K. *J. Phys. Chem. B* **2011**, *115*, 4369-4377.

(22) Kathmann, S. M.; Kuo, I. F.; Mundy, C. J. *J. Am. Chem. Soc.* **2008**, *130*, 16556-16561.

(23) Sokhan, V. P.; Tildesley, D. J. *Mol. Phys.* **1997**, *92*, 625-640.

(24) Tsushima, S.; Wahlgren, U.; Grenthe, I. *J. Phys. Chem. A* **2006**, *110*, 9175-9182.

(25) Uudsemaa, M.; Tamm, T. *J. Phys. Chem. A* **2003**, *107*, 9997-10003.

(26) Li, J. F., C. L.; Chen, J. L.; Bashford, D.; Noodleman, L. *Inorg. Chem.* **1996**, *35*, 4694-4702.

(27) Blumberger, J.; Bernasconi, L.; Tavernelli, I.; Vuilleumier, R.; Sprik, M. *J. Am. Chem. Soc.* **2004**, *126*, 3928-3938.

(28) Torres, R. A.; Lovell, T.; Noodleman, L.; Case, D. A. *J. Am. Chem. Soc.* **2003**, *125*, 1923-1936.

(29) Baik, M. H.; Schauer, C. K.; Ziegler, T. *J. Am. Chem. Soc.* **2002**, *124*, 11167-11181.

(30) Baik, M. H.; Ziegler, T.; Schauer, C. K. *J. Am. Chem. Soc.* **2000**, *122*, 9143-9154.

(31) Roy, L. E.; Jakubikova, E.; Guthrie, M. G.; Batista, E. R. *J. Phys. Chem. A* **2009**, *113*, 6745-6750.

(32) Jiao, D.; Leung, K.; Rempe, S. B.; Nenoff, T. M. *J. Chem. Theory. Comput.* **2011**, *7*, 485-495.

(33) Jaque, P.; Marenich, A. V.; Cramer, C. J.; Truhlar, D. G. *J. Phys. Chem. C* **2007**, *111*, 5783-5799.

(34) Blumberger, J.; Sprik, M. *J. Phys. Chem. B* **2005**, *109*, 6793-6804.

(35) Jiao, D. A.; Leung, K.; Rempe, S. B.; Nenoff, T. M. *J. Chem. Theory Comput.* **2011**, *7*, 485-495.

(36) Cramer, C. J. T., D. G. *Chem. Rev.* **1999**, *99*, 2161-2200.

(37) Fennell, C. J.; Dill, K. A. *J. Stat. Phys.* **2011**, *145*, 209-226.

(38) Donald, W. A.; Williams, E. R. *Pure Appl. Chem.* **2011**, *83*, 2129-2151.

(39) Donald, W. A.; Leib, R. D.; Demireva, M.; O'Brien, J. T.; Prell, J. S.; Williams, E. R. *J. Am. Chem. Soc.* **2009**, *131*, 13328-13337.

(40) Donald, W. A.; Leib, R. D.; O'Brien, J. T.; Bush, M. F.; Williams, E. R. *J. Am. Chem. Soc.* **2008**, *130*, 3371-3381.

(41) Donald, W. A.; Williams, E. R. *J. Phys. Chem. B* **2010**, *114*, 13189-13200.

(42) Donald, W. A.; Williams, E. R. *J. Am. Soc. Mass. Spectr.* **2010**, *21*, 615-625.

(43) Donald, W. A.; Demireva, M.; Leib, R. D.; Aiken, M. J.; Williams, E. R. *J. Am. Chem. Soc.* **2010**, *132*, 4633-4640.

(44) Demireva, M.; Williams, E. R. *J. Am. Soc. Mass. Spectr.* **2010**, *21*, 1133-1143.

(45) Donald, W. A.; Leib, R. D.; O'Brien, J. T.; Williams, E. R. *Chemistry* **2009**, *15*, 5926-5934.

(46) Prell, J. S.; O'Brien, J. T.; Holm, A. I. S.; Leib, R. D.; Donald, W. A.; Williams, E. R. *J. Am. Chem. Soc.* **2008**, *130*, 12680-12689.

(47) O'Brien, J. T.; Prell, J. S.; Holm, A. I. S.; Williams, E. R. *J. Am. Soc. Mass. Spectr.* **2008**, *19*, 772-779.

(48) Donald, W. A.; Williams, E. R. *J. Phys. Chem. A* **2008**, *112*, 3515-3522.

(49) Donald, W. A.; Leib, R. D.; O'Brien, J. T.; Holm, A. I. S.; Williams, E. R. *Proc. Natl. Acad. Sci. U.S.A.* **2008**, *105*, 18102-18107.

(50) Leib, R. D.; Donald, W. A.; O'Brien, J. T.; Bush, M. F.; Williams, E. R. *J. Am. Chem. Soc.* **2007**, *129*, 7716-7717.

(51) Leib, R. D.; Donald, W. A.; Bush, M. F.; O'Brien, J. T.; Williams, E. R. *J. Am. Soc. Mass. Spectr.* **2007**, *18*, 1217-1231.

(52) Leib, R. D.; Donald, W. A.; Bush, M. F.; O'Brien, J. T.; Williams, E. R. *J. Am. Chem. Soc.* **2007**, *129*, 4894-4895.

(53) Fecko, C. J.; Eaves, J. D.; Loparo, J. J.; Tokmakoff, A.; Geissler, P. L. *Science* **2003**, *301*, 1698-1702.

(54) Fecko, C. J.; Loparo, J. J.; Roberts, S. T.; Tokmakoff, A. *J. Chem. Phys.* **2005**, *122*, 054506.

(55) Ohmine, I.; Tanaka, H. *Chem. Rev.* **1993**, *93*, 2545-2566.

(56) Baxendale, J. H. F., E. M.; Keene, J. P. *Proc. Roy. Soc. A* **1965**, *286*, 320.

(57) Buxton, G. V.; Sellers, R. M.; Mccracken, D. R. *J. Chem. Soc. Farad. Trans.* **1976**, *72*, 1464-1476.

(58) Buxton, G. V.; Sellers, R. M. *J. Chem. Soc. Farad. Trans.* **1975**, *71*, 558-567.

(59) Donald, W. A.; Leib, R. D.; Demireva, M.; Williams, E. R. *J. Am. Chem. Soc.* **2011**, *133*, 18940-18949.

(60) Donald, W. A.; Leib, R. D.; Demireva, M.; Negru, B.; Neumark, D. M.; Williams, E. R. *J. Phys. Chem. A* **2011**, *115*, 2-12.

(61) Bush, M. F.; O'Brien, J. T.; Prell, J. S.; Saykally, R. J.; Williams, E. R. *J. Am. Chem. Soc.* **2007**, *129*, 1612-1622.

(62) Wilm, M.; Mann, M. *Anal. Chem.* **1996**, *68*, 1-8.

(63) Wong, R. L.; Paech, K.; Williams, E. R. *Int. J. Mass. Spectrom.* **2004**, *232*, 59-66.

(64) Guan, S. H.; Marshall, A. G. *Int. J. Mass. Spectrom.* **1996**, *157*, 5-37.

(65) Prell, J. S.; O'Brien, J. T.; Williams, E. R. *J. Am. Soc. Mass. Spectr.* **2010**, *21*, 800-809.

(66) Bush, M. F.; Saykally, R. J.; Williams, E. R. *Int. J. Mass. Spectrom.* **2006**, *253*, 256-262.

(67) Klots, C. E. *J. Chem. Phys.* **1985**, *83*, 5854-5860.

(68) Heiles, S.; Cooper, R. J.; DiTucci, M. J.; Williams, E. R. *Submitted*.

(69) Ciavatta, L.; Ferri, D.; Palombari, R. *J. Inorg. Nucl. Chem.* **1980**, *42*, 593-598.

(70) Fenwick, F. *J. Am. Chem. Soc.* **1926**, *48*, 860-870.

(71) Cooper, R. J.; Heiles, S.; DiTucci, M. J.; Williams, E. R. *J. Phys. Chem. A* **2014**, *118*, 5657-5666.

(72) Tielrooij, K. J.; Garcia-Araez, N.; Bonn, M.; Bakker, H. J. *Science* **2010**, *328*, 1006-1009.

(73) Smith, J. D.; Saykally, R. J.; Geissler, P. L. *J. Am. Chem. Soc.* **2007**, *129*, 13847-13856.

(74) Wachter, W.; Kunz, W.; Buchner, R.; Hefter, G. *J. Phys. Chem. A* **2005**, *109*, 8675-8683.

(75) Cappa, C. D.; Smith, J. D.; Messer, B. M.; Cohen, R. C.; Saykally, R. J. *J. Phys. Chem. B* **2006**, *110*, 5301-5309.

(76) Nam, S. H.; Park, H. S.; Lee, M. A.; Cheong, N. R.; Song, J. K.; Park, S. M. *J. Chem. Phys.* **2007**, *126*, 224302.

(77) Bartmess, J. E. *J. Phys. Chem.* **1994**, *98*, 6420-6424.

(78) Bratsch, S. G. *J. Phys. Chem. Ref. Data* **1989**, *18*, 1-21.

(79) Debethune, A. J.; Licht, T. S.; Swendeman, N. *J. Electrochem. Soc.* **1959**, *106*, 616-625.

(80) Yee, E. L. C., R. J.; Guyer, K. L.; Tyma, P. D.; Weaver, M. J. *J. Am. Chem. Soc.* **1979**, *101*, 1131-1137.

(81) Farrell, J. R.; McTigue, P. *J. Electroanal. Chem.* **1982**, *139*, 37-56.

(82) Madden, W. G. G., R.; Mandell, M. J. *J. Phys. Chem.* **1977**, *81*, 2652-2657.

(83) Wardman, P. *J. Phys. Chem. Ref. Data* **1989**, *18*, 1637.

(84) Baxendale, J. H. *Rad. Res. Supp.* **1964**, *4*, 114-138.

7.6 Tables and Figures

M^{2+}	$-\Delta H_{abs}$ (eV)	E^o_{abs} (V)	E^o_{rel}
Cu	4.67 ± 0.13	5.16	0.17[67]
Ni	3.46 ± 0.10	3.95	-1.05
Co	2.50 ± 0.06	2.99	-2.00
Zn	1.36 ± 0.11	1.85	-3.15

Table 7.1. Absolute one-electron reduction enthalpies at 298 K for Cu^{2+}, Ni^{2+}, Co^{2+} and Zn^{2+} obtained from extrapolating linear fits of $-\Delta H_R(n)$ vs $n^{-1/3}$ to infinite cluster size along with the standard uncertainties of these extrapolated values. Absolute and relative reduction potentials obtained from these nanocalorimetry experiments (E^o_{abs} and E^o_{rel}, respectively) are also shown. The one-electron reduction potential of Cu^{2+} relative to the SHE is known from solution-phase electrochemical measurements.

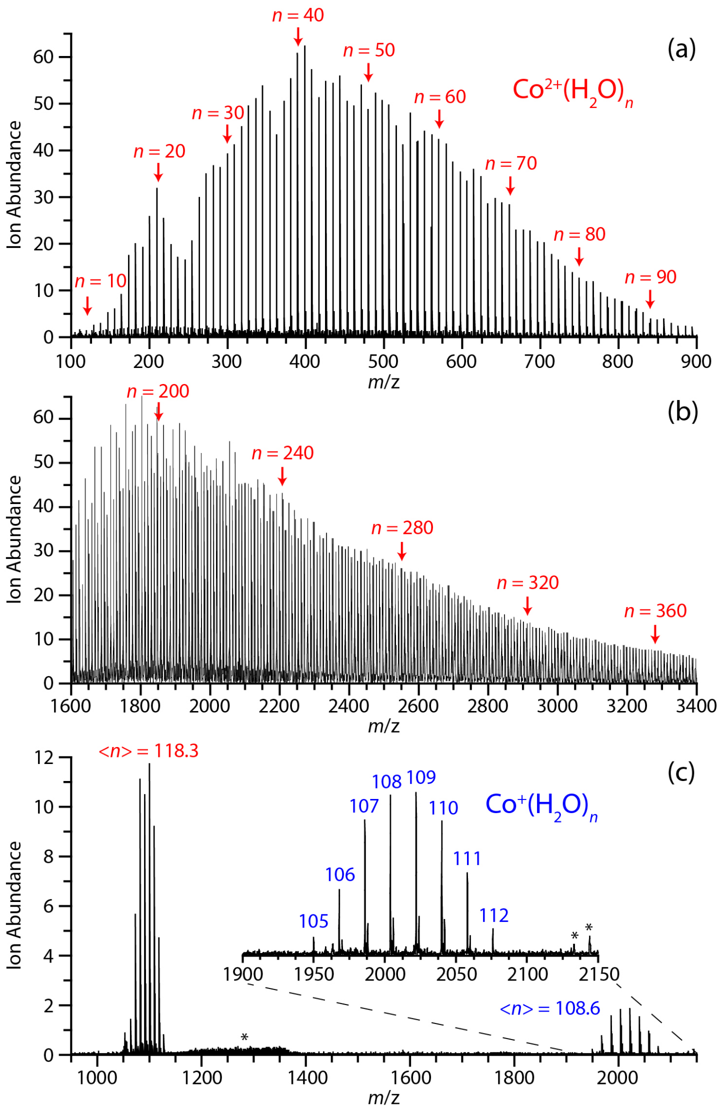

Figure 7.1. Nanoelectrospray mass spectra of $Co^{2+}(H_2O)_n$ ions optimized for (a) smaller and (b) larger cluster sizes, and (c) an electron capture mass spectrum of $Co^{2+}(H_2O)_{118\text{-}122}$ showing the one-electron reduction of Co^{2+} to Co^{+} and loss of 9.7 water molecules due to cluster heating. Asterisks label electronic noise peaks.

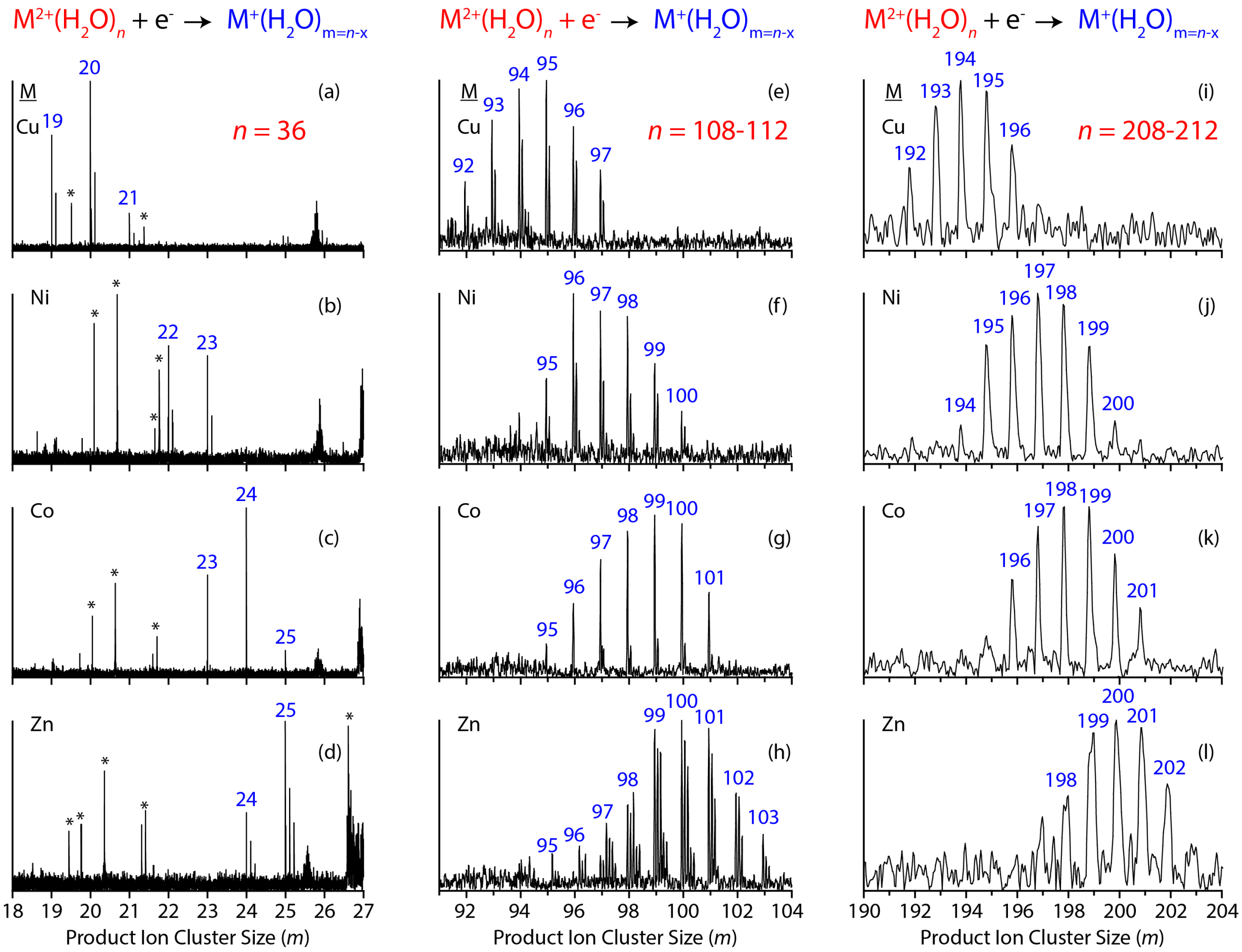

Figure 7.2. Product ion mass spectra resulting from EC of $M^{2+}(H_2O)_n$ clusters for M = Cu, Ni, Co, and Zn where n = 36 (a–d), 108-112 (e–h), and 208–212 (i–l). For the n = 36 clusters, a single precursor ion is isolated, whereas for the larger cluster sizes, distributions of 5 adjacent precursor ions are isolated. The abscissas are plotted on a scale that shows the cluster size of the product ions, m, to facilitate comparisons between ions.

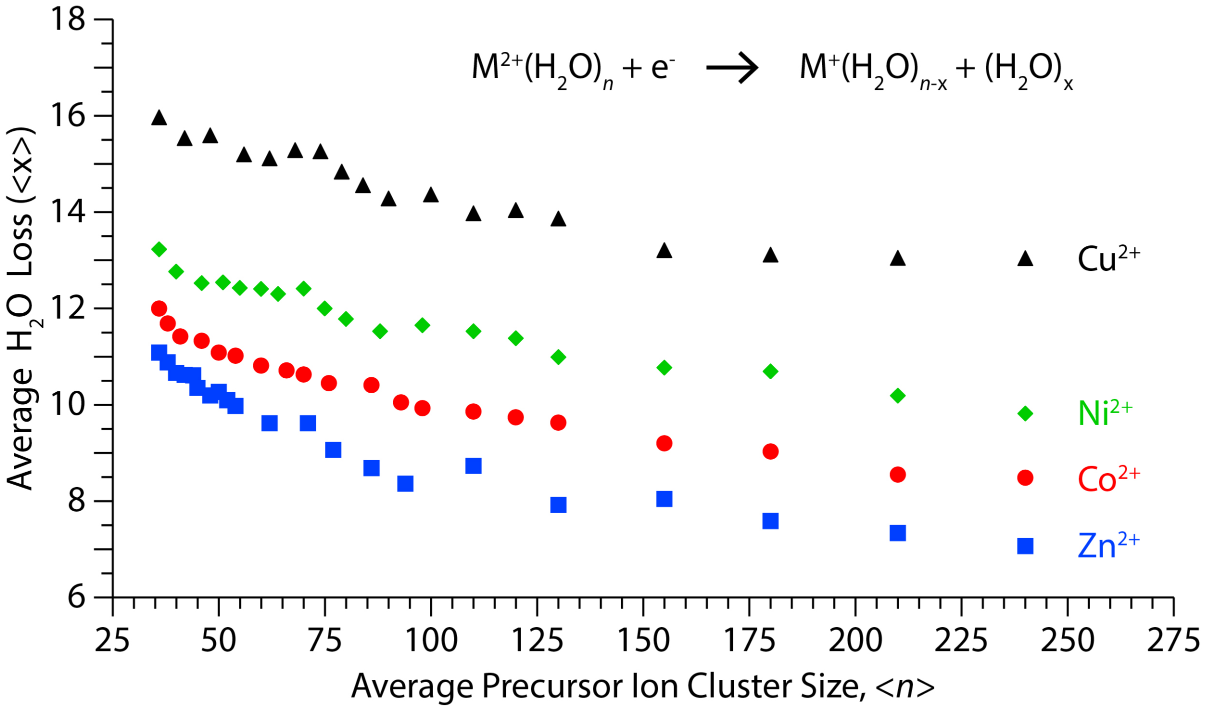

Figure 7.3. Average number of water molecules lost ⟨x⟩ upon electron capture by $M^{2+}(H_2O)_n$ clusters, where M = Cu, Ni, Co, and Zn with between 36 and 240 water molecules attached.

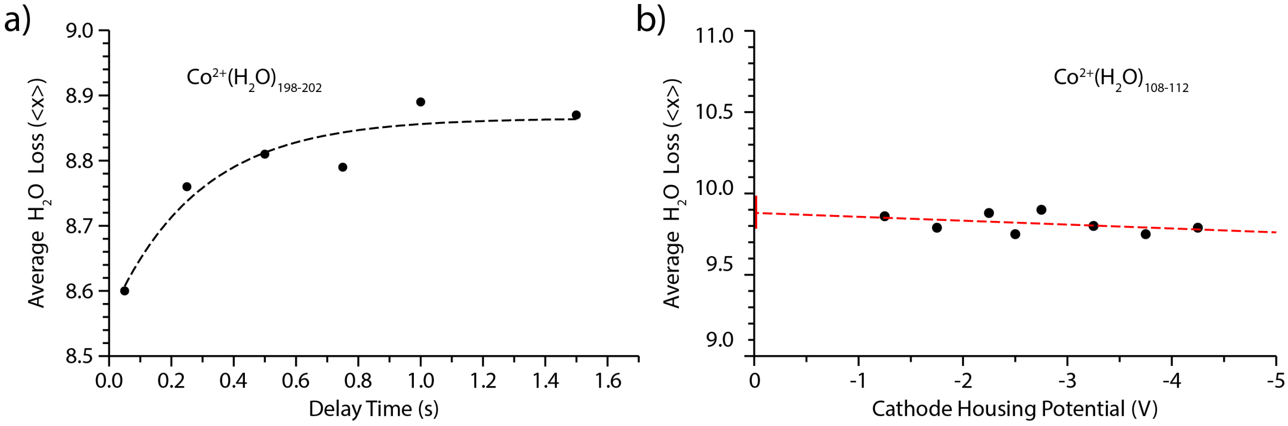

Figure 7.4. (a) Measurements of ⟨x⟩ due to EC by $Co^{2+}(H_2O)_{198-202}$ as a function of the delay time that occurs after electron irradiation but before ion detection. These data are fitted with an exponential function (dashed line) and show the effects of a kinetic shift. (b) Measurements of ⟨x⟩ due to EC by $Co^{2+}(H_2O)_{108-112}$ as the potential applied to the cathode is varied. A least-squares linear fit is shown as a red dashed line and is extrapolated to the vertical intercept with a standard uncertainty of 0.1 water molecules.

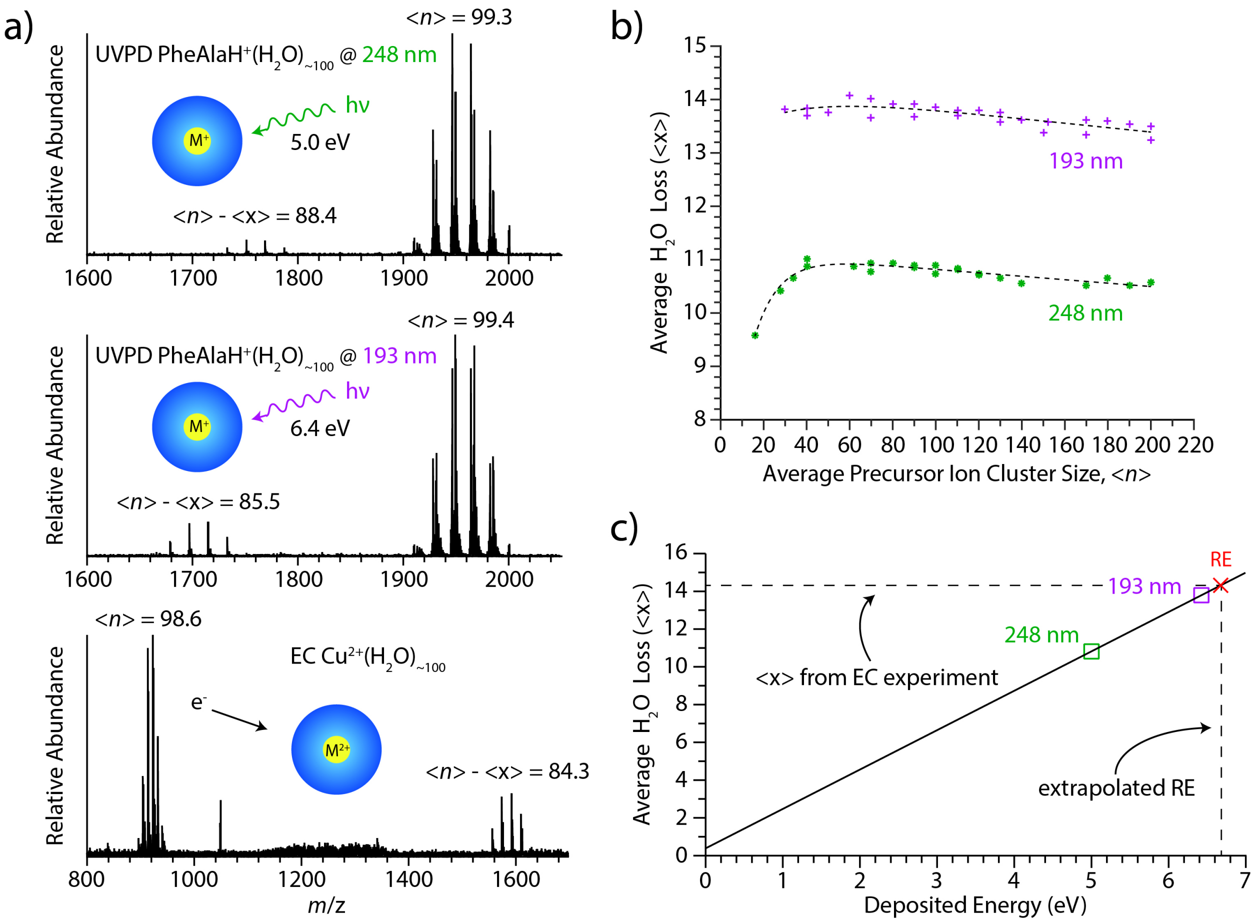

Figure 7.5. (a) Mass spectra of laser photodissociation experiments performed on PheAlaH$^+$(H$_2$O)$_{\sim100}$ clusters for λ = 248 nm (top) and λ = 193 nm (middle), and an EC mass spectrum of Cu^{2+}(H$_2$O)$_{\sim100}$ (bottom). The average cluster sizes of precursor and product ions are labeled as $\langle n \rangle$ and $\langle n \rangle - \langle x \rangle$, respectively. (b) Combined average water loss data measured for PheAlaH$^+$(H$_2$O)$_n$ and Anilinium(H$_2$O)$_n$ using 193 and 248 nm light. Biexponential fits to these data are shown as dashed lines. (c) An example of a linear calibration curve derived from the water loss data taken from (b) for n = 100. This fit is used to extrapolate a RE for Cu^{2+}(H$_2$O)$_{\sim100}$ based on the value of $\langle x \rangle$ measured in the EC experiment.

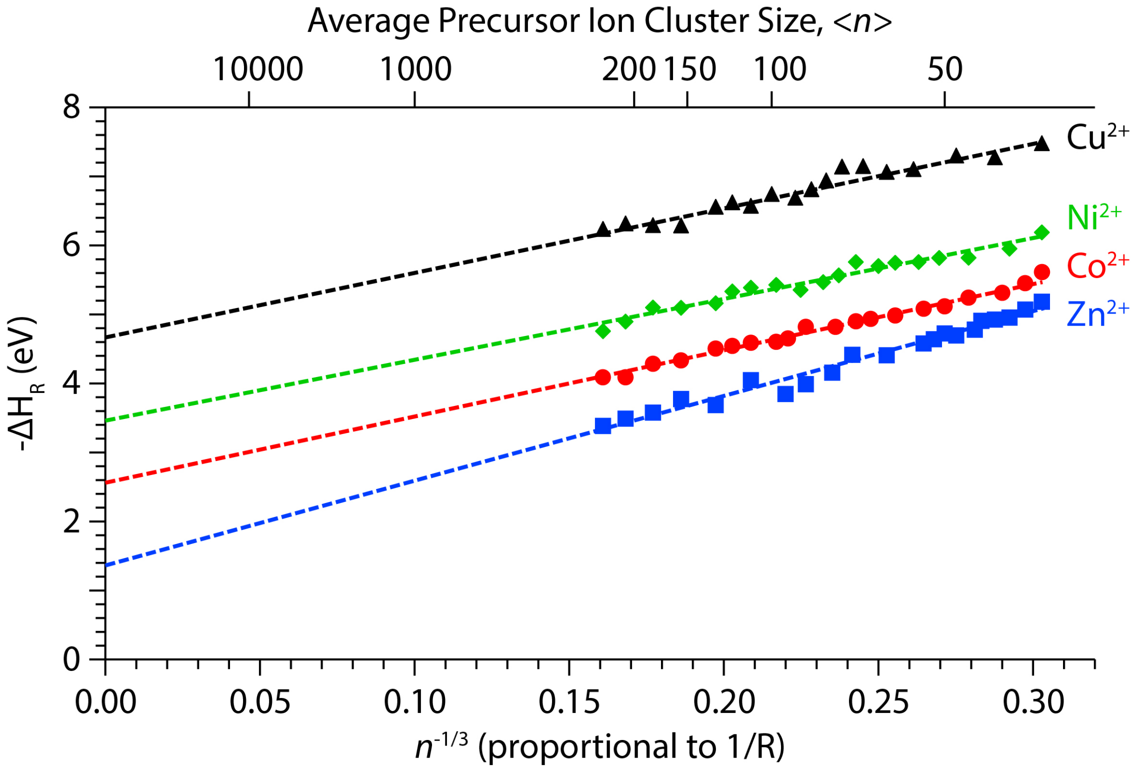

Figure 7.6. Ion–electron recombination enthalpies as a function of $n^{-1/3}$ for $M^{2+}(H_2O)_n$ clusters, where M = Cu, Ni, Co and Zn for $36 \leq n \leq 240$. Linear regression best-fit lines to these data (dashed) are extrapolated to infinite cluster size to obtain absolute solution-phase reduction enthalpies. The average precursor ion cluster sizes for these data are shown on the top horizontal axis.

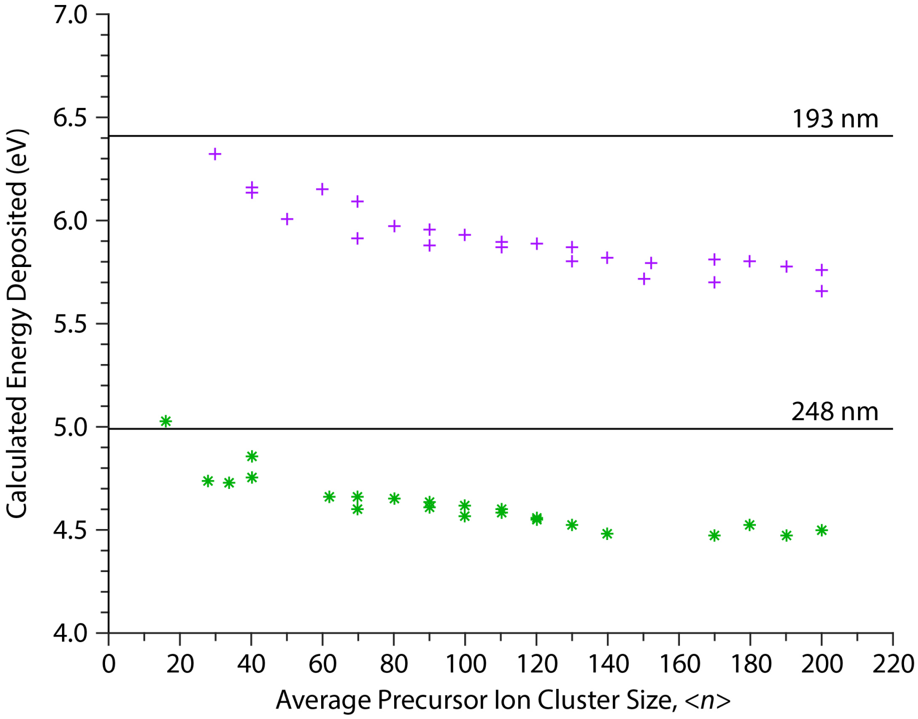

Figure 7.7. Calculated energy deposition in PheAlaH$^+$(H$_2$O)$_n$ and Anilinium(H$_2$O)$_n$ clusters with an average precursor size of ⟨n⟩ upon the absorption of a 193 nm (triangles) and 248 nm (asterisks) photon. Values are obtained from the average number of water molecules lost, their binding energies (obtained from the TLDM), and the energy partitioning model (see text for details). The actual energy deposition, which corresponds to the photon energy, is shown as solid black lines.

Chapter 8

Summary and Outlook

The research presented herein examines various phenomena related to ion hydration including the structure, energetics, and reactivity of hydrated ions. By coupling mass spectrometry and infrared photodissociation spectroscopy, the step-wise hydration structures of single ions were elucidated. In chapter 2, the origin of enhanced abundances in the mass spectra of hydrated alkali metal ions was investigated. Measured BIRD rate constants linked the high abundances of "magic number" clusters for Cs^+, Rb^+, and K^+ with 18 and 20 water molecules attached to their inherently high stabilities. The structures of these MNCs were probed with IRPD spectroscopy, which reveal a spectral simplification in the free O–H stretching region (~3650–3800 cm^{-1}) that is consistent with the formation of cage-like, clathrate hydration structures. In these clathrate hydrates, each water molecule participates in three hydrogen bonds leading to a highly symmetric structure with increased stability. These data represent the first spectroscopic evidence for alkali metal ion clathrate formation, and validate the predictions of earlier theoretical calculations. We demonstrated that for the smaller alkali metal ions Na^+ and Li^+, clathrate formation is not favored due to strong ion-dipole interactions between these ions and water. These interactions disrupt the hydrogen bonding structure of water and inhibit clathrate formation. Whether an ion is a suitable guest in a clathrate therefore depends strongly on its charge density and the delicate balance between ion-water and water-water interactions.

Detailed interactions between an ion and water molecules can account for the bulk properties of the ion in aqueous solution, and this was studied in detail in Chapter 3 for the common protein denaturant guanidinium. Guanidinium is routinely used in thousands of laboratories worldwide to study aspects of protein folding, yet the molecular origins of how this ion denatures proteins remains unclear. IRPD spectroscopy and computational chemistry were used to investigate hydration motifs in the first and second hydration shells of guanidinium, and this was related to its efficacy as a denaturant. In particular, it was determined that guanidinium has a surfactant-like character. Guanidinium can form hydrogen bonds with water molecules in the plane of the ion, but above and below the plane of the ion it is not energetically favorable for water to interact with guanidinium. Molecular orbital calculations indicate a lack of orbital density around guanidinium's carbon atom, explaining why water molecules do not attach there despite the partial positive charge on the atom. These combined experimental and computational data suggest that guanidinium is so effective as a protein denaturant because of its amphiphilic nature. The hydrophobic parts of the ion can associate with hydrophobic portions of proteins including their backbones as well as aromatic and aliphatic side chains. Previous MD simulations provide extensive evidence for the prevalence of these interactions in solution, and the hydration structures assigned herein are consistent with this mechanism. The noncovalent interactions between proteins and guanidinium stabilize more extended conformations of a protein and lower the barrier to unfolding.

In addition to studying the hydration of single ions, the hydration of ion pairs was investigated in chapter 4. IRPD spectra of $PbNO_3^+$ and $SrNO_3^+$ with up to 30 water molecules attached were recorded and reveal significant differences in their hydration motifs. The onset of hydrogen bonded resonances in the bonded O–H region (3000–3600 cm^{-1}) indicate that the inner hydration shell of $[PbNO_3]^+(H_2O)_n$ is complete by $n = 5$ whereas the inner hydration shell of $[SrNO_3]^+(H_2O)_n$ is not complete until $n = 6$ despite the identical size of these ions. Comparisons between measured and calculated spectra reveal that Pb(II) is asymmetrically solvated by water with a noticeable void in its coordination sphere. Natural bond orbital calculations suggest that the anisotropic hydration of Pb(II) is the result of the ion's "inert pair" of electrons. Calculated resonance delocalization energies indicate that this region of asymmetric electron density is the result of electron transfer from the nitrate and water ligands into vacant 6p orbitals on lead. These differences in inner shell hydration motifs propagate into higher hydration shells, and spectral differences between these ions are observed until $n = 25$. The IRPD spectra of $[SrNO_3]^+(H_2O)_n$ indicate that partial clathrate structures may form around the metal ion, but that this is likely disrupted for $[PbNO_3]^+(H_2O)_n$. These experiments provide insight into how contact ion pairs are hydrated, and demonstrate that the electronic structure of an ion can influence how it is solvated.

The cluster approach to understanding ion hydration was also applied to more extensively solvated ions with hundreds of water molecules attached. Obtaining detailed, isomeric structures is generally not possible for these larger clusters, but the effects of an ion on the hydrogen bond network at both the surface and interior of an aqueous nanodrop can be probed. In chapter 5, the effects of ions on inhibiting the onset of crystallinity in cold nanodrops were investigated. IRPD spectra at 133 K of nanodrops doped with a single La^{3+} ion and containing between 50 and 550 water molecules revealed significant spectral changes with increasing cluster size. Bands corresponding to liquid water/amorphous ice and crystalline ice occur at 3400 cm^{-1} and 3200 cm^{-1}, respectively. The onset of crystallinity was exhibited by a decrease in intensity of the liquid-like band and an increase in intensity of the crystalline ice band. It was observed that the onset of crystallinity occurs at ~375 water molecules, an offset of about 100 water molecules from the corresponding neutral droplets. This frustration of crystallization indicates that La^{3+} can influence the hydrogen bond structure of water molecules located remotely from the ion, a point of contentious debate in the current literature. Molecular dynamics simulations on the $Mo^{3+}(H_2O)_{550}$ cluster support the idea that a trivalent ion can induce long-range structural changes in water. In-house software in MATLAB was written to analyze these simulations, and it was found that the electric field of Mo^{3+} can orient water molecules located up to ~1 nm away from the ion. These experimental and computational results provide a molecular-level explanation for the macroscopic phenomenon of freezing point depression.

In chapter 6, the effects of ion charge state and polarity on nanodrop surface structure were investigated. It was observed that multiply charged ions severely disrupt optimal hydrogen bonding at the surfaces of nanodrops containing up to ~40 water molecules, as evidenced by the presence of multiple bands in the free O–H region. In relation to this, it was also found that the frequencies of the O–H stretches of surface water molecules are strongly influenced by the presence of an ion. These dangling O–H oscillators effectively act as antennae that report on the electrostatic environment of the nanodrop surface. The frequency shifts of surface O–H stretches in ion-containing nanodrops where characterized by IRPD spectroscopy. Positively charged ions including La^{3+}, Ca^{2+} and Na^+ tend to red-shift these stretches whereas the negatively charged ions SO_4^{2-} and I^- induce a blue-shift. These frequency shifts were qualitatively reproduced by a computationally inexpensive point charge model that shows the frequency shift is a Stark shift from the ion's electric field. Interestingly, the measured Stark shift is more pronounced for clusters containing multiply charged cations with ~100 or fewer water molecules. This more pronounced Stark shifting was attributed to ion-induced patterning effects in highly charged nanodrops, and serves as a spectroscopic signature for ion-induced patterning that extends to the nanodrop surface. Furthermore, these data were extrapolated to infinite cluster size to obtain the free O–H frequency of neutral water at the air-water interface. In this way, the surface stretches of bulk interfacial water were characterized with better precision than what has been achieved by SFG spectroscopy. These extrapolated measurements also reveal how surface curvature effects can influence the electrostatic environments of nanodrop surfaces.

In addition to these primarily spectroscopic studies, thermodynamic information about the reduction of hydrated metal ions was obtained through ion nanocalorimetry. A new laser-based calibration method for deducing ion-electron recombination energies was introduced in chapter 7. The one-electron reductions of Cu^{2+} in nanodrops with between 36 and 240 water molecules were used to deduce an absolute reduction enthalpy for the Cu^{2+}/Cu^{+} redox pair. These measurements were used to calculate a more accurate value for the absolute standard hydrogen electrode, which can be used to anchor an absolute electrochemical scale. The one-electron reductions of Ni^{2+}, Co^{2+}, and Zn^{2+} were also investigated, and the relative reduction potentials of these ions were measured for the first time. The values of the relative potentials indicate that these ions are also reduced in solution, but that their one-electron reductions are not measurable by convention electrochemical techniques because of potential inversion.

As a whole, the experiments presented herein demonstrate the power of combining FT-ICR mass spectrometry with ion activation techniques to extract structural and thermodynamic information from cluster measurements. These experiments have offered insights into the noncovalent interactions that govern complex processes ranging from protein denaturation to droplet crystallization. Future experiments will certainly focus on more complex systems. With the installation of a $AgGaSe_2$ crystal to our OPO/OPA system, it should be possible to obtain structural information about hydrated ions in the mid-IR region (~1000 – 2800 cm^{-1}). This region includes C=O, N=O, and S=O stretches as well and O–H and N–H bends. A promising application of this laser extension is in the study of ion pairs. Ion pairing between Ce^{3+} and NO_3^- is known to occur in nanodrops containing less than 40 water molecules, but in larger droplets these ions may separate. The transition from contact ion pairing to solvent-separated ion pairing could be monitored spectroscopically by characterizing the frequency shift induced by Ce^{3+} on the N=O stretch. The mid IR extension should further enhance our ability to investigate ion-water and ion-biomolecule interactions, uncovering the origins of specific ion effects such as surface activity and protein stability with unmatched specificity.

Appendix A

Additional Mass Spectra, Infrared Spectra, and Kinetic Data for Guanidinium Hydrates

This appendix is reproduced with permission from
Cooper, R.J.; Heiles, S.; DiTucci, M.J.; Williams, E.R.
"Hydration of Guanidinium: Second Shell Formation at Small Cluster Size"
Journal of Physical Chemistry A **2014**, 118, 5657-5666
© 2014 American Chemical Society

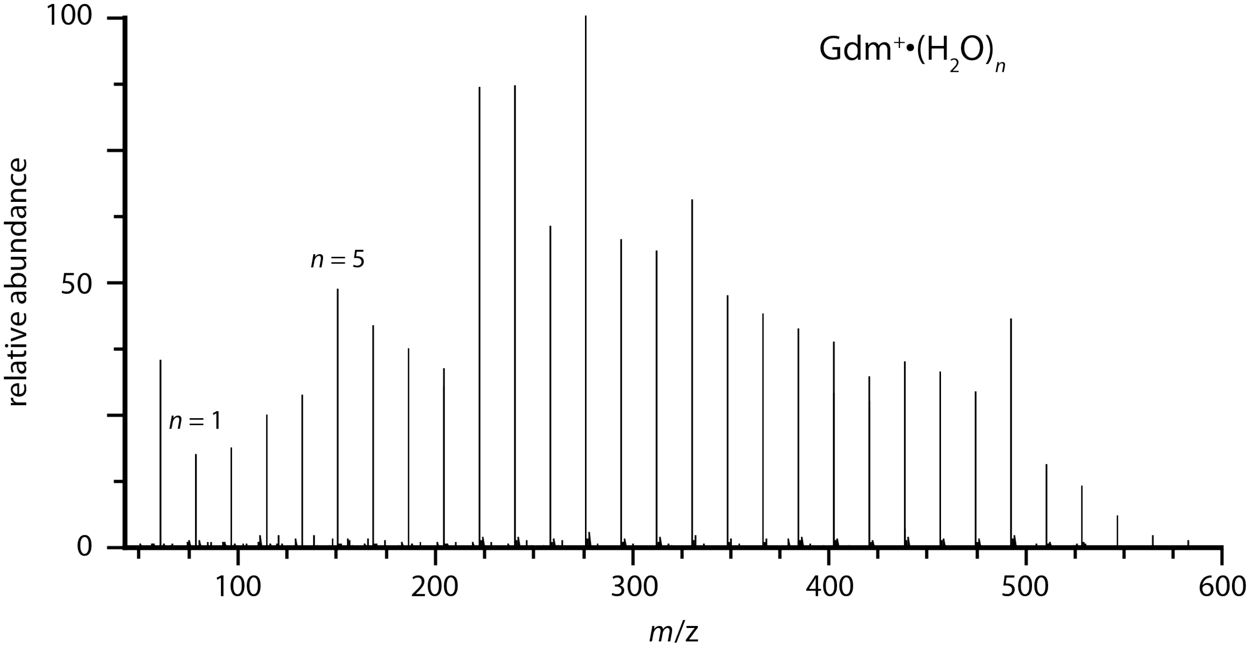

Figure A.1. ESI mass spectrum of $Gdm^+(H_2O)_n$.

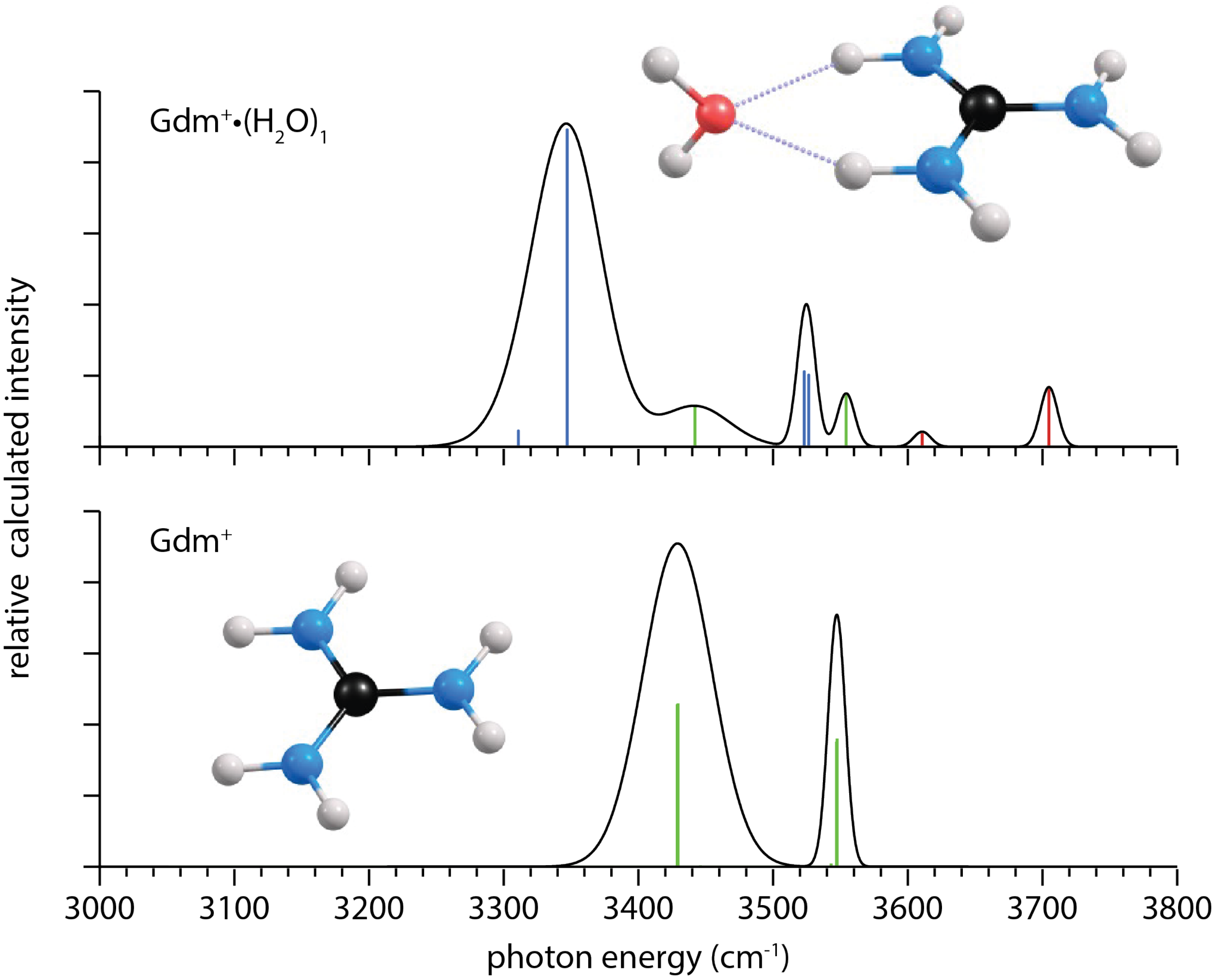

Figure A.2. Calculated IR spectra of Gdm$^+$(H$_2$O)$_1$ (top) and Gdm$^+$ (bottom) at the B3LYP/6-31++G** level of theory. Color-coding is by oscillator type: free O–H (red), free N–H (green), bonded N–H (blue).

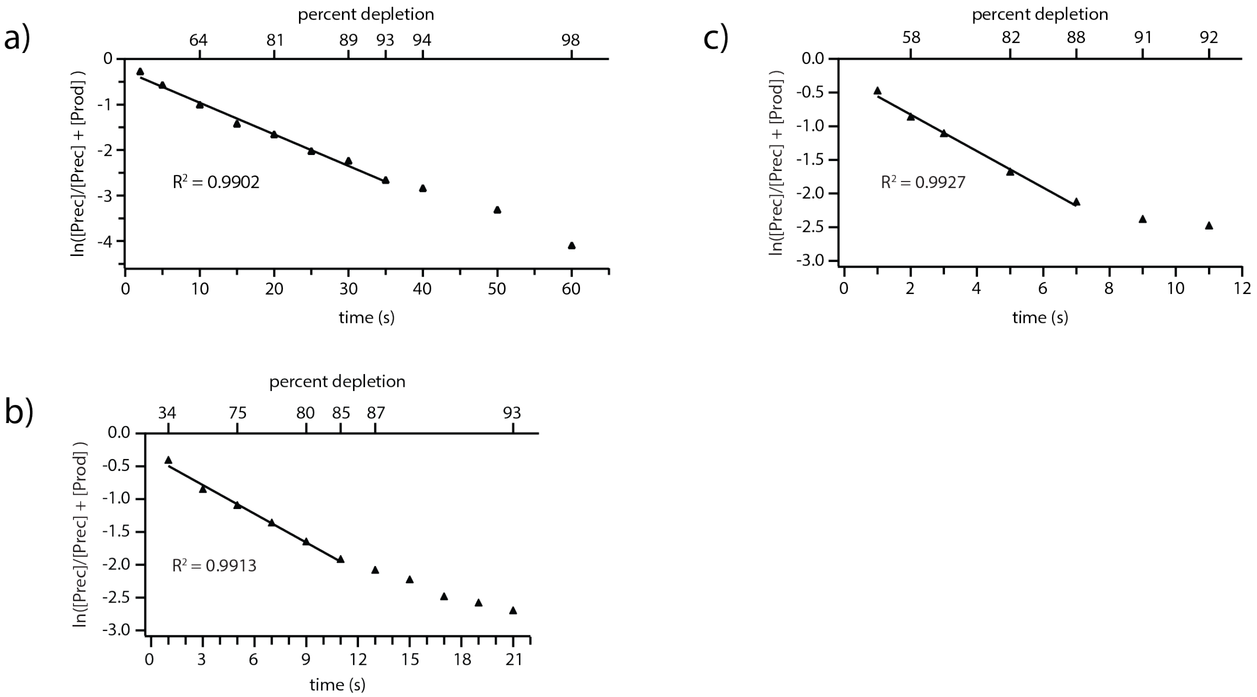

Figure A.3. Photodissociation kinetic data for $Gdm^+(H_2O)_5$ measured at a) 3742 cm^{-1} b) 3725 cm^{-1} and c) 3697 cm^{-1}.

Appendix B

Additional Calculated Spectra, Structures, and Energetics for $PbNO_3^+$ and $SrNO_3^+$ Ion Pairs

This appendix is reproduced with permission from
Cooper, R.J.; Heiles, S.; Williams, E.R.
"Effects of Electronic Structure on the Hydration of $PbNO_3^+$ and
$SrNO_3^+$ Ion Pairs"
Physical Chemistry Chemical Physics **2015**, 17, 15963-15975
© 2015 Royal Society of Chemistry

Table B.1. Calculated 0 K water molecule binding energies (ΔH in kJ/mol) for the reaction $[MNO_3]^+\bullet(H_2O)_n \rightarrow [MNO_3]^+\bullet(H_2O)_{n-1} + H_2O$ at the B3LYP/aug-cc-pVDZ level of theory for the lowest-energy isomers in Table 2.

Ion	n = 2	n = 3	n = 4	n = 5	n = 6	n = 8	n = 10
$[SrNO_3]^+(H_2O)_n$	103	93	81	70	59	47	42
$[PbNO_3]^+(H_2O)_n$	77	66	58	51	36	41	36

Table B.2. Calculated relative Gibbs free energies (in kJ/mol) at 133 K for isomers of $[PbNO_3]^+(H_2O)_4$ and $[SrNO_3]^+(H_2O)_4$.

Ion and Structure	B3LYP/ aug-cc-pVDZ	B3LYP/ 6-31++G**	MP2/ aug-cc-pVDZ	MP2/ 6-31++G**
$SrNO_3^+$_4a	+7.4	+1.6	+3.8	+6.5
$SrNO_3^+$_4b	0.0	0.0	0.0	0.0
$SrNO_3^+$_4c	+2.5	+2.3	+6.2	+7.6
$SrNO_3^+$_4d	+25.1	+26.7	+34.1	+35.8
$PbNO_3^+$_4a	0.0	0.0	0.0	0.0
$PbNO_3^+$_4b	+8.1	+4.5	+8.2	+10.5
$PbNO_3^+$_4c	+9.7	+11.1	+14.5	+18.3
$PbNO_3^+$_4d	+5.9	+7.8	+8.6	+9.1

Table B.3. Calculated Gibbs free energies (in kJ/mol) at 133 K for isomers of $[PbNO_3]^+(H_2O)_5$ and $[SrNO_3]^+(H_2O)_5$. Entries marked with an asterisk (*) indicate that the starting structure relaxed to the indicated structure at the given level of theory.

Ion and Structure	B3LYP/ aug-cc-pVDZ	B3LYP/ 6-31++G**	MP2/ aug-cc-pVDZ	MP2/ 6-31++G**
$SrNO_3^+$_5a	0.0	0.0	0.0	0.0
$SrNO_3^+$_5b	+14.9	+13.9	5c*	5c*
$SrNO_3^+$_5c	+16.6	+15.8	+11.9	+15.0
$SrNO_3^+$_5d	+19.8	+20.9	+22.3	+24.8
$SrNO_3^+$_5e	+22.0	+19.8	+21.2	+22.8
$PbNO_3^+$_5a	+8.9	+10.0	+11.9	+10.5
$PbNO_3^+$_5b	+1.7	+4.5	5c*	+5.8
$PbNO_3^+$_5c	0.0	0.0	0.0	0.0
$PbNO_3^+$_5d	+8.3	+7.5	5c*	5c*

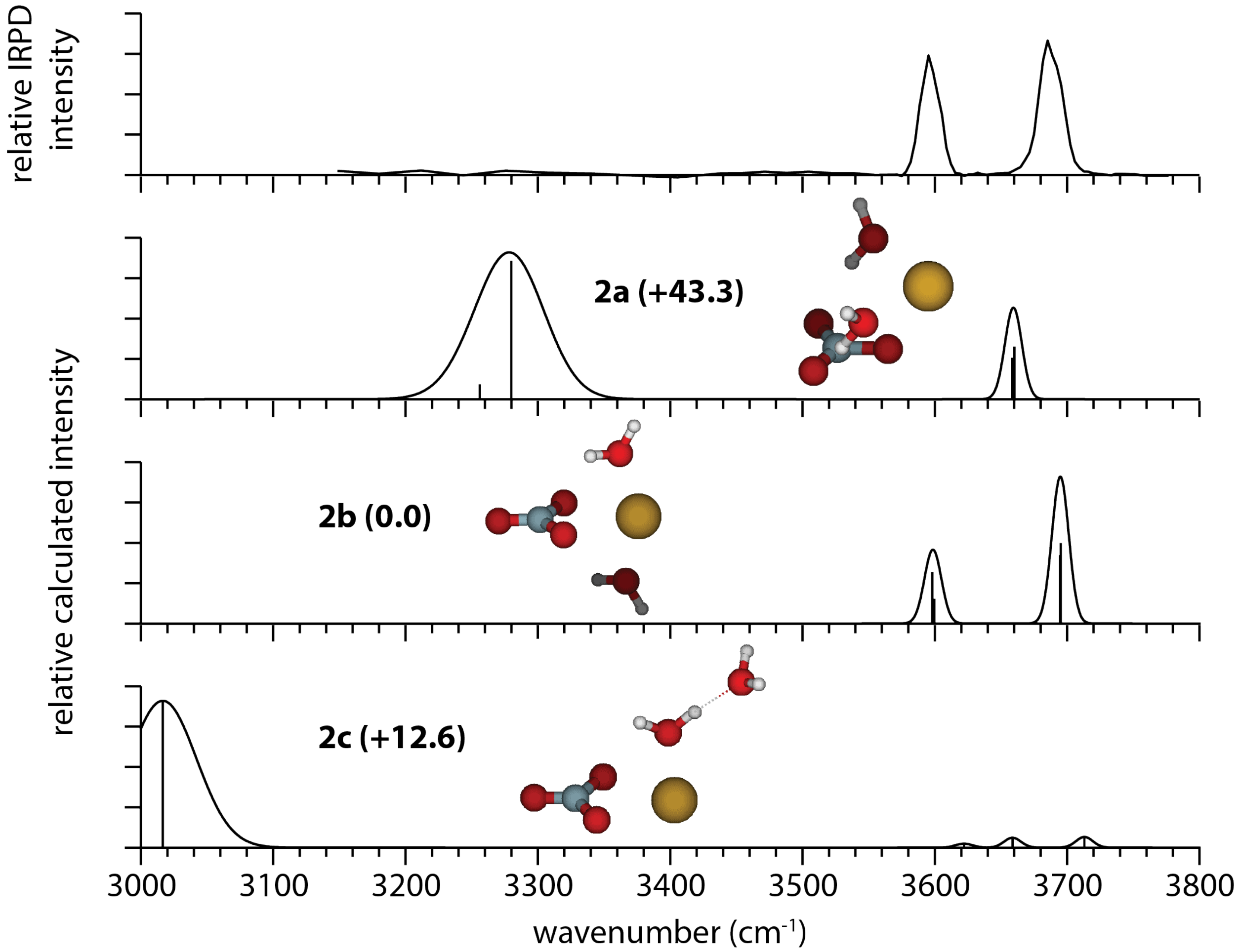

Figure B.1. IRPD spectrum of $[PbNO_3]^+(H_2O)_2$ and calculated spectra of low-energy isomers at the B3LYP/aug-cc-pVDZ level of theory, along with their relative Gibbs free energies in kJ/mol at 133 K.

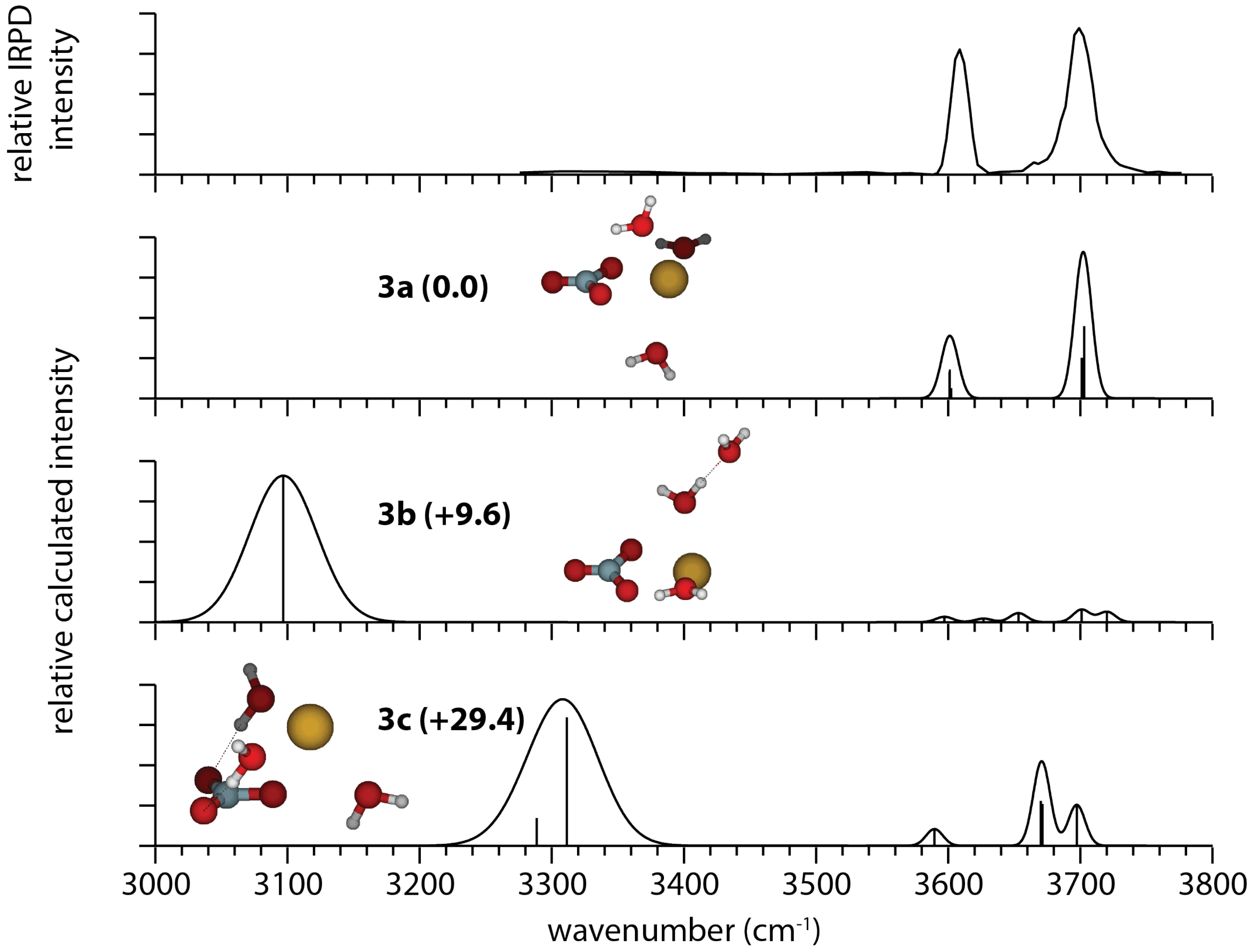

Figure B.2. IRPD spectrum of $[PbNO_3]^+(H_2O)_3$ and calculated spectra of low-energy isomers at the B3LYP/aug-cc-pVDZ level of theory, along with their relative Gibbs free energies in kJ/mol at 133 K.

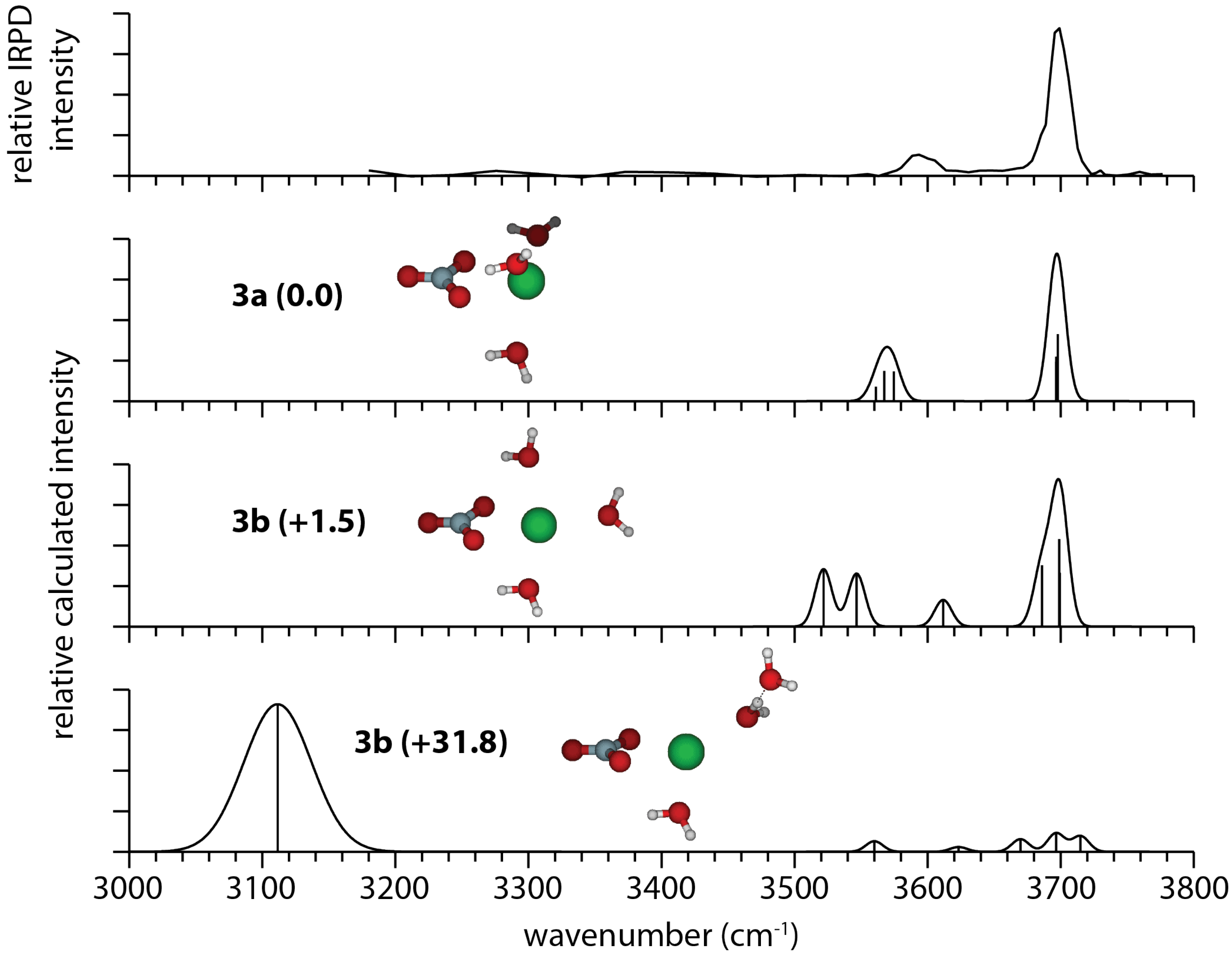

Figure B.3. IRPD spectrum of $[SrNO_3]^+(H_2O)_3$ and calculated spectra of low-energy isomers at the B3LYP/aug-cc-pVDZ level of theory, along with their relative Gibbs free energies in kJ/mol at 133 K.

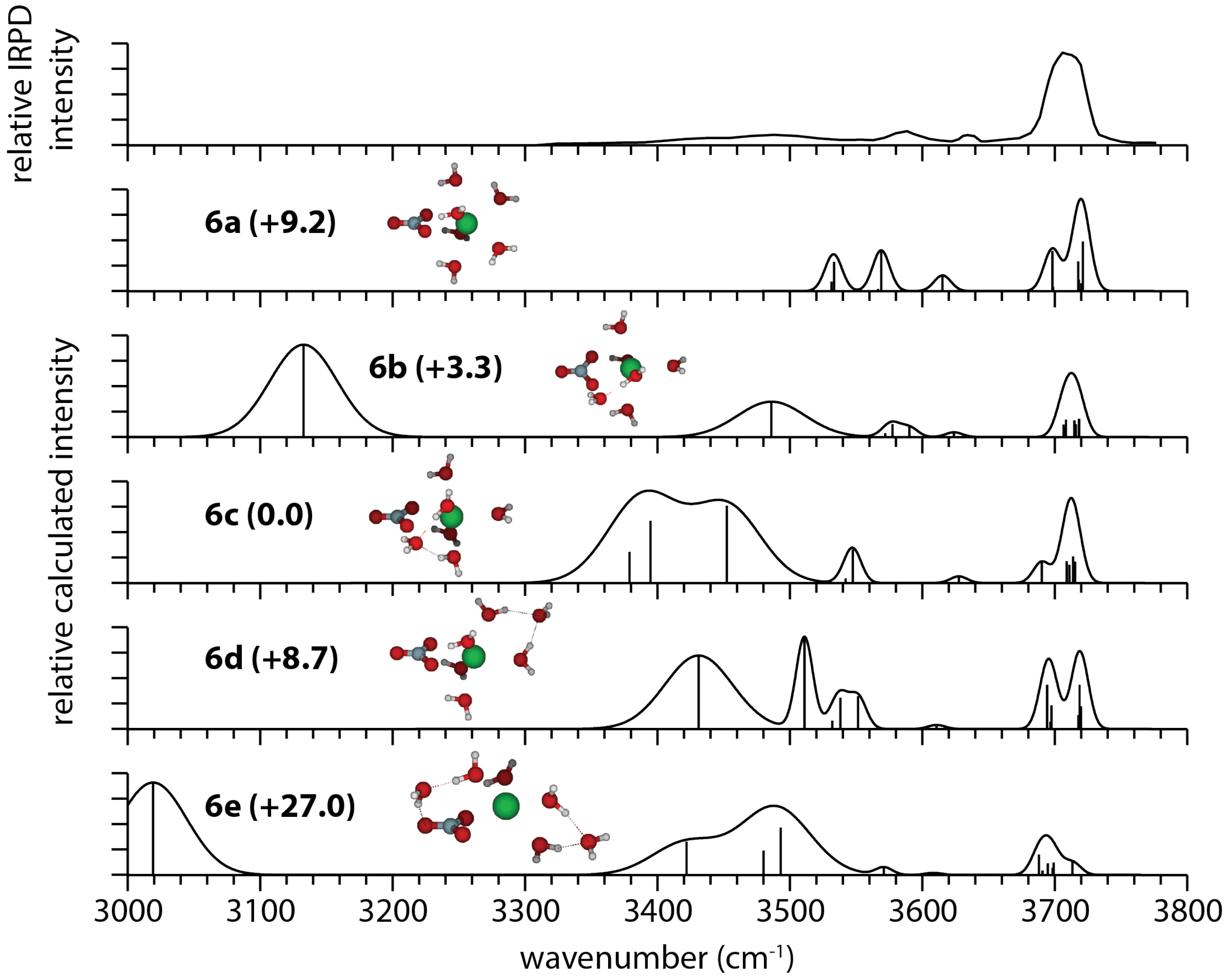

Figure B.4. IRPD spectrum of $[SrNO_3]^+(H_2O)_6$ and calculated spectra of low-energy isomers at the B3LYP/aug-cc-pVDZ level of theory, along with their relative Gibbs free energies in kJ/mol at 133 K.

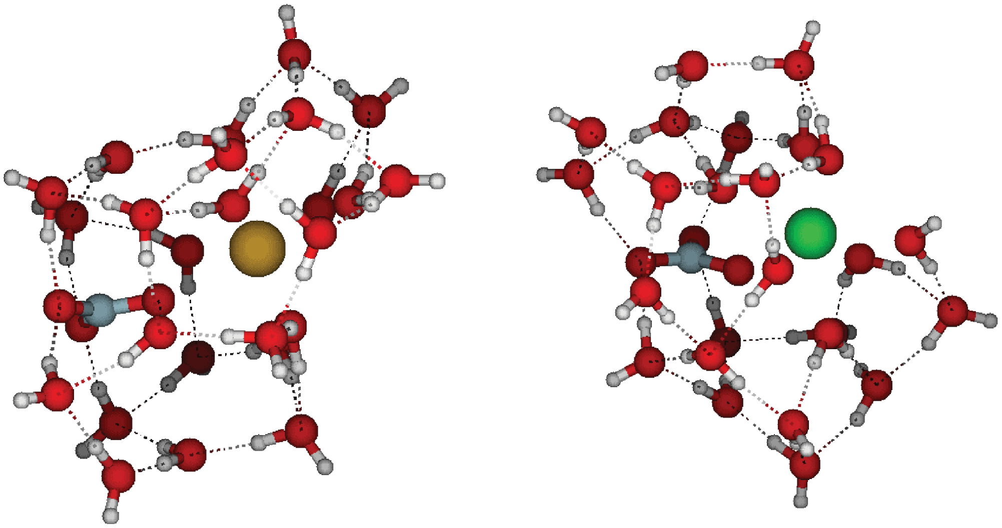

$[PbNO_3]^+(H_2O)_{25}$ $[SrNO_3]^+(H_2O)_{25}$

Figure B.5. Low-energy structures of $PbNO_3^+$ and $SrNO_3^+$ with 25 water molecules attached generated from a conformational search using the OPLS2005 force field. These structures indicate that at this cluster size (which corresponds to a nanodrop diameter of ~1.1 nm) some water molecules are in the third solvation shell.

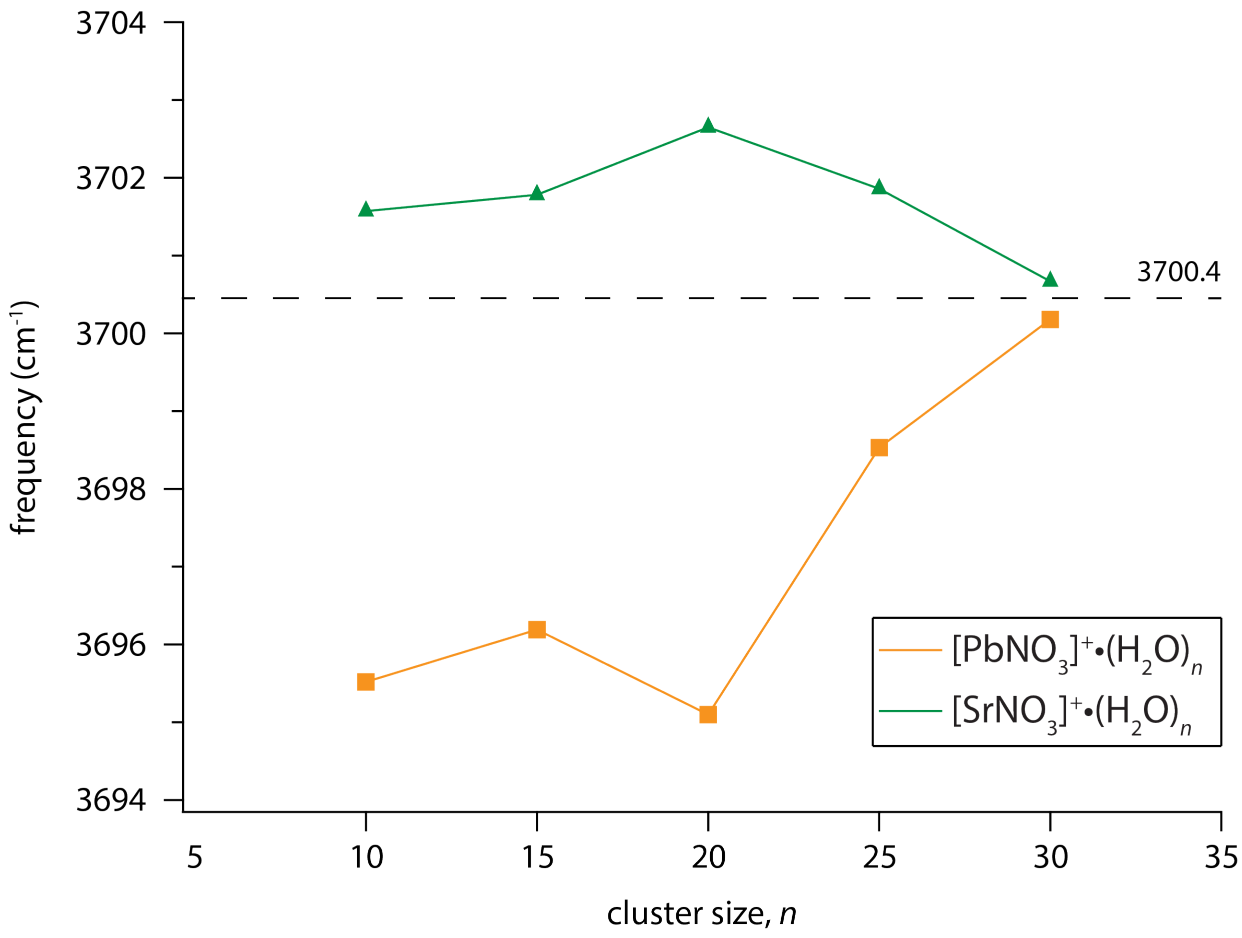

Figure B.6. Centroid frequencies determined by a Gaussian fit of the AAD stretch bands of $[PbNO_3]^+(H_2O)_n$ and $[SrNO_3]^+(H_2O)_n$ with n = 10, 15, 20, 25 and 30 water molecules attached.

Appendix C

Additional Experimental and Computational Details for the Onset Of Crystallinity in Ion-Containing Aqueous Nanodrops

This appendix is reproduced with permission from
Cooper, R.J.; Change, T.M.; DiTucci, M.J.; Williams, E.R.
"Delayed Onset of Crystallinity in Ion-Containing Aqueous Nanodrops"
Journal of the American Chemical Society **2016**, 138, 96-99
© 2016 American Chemical Society

C.1 Methods

C.1.1 IRPD Spectroscopy. IRPD spectra are acquired using a 7.0 T Fourier-transform ion cyclotron resonance mass spectrometer that was recently upgraded from a 2.7 T magnet and that is coupled to a tunable infrared laser.[1] Hydrated lanthanum ions are formed by nanoelectrospray ionization of a ~4 mM solution of $LaCl_3$ (Sigma-Aldrich, St. Louis, MO). Hydrated ions are gently transferred though an electrospray ionization interface[2] by electrostatic lenses into a cylindrical ion cell surrounded by a copper jacket[3] that is regulated to 133 K by a controlled flow of liquid nitrogen. A ~5 s pulse of dry nitrogen gas aids with the trapping and thermal equilibration of the ions. The ions of interest are isolated with stored waveform inverse Fourier transform excitations. An ensemble averaging technique[4] is used to increase the signal-to-noise ratios of the spectra by mass selecting distributions of precursor ions that include between 3 and 11 adjacent cluster sizes. A weighted-average cluster size is reported throughout. The mass-selected clusters are subsequently irradiated with tunable infrared laser light from a OPO/OPA tabletop laser system (LaserVision, Bellevue, WA) pumped by the 1064 nm fundamental of a Nd:YAG laser (Continuum Surelight I-10, Santa Clara, CA) at 10 Hz repetition rate yielding pulse energies between ~1–4 mJ in the spectral range between 3000–3800 cm^{-1}. Irradiation times between 0.5–1 s are used to dissociate the precursor ions by the sequential loss of water molecules, and photodissociation rate constants are obtained from these data. All photodissociation rate constants are corrected for frequency-dependent variations in laser power as well dissociation due to the absorption of blackbody radiation and are plotted as a function of wavelength to give IRPD spectra. Under these conditions, the absorption of one or more photons is sufficient to increase the rate of dissociation such that the IRPD spectra presented here should closely resemble linear absorption spectra.

There are several pieces of evidence that suggest that lanthanum exists as La^{3+} in these clusters, and not as the separate ion pairs, $LaOH^{2+}$ and H_3O^+. Unimolecular dissociation experiments demonstrate that $La^{3+}(H_2O)_n$ clusters are stable with respect to the charge separation reaction, $La^{3+}(H_2O)_n \rightarrow [La(OH)(H_2O)_{n-2}]^{2+} + H_3O^+$ for $n > 17$.[2,5] Measured minimum stable cluster sizes for trivalent lanthanides[5] as well as divalent metal ions[6] are linearly related to their solution phase hydrolysis constants. For nine divalent metal ions where the minimum stable cluster size ranges from zero to 26 water molecules, the hydrolysis constant spans 10 orders of magnitude.[6] IRPD spectroscopy indicates that several of these ions are in their divalent form in clusters at and above their critical size. For example, the minimum stable cluster size for Mn^{2+} is five whereas that for Cu^{2+} is eight.[6] IRPD spectra of both ions as well as computations are consistent with the divalent form in these respective clusters.[7,8] This indicates that the charge separation reaction that occurs when there are fewer water molecules than the critical size does not likely occur in the larger droplets. The stability of trivalent ions in aqueous nanodrops is also supported by gas phase electrochemistry experiments in which Eu^{3+} in clusters containing between 55 and 140 water molecules is directly reduced to form the $Eu^{2+}(H_2O)_n$ products.[9] These results suggest that the nanodrops in these experiments, where $n \geq 50$, should be sufficiently large to stabilize La^{3+}.

C.1.2 MD Simulations. Molecular dynamics simulations were performed using the MacroModel dynamics software (Shrödinger, Inc., Portland, OR) to generate low-energy structures of $Mo^{3+}(H_2O)_{550}$. Mo^{3+} is the largest trivalent metal ion for which there are available parameters for the OPLS 2005 force field implemented in this software, and was therefore used as an analog for La^{3+}. The crystallographic ionic radius of Mo^{3+} is 70% of La^{3+} (83 and 117 pm, respectively)[10] and this difference in size may lead to some discrepancies in how the ions affect the H-bonding network of water, particularly in the primary hydration shell. Previous results from our laboratory indicate that the free O—H stretches of water molecules located remotely from the ion on the surface of aqueous nanodrops are affected primarily by an ion's charge state with ion size having much smaller effect,[11] and we expect that charge state is the most important parameter for solvent patterning at these large cluster sizes. The excluded volume of either ion in a cluster with 550 water molecules is less than 0.1 % of the total nanodrop volume. After an initial geometry relaxation of $Mo^{3+}(H_2O)_{550}$ using molecular mechanics, the system was allowed to equilibrate for 10 ns using canonical ensemble stochastic dynamics at 133 K. Integration time steps of 1.5 fs were used and the SHAKE algorithim was applied to all hydrogen atoms. From the final equilibrated geometry, a dynamics trajectory of 60 ns was run during which a structure was saved every 60 picoseconds generating 1000 structures for $Mo^{3+}(H_2O)_{550}$. The position of La^{3+} within the cluster was not restrained, and the ion was internally solvated near the center of the droplet in the identified structures. An in-house routine written in MATLAB (The Mathworks Inc., Natick, MA) was used to calculate the angle θ between the dipole vector of each water molecule located at a distance d from the metal ion and the vector defined by the metal–oxygen displacement for all the identified structures. The resulting set of data (d, θ) was binned in 0.5 Å increments, and the average angle $<\theta>$ in each bin was calculated. The cutoff distance for the exponential fit to the $<\theta>$ data in Figure 3 was determined from distance measurements performed on 20 structures equally spaced in time throughout the trajectory that indicate surface water molecules are located 15.5 ± 1.6 Å from the ion. Taking into account shell thicknesses of ~2–3 Å (Figure 4), a distance cutoff of 13.5 Å was chosen. An additional 10 ns trajectory from a different starting geometry yielded a decay constant τ of 3.17 Å indicating that the starting geometry does not have a significant impact on the distance of ion-water ordering in these simulations.

C.2 References:

1. Bush, M. F.; O'Brien, J. T.; Prell, J. S.; Saykally, R. J.; Williams, E. R. *J. Am. Chem. Soc.* **2007**, *129*, 1612.
2. Bush, M. F.; Saykally, R. J.; Williams, E. R. *Int. J. Mass. Spectrom.* **2006**, *253*, 256.
3. Wong, R. L.; Paech, K.; Williams, E. R. *Int. J. Mass. Spectrom.* **2004**, *232*, 59.
4. Prell, J. S.; O'Brien, J. T.; Williams, E. R. *J. Am. Soc. Mass. Spectr.* **2010**, *21*, 800.
5. Bush, M. F.; Saykally, R. J.; Williams, E. R. *J. Am. Chem. Soc.* **2008**, *130*, 9122.

6. Chen, X. J.; Stace, A. J. *Chem. Commun.* **2012**, *48*, 10292.
7. O'Brien, J. T.; Williams, E. R. *J. Phys. Chem. A* **2008**, *112*, 5893.
8. O'Brien, J. T.; Williams, E. R. *J. Phys. Chem. A* **2011**, *115*, 14612.
9. Donald, W. A.; Leib, R. D.; Demireva, M.; O'Brien, J. T.; Prell, J. S.; Williams, E. R. *J. Am. Chem. Soc.* **2009**, *131*, 13328.
10. Shannon, R. D. *Acta. Crystallogr. A* **1976**, *32*, 751.
11. Prell, J. S.; O’Brien, J. T.; Williams, E. R. *J. Am. Chem. Soc.* **2011**, *133*, 4810.